Synoptic-Scale Climate Dynamics in Southern Patagonia Revealed through Stable Isotopes in Precipitation and Peat Mosses

by

Zhengyu Xia

A Dissertation

Presented to the Graduate and Research Committee

of Lehigh University

in Candidacy for the Degree of

Doctor of Philosophy

in

Earth and Environmental Sciences

Lehigh University

April 2, 2020

Approved and recommended for acceptance as a dissertation in partial fulfillment of the requirements for the degree of Doctor of Philosophy

Zhengyu Xia

Synoptic-Scale Climate Dynamics in Southern Patagonia Revealed through Stable Isotopes in Precipitation and Peat Mosses

April 02, 2020

Defense Date

Dissertation Director
Dr. Zicheng Yu

Approved Date

Committee Members:

Dr. Robert K. Booth

Dr. Benjamin S. Felzer

Dr. Yongsong Huang

ACKNOWLEDGMENTS

First of all, this dissertation is impossible without the supervision and support from my advisor Zicheng Yu, whose mentorship has inspired me to pursue intellectual challenge. My dissertation committee, Bob Booth, Ben Felzer, and Yongsong Huang have provided help and thoughts in directing my doctoral study. A special thanks to Nicolás Butorovic and Julie Loisel for their valuable suggestions on my research projects. The field and lab work parts of this dissertation received tremendous help from Jon Stelling and Yinsui Zheng. In addition, Alejandro Kusch, Rodrigo Munzenmayer, and Daniel Terán of the Wildlife Conservation Society (Chile) provided logistical support for field work at Karukinka Park, where amazing peat coring happened. EES Department has always been supportive over the blink of five years. Lastly, this dissertation is dedicated to my parents whom I love.

This work was supported by the National Science Foundation P2C2 program and several research grants and fellowships from department, college, and university.

TABLE OF CONTENTS

LIST OF FIGURES

LIST OF TABLES

ABSTRACT

The Southern Hemisphere Westerly Winds (SHWW) exert a critical control not only on regional climate in the Southern Hemisphere mid- and high-latitude regions, but also the global oceanic and atmospheric circulation, the biogeochemical cycle over the Southern Ocean, and the ice sheet in the Antarctic. However, the dynamic nature of the SHWW is still poorly known, which hinders our understanding of the future changes. Southern Patagonia is the only landmass intersecting the core belt of the SHWW, and regional climate is strongly shaped by the SHWW. There are rich *Sphagnum*-dominated peat bogs in southern Patagonia that have the potential to preserve the long-term SHWW variability. In this dissertation, through a systematic approach, I used stable isotopes in precipitation and peat mosses (*Sphagnum*) to present a new process-based understanding of the synoptic-scale climate dynamics in southern Patagonia that in turn reflect the dynamic nature of the SHWW.

The dissertation includes four inter-related but distinct chapters. First, I use a data-driven framework to show that blocking of westerlies is an inherent part of regional synoptic weather types that likely could control long-term precipitation $\delta^{18}O$ variability in southern Patagonia. Second, I provide a detailed analysis on physiological mechanisms underlying the carbon and water (hydrogen and oxygen) isotopic variations in peat mosses collected from southern Patagonian peat bogs. The results refine the potential of peat mosses for extracting paleoenvironmental information from peat archive. Third, I use a compilation of global peat mosses $\delta^{18}O$ data to show that the biochemical enrichment factor in cellulose synthesis that has been assumed to be a constant of +27‰ is temperature-dependent with stronger sensitivity at lower temperature, thereby reconciling the competing interpretations of existing laboratory experimental data. Finally, I use paired *Sphagnum* cellulose $\delta^{13}C$ and $\delta^{18}O$ measurements from a

radiocarbon-dated peat core collected from Tierra del Fuego, southern Patagonia, to reconstruct the SHWW variability during the late Holocene. I find that multiple large-magnitude shifts in synoptic-scale patterns occurred on centennial scale, with periods of much weakened SHWW and more frequent blocking conditions, which in turn are paced with the El Niño-Southern Oscillation.

PREFACE

The Southern Hemisphere Westerly Winds (SHWW) play a critical role in regulating regional and global climate. Not only do the SHWW influence temperature variations in the mid- and high-latitude regions and steer storm tracks, but the SHWW also interact with Southern Ocean current and upwelling systems, thereby affecting CO_2 degassing and the global carbon cycle. A number of studies have investigated the SHWW variability on paleoclimate timescales to understand their dynamic nature thorough reconstructing precipitation variability associated with the dominant westerly flow. Such studies have regarded the SHWW as a simplistic zonal wind-flow but did not consider the role of other synoptic weather types that could predominate at regional scale within the SHWW belt. As a result, the SHWW dynamics over various timescales is still unclear with competing observations and hypotheses in literature. This knowledge gap presents a key challenge in understanding the interactions between the SHWW and Southern Ocean CO_2 degassing process in the past, present, and future. In this dissertation, I focus on the prevailing synoptic-scale patterns in southern Patagonia and use paleoclimate data to provide new insights into the SHWW dynamics.

As the only landmass in the SHWW realm, southern Patagonia has extensive peat-forming ecosystems including rain-fed *Sphagnum*-dominated peat bogs on the eastern side of the Andes. Peat bogs are natural archives of past environmental variability and have been the subject of such studies for about a century. Stable isotopes of peat-forming plant remains are an emerging new proxy for extracting environmental information from peat records. In this dissertation, I further refine this approach for the "peat builder" *Sphagnum* mosses.

Stable isotopes are a powerful tracer in earth and environmental sciences, being applied to a broad range of research questions, which will be the common theme

throughout this dissertation. The dissertation is constructed to understand the fundamental processes and mechanisms that govern the isotopic variations in precipitation and peat mosses in southern Patagonia, with an overarching goal to use isotope data from peat archive for providing cross-scale insights into climate dynamics.

Chapter 1 is focused on the influence of synoptic-scale weather types and moisture transport pathways on precipitation $\delta^{18}O$ in southern Patagonia by analyzing 28-year-long monthly precipitation $\delta^{18}O$ data from Punta Arenas, Chile. I develop a new framework to leverage the value of such monthly-composited precipitation $\delta^{18}O$ data in identifying synoptic-scale mechanisms that could control the long-term precipitation $\delta^{18}O$ variability. In this framework, weather station precipitation data and backward trajectory modeling are combined to quantify the relative role of key synoptic weather types on monthly basis. I find that precipitation $\delta^{18}O$ in southern Patagonia is linked with the proportion of westerly-derived precipitation, while when the role of westerlies weakens, the synoptic weather types with blocking of westerlies become more important for regional precipitation. Such blocking-like conditions increase the proportion of precipitation derived from easterlies and northerlies that are characterized by higher $\delta^{18}O$ values in precipitation. Along-trajectory data further show the varying degrees of rainout-related fractionation for different moisture transport pathways, thereby linking precipitation $\delta^{18}O$ with synoptic-scale atmospheric circulation pattern and, by extension, the SHWW strength. This study provides a process-based understanding on the synoptic controls on precipitation $\delta^{18}O$ in southern Patagonia with implications for paleoclimate and paleoaltimetry studies in the SHWW realm.

Chapter 2 is focused on the environmental controls on the isotopic signals in *Sphagnum* mosses. Although there have been quite a few studies on this topic, there is no coherent understanding of physiological mechanisms underlying the isotopic variations in *Sphagnum*. By collecting and analyzing *Sphagnum* samples from diverse

microtopographical locations in Patagonian peat bogs, I find that both *Sphagnum* cellulose and *n*-alkane $\delta^{13}C$ show strong water film effect and are correlated with *Sphagnum* water content, while cellulose $\delta^{18}O$ and *n*-alkane $\delta^{2}H$ diverge in sensitivity to a common moisture gradient. Additional "bulk" leaf water isotope data reveal a complex mechanism for imprinting the signal of evaporative enrichment into cellulose $\delta^{18}O$, whereas there is a site-specific negative correlation between cellulose $\delta^{13}C$ and $\delta^{18}O$. Isotopic signals in long *Sphagnum* strands, however, show that cellulose $\delta^{18}O$ could track precipitation $\delta^{18}O$ changes at sub-annual scale. These results together demonstrate the potential of *Sphagnum* for preserving various paleoenvironmental information in peat. I propose that a coupled carbon and water isotope measurements provide a robust approach in peat-based paleoclimate reconstruction and particularly in distinguishing autogenic and allogenic processes.

Chapter 3 revisits the problem of the relationship between oxygen isotope fractionation in plant cellulose biosynthesis and temperature. Recently it has been shown that the biochemical enrichment factor, ε_{bio}, which had been always assumed to be a constant of +27‰, could increase with decreasing temperature, whereas there exist competing interpretations on these experimental results. I focus on *Sphagnum* mosses as a model plant and use a global compilation of *Sphagnum* cellulose $\delta^{18}O$ data to extend the experimental results that the ε_{bio} is indeed temperature-dependent with a stronger sensitivity if temperature is below 5°C. This finding is inferred since natural *Sphagnum* mosses have many unique physiological characteristics, including the "water buffer" that minimizes the influence of evaporative enrichment in leaf water. As such, my observational dataset and approach circumvent the complex physiology for vascular plants and limitations brought by laboratory experiments. Although the temperature-dependent ε_{bio} may only become an important factor in alpine and high-latitude regions or

in cold seasons, this factor should be considered in proxy system model for interpreting plant cellulose $\delta^{18}O$ data in paleoclimate and plant physiology studies.

Chapter 4 integrates all the new knowledge in the previous three chapters into developing a new 2000-year record of SHWW variability. I use dual measurements of *Sphagnum* cellulose $\delta^{13}C$ and $\delta^{18}O$ from a radiocarbon-dated peat core collected at Ariel Peatland in Tierra del Fuego to reconstruct past hydroclimate and atmospheric circulation patterns in southern Patagonia. The cellulose $\delta^{18}O$ data show several centennial-scale shifts of at least 2‰, reflecting the dynamic changes in the SHWW that modulate synoptic-scale patterns over the Drake Passage. Notably, when the SHWW are weakened, an increasing occurrence of blocking-like conditions favor more frequent easterly flows that enhance moisture supply sourced from the Atlantic Ocean as a result of tropical teleconnection under the El Niño condition. This scenario challenges the simplistic view of the SHWW as a zonal wind-flow pattern, while my reconstruction demonstrates that regional climate in the SHWW realm is strongly controlled by synoptic-scale processes.

Overall, the research presented in this dissertation will provide a new framework and opportunity for using precipitation isotope data to study the moisture transport; refine the physiological mechanisms that control isotopic variations in plants; expand the toolbox in paleoenvironmental analysis of peat cores; and advance our understanding of the Southern Hemisphere climate dynamics in the past and future.

CHAPTER 1

The influence of moisture transport pathways on monthly oxygen isotope composition of precipitation in southern Patagonia

Zhengyu Xia[1] and Nicolás Butorovic[2]

[1]Department of Earth and Environmental Sciences, Lehigh University, Bethlehem, PA, USA

[2]Laboratorio de Climatologia, Instituto de la Patagonia, Universidad de Magallanes, Punta Arenas, Chile

Abstract

Understanding the controlling factors on oxygen isotope composition of precipitation ($\delta^{18}O_p$) on a regional scale is the basis for interpreting isotope-based paleoclimate and paleoaltimetry records. Here we analyzed 28-year-long monthly $\delta^{18}O_p$ data in the Global Network of Isotopes in Precipitation (GNIP) from Punta Arenas (Chile), to determine the dominant controls on monthly $\delta^{18}O_p$ variability in southern Patagonia. We combined weather station precipitation data and atmospheric back trajectories to quantify the proportions of precipitation derived from different trajectory clusters for each month. Results show that the proportion of westerly-derived precipitation is the key driver of $\delta^{18}O_p$ variability on monthly timescales, partly caused by the amplifying effect of Andean isotopic rain shadow, despite that the percentage distribution of westerly-derived precipitation is skewed towards 100% due to the dominance of the Southern Hemisphere westerly winds. When the westerlies are weakened, other moisture transport pathways become more important. In particular, increasing northerly-derived precipitation—with trajectory path evading the influence of Andean isotopic rain shadow and having less rainout—increases $\delta^{18}O_p$. Reanalysis data indicate that the northerly-derived precipitation is related to blocking of the westerlies that would occur more frequently under the negative phase of the Southern Annular Mode. However, we did not find consistent evidence for the importance of the easterlies that were previously found to cause high $\delta^{18}O_p$ close to the Atlantic coast. Our results reinforce the argument that moisture transport pathways influence $\delta^{18}O_p$ due to synoptic-scale atmospheric circulations in modern setting and might have played a more important role over long timescales.

1.1. Introduction

Stable isotopes in water ($\delta^{18}O$ and $\delta^{2}H$) have been widely used as geochemical tracers in the studies of water cycle from regional to global scales (Bowen et al., 2019). Isotopic fractionation occurs in water molecules during phase transitions modulated by transport and also biotic processes within the hydrological cycle, leading to distinct variations in isotopic compositions across the hydrosphere (Gat, 2010). Of particular importance is the isotopic composition in precipitation (most of studies focus on oxygen isotopes in precipitation, $\delta^{18}O_p$) with a large number of data collected since the 1950s (Dansgaard, 1953). The $\delta^{18}O_p$ data showed empirical relationships with climatic variables such as air temperature in the high-latitude regions and precipitation amount in the tropical regions (Dansgaard, 1964). The Rayleigh distillation model that depicts isotopic fractionations in air mass rainout processes could explain much of $\delta^{18}O_p$ variability at various temporal and spatial scales in both observations and models (Dansgaard, 1964; Rozanski et al., 1993; Jouzel et al., 2000). These well-established relationships between $\delta^{18}O_p$ and climatic variables led to applying stable isotope proxies in terrestrial climate archives to reconstruct past hydrological and climatic conditions (e.g., Libby et al., 1976; Jouzel et al., 1987; von Grafenstein et al., 1999; Wang et al., 2001). Over geological timescales, because of the strong connections among topography, climate, and atmospheric circulations, stable isotopes also have been used as proxies for terrain elevation to reconstruct landscape evolution (e.g., Chamberlain & Poage, 2000; Blisniuk et al., 2005). However, studies also revealed that the drivers controlling $\delta^{18}O_p$ variations are more complex and that air mass origin and history (Rindsberger et al., 1983; Sjostrom & Welker, 2009; Bailey et al., 2019), in-cloud and below-cloud processes (Risi et al., 2008; Aggarwal et al., 2016; Crawford et al., 2017), as well as moisture recycling (Friedman et al., 2002; Winnick et al., 2014; Kong & Pang, 2016), are also important in some regions. It is particularly relevant in regions with complex terrain, where regional

topographic features can additionally influence air mass transport and water vapor condensation, and consequently the isotopic fractionations in water vapor and precipitation (Galewsky, 2009; Guan et al., 2009; Sinclair et al., 2011; Lechler & Galewsky, 2013; Callow et al., 2014; Bailey et al., 2019).

Monitoring temporal variations in $\delta^{18}O_p$ provides an excellent opportunity to elucidate the confounding factors that influence $\delta^{18}O_p$ for a specific location or region. For many studies of this kind, precipitation samples were collected for individual events or at daily intervals. Rather than simply analyzing the relationships between $\delta^{18}O_p$ and local meteorological parameters, event-based studies usually link the $\delta^{18}O_p$ signal in each individual sample with the origin and history of an air mass preceding that event or a specific synoptic weather type (e.g., Friedman et al., 2002; Mayr et al., 2007a; Barras & Simmonds, 2008; Sjostrom & Welker, 2009; Crawford et al., 2013; Wang et al., 2017; Bailey et al., 2019), using tools such as the U.S. National Oceanic and Atmospheric Administration (NOAA) Air Resources Laboratory (ARL) Hybrid Single-Particle Lagrangian Integrated Trajectory (HYSPLIT) model (Stein et al., 2015). The rationale behind this practice is that the $\delta^{18}O_p$ signal reflects isotopic fractionation that occurs in evaporative source and during moisture transport more than local meteorology (Putman et al., 2017), although precipitation type (convective vs. stratiform) is also an important local factor affecting $\delta^{18}O_p$ in the tropical and mid-latitude regions (Aggarwal et al., 2016; Sun et al., 2019). Another important precipitation isotope database is the Global Network of Isotopes in Precipitation (GNIP) that archive isotope data from monthly-composited precipitation (IAEA/WMO, 2019). Because isotope data from monthly-composited precipitation may have mixed isotopic signals from multiple precipitation events during that month, studies using GNIP data usually focus on precipitation isotope seasonality, long term trends, empirical relationship with climatic variables, and statistics of meteoric water lines inferred from each individual GNIP station (Rozanski et al.,

1993). The influence of moisture sources and transport pathways on individual GNIP monthly $\delta^{18}O_p$ observations is rarely explored (Bailey et al., 2015) due to the mixing signals from multiple precipitation events that make identifying process-based mechanisms difficult (Bailey et al., 2019). In fact, some of the GNIP stations have observational data over several decades. These observational data encompass longer-term $\delta^{18}O_p$ variability originated from shifts in prevailing synoptic-scale atmospheric circulation patterns than event-based data that usually only span one or a few years (Sjostrom & Welker, 2009).

Here, we developed a new framework to leverage the value of GNIP monthly-composited $\delta^{18}O_p$ data in identifying process-based synoptic-scale mechanisms that control $\delta^{18}O_p$ variability. We analyzed 28-year-long GNIP monthly $\delta^{18}O_p$ data from Punta Arenas (Chile) to understand the influence of moisture transport pathways on monthly-composited $\delta^{18}O_p$ in southern Patagonia, a region surrounded by ocean and with complex terrain. Southern Patagonia is in the core belt of the Southern Hemisphere Westerly Winds (SHWW) that exert strong and year-round influence on regional climate. Previous isotope-based paleoclimate and paleoaltimetry studies in this region (and northern Patagonia) assumed that the westerlies—that pass over the Andes—are the sole moisture transport path for the eastern side of Patagonia (Blisniuk et al., 2005; Colwyn et al., 2019; Colwyn & Hren, 2019), but did not consider any shifts in prevailing synoptic-scale atmospheric circulations that would have modified the moisture transport paths and consequently the observed $\delta^{18}O_p$ signals (Xia et al., 2018). To extract the effect of moisture trajectory paths on monthly-composited $\delta^{18}O_p$, if any, we combined weather station precipitation data and the HYSPLIT back-trajectory model to quantify the proportions of precipitation attributed to different trajectory clusters for each month. The aim of this study is to answer the following three questions: (1) Are the prevailing SHWW the sole moisture transport pathway in southern Patagonia? (2) Does the

proportion of westerly-derived precipitation influence $\delta^{18}O_p$ in southern Patagonia? (3) Is the proportion of westerly-derived precipitation linked with synoptic-scale atmospheric circulation pattern?

1.2. Regional setting

Punta Arenas is the capital city of Chile's southernmost Magallanes Region, and one of the southernmost cities in the world. The city is situated with the Strait of Magellan to the east and low-lying hills and plateaus to the west. The GNIP Punta Arenas station (53.00°S, 70.83°W, 38 m above sea level (asl)) is located ~20 km north of the main city at Punta Arenas airport (PUQ). The local terrain to the west is flat at airport without low-lying hills and plateaus, unlike the main city.

Punta Arenas is in the unique topographic context of southern Patagonia where climate is strongly influenced by the interaction between the strong SHWW and the north-to-south oriented Andean mountain ranges (Figure 1.1). A large precipitation gradient occurs from the Pacific to Atlantic coasts as a result of uplift and downslope subsidence of westerlies and their embedded disturbances (Garreaud et al., 2013; Lenaerts et al., 2014). Therefore, Punta Arenas (including its airport) is clearly in the Andean rain shadow (Berman et al., 2012), although the Andean topographic barrier on the west is lower, with most terrain elevations less than 1000 m asl, than the rest of Patagonia (Figure 1.1). The mean annual precipitation amount in Punta Arenas airport was 402 mm, based on data from the Global Historical Climatology Network (GHCN) Version 2 (NOAA, 2019) during the period 1990–2017. It is an order of magnitude less than Andean locations in the same latitude where mean annual precipitation amounts are more than 3000 mm (Schneider et al., 2003; Weidemann et al., 2018). Our analysis of combined wind sensor and precipitation data from airport weather station indicates that "local" westerlies (NW, WNW, W, WSW, and SW) account for 72% of total hours but

only 41% of total precipitation amount during the period 1990–2017 (Figures A1a and A1b). In terms of the quotient between precipitation and frequency of the respective "local" wind direction (Mayr et al., 2007b), however, "local" non-westerlies are over three times more effective in bringing precipitation to Punta Arenas (Figure A1c). This reinforces the prevailing rain shadow effect on the leeward side of the Andes, while westerlies are still able, although less effectively, to deliver moisture to Punta Arenas.

The influence of the SHWW on Punta Arenas is year-round. During austral summer, the SHWW form a condensed and strong belt between 45°S and 55°S and maximum wind speeds are reached in Punta Arenas. During austral winter, the SHWW belt expands northward as far as 30°S while the wind speed only relatively weakens in the south, including at Punta Arenas (Garreaud et al., 2009). Despite the seasonal variations in the SHWW, the seasonality of precipitation in Punta Arenas is very weak with only slightly more precipitation during austral autumn (Daley et al., 2012). The mean annual air temperature in Punta Arenas airport was 6.2 °C, while the mean warmest month (January) air temperature was 10.8 °C and the mean coldest month (July) air temperature was 1.6 °C during the period 1990–2017 based on data from GHCN Version 3 (NOAA, 2019).

Inter-annual or long-term climate variability in southern Patagonia is tied to the large-scale Southern Annular Mode (SAM), which is defined as the difference in zonal mean sea level pressure (SLP) between 40° S and 65° S (Marshall, 2003). This pressure gradient controls hemisphere-wide strength and latitudinal position of the SHWW, and consequently, their associated storm tracks. Instrumental and reanalysis data suggest the leading role of the SAM on both temperature and precipitation patterns in broad regions of the extratropical Southern Hemisphere, including southern Patagonia (Gillett et al., 2006; Garreaud et al., 2009). Specifically, a positive phase of the SAM, through stronger and southwardly positioned SHWW, increases air temperature but only marginally

decreases precipitation in the domain of Punta Arenas, and vice versa (Gillett et al., 2006; Garreaud et al., 2009; Moreno et al., 2014). The weak influence of the SAM on precipitation in southern Patagonia is partly due to the fact that the SAM is a hemisphere-wide climate mode, while regional precipitation variability is mostly tied to synoptic-scale processes.

1.3. Data and methods

1.3.1. GNIP isotope data

Monthly precipitation isotope data from the GNIP Punta Arenas (airport) station are available from 1990 to 2017 with some short data gaps (Table A1) (IAEA/WMO, 2019). In total there are 298 individual $\delta^{18}O_p$ measurements. The dataset contains some very high or even positive $\delta^{18}O_p$ values after 2002 (see Figure 1.2b), which have been pointed out by Daley et al. (2012). These samples likely experienced evaporation for unknown reasons, and the reason why these very high $\delta^{18}O_p$ values only appeared after 2002 is unknown. Since 2010, GNIP Punta Arenas station has started to label isotope data that showed a hint of evaporation if the calculated deuterium excess (*d*-excess, defined as $\delta^2H - 8 \times \delta^{18}O$) value was below zero, although some of these potential problematic data were not necessarily impacted by sample evaporation as *d*-excess usually have a relatively large scatter and a value lower than zero is not unusual in maritime climate (Gat, 2010) such as in Punta Arenas. For the following HYSPLIT analysis, we filtered out GNIP data by removing those $\delta^{18}O_p$ data that were above –3‰ *or* that had corresponding *d*-excess below –10‰ (Figure 1.2a). These criteria were subjectively chosen but reasonable as $\delta^{18}O_p$ and *d*-excess values falling in these ranges are indeed too extreme to occur in monthly-composited precipitation at this latitude. Another GNIP station in Ushuaia (Argentina), located ~250 km southeast to Punta Arenas (see Figure 1.1), does not have any $\delta^{18}O_p$ data above –6.8‰ during its monitoring period 1981–2002.

These two stations have a similar climate, yet Punta Arenas has a weighted mean annual $\delta^{18}O_p$ value 2–3‰ higher than Ushuaia; the exact value depends on how the potential outliers in both datasets are treated (Daley et al., 2012). Considering this 2–3‰ offset would justify our conservative cut-off value (–3‰) for $\delta^{18}O_p$. There are a few data with *d*-excess below –10‰ in Ushuaia likely due to sample evaporation as well, but these data only occurred before 1988 and were not an intermittent and common feature. This observation would also justify our cut-off value (–10‰) for *d*-excess. Nonetheless, we cannot rule out the small possibility that a few of these anomalously high $\delta^{18}O_p$ or low *d*-excess values are naturally occurring. If they were, the collected precipitation samples might be caused by a dominant contribution of local convective precipitation (Aggarwal et al., 2016; Sun et al., 2019) or by a significant role of raindrop post-condensation re-evaporation (Mayr et al., 2007a; Crawford et al., 2017). Both mechanisms would underplay the role of large-scale moisture transport pathway in shaping the $\delta^{18}O_p$ value, thus removing a few of such values does not affect our analysis on robust data. We also removed two very low monthly $\delta^{18}O_p$ values. These two data points appear out of bound of typical observations (Figure 1.2a) and likely suggest additional factors that are not considered in our HYSPLIT framework, otherwise these two extremes would have skewed the analysis. After the step of data filtering (all filtered out data are listed in Table A1), we obtained a final dataset with 265 $\delta^{18}O_p$ measurements. Each $\delta^{18}O_p$ datum has a corresponding *d*-excess value calculated from its paired $\delta^{2}H_p$ (hydrogen isotope composition of precipitation) datum.

Among the selected data, it is clear that monthly air temperature has a primary control on monthly $\delta^{18}O_p$ value as shown by a significant, though weak, linear correlation ($p < 0.001$) (Figure 1.2c). By contrast, monthly precipitation amount is not significantly correlated with monthly $\delta^{18}O_p$ at the 0.05 significance level ($p = 0.07$) (Figure 1.2d).

A linear regression yields the relationship between monthly $\delta^{18}O_p$ and monthly air temperature (T) as:

$$\delta^{18}O_p = 0.403 \times T - 12.075 \ (r = 0.50) \quad (1)$$

where data for T are from GHCN version 3 (NOAA, 2019) (Figure 1.2c). The observed seasonality in $\delta^{18}O_p$ is a prevalent phenomenon across the mid- and high-latitude regions even in maritime climate (Gat, 2010). This $\delta^{18}O_p$ seasonality is driven by multiple processes including changing moisture source region and condition as well as changing transport path and condensation history of water vapor among different seasons via the Rayleigh mechanism (Rozanski et al., 1993; Gat, 2010; Putman et al., 2017). These net effects on $\delta^{18}O_p$ can be simply summarized by the empirical correlation with local air temperature. However, monthly air temperature is no more significantly correlated with $\delta^{18}O_p$ for summer (December–February; DJF) ($p = 0.52$) and winter (June–August; JJA) ($p = 0.67$), and it explains less variance in $\delta^{18}O_p$ for autumn (March–May; MAM) ($r = 0.38$, $p < 0.01$) and spring (September–November; SON) ($r = 0.38$, $p < 0.01$). We define the $\delta^{18}O_p$ residual ($\delta^{18}O_p^e$) as the observed $\delta^{18}O_p$ value ($\delta^{18}O_p^o$) minus the regressed $\delta^{18}O_p$ value ($\delta^{18}O_p^r$) in equation (1):

$$\delta^{18}O_p^e = \delta^{18}O_p^o - \delta^{18}O_p^r \quad (2)$$

which allows us to explore the influence of moisture transport pathway on monthly $\delta^{18}O_p$ variability that is unrelated to $\delta^{18}O_p$ seasonality and/or air temperature. This approach is similar but not the same with the multivariate regression approach by Krklec and Domínguez-Villar (2014) who included both air temperature and monthly percentages of different moisture sources into their multivariate models.

1.3.2. Weather station precipitation data

Punta Arenas airport cumulative precipitation amount data at 6-hour intervals (at UTC time 00/06/12/18 hour) are provided by the Dirección Meteorológica de Chile

(available for download at https://climatologia.meteochile.gob.cl). The data were collected by Punta Arenas airport weather station. This same weather station also reports monthly climatology data to the GHCN (as presented in Section 1.3.1) and operates isotope sample collection for the GNIP (Stefan Terzer-Wassmuth, personal communication, 2019). The quality of 6-hour cumulative precipitation data is robust as we find the monthly cumulative precipitation amount data, calculated from the sum of all 6-hour precipitation data for each month, are clustering on the 1:1 line when plotted against either reported GHCN or GNIP monthly precipitation amount data (Figures A2a and A2b). Precipitation events (at least 0.1 mm) were recorded during 17% of all 6-hour intervals. With this 6-hour cumulative precipitation data, we can explicitly know the time and precipitation amount of each precipitation event that together constitute the monthly precipitation sample that GNIP measured for isotopic composition.

1.3.3. Air mass back trajectories

We run HYSPLIT back-trajectory model to reconstruct the origin and path of air mass that resulted in precipitation event recorded by the weather station described above. We employed a Python-based package for HYSPLIT (PySPLIT) to achieve a fast and flexible workflow in trajectory generation and analysis (Cross, 2015). Five-day (120-hour) air mass backward trajectory was generated four times (at UTC time 00/06/12/18 hour) for each day from 1990 to 2017 to match with the 6-hour cumulative precipitation data from weather station. We tested four different initial back-trajectory heights at 500, 1000, 1500, and 2000 m above ground level (agl). For gridded meteorological datasets, we used the Global Data Assimilation System (GDAS) reanalysis dataset (1.0° spatial resolution) for the period 2005–2017. For the period 1990–2004 during which the GDAS dataset was not available, we used the National Centers for Environmental Prediction/National Center for Atmospheric Research (NCEP/NCAR) reanalysis dataset

(2.5° spatial resolution). Both datasets are archived on NOAA ARL website (https://www.ready.noaa.gov/archives.php) (Kalnay et al., 1996). Based on the 6-hour cumulative precipitation data from weather station, trajectory files that are not "precipitation-producing" were deleted. Then, all remaining trajectory files used for analysis are associated with documented precipitation events. To visualize the general trajectory pathway and to compare the difference between different initial back-trajectory heights and between gridded meteorological datasets, we generated trajectory frequency contours by binning all trajectory end point data in each 1.0° grid following Xia et al. (2018).

1.3.4. Trajectory clustering

For each initial back-trajectory height, we grouped our trajectories into four clusters based on where trajectories entered into southern Patagonian landmass. Although HYSPLIT GUI has provided a *k*-means clustering algorithm, it suggests that only a large number of clusters are appropriate to represent all trajectories in an acceptably low total spatial variance. To simplify the solution, we grouped trajectories based on the locations of back-trajectory end points when trajectories came across the eastern, northern, western, and southern boundaries of southern Patagonian landmass (Figure A3). These trajectories were then clustered as the *distal* easterlies, northerlies, westerlies, and southerlies, respectively (Figure 1.3). These trajectory clusters represent major synoptic weather types in this region (see Schneider et al., 2003). Here the word "*distal*" is to discern our definition of air mass transport direction that is based on modeling its back-trajectory over a course of time from those define transport direction based on "local" weather station wind direction (e.g., Figure A1 introduced in Section 1.2 and Bailey et al., 2019). Using four simplified distal trajectory clusters reflects our goal that we are mainly interested in how Patagonian "upstream" terrains influence $\delta^{18}O_p$ in relatively

inland Punta Arenas. Costal terrains on western (the Andes) and southern (the Cordillera Darwin) boundaries would produce the isotopic rain shadow effect (Chamberlain & Poage, 2000; Stern & Blisniuk, 2002) on their leeward side—air masses would have to experience orographic uplift, condensation, and rainout before reaching Punta Arenas (Figure 1.1). By contrast, terrains on northern and eastern boundaries are relatively flat without main topographic barrier, thus air masses would experience different degrees of fractionation.

To further understand the rainout processes that occur among different trajectory clusters, we calculated median, lower quartile, and upper quartile values for specific humidity and precipitation rate (both are meteorological output variables in HYSPLIT) in each hour along modeled trajectories. The meteorological output variables have been used to characterize air mass rainout history in some event-based studies (e.g., Barras & Simmonds, 2008; Crawford et al., 2017). In reality, each trajectory has its own air mass history, not only in terms of trajectory path but also along-trajectory meteorological data. Thus, the aim of this analysis is to characterize the general evolutions of air masses in different trajectory clusters rather than to quantitively model the degree of rainout and isotopic fractionation in air masses.

1.3.5. Proportion of precipitation from different trajectory clusters

Because each trajectory is corresponding to a 6-hour precipitation event, then the fraction of each trajectory cluster contributing to monthly total precipitation is calculated as (using the cluster of distal easterlies as an example):

$$dE\ (\%) = \frac{\sum p_E}{P} \times 100\% \tag{3}$$

where dE is the percentage of distal easterly-derived precipitation, Σp_E is the sum of distal easterly-derived 6-hour precipitation, and P is the sum of all 6-hour precipitation

for a particular month. Following the equation (3), the percentages of distal northerly-derived (dN), westerly-derived (dW), and southerly-derived (dS) precipitation can be also calculated (Figure 1.3). As such, we could quantify the contributions of major synoptic weather types to total monthly precipitation.

To investigate the influence of moisture transport pathways on $\delta^{18}O_p$ in Punta Arenas, we evaluated if $\delta^{18}O_p^e$ metric is significantly correlated with dE, dN, dW, and dS, using Pearson correlation coefficient. The statistical analysis was run for four different austral seasons and also all months combined. Correlation is considered significant if *p*-value is less than 0.1. If so, it would indicate that precipitation derived from that trajectory cluster has on average a distinct high or low $\delta^{18}O_p$ value relative to others, leading to statistical correlation between its proportion and monthly $\delta^{18}O_p^e$ in our framework. If significant correlation was found between $\delta^{18}O_p^e$ and dW within a specific season, we calculated the regression coefficient (the slope of the regression line) to determine the sensitivity of $\delta^{18}O_p$ to changing proportion of westerly-derived precipitation. To further investigate the cause for the distinct $\delta^{18}O_p$ value in certain trajectory cluster, we run a similar analysis of *d*-excess data to diagnose if moisture recycling or post-condensation raindrop re-evaporation is the driver of $\delta^{18}O_p$.

To understand the prevailing synoptic-scale atmospheric circulation patterns that drive variations in the proportions of distal easterly- and northerly-derived precipitation, we examined their spatial relationships with SLP and zonal wind speed fields from the independent European Centre for Medium-Range Weather Forecasts (ECMWF) ERA-interim reanalysis product on KNMI Climate Explorer (https://climexp.knmi.nl/). Spatial correlation is considered significant if *p*-value is less than 0.1.

1.4. Results and Discussion

1.4.1 Precipitation origin from the HYSPLIT framework

Mean monthly proportions of precipitation derived from the HYSPLIT framework are consistent with empirical observations that the strong SHWW belt dominates over Punta Arenas all year long (Table 1.1). The distal westerlies for all months combined contribute at least 76.4% of precipitation despite that Punta Arenas is on the leeward side of the Andes under the influence of the SHWW. In general, the dW histogram is highly skewed towards the range of 95–100%, meaning that for most months the dW are higher than 95% while other trajectory cluster proportions are less than 5% (Figure A4). The dW have clear seasonal variations that are also consistent with the observed SHWW seasonal migration (see Section 1.2). The dW are higher and lower during summer and winter, respectively, while the shoulder seasons (autumn and spring) have intermediate dW (Table 1.1).

The derived monthly proportions of precipitation for each trajectory cluster are sensitive to the meteorological reanalysis dataset used for modeling back trajectories. Although back trajectories were modeled over different periods, using the GDAS reanalysis dataset would generate lower dW than using the NCEP/NCAR reanalysis dataset, especially during winter by at least 10%, but not for summer (Table 1.1). In addition, using GDAS would also generate higher dE than dN, while using NCEP/NCAR would generate the opposite. Considering that the NCEP/NCAR reanalysis dataset has a lower resolution, some of their modeled back-trajectory paths likely would be deflected compared to the GDAS-based back-trajectory paths, leading to biased mean estimates on the origin of precipitation. Therefore, back-trajectory clustering results for periods 1990–2004 and 2005–2017 should be treated separately in the following discussion because these were derived from different meteorological reanalysis datasets.

Furthermore, the derived monthly proportions of precipitation for each trajectory cluster are also sensitive to the choice of initial back-trajectory height. Although the four selected initial back-trajectory heights represent the levels at which most of atmospheric moisture is entrained (Bershaw et al., 2012), higher initial back-trajectory heights would generate higher dW. These results demonstrate the role of boundary-layer wind shear on modifying back-trajectory path, although many studies have concluded that different initial back-trajectory heights would not affect the general path of back-trajectory (Bershaw et al., 2012; Krklec & Domínguez-Villar, 2014; Fiorella et al., 2015; Brittingham et al., 2019). The influence of initial back-trajectory height is also illustrated in the plots of precipitation-producing trajectory frequency contours that encompassed the Atlantic Ocean and northern Patagonia underscoring distal easterlies and northerlies when back trajectories were initiated at 500 m agl (Figures 1.4a and 1.4c), but not so when back trajectories were initiated at higher levels (Figures 1.4b and 1.4d).

1.4.2. The influence of moisture transport pathways on $\delta^{18}O_p$

In the correlation coefficient heat map (Figure 1.5), the statistically significant correlation pairs are mainly found when trajectories were modeled at initial heights of 1500 m and 2000 m agl. No significant correlation is found if initial back-trajectory height was 500 m agl, although a lower initial back-trajectory height tends to better represent the synoptic weather types related to non-westerlies as shown in Table 1.1 and Figure 1.4. If different trajectory clusters indeed have distinct $\delta^{18}O_p$ values and their monthly variations can influence monthly-composited $\delta^{18}O_p$ in Punta Arenas, the results shown in Figure 1.5 might indicate that the 1500 and 2000 m agl levels are close to the actual heights of water vapor transport. Therefore, we mainly discuss the results derived from the initial back-trajectory heights of 1500 and 2000 m agl.

The dW show negative correlations with $\delta^{18}O_p^e$ when all months are combined in both GDAS- and NCEP/NCAR-based results. The statistically significant correlation is mainly manifested during winter for the NCEP/NCAR reanalysis dataset, and during shoulder seasons for the GDAS reanalysis dataset. Neither GDAS nor NCEP/NCAR reanalysis datasets generated statistically significant correlation between dW and $\delta^{18}O_p^e$ in summer, while the GDAS reanalysis dataset generated negative correlations between dS and $\delta^{18}O_p^e$ in summer. The dN show positive correlations with $\delta^{18}O_p^e$ when all months are combined or within a specific season (except summer). These positive correlations are found in both GDAS and NCEP/NCAR-based results. For dE, the results diverge between the GDAS and NCEP/NCAR reanalysis datasets. Specifically, the NCEP/NCAR reanalysis dataset did not generate any statistically significant correlation between dE and $\delta^{18}O_p^e$, while the GDAS reanalysis dataset did generate significant correlation between dE and $\delta^{18}O_p^e$, but it is negative during winter and positive during autumn (Figure 1.5).

Our results present evidence that an increasing proportion of distal westerly-derived precipitation decreases $\delta^{18}O_p$ in Punta Arenas. This moisture transport pathway effect is not manifested for summer during which the SHWW strength reaches maximum at this latitude and causes the distal westerlies almost the sole moisture transport pathway (Table 1.1). Nonetheless, an increasing proportion of distal southerly-derived precipitation might be able to decrease $\delta^{18}O_p$ during summer, although in general southerlies contribute very little to total precipitation (Table 1.1). These findings are consistent with the Rayleigh distillation model that predicts lower $\delta^{18}O_p$ on the leeward side of mountains due to the "upstream" orographic and rainout effects of westerlies (Stern & Blisniuk, 2002) and potentially southerlies. This isotopic rain shadow effect may not be as strong as other parts of Patagonia due to the lower Andean elevation at the latitude of Punta Arenas (Figure 1.1), but our analysis still demonstrated this link. Along-trajectory meteorological data in distal westerlies indeed show orographic rainout during

air mass transport. The specific humidity starts to slightly decrease about 5 hours prior to reaching Punta Arenas (Figure 1.6e). The precipitation rate increases and decreases about 10 hours and 3 hours before reaching Punta Arenas, respectively, consistent with the orographic effect as "wet windward and dry leeward" conditions (Figure 1.6f).

The decrease in the proportion of distal westerly-derived precipitation implies that precipitation derived from secondary transport pathways become more important, in particular the distal easterlies and northerlies (Table 1.1). However, because the NCEP/NCAR and GDAS reanalysis datasets have discrepancy in resolving the trajectory paths for distal easterlies and northerlies, caution should be taken in our interpretations. For the higher-resolution GDAS dataset, an increasing proportion of distal northerly-derived precipitation would increase $\delta^{18}O_p$, meaning that distal northerly-derived precipitation has a relatively higher $\delta^{18}O_p$. There are two possible causes. First, distal northerlies tend to have a less orographic rainout during moisture transport. This is supported by along-trajectory meteorological data showing that the specific humidity does not have appreciable changes, although the specific humidity does slightly decrease if initial back-trajectory height was 2000 m agl (Figure 1.6c). In addition, the precipitation rate increases only around 4 hours prior to reaching Punta Arenas, unlike distal westerlies that show clear "up-and-down" pattern (Figure 1.6f). Second, air masses associated with distal northerlies are likely supplied by recycled moisture through plant transpiration flux. In reality, the distal northerlies in our HYSPLIT framework have a longer transport length on continent, similar to the setting with a stronger isotopic "continental effect" that should have increased the degree of rainout and decreased $\delta^{18}O_p$ (Dansgaard, 1964; Rozanski et al., 1993). However, only minimal changes in along-trajectory specific humidity require an efficient moisture recycling. If most of the moisture were recycled through evaporation of surface water from landmass, which induced an additional kinetic fractionation, we would expect a lower $\delta^{18}O_p$ signal for

distal northerlies, in opposite to the results. Therefore, it is possible that plant transpiration from Patagonian grasslands, which return water vapor without kinetic fractionation, might account for the majority of evapotranspiration flux (Jasechko et al., 2013). Recent studies have paid attention to the role of grassland ecosystem in modulating the hydrological cycle, as grasslands are efficient in recycling moisture and could reach a dynamic balance between precipitation and evapotranspiration fluxes (Mix et al., 2013; Chamberlain et al., 2014). This role of grassland transpiration is at least supported by the finding that the *d*-excess—a metric that would have been higher if the proportion of recycled moisture through evaporation was higher (Gat et al., 1994)—is not significantly correlated with dN except during spring (Figure 1.7). In fact, we found that the dW and dE are negatively and positively correlated with *d*-excess, respectively (Figure 1.7). We speculate that the degree of raindrop post-condensation re-evaporation is the main mechanism controlling *d*-excess variability in Punta Arenas. Specifically, distal westerlies have a higher proportion of drizzle precipitation (Figure 1.8) in which raindrop re-evaporation is significant in decreasing *d*-excess (Mayr et al., 2007a), while distal easterlies have a higher precipitation rate, thereby minimizing the raindrop re-evaporation effect (Figure 1.8). Precipitation event samples collected at Río Gallegos and Laguna Potrok Aike in eastern Patagonia (Mayr et al., 2007a; see Figure 1.1 for locations) and other semi-arid regions such as southeast Australia (Crawford et al., 2017) also showed that drizzle precipitation was subjective to raindrop re-evaporation and support our speculation. Nonetheless, grassland transpiration flux is also seasonal and probably only dominant during warmer seasons when biomass is built up (Mix et al., 2013). Additional studies are needed to partition evaporation and transpiration fluxes from terrestrial ecosystems and to investigate their effects on stable isotope compositions of water vapor and precipitation.

For GDAS-based distal easterlies, from along-trajectory meteorological data we found that the specific humidity decreases around 10 hours prior to reaching Punta Arenas (Figure 1.6a). At the same time, the precipitation rate increases and remains high (Figure 1.6b). Such a sustained rainout process would likely result in lower $\delta^{18}O_p$ with increasing dE. This could occur if $\delta^{18}O_p$ derived from distal easterlies was even relatively lower than that derived from other trajectory clusters, in particular the distal westerlies. This scenario is, however, only found in winter, while the direction of correlation shifts to opposite in autumn (Figure 1.5). To understand the reason for this seasonal shift in the correlation between dE and $\delta^{18}O_p^e$, we examined the along-trajectory specific humidity and precipitation rate changes separately for these two seasons (Figure A5). The results show that the sustained rainout might be the case for winter, but not for autumn. In the latter case, the precipitation rate decreases around 5 hours prior to reaching Punta Arenas, thus decreasing the degree of rainout en route to Punta Arenas (Figure A5d). Overall, these results indicate that the degree of rainout en route to Punta Arenas matters for $\delta^{18}O_p$ in distal easterlies for different seasons.

The along-trajectory meteorological data from the lower-resolution NCEP/NCAR reanalysis dataset show patterns discrete and less clear than the GDAS reanalysis dataset, although the key characteristics for distal westerlies shown in GDAS is also reproduced (Figure A6). As mentioned in Section 1.4.1, the trajectory paths modeled from the NCEP/NCAR dataset might be deflected, particularly for distal northerlies that were relatively overestimated compared to GDAS, thus along-trajectory meteorological data might be misleading. Instead, we focus on the general synoptic-scale atmospheric circulation patterns that might have caused high dN. With independent ERA-interim reanalysis fields, we found that the dN is correlated with negative SLP anomaly over northwestern Patagonia and its adjacent Pacific Ocean, and positive SLP anomaly centered over the eastern Antarctic Peninsula (Figure 1.9e). This synoptic-scale feature

resembles a regional negative phase of the SAM and provides high-latitude blocking for the westerlies (Figure 1.9f) (Agosta et al., 2015). The dE also show a similar but weaker correlation with SLP or zonal wind speed fields (Figures 1.9g and 1.9h). Therefore, although the trajectory paths for distal easterlies and northerlies modeled from the NCEP/NCAR reanalysis dataset are less reliable than GDAS, their synoptic-scale features are not.

1.4.3. Implications for paleoclimate and paleoaltimetry reconstruction

The response of $\delta^{18}O_p^e$ to dW in Punta Arenas as shown in our analysis indicates that $\delta^{18}O_p$ variations preserved in terrestrial climate archives on the leeward side of the Andes are suitable for reconstructing past variability of the SHWW. When the SHWW were strengthened at this latitude, regional precipitation is governed by prevailing westerlies and their associated storm tracks (Garreaud, 2007; Garreaud et al., 2013). When the SHWW were weakened with an overall reduced SLP gradient over the Drake Passage (Figure 1.9), other moisture transport pathways such as easterlies and northerlies that are often a result of occasional atmospheric blockings would become more important. A progressively positive shift in the SAM and an overall strengthening and poleward shift in the SHWW and their associated storm tracks during recent decades have been observed (Marshall, 2003; Abram et al., 2014). The current dominance of SHWW is, however, not always the case in the past. For instance, proxy data have shown that the SAM was in an extreme negative phase during the fifteenth century, meaning that the SHWW strength was much reduced during that time (Abram et al., 2014). Therefore, the role of other moisture transport pathways during the waning of SHWW is important for understanding the connection between the SHWW and $\delta^{18}O_p$.

A previous study close to the Atlantic coast (Río Gallegos and Laguna Potrok Aike (see Figure 1.1) suggested that precipitation event samples associated with easterlies

and northerlies have $\delta^{18}O_p$ signals ~7‰ higher than westerlies due to a much less orographic and rainout effect (Mayr et al., 2007a). However, our results presented here show that an increasing dE does not necessarily increases $\delta^{18}O_p$ but could decrease $\delta^{18}O_p$ in Punta Arenas during winter when the rainout effect is significant for easterlies. This may reflect the fact that Punta Arenas is in a central locus of Patagonian landmass, ~170 km away from the Atlantic coast. In addition, the Andean divide at this latitude is not as high as other parts of Patagonia. This may further reduce the "upstream" fractionation that has occurred in air masses delivered by westerlies. Therefore, terrestrial climate archives such as lakes and peat bogs closer to the Atlantic Ocean would be more sensitive in detecting the long-term variability in the SHWW from the $\delta^{18}O_p$ records. Indeed, sensitivity analysis indicates that a 20% less westerly-derived precipitation could cause a 0.8–1.3‰ higher $\delta^{18}O_p$ in Punta Arenas, which is not as high as at sites close to the Atlantic coast where it would be 1.4‰ (Table 1.2) (Mayr et al., 2007a). Peat moss cellulose data from Ariel Peatland (see Figure 1.1), which was ~80 km from the Atlantic coast, showed that the $\delta^{18}O_p$ was ~2‰ higher than during the early twentieth century than the current period (Xia et al., 2018). Taking the sensitivity into consideration, this shift might indicate that westerly-derived precipitation was ~30% less during the early twentieth century compared to today as a recent analogue for the period of weakened SHWW.

The SHWW also regulate hydrological regimes in southern Patagonia. Although today the SHWW deliver a large amount of precipitation even to the leeward side of southern Patagonia, they are not as efficient as other wind directions (Figures 1.8 and A1). Some historical extreme precipitation events along the Atlantic coast of Patagonia have been linked with enhanced moisture flux derived from easterlies (Agosta et al., 2015). Our HYSPLIT back-trajectory modeling also shows that the extreme precipitation event on 11–12 March 2012, which caused historic flooding of river Río Las Minas in the

main city of Punta Arenas (Butorovic, 2013), occurred under bursts of easterlies (Figure A7). For this month, the dE is as high as 82%. The monthly precipitation amount is 63 mm (102 mm from conventional weather station Jorge C. Schythe in the main city of Punta Arenas; Butorovic, 2013), which is around twice as large as the monthly average (Figure 1.2c). The GNIP $\delta^{18}O_p$ value for this month is –4.75‰, which corresponds to +3.4‰ of $\delta^{18}O_p^e$. The *d*-excess for this month is 1.6‰, suggesting that the high $\delta^{18}O_p$ value is not an artifact from sample evaporation. This month is a good example showing that changes in synoptic-scale patterns in the past were able to influence both $\delta^{18}O_p$ and hydroclimate. If the proportion of precipitation derived from non-westerlies increased, it might also indicate an increase in moisture availability for grasslands and desserts in eastern Patagonia. Therefore, from terrestrial climate archives the $\delta^{18}O_p$ proxy can be tied to other hydrological proxies to understand the coupled evolution of synoptic-scale patterns and hydrological regimes in southern Patagonia over long timescales.

Our results also have implications for isotope-based paleoaltimetry reconstruction in southern Patagonia and, by extension, northern Patagonia and other regions with similar settings such as the South Island in New Zealand (leeward side with a single dominant moisture transport pathway) (Chamberlain & Poage, 2000; Wheeler & Galewsky, 2017). Traditionally, these studies have assumed that a single dominant moisture transport pathway such as the strong SHWW in Patagonia has also persisted throughout geological timescales. Under this assumption, any negative temporal shift in $\delta^{18}O_p$ in the modern leeward side is interpreted as the development of isotopic rain shadow and used to estimate the surface elevation in upwind locations using an empirical isotopic lapse rate (Blisniuk et al., 2005; Colwyn et al., 2019). This study, however, shows that an additional complexity is involved in properly interpreting the signal of surface uplift from leeward isotope data. Specifically, the shifts in $\delta^{18}O_p$ can be alternatively caused by changes in moisture transport pathways under different

atmospheric circulation patterns even in a region where today there seems to only have a single dominant moisture transport pathway. As such, shifts in Antarctic sea ice extent, Southern Hemisphere meridional sea surface temperature gradient, and tropical ocean-atmosphere system, can also impose large shifts in SHWW strength and position (Lamy et al., 2010; Sime et al., 2013; Groeneveld et al., 2017), and consequently the synoptic-scale patterns and $\delta^{18}O_p$ signals preserved in terrestrial climate archives in the leeward side of Patagonia. Therefore, any leeward isotope-based paleoaltimetry studies should consider how atmospheric circulation was operated in the past under different paleogeography and climate boundary conditions, which could be constrained by isotope-enabled general circulation models (Insel et al., 2012; Mulch, 2016; Botsyun et al., 2019). Because our sensitivity analysis (Table 1.2) indicated that $\delta^{18}O_p$ at sites farther away from Atlantic coast is less affected by shifting synoptic-scale patterns and moisture transport pathways, we would expect that sites from the nearest leeward locations are most suitable for detecting the major uplift signal of the Patagonian Andes from $\delta^{18}O_p$ proxy data. The effect of changing moisture transport pathway on $\delta^{18}O_p$ might be not as large as the effect of mountain uplift, it could result in a biased estimate on uplift history if proxy data are collected from sites close to the Atlantic coast where a larger fraction of moisture could be advected from easterlies that break the rule of leeward paleoaltimetry.

1.5. Summary

Other than air temperature and precipitation amount, it has been well recognized that air mass source and transport pathway could also influence $\delta^{18}O_p$ for individual precipitation event on regional scale. However, only a few paleoclimate studies are able to link $\delta^{18}O_p$ variations over time with synoptic-scale shifts in atmospheric circulation patterns. We here provide a new framework for extracting the relationship between moisture transport pathway and $\delta^{18}O_p$ hidden in decades-long GNIP monthly $\delta^{18}O_p$

record at a specific station. In this framework, weather station precipitation data and back-trajectory modeling are combined to quantify the proportions of precipitation delivered from different trajectory clusters that are characterized by different major synoptic weather types on monthly basis. We apply this framework to GNIP monthly $\delta^{18}O_p$ record in Punta Arenas located in southern Patagonia that today is under year-round influence of the strong SHWW. We show that distal westerlies indeed contribute to a majority of precipitation in Punta Arena even though it is located in the Andean rain shadow, but not all of the precipitation. Instead, there is a considerable amount of precipitation originated from the distal easterlies and northerlies, particularly during non-summer seasons. We further show that a decreasing proportion of distal westerly-derived precipitation would increase $\delta^{18}O_p$, caused by a concurrently increasing proportion of distal northerly-derived precipitation that has a relatively higher $\delta^{18}O_p$ signal. Inconsistent with a previous event-based study close to the Atlantic coast, we do not find consistent evidence suggesting that distal easterlies would also bring in a relatively high $\delta^{18}O_p$ signal, likely due to a large degree of rainout effect en route for the easterlies to Punta Arenas. We then link the proportions of precipitation origin with synoptic-scale atmospheric circulation patterns to provide an observational basis and a process-based mechanism for reconstructing past SHWW variability from $\delta^{18}O_p$ data preserved in terrestrial climate archives. Our analysis highlights the importance of site location in preserving the most sensitive SHWW record inferred from $\delta^{18}O_p$ data, as sensitivity analysis indicates that the Atlantic coast might have the largest contrast in $\delta^{18}O_p$ between the westerlies and non-westerlies. Our results have implications for isotope-based leeward paleoaltimetry not only in Patagonia but also for other similar regions. Leeward paleoaltimetry studies often assume a single moisture transport pathway or source region has persisted throughout time, while our study suggests that different atmospheric circulation patterns in the past were also able to cause shifts in $\delta^{18}O_p$, which sometimes

were, however, interpreted as the sign of surface uplift or evaporative enrichment in soil water.

Finally, the framework introduced in this study provides new opportunities in linking large dataset of GNIP monthly precipitation isotopes with synoptic-scale patterns of moisture transport. Such framework utilizes station-based hourly or daily precipitation data to quantify the contributions of different synoptic weather types on each monthly-composited $\delta^{18}O_p$ datum. These monthly-composited $\delta^{18}O_p$ data readily available from multiple sites and over a long monitoring period, if put in a reasonable context of moisture transport, could provide insights into hydrological processes on terrestrial landscape, with implications for partitioning terrestrial water fluxes and reconstructing atmospheric circulation patterns using isotope data.

1.6. Acknowledgements

This study would be impossible without the PySPLIT package developed by Mellissa S. C. Warner and the weather station precipitation data provided by the Dirección Meteorológica de Chile. Hannah Bailey and two anonymous reviewers are acknowledged for their thoughtful comments on an earlier version of this manuscript. We thank Zicheng Yu for helpful comments and discussion. Z. Xia was supported by Presidential Fellowship, EES Graduate Student Research Funds, College of Arts and Sciences Summer Research Fellowship, and Williams-Upton Summer Fellowship from Lehigh University. This project was in part supported by a U.S. National Science Foundation grant (EAR-1502891) to Z. Yu.

The GNIP database is accessible at https://nucleus.iaea.org/wiser. The GHCN monthly climatology data are available at https://www.ncdc.noaa.gov/data-access/land-based-station-data/land-based-datasets/global-historical-climatology-network-ghcn. The Punta Arenas airport weather station data are provided by the Dirección Meteorológica de

Chile, available for download at https://climatologia.meteochile.gob.cl. The HYSPLIT model is accessible at http://www.ready.noaa.gov. The PySPLIT package is available on GitHub contributed by M.S.C. Warner at https://github.com/mscross/pysplit. The reanalysis datasets used for HYSPLIT back-trajectory modeling are archived on https://www.ready.noaa.gov/archives.php. The ERA-interim reanalysis dataset used for spatial analysis was conducted on the KNMI Climate Explorer (https://climexp.knmi.nl/). The codes for reproducing the results of this study is hosted on a GitHub repository at https://github.com/zhx215/Patagonia_HYSPLIT.

References

Abram, N. J., Mulvaney, R., Vimeux, F., Phipps, S. J., Turner, J., & England, M. H. (2014). Evolution of the Southern Annular Mode during the past millennium. *Nature Climate Change*, *4*(7), 564–569.

Aggarwal, P. K., Romatschke, U., Araguas-Araguas, L., Belachew, D., Longstaffe, F. J., Berg, P., et al. (2016). Proportions of convective and stratiform precipitation revealed in water isotope ratios. *Nature Geoscience*, *9*(8), 624–629.

Agosta, E., Compagnucci, R., & Ariztegui, D. (2015). Precipitation linked to Atlantic moisture transport: clues to interpret Patagonian palaeoclimate. *Climate Research*, *62*(3), 219–240.

Bailey, H. L., Kaufman, D. S., Henderson, A. C. G., & Leng, M. J. (2015). Synoptic scale controls on the $\delta^{18}O$ in precipitation across Beringia. *Geophysical Research Letters*, *42*(11), 4608–4616.

Bailey, H. L., Klein, E. S., & Welker, J. M. (2019). Synoptic and mesoscale mechanisms drive winter precipitation $\delta^{18}O/\delta^{2}H$ in south-central Alaska. *Journal of Geophysical Research: Atmospheres*, *124*(7), 4252–4266.

Barras, V. J. I., & Simmonds, I. (2008). Synoptic controls upon $\delta^{18}O$ in southern Tasmanian precipitation. *Geophysical Research Letters*, *35*, L02707.

Berman, A. L., Silvestri, G., & Compagnucci, R. (2012). Eastern Patagonia seasonal precipitation: influence of Southern Hemisphere circulation and links with subtropical South American precipitation. *Journal of Climate*, *25*(19), 6781–6795.

Bershaw, J., Penny, S. M., & Garzione, C. N. (2012). Stable isotopes of modern water across the Himalaya and eastern Tibetan Plateau: Implications for estimates of paleoelevation and paleoclimate. *Journal of Geophysical Research: Atmospheres*, *117*, D02110.

Blisniuk, P. M., Stern, L. A., Chamberlain, C. P., Idleman, B., & Zeitler, P. K. (2005). Climatic and ecologic changes during Miocene surface uplift in the Southern Patagonian Andes. *Earth and Planetary Science Letters*, *230*(1), 125–142.

Botsyun, S., Sepulchre, P., Donnadieu, Y., Risi, C., Licht, A., & Caves Rugenstein, J. K. (2019). Revised paleoaltimetry data show low Tibetan Plateau elevation during the Eocene. *Science*, *363*(6430), eaaq1436.

Bowen, G. J., Cai, Z., Fiorella, R. P., & Putman, A. L. (2019). Isotopes in the water cycle: regional- to global-scale patterns and applications. *Annual Review of Earth and Planetary Sciences*, *47*(1), 453–479.

Brittingham, A., Petrosyan, Z., Hepburn, J. C., Richards, M. P., Hren, M. T., & Hartman, G. (2019). Influence of the North Atlantic Oscillation on δD and $\delta^{18}O$ in meteoric water in the Armenian Highland. *Journal of Hydrology*, *575*, 513–522.

Butorovic, N. (2013). Resumen Metereológico año 2012 Estación "Jorge C. Schythe" (53° 08’ S; 70°53’W; 6m.s.n.m). *Anales Instituto Patagonia (Chile)*, *41*(1), 153–162.

Callow, N., McGowan, H., Warren, L., & Speirs, J. (2014). Drivers of precipitation stable oxygen isotope variability in an alpine setting, Snowy Mountains, Australia. *Journal of Geophysical Research: Atmospheres*, *119*(6), 3016–3031.

Chamberlain, C. P., & Poage, M. A. (2000). Reconstructing the paleotopography of mountain belts from the isotopic composition of authigenic minerals. *Geology*, *28*(2), 115–118.

Chamberlain, C. P., Winnick, M. J., Mix, H. T., Chamberlain, S. D., & Maher, K. (2014). The impact of neogene grassland expansion and aridification on the isotopic composition of continental precipitation. *Global Biogeochemical Cycles*, *28*(9), 992–1004.

Colwyn, D. A., Brandon, M. T., Hren, M. T., Hourigan, J., Pacini, A., Cosgrove, M. G., et al. (2019). Growth and steady state of the Patagonian Andes. *American Journal of Science*, *319*(6), 431–472.

Colwyn, D. A., & Hren, M. T. (2019). An abrupt decrease in Southern Hemisphere terrestrial temperature during the Eocene–Oligocene transition. *Earth and Planetary Science Letters*, *512*, 227–235.

Crawford, J., Hughes, C. E., & Parkes, S. D. (2013). Is the isotopic composition of event based precipitation driven by moisture source or synoptic scale weather in the Sydney Basin, Australia? *Journal of Hydrology*, *507*, 213–226.

Crawford, J., Hollins, S. E., Meredith, K. T., & Hughes, C. E. (2017). Precipitation stable isotope variability and subcloud evaporation processes in a semi-arid region. *Hydrological Processes*, *31*, 20–34.

Cross, M. (2015). *PySPLIT: a Package for the Generation, Analysis, and Visualization of HYSPLIT Air Parcel Trajectories.* Paper presented at Proceedings of the 14th Python in Science Conference (SciPy 2015), Austin, TX.

Daley, T. J., Mauquoy, D., Chambers, F. M., Street-Perrott, F. A., Hughes, P. D. M., Loader, N. J., et al. (2012). Investigating late Holocene variations in hydroclimate and the stable isotope composition of precipitation using southern South American peatlands: an hypothesis. *Climate of the Past*, *8*(5), 1457–1471.

Danielson, J. J., & Gesch, D. B. (2011). Global multi-resolution terrain elevation data 2010 (GMTED2010) (Open-File Report 2011–1073). Reston, VA: United States Geological Survey.

Dansgaard, W. (1953). The abundance of O^{18} in atmospheric water and water vapour. *Tellus*, *5*(4), 461–469.

Dansgaard, W. (1964). Stable isotopes in precipitation. *Tellus*, *16*(4), 436–468.

Fiorella, R. P., Poulsen, C. J., Pillco Zolá, R. S., Barnes, J. B., Tabor, C. R., & Ehlers, T. A. (2015). Spatiotemporal variability of modern precipitation $\delta^{18}O$ in the central Andes and implications for paleoclimate and paleoaltimetry estimates. *Journal of Geophysical Research: Atmospheres*, *120*(10), 4630–4656.

Friedman, I., Harris, J. M., Smith, G. I., & Johnson, C. A. (2002). Stable isotope composition of waters in the Great Basin, United States 1. Air-mass trajectories. *Journal of Geophysical Research: Atmospheres*, *107*(D19), 4400.

Galewsky, J. (2009). Orographic precipitation isotopic ratios in stratified atmospheric flows: Implications for paleoelevation studies. *Geology*, *37*(9), 791–794.
Garreaud, R. (2007). Precipitation and circulation covariability in the extratropics. *Journal of Climate*, *20*(18), 4789–4797.
Garreaud, R., Lopez, P., Minvielle, M., & Rojas, M. (2013). Large-scale control on the Patagonian climate. *Journal of Climate*, *26*(1), 215–230.
Garreaud, R. D., Vuille, M., Compagnucci, R., & Marengo, J. (2009). Present-day South American climate. *Palaeogeography, Palaeoclimatology, Palaeoecology*, *281*(3), 180–195.
Gat, J. R., Bowser, C. J., & Kendall, C. (1994). The contribution of evaporation from the Great Lakes to the continental atmosphere: estimate based on stable isotope data. *Geophysical Research Letters*, *21*(7), 557–560.
Gat, J. R. (2010). *Isotope Hydrology: A Study of the Water Cycle.* (Vol. 6). London: Imperial College Press.
Gillett, N. P., Kell, T. D., & Jones, P. D. (2006). Regional climate impacts of the Southern Annular Mode. *Geophysical Research Letters*, *33*, L23704.
Groeneveld, J., Henderiks, J., Renema, W., McHugh, C. M., De Vleeschouwer, D., Christensen, B. A., et al. (2017). Australian shelf sediments reveal shifts in Miocene Southern Hemisphere westerlies. *Science Advances*, *3*(5), e1602567.
Guan, H., Simmons, C. T., & Love, A. J. (2009). Orographic controls on rain water isotope distribution in the Mount Lofty Ranges of South Australia. *Journal of Hydrology, 374*(3), 255–264.
IAEA/WMO. (2019). *Global Network of Isotopes in Precipitation. The GNIP Database.*, Retrieved from https://nucleus.iaea.org/wiser
Insel, N., Poulsen, C. J., Ehlers, T. A., & Sturm, C. (2012). Response of meteoric $\delta^{18}O$ to surface uplift — Implications for Cenozoic Andean Plateau growth. *Earth and Planetary Science Letters*, *317–318*, 262–272.
Jasechko, S., Sharp, Z. D., Gibson, J. J., Birks, S. J., Yi, Y., & Fawcett, P. J. (2013). Terrestrial water fluxes dominated by transpiration. *Nature*, *496*(7445), 347–350.
Jouzel, J., Lorius, C., Petit, J. R., Genthon, C., Barkov, N. I., Kotlyakov, V. M., & Petrov, V. M. (1987). Vostok ice core: a continuous isotope temperature record over the last climatic cycle (160,000 years). *Nature*, *329*(6138), 403–408.
Jouzel, J., Hoffmann, G., Koster, R. D., & Masson, V. (2000). Water isotopes in precipitation:: data/model comparison for present-day and past climates. *Quaternary Science Reviews*, *19*(1), 363–379.
Kalnay, E., Kanamitsu, M., Kistler, R., Collins, W., Deaven, D., Gandin, L., et al. (1996). The NCEP/NCAR 40-year reanalysis project. *Bulletin of the American Meteorological Society*, *77*(3), 437–472.
Kong, Y., & Pang, Z. (2016). A positive altitude gradient of isotopes in the precipitation over the Tianshan Mountains: effects of moisture recycling and sub-cloud evaporation. *Journal of Hydrology*, *542*, 222–230.

Krklec, K., & Domínguez-Villar, D. (2014). Quantification of the impact of moisture source regions on the oxygen isotope composition of precipitation over Eagle Cave, central Spain. *Geochimica et Cosmochimica Acta*, *134*, 39–54.

Lamy, F., Kilian, R., Arz, H. W., Francois, J.-P., Kaiser, J., Prange, M., & Steinke, T. (2010). Holocene changes in the position and intensity of the southern westerly wind belt. *Nature Geoscience*, *3*(10), 695–699.

Lechler, A. R., & Galewsky, J. (2013). Refining paleoaltimetry reconstructions of the Sierra Nevada, California, using air parcel trajectories. *Geology*, *41*(2), 259–262.

Lenaerts, J. T. M., van den Broeke, M. R., van Wessem, J. M., van de Berg, W. J., van Meijgaard, E., van Ulft, L. H., & Schaefer, M. (2014). Extreme precipitation and climate gradients in Patagonia revealed by high-resolution regional atmospheric climate modeling. *Journal of Climate*, *27*(12), 4607–4621.

Libby, L. M., Pandolfi, L. J., Payton, P. H., Marshall, J., Becker, B., & Giertz-Sienbenlist, V. (1976). Isotopic tree thermometers. *Nature*, *261*(5558), 284–288.

Marshall, G. J. (2003). Trends in the Southern Annular Mode from observations and reanalyses. *Journal of Climate*, *16*(24), 4134–4143.

Mayr, C., Lücke, A., Stichler, W., Trimborn, P., Ercolano, B., Oliva, G., et al. (2007a). Precipitation origin and evaporation of lakes in semi-arid Patagonia (Argentina) inferred from stable isotopes ($\delta^{18}O$, $\delta^{2}H$). *Journal of Hydrology*, *334*(1), 53–63.

Mayr, C., Wille, M., Haberzettl, T., Fey, M., Janssen, S., Lücke, A., et al. (2007b). Holocene variability of the Southern Hemisphere westerlies in Argentinean Patagonia (52°S). *Quaternary Science Reviews*, *26*(5), 579–584.

Mix, H. T., Winnick, M. J., Mulch, A., & Page Chamberlain, C. (2013). Grassland expansion as an instrument of hydrologic change in Neogene western North America. *Earth and Planetary Science Letters*, *377–378*, 73–83.

Moreno, P. I., Vilanova, I., Villa-Martínez, R., Garreaud, R. D., Rojas, M., & De Pol-Holz, R. (2014). Southern Annular Mode-like changes in southwestern Patagonia at centennial timescales over the last three millennia. *Nature Communications*, *5*, 4375.

Mulch, A. (2016). Stable isotope paleoaltimetry and the evolution of landscapes and life. *Earth and Planetary Science Letters*, *433*, 180–191.

NOAA. (2019). *National centers for environmental information: Global Historical Climatology Network (GHCN)*. Retrieved from https://www.ncdc.noaa.gov/data-access/land-based-station-data/land-based-datasets/global-historical-climatology-network-ghcn

Putman, A. L., Feng, X., Sonder, L. J., & Posmentier, E. S. (2017). Annual variation in event-scale precipitation $\delta^{2}H$ at Barrow, AK, reflects vapor source region. *Atmospheric Chemistry and Physics*, *17*(7), 4627–4639.

Rindsberger, M., Magaritz, M., Carmi, I., & Gilad, D. (1983). The relation between air mass trajectories and the water isotope composition of rain in the Mediterranean Sea area. *Geophysical Research Letters*, *10*(1), 43–46.

Risi, C., Bony, S., & Vimeux, F. (2008). Influence of convective processes on the isotopic composition ($\delta^{18}O$ and δD) of precipitation and water vapor in the tropics: 2.

Physical interpretation of the amount effect. *Journal of Geophysical Research: Atmospheres*, *113*, D19306.

Rozanski, K., Araguás-Araguás, L., & Gonfiantini, R. (1993). Isotopic patterns in modern global precipitation. In P. K. Swart, K. C. Lohmann, J. Mckenzie, & S. Savin (Eds.), *Climate Change in Continental Isotopic Records* (pp. 1–36). Washingtong, DC: American Geophysical Union.

Schneider, C., Glaser, M., Kilian, R., Santana, A., Butorovic, N., & Casassa, G. (2003). Weather observations across the southern Andes at 53°S. *Physical Geography*, *24*(2), 97–119.

Sime, L. C., Kohfeld, K. E., Le Quéré, C., Wolff, E. W., de Boer, A. M., Graham, R. M., & Bopp, L. (2013). Southern Hemisphere westerly wind changes during the Last Glacial Maximum: model-data comparison. *Quaternary Science Reviews*, *64*, 104–120.

Sinclair, K. E., Marshall, S. J., & Moran, T. A. (2011). A Lagrangian approach to modelling stable isotopes in precipitation over mountainous terrain. *Hydrological Processes*, *25*(16), 2481–2491.

Sjostrom, D. J., & Welker, J. M. (2009). The influence of air mass source on the seasonal isotopic composition of precipitation, eastern USA. *Journal of Geochemical Exploration*, *102*(3), 103–112.

Stein, A. F., Draxler, R. R., Rolph, G. D., Stunder, B. J. B., Cohen, M. D., & Ngan, F. (2015). NOAA's HYSPLIT atmospheric transport and dispersion modeling system. *Bulletin of the American Meteorological Society*, *96*(12), 2059–2077.

Stern, L. A., & Blisniuk, P. M. (2002). Stable isotope composition of precipitation across the southern Patagonian Andes. *Journal of Geophysical Research: Atmospheres*, *107*(D23), 4667.

Sun, C., Shanahan, T. M., & Partin, J. (2019). Controls on the isotopic composition of precipitation in the south-central United States. *Journal of Geophysical Research: Atmospheres*, *124*(14), 8320–8335.

von Grafenstein, U., Erlenkeuser, H., Brauer, A., Jouzel, J., & Johnsen, S. J. (1999). A mid-European decadal isotope-climate record from 15,500 to 5000 years B.P. *Science*, *284*(5420), 1654–1657.

Wang, S., Zhang, M., Crawford, J., Hughes, C. E., Du, M., & Liu, X. (2017). The effect of moisture source and synoptic conditions on precipitation isotopes in arid central Asia. *Journal of Geophysical Research: Atmospheres*, *122*(5), 2667–2682.

Wang, Y. J., Cheng, H., Edwards, R. L., An, Z. S., Wu, J. Y., Shen, C.-C., & Dorale, J. A. (2001). A high-resolution absolute-dated late Pleistocene monsoon record from Hulu Cave, China. *Science*, *294*(5550), 2345–2348.

Weidemann, S. S., Sauter, T., Kilian, R., Steger, D., Butorovic, N., & Schneider, C. (2018). A 17-year record of meteorological observations across the Gran Campo Nevado Ice Cap in southern Patagonia, Chile, related to synoptic weather types and climate modes. *Frontiers in Earth Science*, *6*(53).

Wheeler, L. B., & Galewsky, J. (2017). Atmospheric flow patterns around the Southern Alps of New Zealand and implications for paleoaltimetry. *Geophysical Research Letters*, *44*(22), 11601–11605.

Winnick, M. J., Chamberlain, C. P., Caves, J. K., & Welker, J. M. (2014). Quantifying the isotopic 'continental effect'. *Earth and Planetary Science Letters*, *406*, 123–133.

Xia, Z., Yu, Z., & Loisel, J. (2018). Centennial-scale dynamics of the Southern Hemisphere Westerly Winds across the Drake Passage over the past two millennia. *Geology*, *46*(10), 855–858.

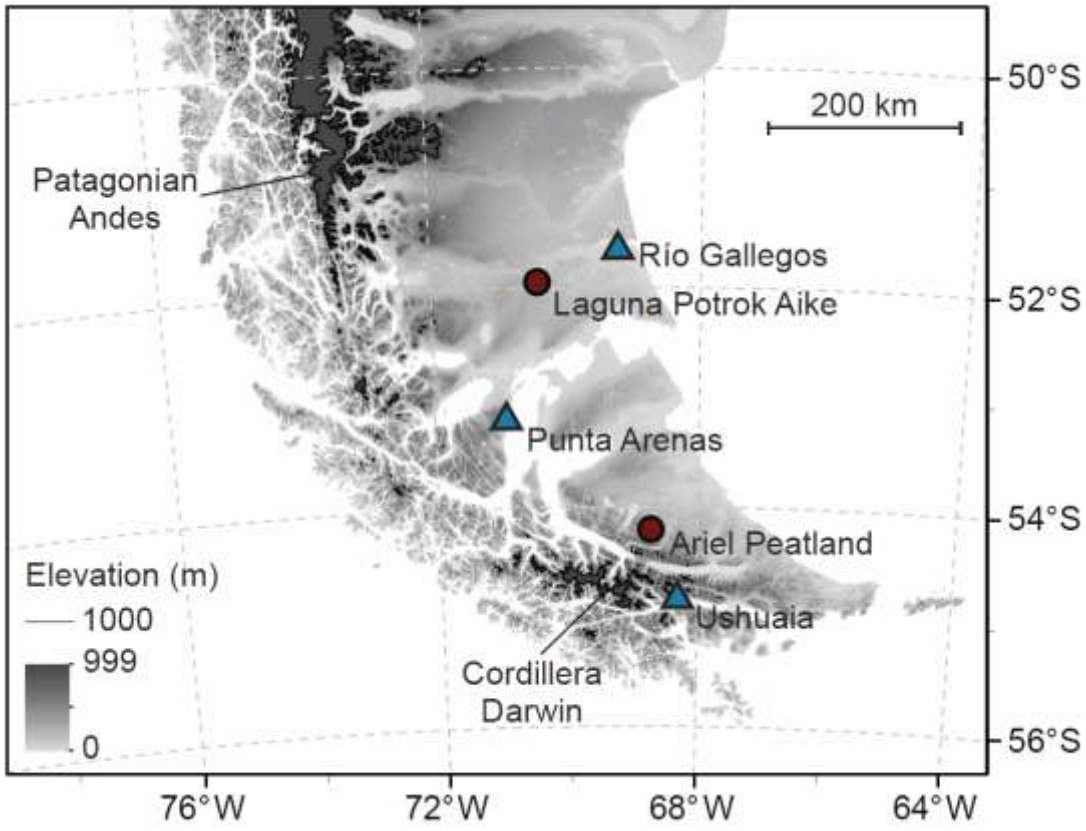

Figure 1.1. Digital elevation map of southern Patagonia. Also shown are major cities (cyan triangles) and field sites (red dots) discussed in this paper, and the elevation contour of 1000 m asl. The digital elevation model is from the Global Multi-resolution Terrain Elevation Data 2010 (GMTED2010) at 30-arc-second resolution (Danielson & Gesch, 2011) distributed by the United States Geological Survey and the National Geospatial Intelligence Agency (http://earthexplorer.usgs.gov/).

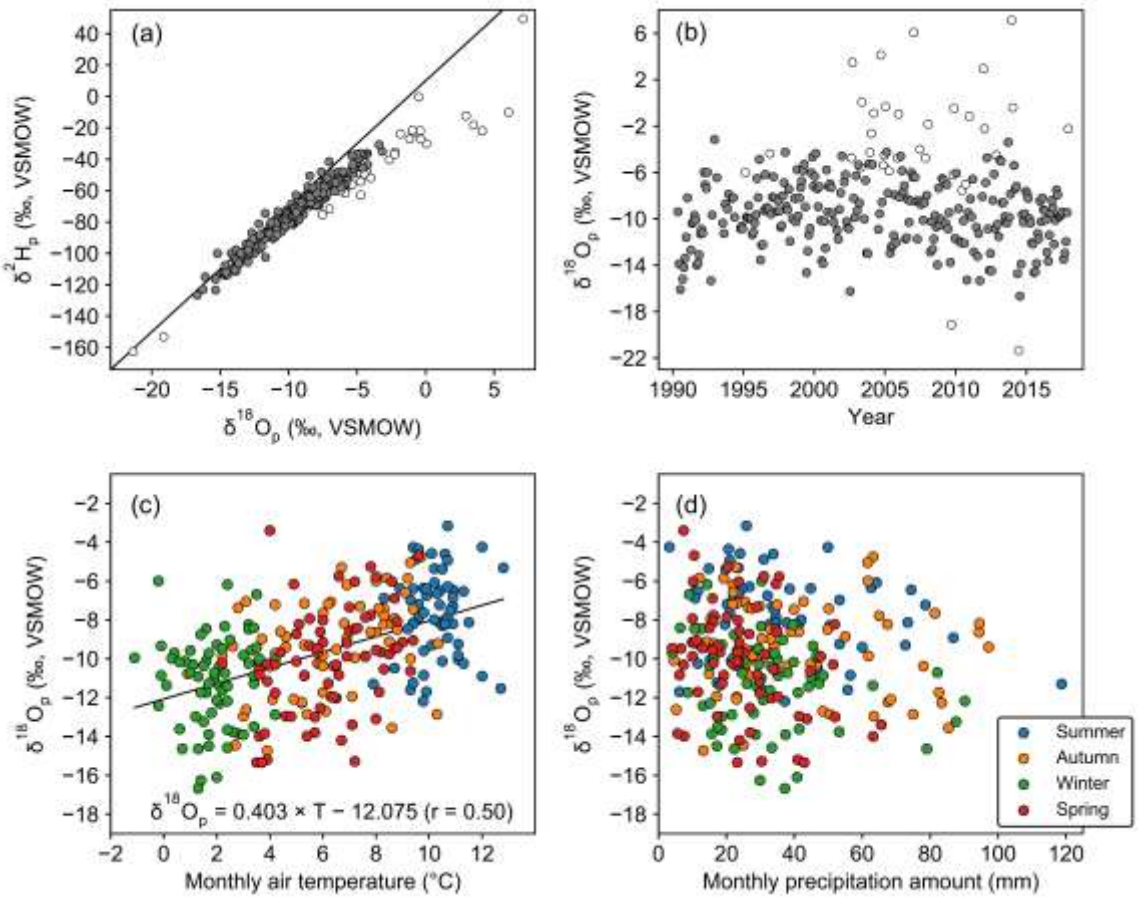

Figure 1.2. Summary of GNIP precipitation isotope data from Punta Arenas. (a) Scatter plot between monthly δ^2H_p and $\delta^{18}O_p$. The black line is the Global Meteoric Water Line (GMWL). (b) Long-term variations in monthly $\delta^{18}O_p$ during the period 1990–2017. Open dots in (a) and (b) are the raw data points that were excluded from the analysis hereafter (see Section 1.3.1 and Table A1 for details). (c) Scatter plot between monthly $\delta^{18}O_p$ and GHCN monthly air temperature showing positive correlation with a linear regression line. The use of GHCN monthly air temperature data (NOAA, 2019) rather than GNIP monthly air temperature data is due to several potential erroneous data recordings in GNIP database (see Figure A2d for details). One data gap in GHCN (February 2011) is filled by GNIP data. (d) Scatter plot between monthly $\delta^{18}O_p$ and Punta Arenas airport monthly cumulative precipitation (calculated from the sum of all 6-hour precipitation data for each month; see Section 1.3.2 for details) showing no correlation. There are 6

individual months during which precipitation data have temporal gaps, and these data are replaced by GHCN monthly precipitation amount data (see Figure A2a). In (c) and (d), dots are color-coded to represent different austral seasons: summer (December–February), autumn (March–May), winter (June–August), and spring (September–November).

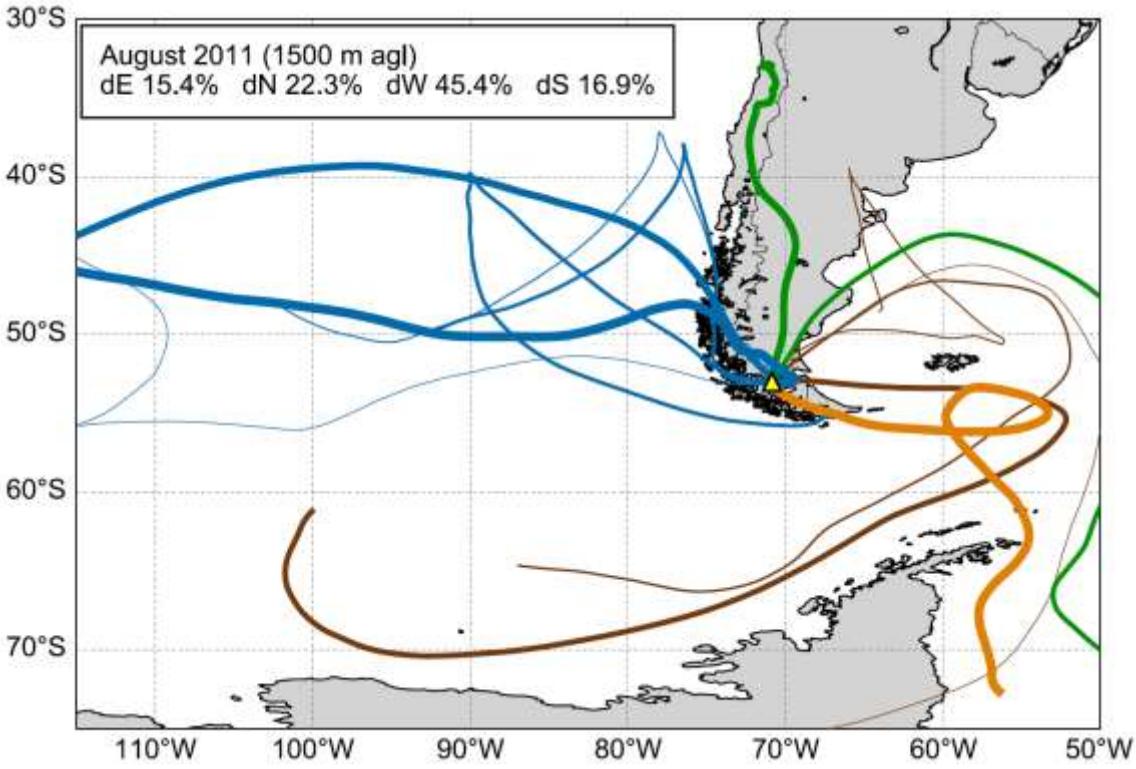

Figure 1.3. Visualization of precipitation-producing back-trajectory results from an example month (August 2011) and an example initial back-trajectory height (1500 m agl). There are 13 precipitation events based on the 6-hour precipitation data in this month. The total monthly precipitation amount is 26 mm. Trajectory paths that enter eastern, northern, western and southern boundaries of southern Patagonian landmass are grouped into clusters of distal easterlies (brown), northerlies (green), westerlies (blue), and southerlies (orange), respectively. The trajectory line width is proportional to the 6-hour precipitation amount associated with each trajectory. For reference, the thickest and thinnest paths on this graph represent 4.6 mm and 0.2 mm precipitation, respectively. Yellow triangle mark Punta Arenas. The proportions of precipitation contributed by different trajectory clusters (dE, dN, dW, and dS) in that month can be calculated. This provides an additional metric that allows us to investigate if the proportion of precipitation derived from certain trajectory cluster could influence monthly-composited $\delta^{18}O_p$ in GNIP data.

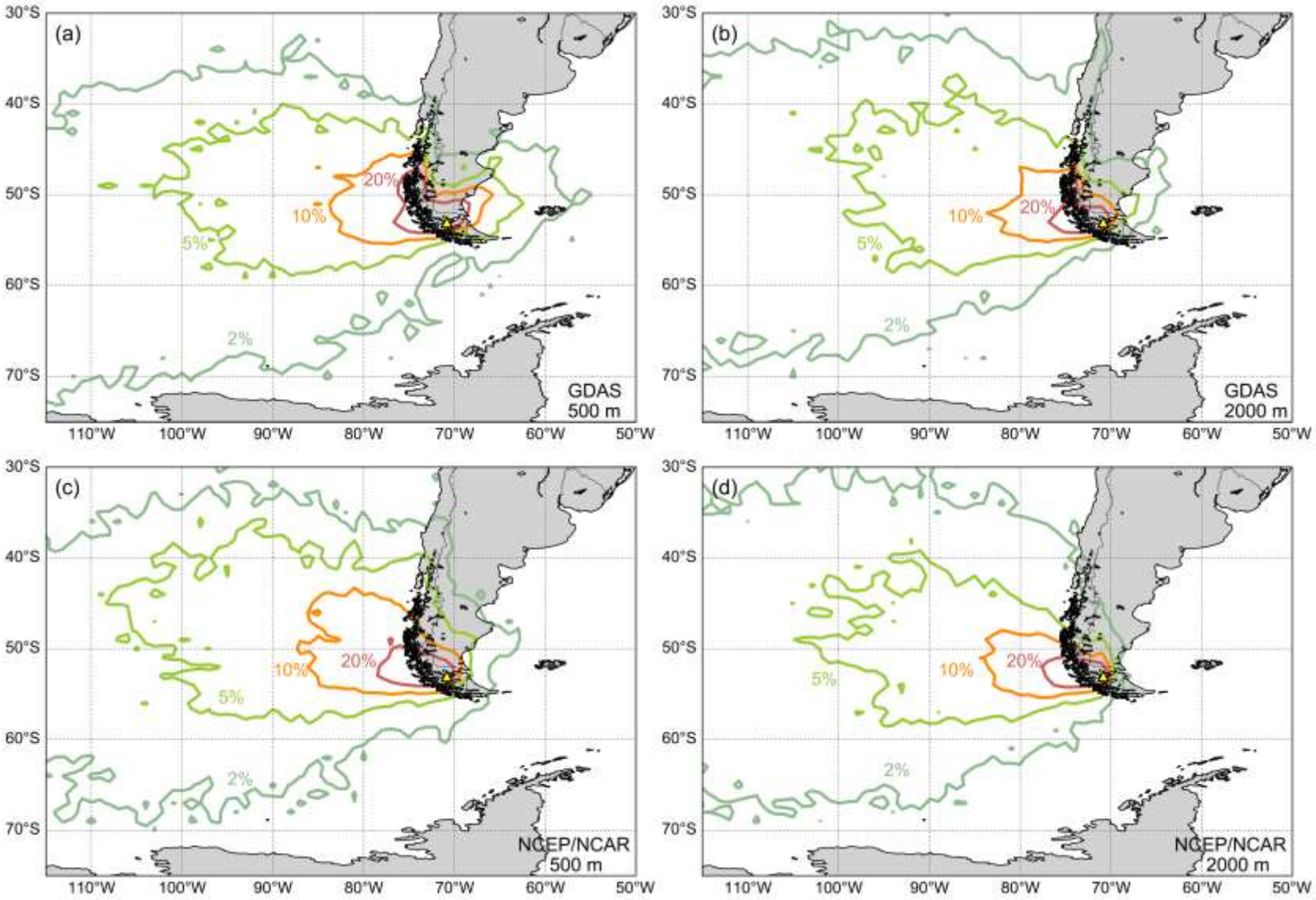
(a)
(b)
(c)
(d)
30°S
40°S
50°S
60°S
70°S
110°W
100°W
90°W
80°W
70°W
60°W
50°W
2%
5%
10%
20%
GDAS
500 m
GDAS
2000 m
NCEP/NCAR
500 m
NCEP/NCAR
2000 m

Figure 1.4 (previous page). Precipitation-producing trajectory frequency contour plots for an initial back trajectory height of 500 m (a and c) and 2000 m agl (b and d) during the period 2005–2017 generated from the GDAS reanalysis dataset (a and b) and during the period 1990–2004 generated from the NCEP/NCAR reanalysis dataset (c and d).

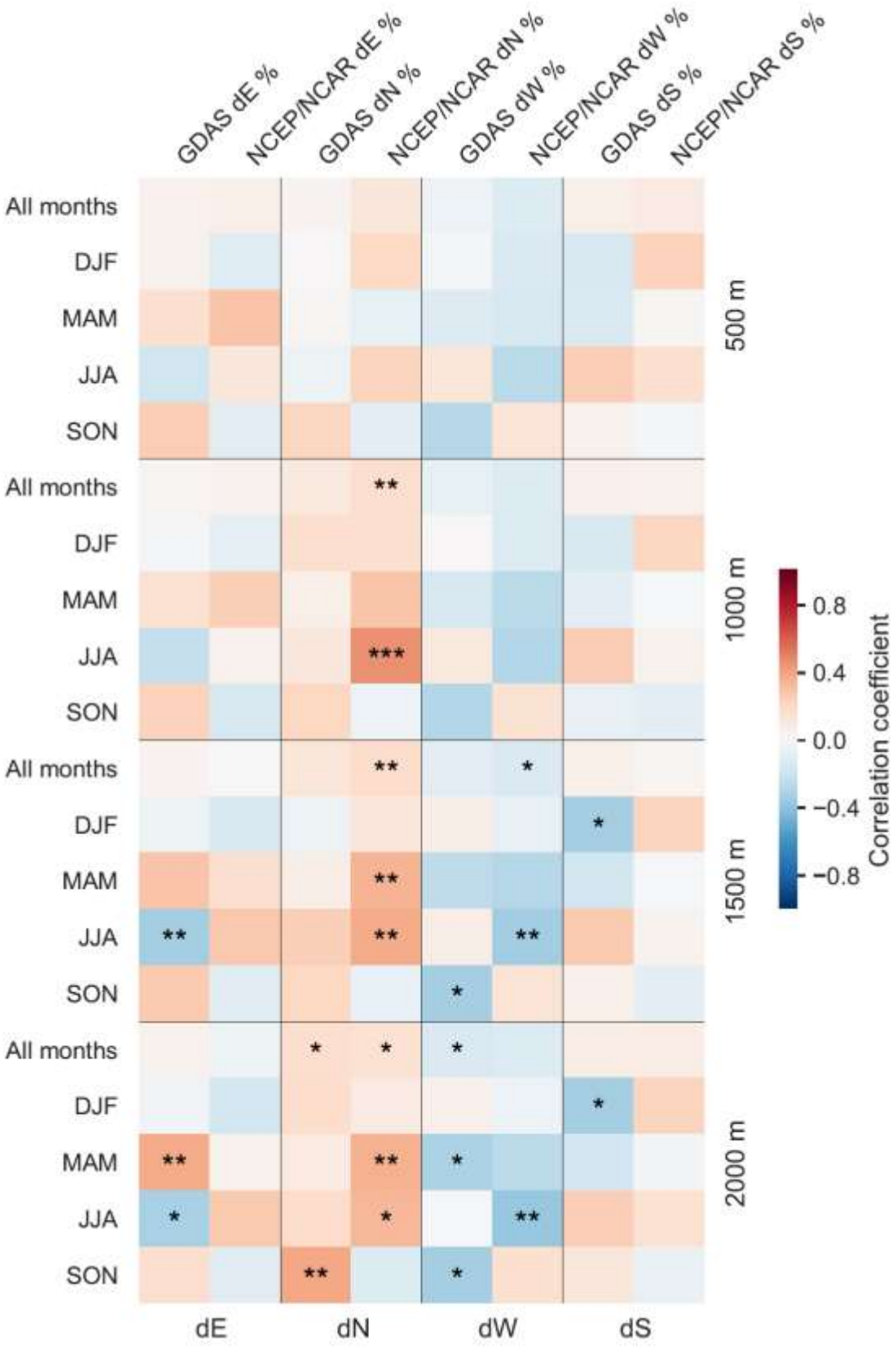
GDAS dE %
NCEP/NCAR dE %
GDAS dN %
NCEP/NCAR dN %
GDAS dW %
NCEP/NCAR dW %
GDAS dS %
NCEP/NCAR dS %
All months
DJF
MAM
JJA
SON
500 m
1000 m
1500 m
2000 m
dE
dN
dW
dS
0.8
0.4
0.0
−0.4
−0.8
Correlation coefficient

Figure 1.5 (previous page). Correlation coefficient heat map between monthly proportions of precipitation derived from different trajectory clusters and monthly $\delta^{18}O_p^e$. Results are shown for all months combined and four different austral seasons (see Section 1.3.1) that are also separated for different initial back-trajectory heights (agl) and different reanalysis dataset inputs. Significance levels are noted by the following: * $p < 0.1$, ** $p < 0.05$, *** $p < 0.01$. The number of data for correlation analysis are listed in Table A2.

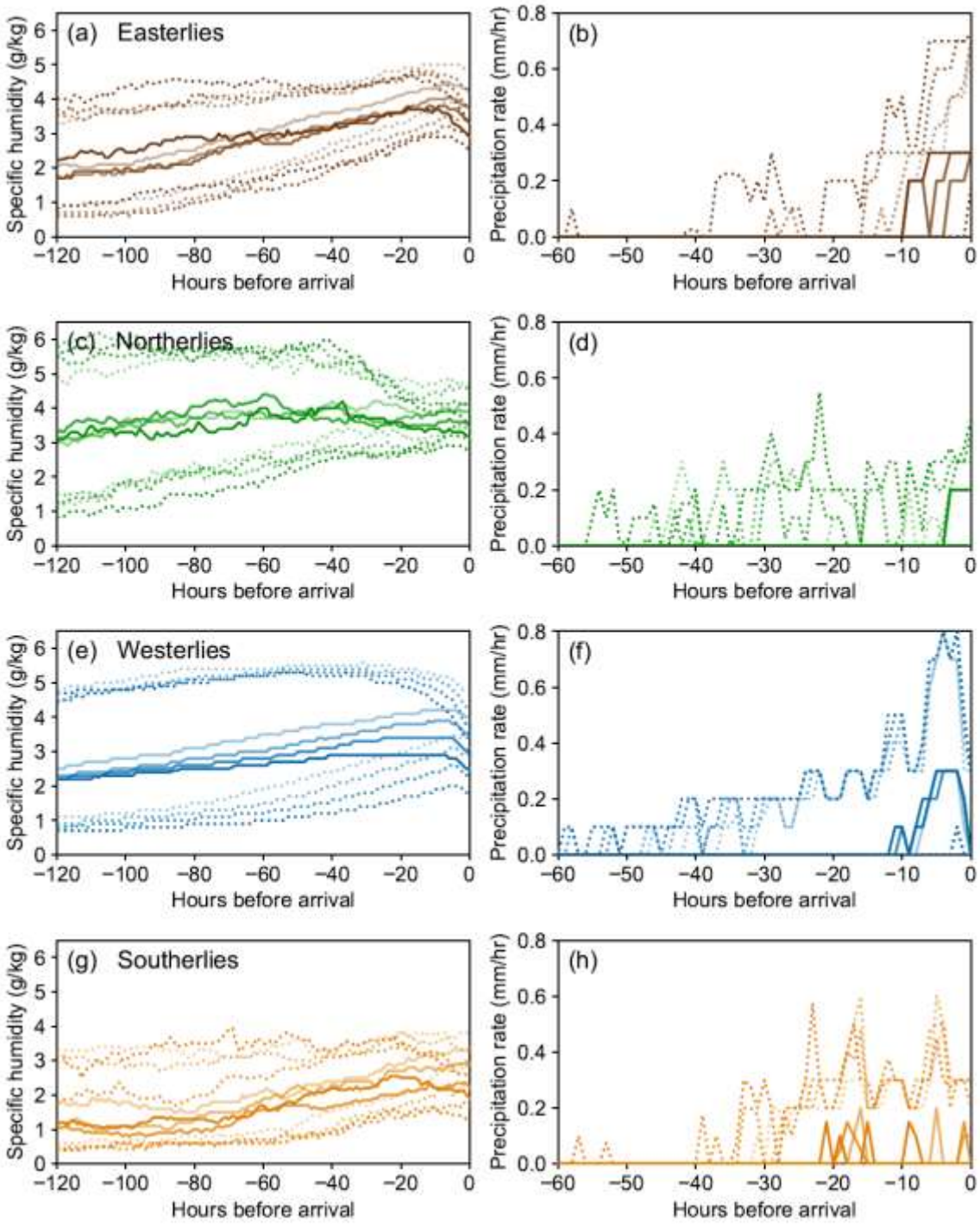

Figure 1.6. Median (solid lines) and lower/upper quartile (dotted lines) values of specific humidity (a, c, e, and g) and precipitation rate (b, d, f, and h) in each hour along GDAS-modeled trajectories in the clusters of distal easterlies (a and b), northerlies (c and d), westerlies (e and f), and southerlies (g and h). The transparency of lines is coded to

represent results derived from different initial back-trajectory heights. The results derived from an initial back-trajectory height of 2000 m agl have zero transparency. The transparency increases (showing lighter color) with a decreasing initial back-trajectory height from 1500 m to 500 m agl.

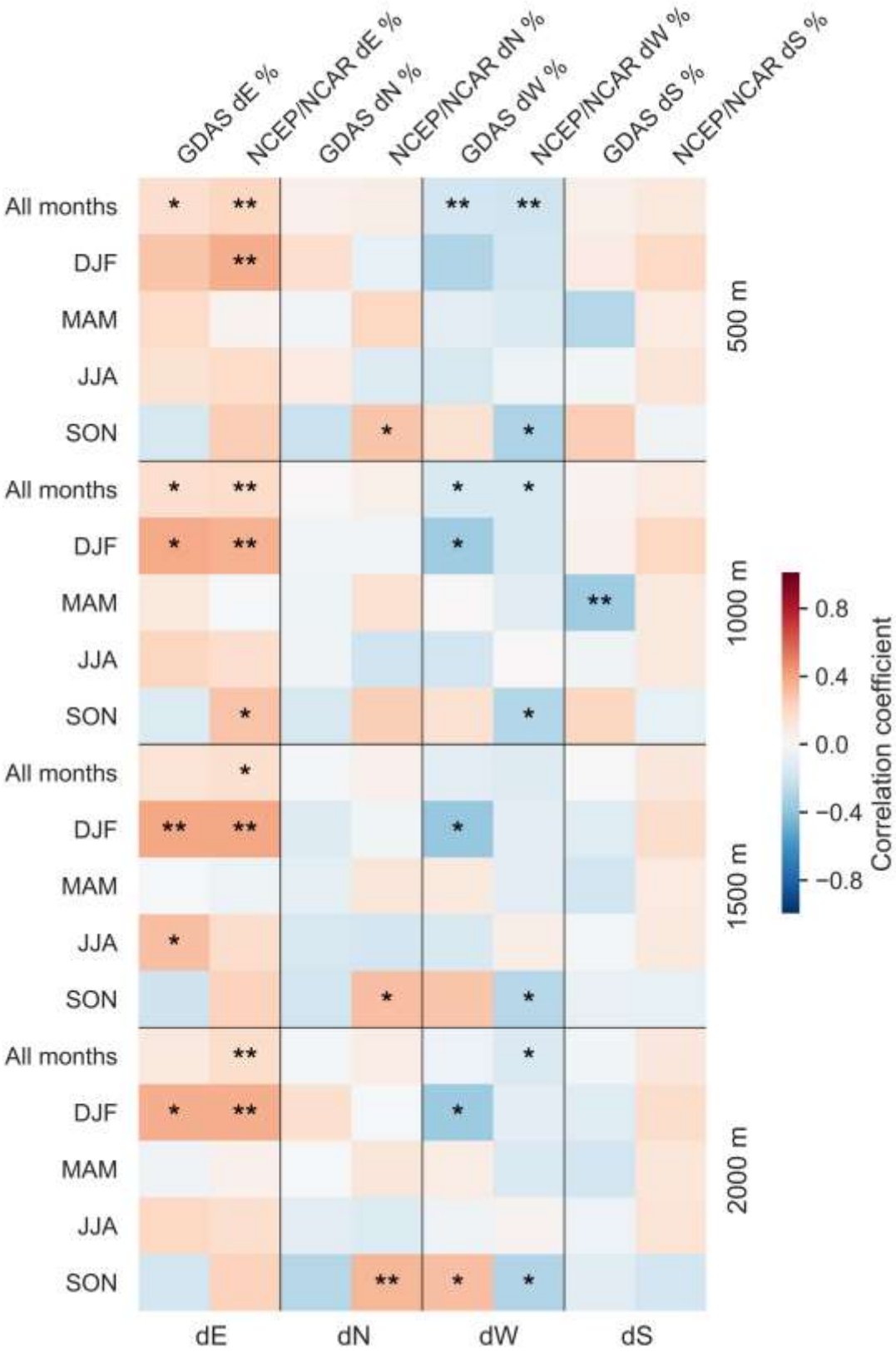
GDAS dE %
NCEP/NCAR dE %
GDAS dN %
NCEP/NCAR dN %
GDAS dW %
NCEP/NCAR dW %
GDAS dS %
NCEP/NCAR dS %
All months
DJF
MAM
JJA
SON
500 m
1000 m
1500 m
2000 m
dE
dN
dW
dS
Correlation coefficient
0.8
0.4
0.0
−0.4
−0.8

Figure 1.7 (previous page). Similar to Figure 1.5 but it is the correlation coefficient heat map between monthly proportions of precipitation derived from different trajectory clusters and monthly *d*-excess.

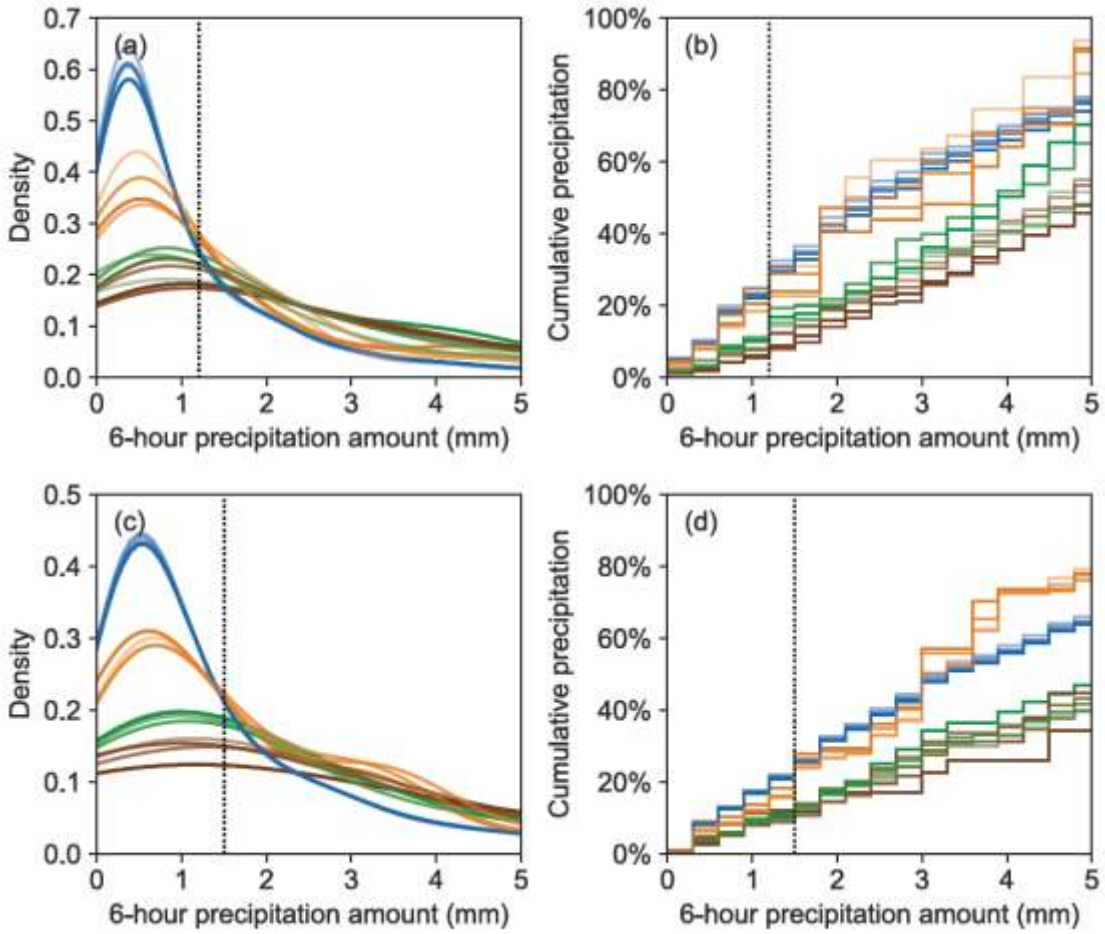

Figure 1.8. Kernel density estimation plots for 6-hour cumulative precipitation data (a and c) and amount-weighted cumulative 6-hour precipitation histogram (with a bin size of 0.3 mm) (b and d) related to different trajectory clusters. Results are separated for the GDAS (a and b) and the NCEP/NCAR (c and d) reanalysis datasets. The color coding follows Figure 1.6. Clearly, distal westerlies have higher frequency of precipitation amount less than 1.2 mm (for the GDAS) and 1.5 mm (for the NCEP/NCAR) in 6 hours (shown as vertical dotted lines). Thus, distal westerly-derived precipitation consists of ~25% of this "drizzle" precipitation, which is more than double that of distal easterlies and northerlies, whereas distal easterlies have at least 50% of precipitation that has rainfall rate more than 5 mm within 6 hours.

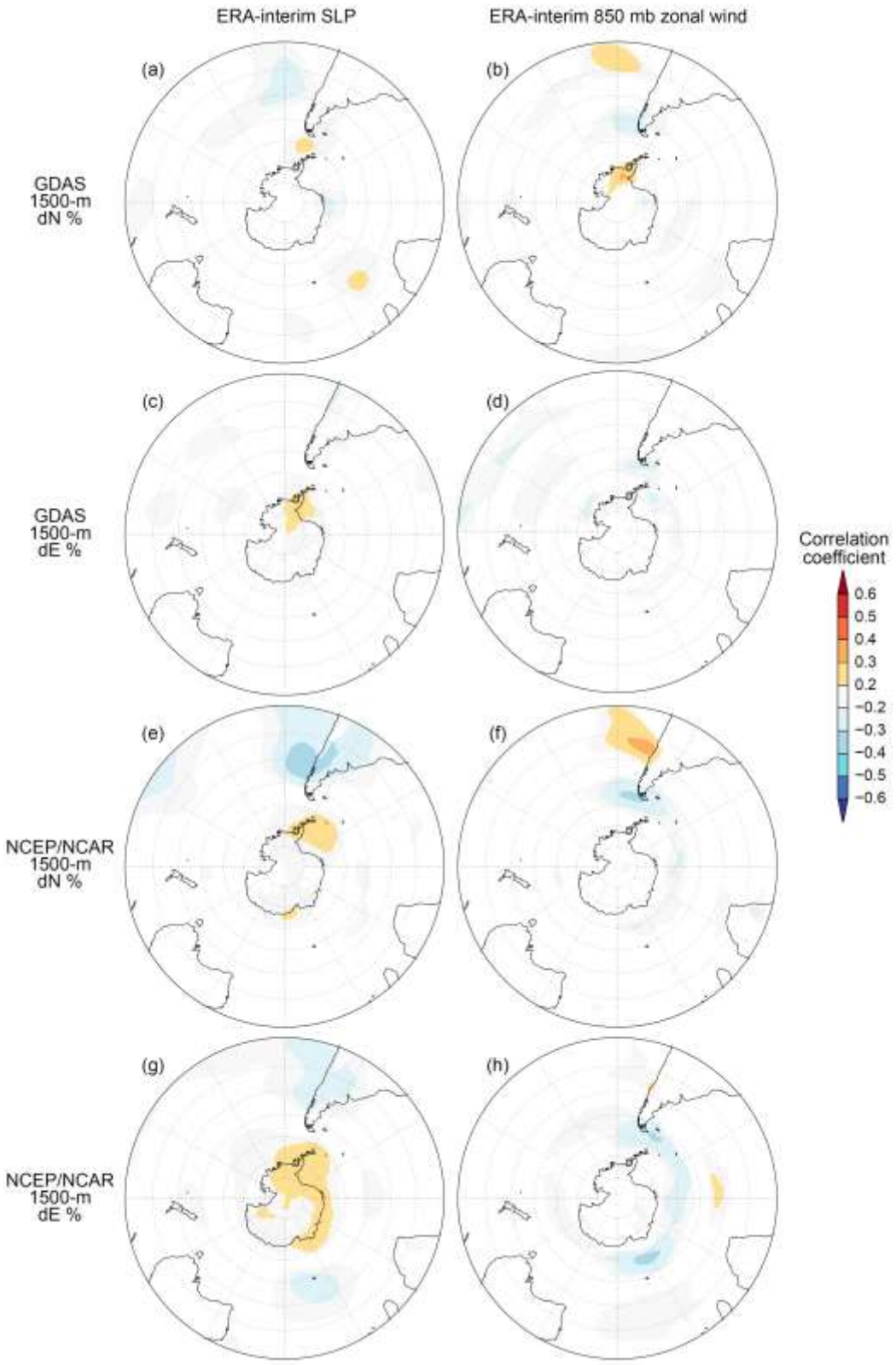
ERA-interim SLP
ERA-interim 850 mb zonal wind
(a)
(b)
GDAS
1500-m
dN %
(c)
(d)
GDAS
1500-m
dE %
(e)
(f)
NCEP/NCAR
1500-m
dN %
(g)
(h)
NCEP/NCAR
1500-m
dE %
Correlation
coefficient
0.6
0.5
0.4
0.3
0.2
−0.2
−0.3
−0.4
−0.5
−0.6

Figure 1.9 (previous page). Spatial correlation between monthly proportion of precipitation related to secondary trajectory clusters and ERA-interim reanalysis fields. The results from an initial back-trajectory height of 1500-m were used because this level is close to 850 mb and likely represents the level of moisture transport (see Section 1.4.2). (a–d) Spatial correlation of dN and dE with SLP and 850 mb zonal wind speed derived from the GDAS reanalysis dataset for the period 2005–2017. (e–h) The same as (a–d) but derived from the NCEP/NCAR reanalysis dataset for the period 1990–2004. The dN and dE data from all months during the corresponding period are used, including those months during which $\delta^{18}O_p$ data were missing or filtered. Areas with *p*-value higher than 0.1 were masked out. Plots were produced on KNMI Climate Explorer (https://climexp.knmi.nl/).

Table 1.1. Mean monthly proportions of precipitation in Punta Arenas derived from different trajectory clusters in the HYSPLIT framework. Results are compared among different meteorological reanalysis datasets, different initial air mass heights, and different seasons.

Initial air mass height (m agl)	Month	dE (%)		dN (%)		dW (%)		dS (%)	
		GDAS	NCEP/NCAR	GDAS	NCEP/NCAR	GDAS	NCEP/NCAR	GDAS	NCEP/NCAR
500	All months	17.4	4.9	4.1	7.3	76.4	84.9	2.1	2.9
	DJF	9.6	3.0	1.2	5.1	88.5	89.9	0.7	2.0
	MAM	16.7	6.1	6.5	6.2	74.7	84.5	2.0	3.3
	JJA	28.5	7.1	7.0	11.3	61.0	77.6	3.5	4.0
	SON	14.7	3.3	1.8	6.7	81.5	87.8	2.1	2.2
1000	All months	12.2	3.1	4.7	6.1	81.4	88.0	1.7	2.7
	DJF	7.4	1.8	0.4	4.1	91.7	92.2	0.4	1.9
	MAM	11.8	4.7	6.3	4.9	80.3	87.5	1.6	2.9
	JJA	19.0	3.8	8.8	8.6	68.8	83.3	3.4	4.3
	SON	10.5	2.2	3.3	7.0	84.9	89.2	1.3	1.6
1500	All months	9.4	1.2	4.4	5.7	84.9	90.8	1.4	2.2
	DJF	6.5	0.9	0.0	4.3	93.2	94.1	0.3	0.6
	MAM	8.6	1.6	5.1	5.3	85.0	90.4	1.2	2.7
	JJA	14.0	1.1	8.9	7.5	73.7	87.4	3.4	4.0
	SON	8.4	1.3	3.4	5.8	87.7	91.3	0.5	1.6
2000	All months	6.1	1.0	4.3	5.0	88.1	92.5	1.5	1.5
	DJF	5.2	0.8	0.3	4.3	94.4	94.3	0.2	0.6
	MAM	5.3	1.1	4.6	5.2	88.9	91.6	1.2	2.1
	JJA	9.3	0.7	7.5	6.2	79.9	90.6	3.3	2.5
	SON	4.7	1.3	4.9	4.5	89.1	93.4	1.2	0.8

Note. DJF (December–February), MAM (March–May), JJA (June–August), and SON (September–November) are austral summer, autumn, winter, and spring, respectively.

Table 1.2. Effect of a 20% less westerly-derived precipitation on $\delta^{18}O_p$ based on regression coefficients between $\delta^{18}O_p^e$ and dW if within a specific season they are statistically significant from Figure 1.5. Results are compared with the study by Mayr et al. (2007a) who, based on event-based precipitation samples, concluded that precipitation derived from westerlies are on average 7‰ lower than non-westerlies at Río Gallegos and Laguna Potrok Aike. From a simple isotopic and mass balance calculation, it could be converted that a 20% less westerly-derived precipitation would have an effect of +1.4‰ in $\delta^{18}O_p$ for their sites.

Meteorological reanalysis dataset	Initial air mass height (m agl)	Season	$\delta^{18}O_p$ change (‰)
GDAS	1500	SON	+1.0
GDAS	2000	MAM	+0.8
GDAS	2000	SON	+1.0
NCEP/NCAR	1500	JJA	+1.0
NCEP/NCAR	2000	JJA	+1.3

Appendix A: Supporting information for Chapter 1

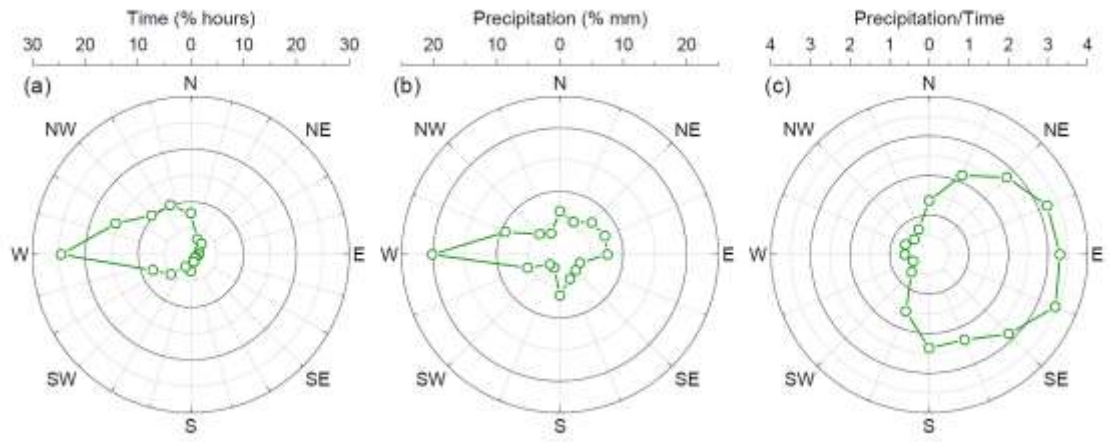

Figure A1. Wind sensor (every 1 hour) and rain gauge (every 6 hours) data from weather station in Punta Arenas airport during the period 1990–2017 plotted on the 16-point compass rose. (a) Frequency percentage of hourly wind direction observations (n = 232,277). There are 13,177 observational gaps (5.4% of all hours). (b) Precipitation percentage from each wind direction. Six-hour cumulative precipitation amount (n = 40,769) was divided by 6 to match with each hourly wind direction data prior to each precipitation measurement, assuming that wind in each of that 6 hours contributes to that 6-hour cumulative precipitation equally. There are 140 observational gaps (0.3% of all hours). (c) The quotient between precipitation percentage and time percentage for each respective wind direction. The weather station data are available for public download on the website of Meteorological Direction of Chile (https://climatologia.meteochile.gob.cl).

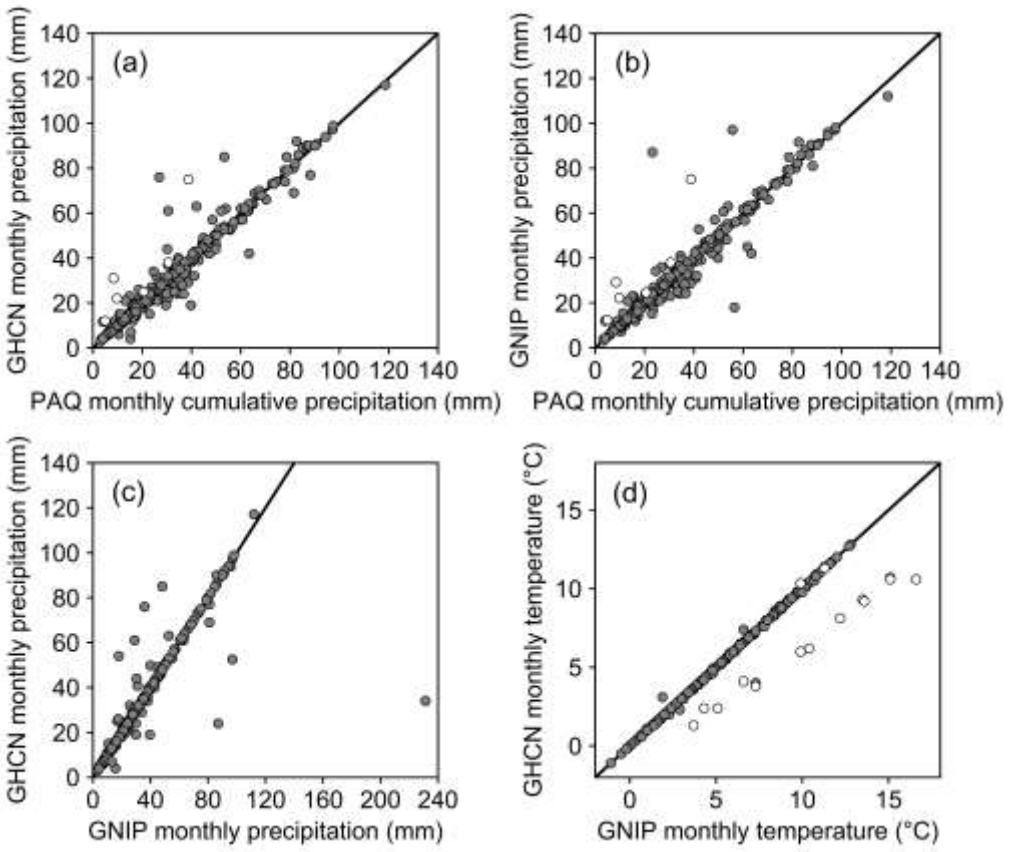

Figure A2. Comparisons between different weather station databases of Punta Arenas airport. Solid lines in all plots indicate 1:1 relationship. (a) Scatter plot between GHCN Version 2 reported monthly precipitation amount and monthly cumulative precipitation amount (calculated from the sum of all 6-hour precipitation data for each month). The open dots indicate 6 individual months (March–June 2011, December 2011, and May 2012) during which 6-hour precipitation data have temporal gaps (27%, 16%, 22%, 14%, 11%, and 6% of all 6-hour intervals, respectively), which are responsible for their monthly cumulative precipitations amount underestimated compared to GHCN monthly precipitation amount data. It is still likely that a few GHCN monthly precipitation amount data are erronrous as well, which might explain the deviations from the monthly cumulative precipitation amount (Stefan Terzer-Wassmuth, personal communication, 2019). (b) Scatter plot between reported GNIP monthly precipitation amount and Punta

Arenas monthly cumulative precipitation amount similar as (a). (c) Scatter plot between GHCN Version 2 monthly precipitation amount and GNIP monthly precipitation amount. Clearly there are also several important erroneous data recordings in GNIP database. (d) Scatter plot between GHCN Version 3 monthly air temperature and GNIP monthly air temperature. Most data are following the 1:1 line, but there are still several important erroneous GNIP data recordings. These data are mainly found from January 2015 to March 2016 (shown as open dots). These GNIP monthly air temperature values are much higher than normal, while weather station data from nearby city do not show any corresponding high air temperature, confirming that these GNIP data are erroneous.

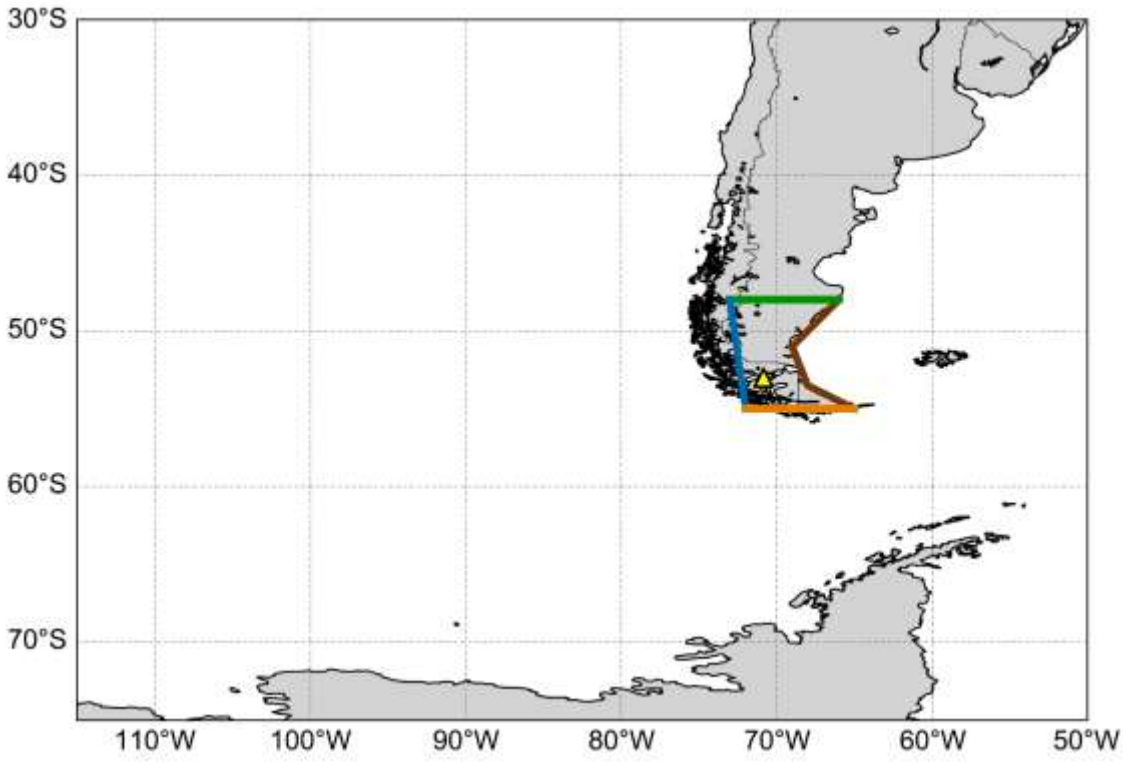

Figure A3. Map showing the delineations of eastern (brown), northern (green), western (blue) and southern (orange) boundaries of southern Patagonia landmass used in this study. If a back trajectory came across one of the above boundaries, that trajectory was clustered into distal easterlies, northerlies, westerlies, and southerly trajectories, respectively.

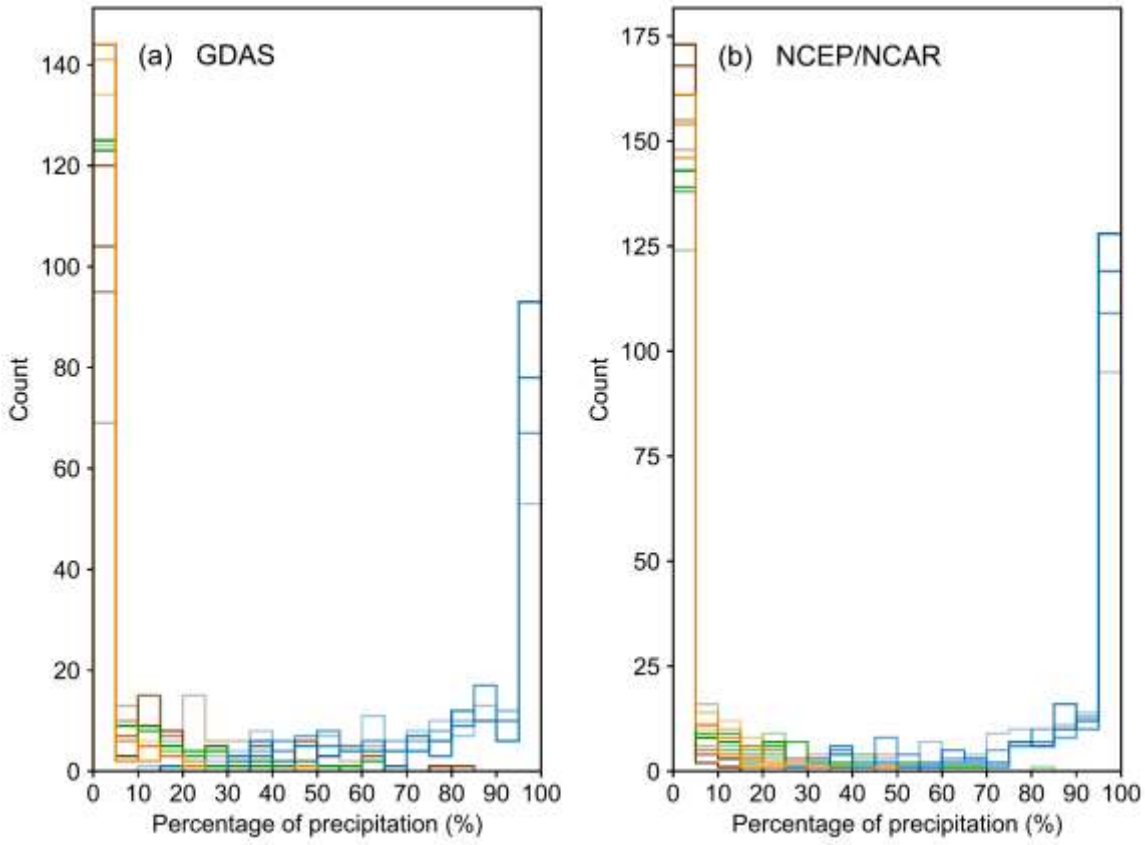

Figure A4. Histogram of monthly dE (brown), dN (green), dW (blue), and dS (orange) derived from (a) the GDAS and (b) the NCEP/NCAR reanalysis datasets with a bin size of 5%. The transparency of histogram plots is coded to represent results derived from different initial back-trajectory heights. The results derived from an initial back-trajectory height of 2000 m agl have zero transparency. The transparency increases (showing lighter color) with a decreasing initial air back-trajectory height from 1500 m to 500 m agl.

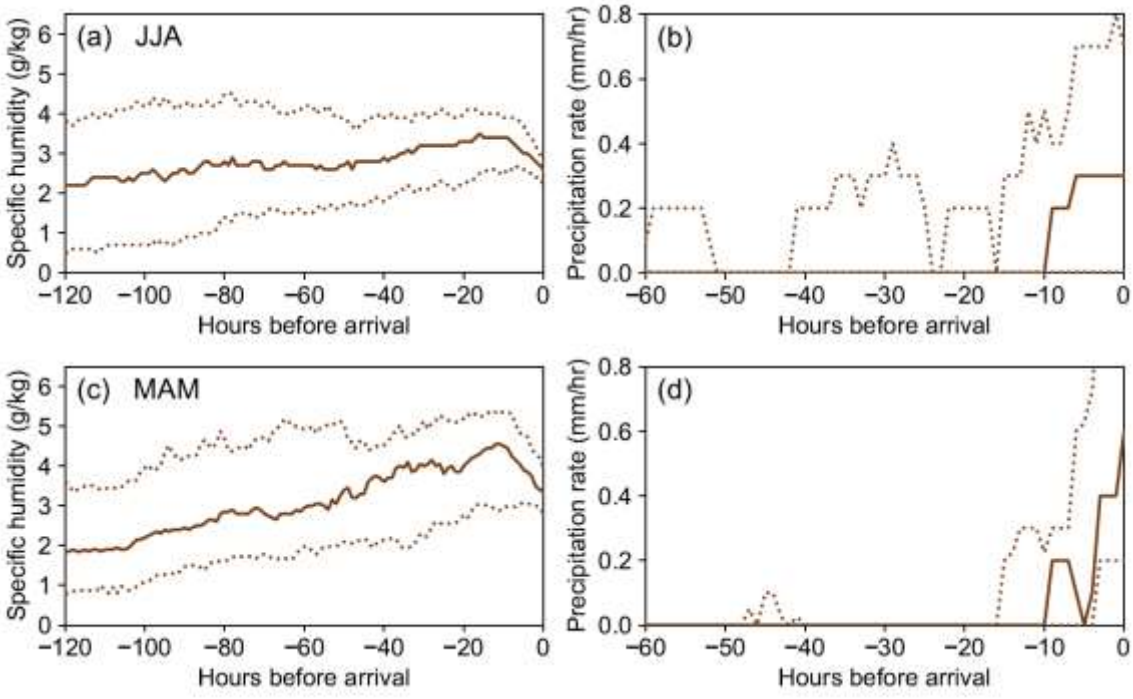

Figure A5. Median (solid lines) and lower/upper quartile (dotted lines) values of specific humidity (a and c) and precipitation rate (b and d) in each hour along all GDAS-modeled trajectories in the cluster of distal easterlies for winter (a and b) and autumn (c and d). The initial air back-trajectory height is 2000 m agl as the opposite correlation relationships between dE and $\delta^{18}O_p$ residual (see Figure 1.5) were found at this level.

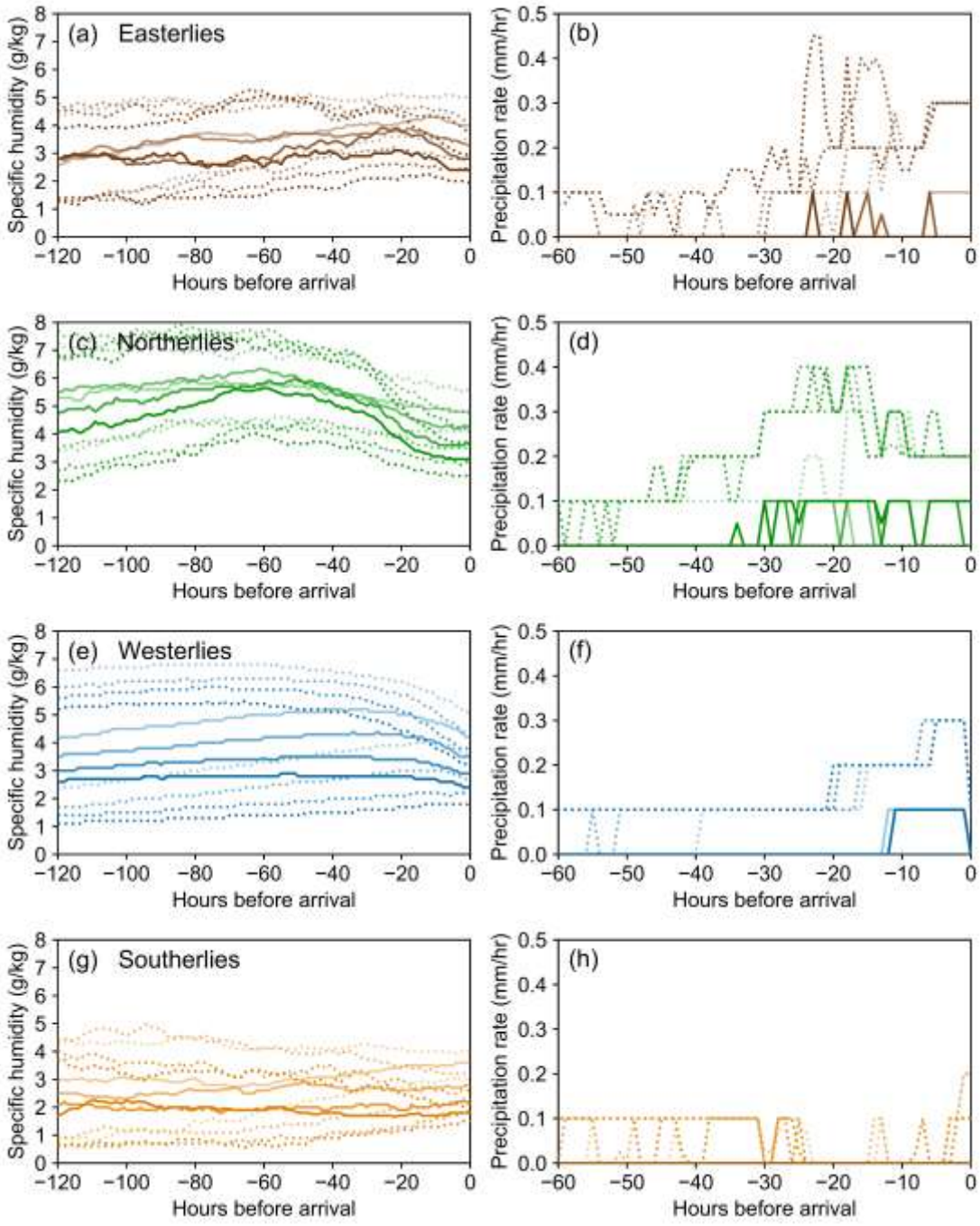

Figure A6. Median (solid lines) and lower/upper quartile (dotted lines) values of specific humidity (a, c, e, and g) and precipitation rate (b, d, f, and h) in each hour along NCEP/NCAR-modeled trajectories in the clusters of distal easterlies (a and b), northerlies (c and d), westerlies (e and f), and southerlies (g and h). The color coding follows Figure A4.

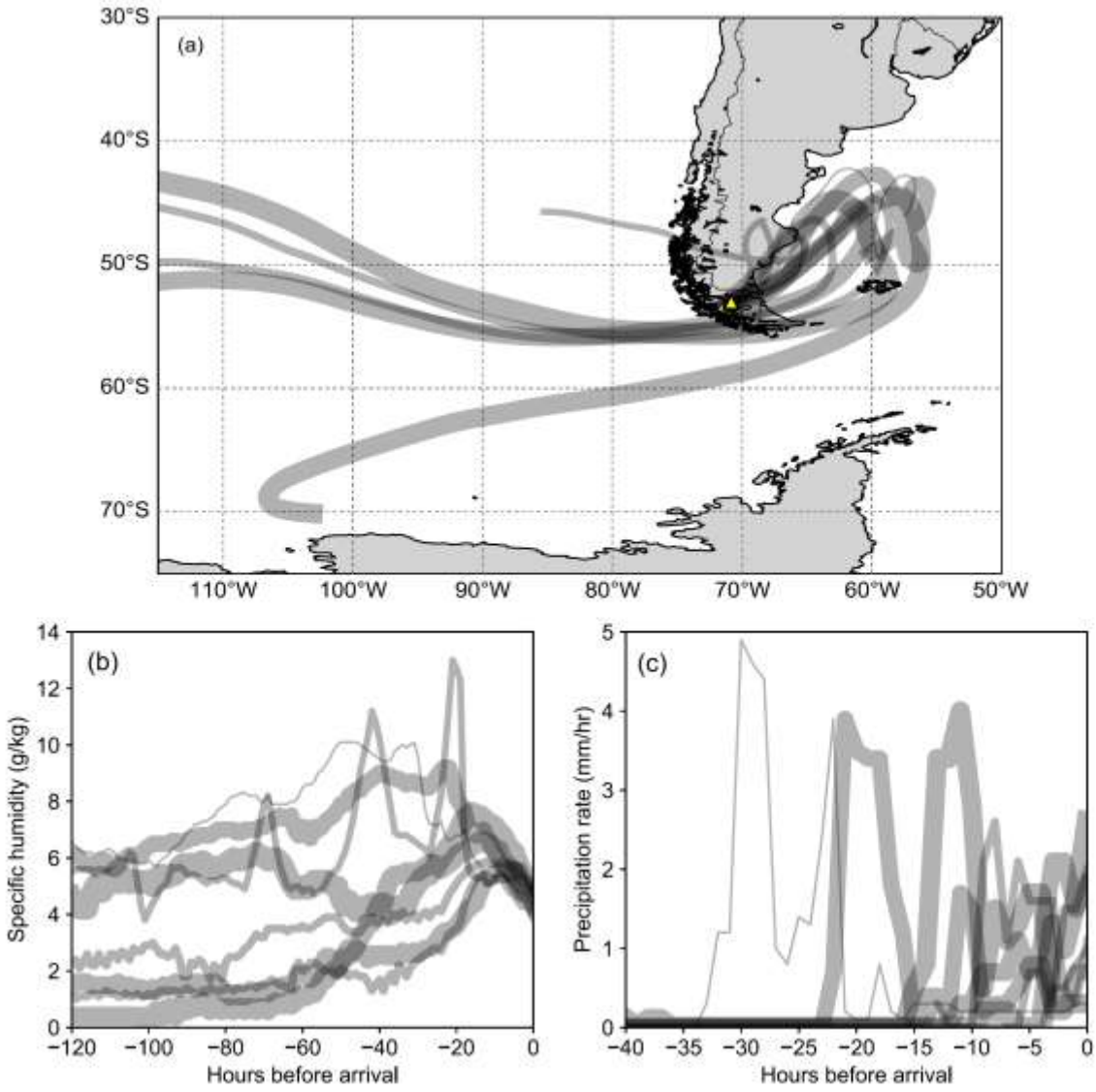

Figure A7. Back-trajectory characteristics of the historic extreme precipitation event occurred on 11–12 March 2012, including general transport pathway (a), along-trajectory specific humidity (b) and precipitation rate (c) in each hour. There are 8 trajectories plotted, with their UTC time starting from 12:00 on 11 March 2012 to 06:00 on 13 March 2012. The initial air back-trajectory height is 2000 m agl. The trajectory line width is proportional to the 6-hour precipitation amount associated with each trajectory. For reference, the thickest and thinnest paths on this graph represent 11.4 mm and 0.8 mm precipitation, respectively. Yellow triangle in (a) mark Punta Arenas.

Table A1. Summary of all missing data or filtered dataset from GNIP Punta Arenas.

Year	Month	$\delta^{18}O$	$\delta^{2}H$	*d*-excess	GNIP precipitation (mm)	GHCN precipitation (mm)	Sum of all 6-hour cumulative precipitation (mm)	GNIP temperature (°C)	GHCN temperature (°C)
1990	1	NaN[a]	NaN	NaN	39	39.5	39.5	10.4	10.4
1990	2	NaN	NaN	NaN	20	19.6	19.6	12	12
1990	3	NaN	NaN	NaN	40	49.8	49.8	8.9	8.9
1990	4	NaN	NaN	NaN	48	48.4	48.4	4.8	4.8
1990	8	NaN	NaN	NaN	91	90.7	90.7	2	2
1991	2	NaN	NaN	NaN	47	46.7	44.4	10	10
1991	3	NaN	NaN	NaN	98	98.8	97.5	8.1	8.1
1992	7	NaN	−53.7	NaN	7	7	6.5	−0.5	−0.5
1992	8	NaN	−53.7	NaN	11	11	11	2.1	2.1
1992	11	NaN	NaN	NaN	14	NaN	13.9	8.8	8.8
1993	1	NaN	NaN	NaN	66	66	70.3	10.2	10.2
1993	3	NaN	NaN	NaN	61	61	61.2	8.5	8.5
1993	4	NaN	NaN	NaN	23	23	25.5	5.3	5.3
1993	5	NaN	NaN	NaN	17	17	17.3	3	3
1993	6	NaN	NaN	NaN	4	4	3.5	−0.1	−0.1
1993	10	NaN	NaN	NaN	23	23	22.5	7.1	7.1
1994	1	NaN	NaN	NaN	24	24	34.4	11.6	11.6
1994	2	NaN	NaN	NaN	63	62	53.9	9.8	9.8
1994	6	NaN	NaN	NaN	31	NaN	32	1	1.1
1994	7	NaN	NaN	NaN	28	28	32.5	0.8	0.8
1994	8	NaN	NaN	NaN	12	12	11.5	2.9	2.9
1994	9	NaN	NaN	NaN	35	35	35.3	2.9	2.9
1995	1	NaN	NaN	NaN	27	25	26.7	11.1	11.1
1995	2	−6.02	−58.3	−10.14	49	49	49.1	10.6	10.6
1996	11	−4.38	−46	−10.96	23	23	23.9	8.1	8.1
1997	4	NaN	NaN	NaN	81	77	88.2	5.6	5.6
1998	5	NaN	NaN	NaN	81	69	81.5	4.4	4.4
1998	7	NaN	NaN	NaN	44	44	44.2	3	3
2001	6	NaN	NaN	NaN	47.3	46	47.3	1.9	3.1
2001	7	NaN	NaN	NaN	21.1	22	19.1	NaN	0
2002	1	NaN	NaN	NaN	10.6	10	10.8	10.4	10.4
2002	8	−4.74	−62.9	−24.98	231.3	34	35.2	2.1	2.1
2002	9	3.49	−18.3	−46.22	43.1	43	43.1	4.4	4.4
2003	4	−5.58	−56.9	−12.26	8.7	9	7.4	6.5	6.5
2003	5	0.06	−30.1	−30.58	57.3	57	59.8	5.6	5.6
2003	6	NaN	NaN	NaN	45	45	46.6	1.8	1.8
2003	12	−4.28	−48.4	−14.16	56.7	57	60.7	9.9	9.9
2004	1	−2.65	−40.3	−19.1	35	35	34.1	11.7	11.7

Table A1 (continued)

Year	Month	$\delta^{18}O$	$\delta^{2}H$	*d*-excess	GNIP precipitation (mm)	GHCN precipitation (mm)	Sum of all 6-hour cumulative precipitation (mm)	GNIP temperature (°C)	GHCN temperature (°C)
2004	3	−0.9	−23.2	−16	20	20	21.1	9.1	9.1
2004	4	NaN	NaN	NaN	56	56	57.1	6.5	6.5
2004	5	NaN	NaN	NaN	14	14	12.3	5.3	5.3
2004	6	NaN	NaN	NaN	50	50	49.2	4.1	4.1
2004	9	4.13	−22	−55.04	29	29	32	4.6	4.6
2004	11	−5.38	−56.4	−13.36	37	37	37.2	9.9	9.9
2004	12	−4.51	−49	−12.92	19	19	19.6	10.9	10.9
2005	1	−0.35	−27.3	−24.5	29	29	32.8	10.6	10.6
2005	4	−5.88	−61.6	−14.56	79.2	79	77.8	6.3	6.3
2005	11	−4.74	−54.2	−16.28	33.2	33	33.8	8.6	8.6
2005	12	−0.97	−21.5	−13.74	13.2	12	13.2	10.2	10.1
2007	1	6.06	−10.2	−58.68	24.4	24	36.8	10.7	10.7
2007	6	−4.01	−51.9	−19.82	47	47	47.8	2.2	2.2
2007	11	−4.75	−48.7	−10.7	10.2	10	11	7.8	7.8
2008	1	−1.85	−23.9	−9.1	9.2	9	9.4	11.6	11.6
2008	2	NaN	NaN	NaN	45	45	44.4	11.3	11.4
2009	3	NaN	NaN	NaN	29.4	29	29.4	9	9
2009	9	−19.14	−153.2	−0.08	14.2	14	14	5.1	5.1
2009	10	−6.24	−60.4	−10.48	13.8	14	15.2	5.4	5.4
2009	11	−0.5	−0.4	3.6	28.2	28	28	5.5	5.5
2010	2	NaN	NaN	NaN	14	13	13.2	8.7	8.9
2010	6	−7.55	−75.4	−15	38	36	37.8	1.2	1.2
2010	9	−7.02	−71.7	−15.54	12.8	13	12.2	4.6	4.5
2010	12	−1.17	−27.1	−17.74	12	12	12	8.8	8.7
2011	5	NaN	NaN	NaN	29.2	31	8.4[b]	4.8	4.6
2011	10	NaN	NaN	NaN	23.8	24	21.7	6.8	6.8
2011	12	2.95	−12.3	−35.9	12.4	12	5[b]	11.6	11.6
2012	1	−2.23	−35.5	−17.66	20.6	21	20.6	11.6	11.6
2012	11	−4.5	−49.3	−13.3	19.4	19	19.4	8.7	8.7
2013	12	7.12	49.4	−7.56	36	36	36.2	8.9	8.9
2014	1	−0.4	−21.8	−18.6	20	20	20	9.2	9.2
2014	6	−21.36	−162.7	8.18	28.4	28	36.2	2	2
2017	12	−2.26	−36.9	−18.82	31.8	32	30.4	9.4	9.4

[a]NaN: no data

[b]These 6-hour precipitation data have important temporal gaps (see Figure A2).

Table A2. The number of $\delta^{18}O$ data (unfiltered) that are used in correlation heat map analysis shown in Figure 1.5.

	GDAS (2005–2017)	NCEP/NCAR (1990–2004)
All months	130	135
DJF	27	33
MAM	36	32
JJA	36	32
SON	31	38

CHAPTER 2

Environmental controls on the carbon and water (H and O) isotopes in peatland *Sphagnum* mosses

Zhengyu Xia[1], Yinsui Zheng[2], Jonathan M. Stelling[1], Julie Loisel[3], Yongsong Huang[2] and Zicheng Yu[1,4]

[1]Department of Earth and Environmental Sciences, Lehigh University, Bethlehem, PA, USA

[2]Department of Earth, Environmental and Planetary Sciences, Brown University, Providence, RI, USA

[3]Department of Geography, Texas A&M University, College Station, TX, USA

[4]School of Geographical Sciences, Northeast Normal University, Changchun, China

Abstract

We conducted a modern process study on *Sphagnum magellanicum* from southern Patagonian peat bogs to improve our understanding of environmental controls on the carbon and water (hydrogen and oxygen) isotope compositions of peat mosses. We found that moisture availability gradients in peat bogs, measured by *Sphagnum* water content, could explain the intra-site variability in both *Sphagnum* cellulose $\delta^{13}C$ and $\delta^{18}O$. Also, there was a site-specific significant negative correlation between cellulose $\delta^{13}C$ and $\delta^{18}O$ across microtopographical gradient. This new finding suggests that *Sphagnum* moisture availability influences cellulose $\delta^{13}C$ via water film effect on discrimination against $^{13}CO_2$ and, similarly, can imprint on cellulose $\delta^{18}O$ via evaporative enrichment of ^{18}O in metabolic leaf water. *Sphagnum* leaf wax *n*-alkane $\delta^{13}C$ also responded to the water film effect as cellulose did, but *n*-alkane $\delta^{2}H$ appears less sensitive than cellulose $\delta^{18}O$ to the moisture availability gradient likely because hydrogen isotopes have a more complex biochemical fractionation pathway and a smaller kinetic fractionation during leaf water evaporation. Furthermore, we used long strands of *Sphagnum* to explore if isotopic signals in moss strand increments were sensitive to recent growing season conditions. We demonstrated that rapidly growing *Sphagnum* strand increments could document the isotopic composition of precipitation and moisture conditions at sub-annual scale. Altogether, these findings highlight the sensitivity of stable isotopes in *Sphagnum* to environmental conditions. On the basis of these results, we propose that paired measurements of carbon and water isotopes in *Sphagnum* cellulose or leaf wax biomarker provide an improved approach in peat-based paleoclimate reconstructions.

2.1. Introduction

Peatland ecosystems—occupying only 3% of the global land area—are terrestrial carbon hot spots that have sequestered over 600 gigatons of organic carbon since the Last Glacial Maximum (ca. 21,000 years before present; Yu et al., 2010). Paleoenvironmental analysis using peat deposits provides valuable insights into peatland evolution, ecosystem dynamics, and past climate conditions. A range of proxy-climate indicators, including bulk density, humification, testate amoebae, charcoal, and plant macrofossils, have been routinely used in peat-based paleoenvironmental reconstructions (e.g., Woodland et al., 1998; Barber et al., 2000; Turney et al., 2004). Stable isotope proxies from peat-forming plant remains are important supplements to the more classic peat-core analysis toolbox (Brenninkmeijer et al., 1982; Chambers et al., 2012). *Sphagnum* mosses are a group of remarkable peat-forming plants as the main "peat builder" that possess many unique physiological characteristics and are resistant to microbial breakdown (Rydin & Jeglum, 2013). Also known as peat mosses, *Sphagnum* have attracted the most attention in exploring the potential of their stable isotope compositions as paleoenvironmental proxies (e.g., Xie et al., 2000; Ménot & Burns, 2001; Ménot-Combes et al., 2002; Xie et al., 2004; Daley et al., 2010; Nichols et al., 2010; Nichols et al., 2014b; Granath et al., 2018). Understanding the physiological processes mechanisms underlying the isotopic variations in modern *Sphagnum* plants is required for robust environmental interpretations of long-term isotopic variations preserved in *Sphagnum* peat records.

Carbon isotope signatures ($\delta^{13}C$) in *Sphagnum* follow the general carbon isotope fractionation model for C3 plants that considers kinetic isotope effects in CO_2 diffusion and carboxylation (Farquhar et al., 1989). The model has been further adapted for mosses that lack stomata and have an external water film on outer surface (Meyer et al., 2008; Royles et al., 2012). Royles et al. (2012) showed that several factors can affect carbon isotope discrimination, but CO_2 assimilation rate is the dominant factor for aerobic (non-

waterlogged) peatbank moss species in maritime Antarctic. In their theoretical study, mosses only attain external water film after a rain or snow melt event but then dry out quickly. In contrast, *Sphagnum* mosses often inhabit waterlogged peatlands and have great water retention capacity with a persistent external water film. As a result, moisture regime affects both *Sphagnum* CO_2 assimilation rate and carbon isotope fractionation caused by diffusion resistance, as CO_2 diffusivity is much lower in water than in air (Rice & Giles, 1996; Rice, 2000). Empirical studies supported that moisture availability exerts a major control on *Sphagnum* $\delta^{13}C$ known as the water film effect (Price et al., 1997; Ménot & Burns, 2001; Loisel et al., 2009; Loader et al., 2016): drier *Sphagnum* mosses are characterized by thinner water films that have less diffusion resistance and result in more discrimination against $^{13}CO_2$, leading to more negative $\delta^{13}C$ values in plant tissues, and vice versa. This effect is expressed at microtopographical gradients (e.g., hummock vs. hollow) within a peatland. A few additional factors were also shown to affect peatland *Sphagnum* $\delta^{13}C$, which include (1) the contribution of recycled CO_2 (Price et al., 1997), in particular the methane-derived CO_2 that is strongly depleted in ^{13}C and is efficiently fixed by *Sphagnum* in wet habitats (Raghoebarsing et al., 2005; Nichols et al., 2009; Nichols et al., 2014b); and (2) air temperature, although both positive and negative correlations between temperature and *Sphagnum* $\delta^{13}C$ have been reported in the literature (Skrzypek et al., 2007; Kaislahti Tillman et al., 2013). Therefore, *Sphagnum* cellulose and leaf wax $\delta^{13}C$ have been used to reconstruct past temperature and hydroclimate changes from peat records, often with contrasting interpretations (Xie et al., 2004; Nichols et al., 2009; Loisel et al., 2010; Moschen et al., 2011; Kaislahti Tillman et al., 2013).

For ombrotrophic (rain-fed) peat bogs, water (hydrogen and oxygen) isotope signatures in *Sphagnum* are determined by the isotopic composition of precipitation, subsequent evaporative enrichment of ^{18}O and ^{2}H in leaf water, and biochemical

fractionation. The fractionation process in cellulose biosynthesis has been shown to follow the form of (Anderson et al., 2002; Zanazzi & Mora, 2005; Daley et al., 2010):

$$\delta^{18}O_{cell} = \delta^{18}O_p + \varepsilon_b + (\varepsilon_e + \varepsilon_k)(1 - h) \quad (1)$$

where $\delta^{18}O_{cell}$ and $\delta^{18}O_p$ are the oxygen isotope composition of cellulose and precipitation, respectively; ε_b is the biochemical enrichment factor during cellulose biosynthesis; ε_e and ε_k are liquid–vapor equilibrium and kinetic enrichment factor associated with leaf water evaporation, respectively; and h is the relative humidity. It was argued that the evaporation term in Eq. (1) could be removed, because *Sphagnum* mosses lack stomata and inhabit moist environments with h close to 100% (Zanazzi & Mora, 2005; Daley et al., 2010). If assuming that biochemical fractionation term ε_b is a stationary value over time, then *Sphagnum* cellulose $\delta^{18}O$ and $\delta^{2}H$ as well as leaf wax $\delta^{2}H$ can be used to infer the isotopic compositions of past precipitation, which provide information about large-scale macroclimate drivers such as air temperature, precipitation sources, and atmospheric circulation patterns (Xie et al., 2000; Pendall et al., 2001; Daley et al., 2009; Daley et al., 2010; Bilali et al., 2013; Xia et al., 2018). However, the model given above have two deficiencies that need to be considered when applied to mosses. First, Eq. (1) was based on the Craig–Gordon model (Craig & Gordon, 1965) that depicted leaf water evapotranspiration through stomata as an analogue to steady-state evaporation of a closed lake (Ménot-Combes et al., 2002). It considered leaf water exchange with ambient water vapor through stomata and assumed that all leaf water was subject to evaporation (Anderson et al., 2002). It might be inappropriate to apply Eq. (1) to *Sphagnum* mosses, which lack stomata and evaporate leaf water through tiny pores on water-reservoir hyaline cells, preventing liquid-vapor interaction (Nichols et al., 2010). Second, the assumption of no evaporation with h at 100% is not always justified, as it would predict that $\delta^{18}O_{cell}$ values were conservative and independent from microhabitat within a peatland. This is in contradiction with empirical evidence showing that

Sphagnum leaf water is more enriched in ^{18}O and ^{2}H than meteoric water input and there is a clear hydrogen and oxygen isotope variability in *Sphagnum* tissues explained by differential degree of evaporative enrichment at microtopographical scale (Aravena & Warner, 1992; Ménot-Combes et al., 2002; Zanazzi & Mora, 2005; Nichols et al., 2010; Loader et al., 2016).

Our understanding of environmental controls on the carbon and water (H and O) isotope variability in *Sphagnum* tissues has improved in recent years, but a coherent physiological interpretation is not achieved. Still, most peat-core studies that undertook stable isotope analyses only utilized a single isotope proxy, such that the investigators were unable to examine the intrinsic relationships between the carbon and water (H and O) isotope ratios in *Sphagnum* organic compounds. Without a multi-proxy framework, it can be challenging to reconcile the multiple controlling factors on *Sphagnum* isotope ratios for paleoenvironmental interpretations, particularly for the relative role of evaporative enrichment on water isotope proxies (Daley et al., 2009; Finkenbinder et al., 2016). Given that moisture availability influences *Sphagnum* carbon isotope signatures via the water film effect, and that the degree of evaporative enrichment of ^{18}O and ^{2}H in leaf water also depends on moisture availability that is highly variable at microtopographical scale, there should be a negative correlation between these two isotope ratios. Demonstrating this carbon–water isotopic link in modern *Sphagnum* samples would provide a useful means to properly interpret peat-based climate-proxy records with a "dual isotopes" approach (Roland et al., 2015; Xia et al., 2018).

Here we present a dataset of paired cellulose $\delta^{13}C$ and $\delta^{18}O$ measurements of modern *Sphagnum magellanicum* from southern Patagonian peat bogs. Plant and leaf water samples were collected along a wide range of habitats and moisture gradients across multiple sites. We measured the water content (WC; the ratio of mass between water and dry plants) of each *Sphagnum* sample as an independent indicator of *Sphagnum*

moisture availability, in an attempt to explore how moisture availability influences cellulose $\delta^{13}C$ and $\delta^{18}O$ concurrently. We also present data from *Sphagnum* leaf wax biomarker *n*-alkane $\delta^{13}C$ and $\delta^{2}H$ measurements to test the same hypothesis. Furthermore, our previous work found that *S. magellanicum* in southern Patagonian peat bogs were growing fast and formed long strands that could reach over 45 cm in length, and indeed these peatlands had rapid accumulation rates due to enhanced *Sphagnum* growth (Loisel & Yu, 2013a, 2013b). As an extreme example, a Patagonian peatland has accumulated over 300 cm of *Sphagnum* peat in less than 500 years, which is an order of magnitude faster than boreal peatlands (Loisel & Yu, 2013a, 2013b). Therefore, we additionally explored if isotopic signals in *Sphagnum* strand increments could document recent growing season conditions at sub-annual scale, including monthly and seasonal changes in isotopic composition of precipitation and precipitation anomalies, to understand the nature and sensitivity of *Sphagnum* isotopic signals preserved in peat records. With this new understanding of *Sphagnum* isotopic physiology, we then further discussed the potential of using paired carbon and water (H or O) isotope measurements in peat-core analysis for paleoclimate reconstructions.

2.2. Methods

2.2.1. Study sites and sample collections

Southern Patagonia is characterized by a large precipitation gradient driven by interactions between strong westerly winds and north-south oriented mountain ranges of the Andes. Despite the widespread distribution of peatlands in Patagonia (Figure 2.1), *Sphagnum*-dominated peat bogs are only present on the eastern side (leeward side) of the Andes, where annual precipitation amounts are generally between 400 and 1000 mm (Loisel & Yu, 2013a). *Sphagnum magellanicum* is the dominant species in these peat bogs, forming large carpets that cover a vast peatland complex (Figure 2.2). Field

sampling was carried out at six sites in January 2016 and another site (Ariel Peatland) in January 2018 (Table 2.1). These sites are located between 52.1° S and 54.5° S and between 68.7° W and 71.9° W (Figure 2.1). High-resolution (5.5 km) regional climate modeling (Lenaerts et al., 2014) indicates an existing climate gradient (precipitation in particular) across these sites (Table 2.1), but more importantly these peatlands differ in hydromorphological characteristics (Figure 2.2). According to Rydin and Jeglum (2013), *hydromorphology* is a term used to express interactions between biotic and abiotic factors that shape the surface morphology and patterning of peatlands. As described below, our sampling strategy was designed to capture the greatest local moisture gradient of *Sphagnum* habitat within each site.

2.2.1.1. Surface *Sphagnum*

Our first site, Valle de Consejo (VC), is characterized by well-developed hummock-hollow-pool surface patterning. We established a 450-cm sampling transect along a large hummock-to-pool gradient (north-facing) with a relative relief of ~70 cm (Figures 2.2a and 2.2b). The entire gradient was mainly colonized by *S. magellanicum*. Another species (*S. cuspidatum*) was found on the edge of the open-water pool (Figure 2.2b). We collected surface samples (top ~3 cm) of living *Sphagnum* at 30-cm intervals from the hummock top down to the pool, with an additional sample at the boundary between the two *Sphagnum* species (n = 17, including three *S. cuspidatum* samples). We collected duplicate samples that were kept in sealable bags for subsequent water content (WC) measurements in the laboratory. We also measured *in situ* water table depth (WTD) at some sampling locations along the transect by digging small pits with a peat borer. Similarly, a 250-cm transect was sampled across a northeast-facing hummock-to-hollow gradient at Villa Runeval (VR) with a relative relief of ~60 cm. This site, which was only

sampled for *S. magellanicum* (n = 5), is characterized by very dry bog surface (Figure 2.2c). WC samples were collected for this site, but *in situ* WTD was not measured.

The Ariel Peatland (AP) has less pronounced microtopographical structures with a relatively flat and moist peatland surface at the center (Figures 2.2d and 2.2e). The sampled moisture gradient thus extended from the peatland's edge, where dry-adapted shrubs were found, to the center of the site, where *S. magellanicum* was abundant. We collected nine evenly distributed *S. magellanicum* samples across this peatland-wide moisture gradient. Similarly, site Cordillera Chilena (CC) is a high-elevation slope bog (Figures 2.2f and 2.2g), where we collected six *S. magellanicum* samples along the slope (with an elevation difference of ~20 m) following the same sampling strategy as for site AP. Lastly, opportunistic *S. magellanicum* samples were collected at three additional sites: (1) six samples from site Monte Tarn (MT), which is a wooded bog developing on a mountain slope where vegetation changes from forest to tundra within a 600-m elevation increase with *Sphagnum* widely present along a hiking trail (Figures 2.2h and 2.2i); (2) two samples from site Mirador Laguna Cura (MLC); and (3) two samples from site Azopardo (AZ). Again, for all these samples, duplicate WC samples were also collected.

2.2.1.2. Plant water and bog water sampling

During surface *Sphagnum* sampling, each of the same living plants were immediately squeezed using a syringe to collect "bulk" leaf water into 2 mL vials in the field. Opportunistic bog water samples were collected at site VC, AP, and CC, after small pits were dug using a peat borer at the exact location where surface *Sphagnum* was sampled.

2.2.1.3. *Sphagnum* strands

At site CC and VC, we found that *Sphagnum* often maintained >20 cm long intact strands that likely indicated rapid growth over the course of recent growing seasons (Figure 2.3). Similar long strands were also found at some sites in our previous field excursion in southern Patagonia (Loisel & Yu, 2013a). We collected the uppermost section of peat as a monolith from both sites that contained those long strands of *Sphagnum*, which were individually extracted and further subsampled in the laboratory.

2.2.2. Laboratory analysis

2.2.2.1. Water content measurements

Samples for water content (WC) measurements were dried in an oven at 50°C overnight. The sample weights before and after oven drying were measured. The WC was calculated as (Rydin & McDonald, 1985; Murray et al., 1989; Schipperges & Rydin, 1998):

$$\mathrm{WC}\ (\%) = \frac{m_w - m_d}{m_d} \times 100 \qquad (2)$$

where m_w and m_d are the wet weight and dry weight, respectively. Note that a few studies defined the metric using the same formula as relative water content (RWC) (e.g., Royles et al., 2013b; Royles et al., 2013a), which is a term originally defined as the ratio of the amount water in the leaf tissue to that present when fully turgid (Smart & Bingham, 1974). Despite being applied to vascular plants, the RWC is not easy to determine for bryophytes due to the difficulty to estimate turgid weight (Dilks & Proctor, 1979). Furthermore, other studies defined the ratio of wet weight to dry weight as WC (e.g., Titus et al., 1983; Titus & Wagner, 1984).

2.2.2.2. Surface *Sphagnum* subsampling

To prepare cellulose samples, surface *Sphagnum* samples (n = 47 in total) were examined under a stereomicroscope to make sure that only the topmost 1-cm sections of stem below the *Sphagnum* capitulum, which represented the most recent growth, were used for cellulose extraction. For each subsample, around 15 individual stems were combined. Other moss components (leaves, branches, and older stems) were removed. The reason for restricting our analysis on stem tissues is to make our pre-treatment procedure and cellulose isotopic signatures comparable with peat-core studies, in which *Sphagnum* stem macrofossils could easily be collected to sufficient amount (Xia et al., 2018), and to avoid mixture of different tissues that showed somewhat isotopic offsets (Loader et al., 2007; Moschen et al., 2009; Kaislahti Tillman et al., 2010).

To prepare leaf wax samples, we just used bulk *Sphagnum* capitula (~0.6 g dry wt.) from selective samples for lipid extraction. For site VC, we analyzed seven samples. For other sites, we analyzed only one sample from each site.

2.2.2.3. *Sphagnum* strand subsampling

For *Sphagnum* strand samples, we noticed that stem bifurcations or innovation formations were quite frequent as a result of vegetative reproduction, but new bifurcated strands showed similar length with their siblings (Figure 2.3c). To prepare cellulose samples, we picked out one individual *Sphagnum* strand that possessed multiple bifurcations from the CC monolith, cut it into 1-cm sections, and combined corresponding sections from bifurcated strands to generate enough materials for cellulose extraction. We had to assume that bifurcated strands had similar incremental rate. We followed the same procedure for one strand from the VC monolith, but they were cut into 2-cm sections. The sectioned samples were then examined under a stereomicroscope to isolate stem tissues for cellulose extraction.

Among the individual *Sphagnum* strands, we observed that the stem bifurcations were roughly consistent with an occurrence rhythm of ~7 cm, likely indicating similar growth rate even among multiple individuals (Figure 2.3c). Although there are very few studies on *Sphagnum* stem bifurcations (Sobotka, 1976), we tested the hypothesis that bifurcations could be used as a roughly time marker by lining up 18 individuals picked out from the CC monolith and comparing the occurrences of stem bifurcations along the *Sphagnum* strands. Then we selected the 10 *Sphagnum* individuals with the highest bifurcation match, cut them into 1-cm sections, and combined them to generate enough materials for lipid extraction (~0.25 g dry wt.). We analyzed seven sectioned strand samples at 2-cm intervals.

2.2.2.4. Cellulose isotope analysis

The method of cellulose extraction followed the alkaline bleaching method (Kaislahti Tillman et al., 2010). Stem collections were transferred to disposable polypropylene columns (Poly-Prep). Samples were subjected to 5 rounds of 1.4% (w/v) sodium chlorite bleaching acidified with glacial acetic acid in a hot water bath at 80°C, each round for 50 min. Then, they were reacted with 10% (w/v) sodium hydroxide at 75°C for 45 min and another 2 rounds of acidified sodium chlorite bleaching. The yielded α-cellulose was rinsed with distilled deionized water and transferred to small vials. Afterwards, samples were homogenized using an ultrasonic probe and freeze-dried.

For oxygen and carbon isotope analysis, ~0.4 mg and ~1.1 mg cellulose materials were enclosed in silver and tin capsules, respectively. Strand subsamples were small in sample size, thus only ~0.25 mg and ~0.5 mg materials were used. Oxygen isotope compositions were determined on an Elementar PyroCube interfaced to an Isoprime VisION isotope-ratio mass spectrometer (IRMS). Carbon isotope compositions were determined on a PDZ Europa ANCA-GSL elemental analyzer interfaced to a PDZ

Europa 20-20 IRMS. Both isotopic analyses were carried out at the Stable Isotope Facility (SIF) of University of California, Davis. By convention, results of isotope ratio measurements were reported as δ notation (in per mille) referenced to VPDB (Vienna Pee Dee Belemnite) for $\delta^{13}C$ and to VSMOW (Vienna Standard Mean Ocean Water) for $\delta^{18}O$. During analysis, samples were interspersed with replicates of established calibration standards and several check standards with known isotopic compositions. The check standards were used to monitor the analytical drift and size effect and corrections were applied when necessary to ensure analytical accuracy for sample measurements. Precision of measurements was assessed by standard deviation (1σ) of replicate analyses of standards, which was less than 0.09‰ for $\delta^{13}C$ and 0.22‰ for $\delta^{18}O$. The standard deviation (1σ) of replicate analyses of samples for $\delta^{18}O$ was less than 0.21‰, suggesting our cellulose samples were well homogenized.

2.2.2.5. Leaf wax isotope analysis

Prepared leaf wax samples were washed, freeze dried, and extracted for lipids using a Dionex Accelerated Solvent Extractor (ASE) with a 9:1 (v/v) solution of dichloromethane and methanol at 120 °C and 1200 psi. The total lipid extracts were separated over flash column chromatography with silica gel (40-63 μm, 60 Å), and the *n*-alkanes were eluted with hexane. Concentrations of *n*-alkane compounds were determined on an Agilent 6890 gas chromatography-flame ionization detector (GC-FID), with an internal standard (hexamethylbenzene) added into each sample vial. The *n*-alkane compounds were identified by comparing the retention times with a mixture of external *n*-alkane standards (C_{25}, C_{27}, C_{29}, C_{30}, and C_{32} *n*-alkane). Compound-specific carbon isotope ratios and hydrogen isotope ratios for *n*-alkanes were determined on an Agilent HP-6890 gas chromatograph (GC) interfaced to a Thermo Finnigan Delta + XL stable isotope ratio mass spectrometry (IRMS) through a high-temperature pyrolysis reactor.

Both GC-FID and GC-IRMS analyses were carried out at Brown University. Detailed information about analytical methods could be found in Li et al. (2018). The compound-specific *n*-alkane $\delta^{13}C$ (referenced to VPDB) were measured once or twice, while $\delta^{2}H$ (referenced to VSMOW) were measured in triplicate with means and standard deviations (1σ) determined. External standard mixture was also interspersed and measured throughout to monitor instrument performance. The isotopic compositions of these laboratory standards were established by repeated measurements after verifying the instrument performance using the standard compounds acquired from Indiana University. The offsets between measured and established $\delta^{2}H$ values for laboratory standards during analyses of individual sample batches can range from 3 to 7‰. The offsets were used to correct sample $\delta^{2}H$ on daily batches and ensure accuracy. Correction was not needed for sample $\delta^{13}C$ as the offsets were very small (less than 0.1‰). The overall analytical precision was assessed using pooled standard deviation (1σ) of replicate analyses of standards or samples (C_{21}, C_{23}, and C_{25} *n*-alkane only) following Daniels et al. (2017), which was less than 0.23‰ for $\delta^{13}C$ and 3.14‰ for $\delta^{2}H$.

2.2.2.6. Water sample isotope analysis

The squeezed leaf water and bog water samples were treated with activated charcoal and filtered to remove dissolved organic matter before being analyzed for hydrogen and oxygen isotope compositions using a Picarro model L1102-i isotopic liquid water and water vapor analyzer at Brown University. Samples were analyzed with Picarro ChemCorrect software and no sample was flagged as being contaminated. Each sample was measured in eight injections and the first two injections were discarded for between-sample memory. Four secondary isotopic standards were established by directly being calibrated against primary isotopic standards (VSMOW, USGS-46, and USGS-49). Accuracy was assessed by interspersing these secondary isotopic standards throughout

samples and comparing their measured values with established values. The offset was less than 0.43‰ for δ^2H and 0.22‰ for $\delta^{18}O$. The overall analytical precision was assessed using pooled standard deviation (1σ) of replicate analyses of samples, which was 0.61‰ for δ^2H and 0.10‰ for $\delta^{18}O$.

2.2.2.7. Statistical analysis

To statistically test the correlation among isotope data and WC measurements, we performed the Pearson correlation using *scipy.stats.pearsonr* function on Python v2.7.13 to derive correlation coefficient (r) and *p* value. The correlation is considered significant when *p* is less than 0.05.

2.3. Results

Full datasets for field measurements and isotope analysis for surface samples are given in the Supplementary Table B1. The measured *Sphagnum* WC varied from 444% to 1928% among all surface *Sphagnum* samples. The maximum WTD was 65 cm at hummock-to-tool transect at site VC. The sites AP and CC had WTD of 42 cm and 70 cm, respectively. Surface *Sphagnum* cellulose $\delta^{13}C$ values ranged from −32.1‰ to −24.1‰, and $\delta^{18}O$ values ranged from 18.0‰ to 21.9‰. The concentrations of *n*-alkanes in surface *Sphagnum* samples ranged from 61 to 152 μg/g dry wt., and their distribution was dominated by *n*-C_{23}, followed by *n*-C_{21} and *n*-C_{25}, confirming *n*-C_{23} as the major biomarker for *Sphagnum* (Figure B1; Nichols et al., 2006). We observed that *n*-alkane distribution changed with WC (Figure B2), but we only presented and discussed isotope data in *Sphagnum* leaf wax biomarker *n*-C_{23} hereafter. Surface *Sphagnum n*-C_{23} $\delta^{13}C$ values ranged from −42.3‰ to −37.9‰, and *n*-C_{23} δ^2H values ranged from −219.4‰ to −196.4‰. Squeezed *Sphagnum* leaf water δ^2H and $\delta^{18}O$ values ranged from −72.3‰ to −19.1%, and from −8.9‰ to 0‰, respectively. Bog water δ^2H and $\delta^{18}O$ values ranged

from −89.2‰ to −77.1‰, and from −12.1‰ to −10.3‰, respectively, which were distinctly lower than squeezed leaf water data.

Isotope data for long strand samples are given in the Supplementary Table B2. Cellulose $\delta^{13}C$ and $\delta^{18}O$ values along the long strands at site CC (1-cm increments) ranged from −29.5‰ to −28.3‰, and from 18.8‰ to 21.0‰, respectively. These ranges of isotopic variability are smaller for $\delta^{13}C$ and larger for $\delta^{18}O$ than that in surface *Sphagnum* samples at the same site. The concentrations of *n*-alkanes along the CC strands (seven samples) ranged from 51 to 90 µg/g dry wt., and their *n*-C_{23} $\delta^{13}C$ and $\delta^{2}H$ values ranged from −41.7‰ to −40.2‰, and from −216.7‰ to −212.3‰, respectively. Cellulose $\delta^{18}O$ and $\delta^{13}C$ values along the long strands at site VC (2-cm increments) ranged from −29.7‰ to −28.6‰, and from 20.4‰ to 21.4‰, respectively. However, for VC strands, both these ranges of variability are smaller than that in VC surface *Sphagnum* samples, and such narrow variability impeded detecting sub-annual signals on the strands, likely due to the coarser analytical resolution (2cm increments rather than 1cm; Figure B3). We thus only discussed the results from long strands of site CC hereafter.

2.3.1. Surface *Sphagnum* cellulose isotopic variability across moisture gradient

The overall correlation between cellulose $\delta^{13}C$ and WC among all samples across multiple sites is positive and significant ($r = 0.78$, $p < 0.001$), with lower $\delta^{13}C$ values correlated with drier conditions (Figure 2.4a). In contrast, the overall correlation between cellulose $\delta^{18}O$ and WC is negative but not statistically significant at the 95% level ($r = -0.29$, $p = 0.051$). Despite this, their correlations are statistically significant at the regional scale (see caption of Figure 2.1) in Karukinka Park ($r = -0.52$, $p < 0.05$) and Laguna Blanca ($r = -0.71$, $p < 0.05$), with higher $\delta^{18}O$ values correlated with drier conditions (Figure 2.4b; Table B3).

For the hummock-to-pool transect at site VC, measured WC of *Sphagnum* was closely linked to the available WTD data, capturing localized moisture availability along the microtopographical transect. Towards the drier end of the transect (0–200 cm from hummock top), the range of WC was narrow with a mean of 840% (Figure 2.5c). Cellulose samples close to the hummock top had relatively lower $\delta^{13}C$ values (lower than −29.5‰) and high $\delta^{18}O$ values (higher than 19.8‰). The central portion of the transect (200–400 cm from hummock top) was characterized by a clear trend towards higher WC and shallower WTD, with increasing cellulose $\delta^{13}C$ and decreasing cellulose $\delta^{18}O$. The highest $\delta^{13}C$ value (−24.1‰) and the lowest $\delta^{18}O$ value (18.0‰) were recorded from *S. cuspidatum* samples growing at the wettest end of the sampling transect (Figures 2.5a and 2.5b). Statistically, cellulose $\delta^{13}C$ and $\delta^{18}O$ from site VC showed significant positive and negative correlations with WC, respectively ($r = 0.94$, $p < 0.001$; $r = -0.83$, $p < 0.001$; Figures 2.4a and 2.4b), even if *S. cuspidatum* data were excluded ($r = 0.92$, $p < 0.001$; $r = -0.72$, $p < 0.01$; Table B3).

At site AP where samples were collected evenly from the edge to the center of peatland along a narrower range of WC than at VC, a significantly positive correlation between cellulose $\delta^{13}C$ and WC was still found ($r = 0.89$, $p < 0.01$; Figure 2.4a), but not between cellulose $\delta^{18}O$ and WC ($r = -0.55$, $p = 0.13$; Figure 2.4b). At site MT where samples were collected along a mountain slope, the reported significant correlations between cellulose $\delta^{13}C$ and WC ($r = 0.92$, $p < 0.01$) and between cellulose $\delta^{18}O$ and WC ($r = -0.84$, $p < 0.05$) appeared to be driven by two samples (Figures 2.4a and 2.4b) collected at high elevations, near the alpine treeline (Figure 2.2h). However, the site-specific correlations between cellulose $\delta^{13}C$ and WC and between cellulose $\delta^{18}O$ and WC are statistically insignificant at sites VR ($r = 0.58$, $p = 0.31$; $r = -0.29$, $p = 0.64$) and CC ($r = 0.22$, $p = 0.67$; $r = -0.34$, $p = 0.51$), where the ranges of WC were narrow. Despite this, both VR and CC sites are in the same region (Laguna Blanca; Figure 2.1), and a

statistically significant correlations were achieved if data from both sites were combined ($r = 0.68$, $p < 0.05$; $r = -0.71$, $p < 0.05$; Figures 2.4a and 2.4b).

2.3.2. Surface *Sphagnum* leaf wax isotopic variability across moisture gradient

The positive correlation between *n*-C_{23} $\delta^{13}C$ and WC is weaker than cellulose dataset, but still significant ($r = 0.24$, $p < 0.05$; Figure 2.4c). We found that the *n*-C_{23} $\delta^{13}C$ data *per se* are highly correlated with their corresponding cellulose $\delta^{13}C$ ($r = 0.93$, $p < 0.001$; Figure B4), thus the weaker correlation between *n*-C_{23} $\delta^{13}C$ and WC is likely an artifact of selective measurements in *n*-alkane isotope dataset. However, there was no significant correlation between *n*-C_{23} $\delta^{2}H$ and WC ($r = 0.18$, $p = 0.56$; Figure 2.4d). Data from seven samples from VC hummock-to-pool transect showed similar pattern (Figure 2.5).

2.3.3. Isotopic relationship among bog water, squeezed leaf water, plant cellulose and leaf wax

Bog water isotope data were plotted very close to either global meteoric water line (GMWL) or local meteoric water lines (LMWL) and were similar to the isotopic composition of mean annual precipitation recorded in Global Network of Isotopes in Precipitation (GNIP; accessed from https://nucleus.iaea.org/wiser) station in Punta Arenas (Figure 2.6a). Squeezed *Sphagnum* leaf water was more enriched in ^{2}H and ^{18}O, and these leaf water isotope data fell on local *Sphagnum* evaporation lines (referred as LSEL hereafter) at a slope of 4.83, 5.60, and 3.87 in Karukinka Park region, Laguna Blanca region, and site MT, respectively (Figure 2.6a). We found that squeezed leaf water $\delta^{18}O$ data were much more scattered than cellulose $\delta^{18}O$ data and they were unexpectedly negatively correlated ($r = -0.48$, $p < 0.01$; Figure 2.6b). Interestingly, the higher squeezed leaf water $\delta^{2}H$ and $\delta^{18}O$ values seemed to be associated with the higher

WC (Figure 2.6b). There was no significant correlation between *n*-C_{23} δ^2H, which were selectively analyzed unlike cellulose dataset, and squeezed leaf water δ^2H ($r = 0.28$, $p = 0.35$; Figure B5).

2.3.4. Isotopic variability along *Sphagnum* long strands

For *Sphagnum* strands at site CC, stem bifurcations occurred mainly at 7−9 cm and 12−16 cm from capitula (Figure 2.7d). Plotting strand cellulose $\delta^{18}O$ data versus each 1-cm strand increment showed a sine function-like pattern, which aligned well with the growing season (likely October−April when average air temperature is higher than 5 °C without snow ground; Daley et al., 2012) monthly precipitation $\delta^{18}O$ data in recent two years (2015 and 2014) recorded by the closest (~130 km away) GNIP station in Punta Arenas (Figures 2.7a and 2.7b). The *n*-C_{23} δ^2H signals along *Sphagnum* strands showed similar seasonal shifts, but the amplitude of variability was only 4.4‰ (Figure 2.7b). A plot of cellulose $\delta^{13}C$ versus stem increment did not show any clear seasonal pattern (Figure 2.7c). Noteworthy were the highest $\delta^{13}C$ values in sections of 18−20 cm and the decline in $\delta^{13}C$ towards recent growth, leading to a roughly parallel trend between cellulose $\delta^{13}C$ and Punta Arenas monthly precipitation anomaly record based on the Global Historical Climatology Network (GHCN; accessed from https://www.ncdc.noaa.gov/ghcnm/) data (Figures 2.7a and 2.7c). The *n*-C_{23} $\delta^{13}C$ data showed a similar decreasing trend as cellulose $\delta^{13}C$ towards recent growth, but with a larger amplitude of shift from −40.1‰ to −41.7‰ (Figure 2.7c).

2.4. Discussion

2.4.1. Water content (WC) as an indicator of *Sphagnum* moisture availability

To validate the response of paleohydrological proxy to moisture gradient in peatlands, usually WTD rather than plant tissue water content is measured, assuming that

a deeper WTD is associated with drier habitat, and vice versa (Markel et al., 2010; Loader et al., 2016; Granath et al., 2018). Indeed, WTD is one of the most important predictors of vegetation distribution and growth in peatlands (Rydin & Jeglum, 2013). In this study, however, we used WC to characterize *Sphagnum* moisture availability at their localized habitats (Van Bellen et al., 2014; Bramley-Alves et al., 2015; Royles et al., 2016), and we argue that WC is an equivalent or even more sensitive moisture indicator than WTD for the following reasons.

First, the difference in the mean and range of WC values between different sites conform to our field observation and sampling strategy (Figure 2.4; Table B1). For example, the site VR had a very low mean WC (595%) with a narrow range (243%), and our field observation indicated that this site was a very dry bog and maintained only a weak moisture gradient even across the sampled hummock-to-hollow transect (Figure 2.2c). In contrast, the sites VC and AP had high mean WC of 1118% and 1203% with wide ranges of 1120% and 950%, respectively, in agreement with our field observation that these two sites were generally wet (Figs 2b and 2e) and with our sampling strategy that maximized the site-specific moisture gradient. WC was not correlated with mean annual precipitation inferred from regional climate model output (Table 2.1; Figure B6), suggesting that WC mainly reflects peatland-specific moisture conditions. Second, southern Patagonian peat bogs are usually characterized by WTD as deep as 70 cm (Table B1). As a result, *Sphagnum* capitula on the peatland surface might have weak hydrological connections with the deep peatland water table, while *Sphagnum* mosses typically only access water stored in the top 20 cm of peat (Nichols et al., 2010). The WTD and WC measurements across hummock-to-pool transect at site VC showed congruent trends, but they were not the same: *Sphagnum* samples collected at 60 cm and 180 cm away from hummock top had WTD of 65 cm and 50 cm, respectively, but almost identical WC of ~880% (Figure 2.5c). Van Bellen et al. (2014) also found that WC was

not sensitive to WTD variations if WTD was greater than 40 cm in southern Patagonian peat bogs. Third, WC measurements have been applied to study how photosynthesis and respiration of bryophytes (in particular *Sphagnum*) respond to moisture regimes under controlled laboratory conditions or in the field known as plant–water relations (Dilks & Proctor, 1979; Titus et al., 1983; Rydin & McDonald, 1985; Murray et al., 1989; Rice & Giles, 1996; Schipperges & Rydin, 1998; Royles et al., 2013b). For example, *Sphagnum* mosses have been shown to have the maximum rate of photosynthesis at WC of 700−1000%, while progressively wetter-than-optimum WC would only gently decrease photosynthesis rate but slightly lower-than-optimum WC would drastically slow or even cease photosynthesis (Schipperges & Rydin, 1998). However, field WC measurements were never applied to validate stable isotope proxies in peatlands, and it impeded our understanding how the expression of stable isotope variations in *Sphagnum* was tied to plant physiology.

We acknowledge that our WC measurements represented only "snapshot" moisture conditions that were often complicated by factors including recent rainfall events, morning dew, evapotranspiration, and shading from co-existing vascular plants (Silvola & Aaltonen, 1984; Titus & Wagner, 1984; Murray et al., 1989; Williams & Flanagan, 1996; Van Bellen et al., 2014). Weather station data from Punta Arenas (not shown) indicated that there was only 1.1 mm precipitation at least two weeks prior to sample collection, thus the impact of recent precipitation was very limited. Microtopography is the major driver of WC variability at the time of sample collection as shown in the transect at site VC (Figures 2.2b and 2.5). Therefore, we think that the measured WC represents the moisture gradient in which *Sphagnum* would experience over the majority course of growing season, at least in the one to three months before sample collection. However, it is unclear how the absolute values of WC at each sampling location would change temporally, particularly for hollow microforms where

desiccation often occurs (Rydin & Jeglum, 2013). Future studies should collect field *Sphagnum* WC data over the complete growing season to understand its natural short-term and long-term variability at different microforms in peatlands. A few existing studies have shown that the WC of *Sphagnum* displays a degree of stability on daily and monthly scales (Silvola & Aaltonen, 1984; Titus & Wagner, 1984).

2.4.2. Carbon isotope signatures in *Sphagnum* controlled by the water film effect

Sphagnum mosses growing at different peatland sites are using the same atmospheric CO_2 source for photosynthesis. If recycled CO_2 was insignificant, their cellulose $\delta^{13}C$ should be primarily affected by plant-specific growth conditions. Species effects of leaf anatomy/physiology were excluded in our study as we focused on single species *S. magellanicum*. The significantly positive correlations between cellulose $\delta^{13}C$ and WC, either from a single site or from all sites together, indicate strong sensitivity of *Sphagnum* cellulose $\delta^{13}C$ to moisture availability, as explained by the water film effect (Figure 2.4a). A few additional measurements on wet-adapted species *S. cuspidatum*—which possesses triangle-shaped photosynthetic cells exposed at the leaf surface instead of being enclosed by hyaline cells as in *S. magellanicum* (Rice & Giles, 1996; Loisel et al., 2009)—showed very high cellulose $\delta^{13}C$ values (−24.7‰ on average) that characterized strong CO_2 diffusional resistance at extreme wetness, consistent with WC data (Figure 2.5b). It suggested that any species effects of leaf anatomy were overprinted by the expression of water film effect. Furthermore, a previous study showed that the pool species *S. cuspidatum* could have $\delta^{13}C$ value as low as −34.7‰ (Proctor et al., 1992), which indicated the contribution of recycled CO_2 in wet habitat, but in our dataset, there was no sign of extremely negative $\delta^{13}C$ signals caused by recycled CO_2. However, we also found that cellulose $\delta^{13}C$ and mean annual precipitation inferred from regional climate output had a weak, but significant, cross-site negative correlation ($r = -0.32$, $p<$

0.05), in opposite to the water film effect (Figure B6). Although the mechanism for this observation was unclear, hereafter we only discuss the WC effect that exhibited strong and multi-level control on cellulose $\delta^{13}C$.

Sphagnum *n*-C_{23} $\delta^{13}C$ data also support the water film effect (Figure 2.4c), and the strong correlation between *n*-C_{23} $\delta^{13}C$ and cellulose $\delta^{13}C$ with a regression equation slope of 1.01 (Figure B4) implied that moisture gradient affected cellulose and *n*-alkanes $\delta^{13}C$ similarly. The interception in regression function perhaps mean the offset of fractionation (~10.7‰) between *n*-alkane and cellulose biosynthesis (Figure B4).

2.4.3. Cellulose oxygen isotope signatures in *Sphagnum* influenced by evaporative enrichment

It has been well understood that *Sphagnum* cellulose $\delta^{18}O$ is controlled by source water $\delta^{18}O$ by an offset of biochemical enrichment factor, but source water in *Sphagnum* leaves likely has been additionally modified by evaporative enrichment relative to precipitation input (Price et al., 2009; Loader et al., 2016). If precipitation $\delta^{18}O$ was invariant and if the degree of evaporative enrichment of ^{18}O in leaf water was higher in drier *Sphagnum* (Ménot-Combes et al., 2002), we would expect a negative correlation between cellulose $\delta^{18}O$ and WC. Our data showed such negative correlations at site-specific scale and at regional scale (Figure 2.4b), supporting the strong influence of evaporative enrichment on *Sphagnum* cellulose $\delta^{18}O$ signals. However, correlation was insignificant when data from all sites were combined. This could be explained by certain spatial variability in precipitation $\delta^{18}O$ signals induced by local topography and air-mass trajectories in terrain-complex Patagonia (Daley et al., 2012; Xia et al., 2018). Despite a lack of regional precipitation isotope measurements, our opportunistic samples of bog water that isotopically were close to yearly averaged precipitation indicated that

precipitation $\delta^{18}O$ in Laguna Blanca region might be 1−2‰ lower than in Karukinka Park region (Figure 2.6a).

However, our squeezed leaf water isotope data appeared to not support the idea that evaporative enrichment of ^{18}O was progressively larger with lower WC. Although our sampling approach can only collect ephemeral "bulk" leaf water during that particular day rather than over a time span, the significantly negative relationship between cellulose and squeezed leaf water $\delta^{18}O$ ($r = -0.48$, $p < 0.01$; Figure 2.6b) is contradictory to the physiological models that have been widely tested. This observation is similar to another study on New Zealand peatland rushes (*Empodisma spp.*) that found root cellulose $\delta^{18}O$ was negatively correlated with root water and precipitation $\delta^{18}O$ (Amesbury et al., 2015). We also suggested that this observation in *Sphagnum* may provide some insights into the nature of metabolic water in *Sphagnum* leaves.

The most plausible explanation is that our "bulk" leaf water collected by squeezing the capitula did not represent the metabolic water used for cellulose biosynthesis. *Sphagnum* have great water retention capacity by hyaline cells in the leaves and the outer cortex of the stems, but most of the water is stored between the leaves known as external capillary spaces, i.e., outside hyaline cells (Murray et al., 1989; Rydin & Jeglum, 2013). This external capillary water is an essential functional component in the physiology of many bryophytes (Dilks & Proctor, 1979; Proctor et al., 1998). Figure 2.6b showed that *Sphagnum* with higher WC tended to have higher squeezed leaf water $\delta^{18}O$, and statistical analysis suggested they were positively correlated ($r = 0.46$, $p < 0.01$). If *Sphagnum* with higher WC had higher percentage of water outside hyaline cells and if this fraction of external water was strongly modified by unsteady-state evaporation, our squeezed leaf water would be biased towards higher $\delta^{18}O$ values that might not represent the isotopic composition of leaf water inside hyaline cells (internal water), driving the observed negative correlation. This situation is very likely, as the

laboratory experiment by Price et al. (2009) found that their squeezed "pore water" in the top 5 cm section of *Sphagnum* peat had the $\delta^{18}O$ value over 6‰ higher than irrigated water after just one day. Another recent study also proposed that *Sphagnum* capitula water collected by squeezing had been more evaporatively enriched relative to the net isotopic composition of the water (here we called "internal water") used for cellulose biosynthesis (Loader et al., 2016), supporting our speculation.

Furthermore, drier *Sphagnum* such as those growing on hummocks could allocate resources into structural carbohydrates at the cost of metabolic carbohydrates and this strategy aided in maintaining high water retention capacity (Turetsky et al., 2008). As a result, *Sphagnum* in drier habitat could survive dry conditions and still grow, and their cellulose $\delta^{18}O$ might be able to record a moderate degree of evaporative enrichment signal (Aravena & Warner, 1992). In contrast, wetter *Sphagnum* such as those growing in hollows or pools had higher collective surface area and could dry out quickly, thus their growth was limited by desiccation (Rydin & Jeglum, 2013). As a result, *Sphagnum* in depressions might cease to grow and fail to register evaporative enrichment signal. However, our field observation found no sign of desiccation for *Sphagnum* growing in depressions during sampling, such as the pool in the site VC (Figure 2.2b). In fact, at this site *S. cuspidatum* floating on the edge of pool had the lowest cellulose $\delta^{18}O$ value (18.0‰; Figure 2.5b), while pool water likely was highly enriched in ^{18}O due to exposure to air. Instead, we further speculate that for *Sphagnum* with higher WC their internal water was partitioned and protected from evaporation by the presence of thicker external water, thus their metabolic water likely was rarely modified by evaporative enrichment, but isotope signals of this internal water were poorly represented in that of squeezed leaf water we measured.

The median enrichment factor between squeezed leaf water and cellulose $\delta^{18}O$ was 26.0‰, but if we used precipitation $\delta^{18}O$ in the recent one to three months from

Punta Arenas GNIP data as the source water input, the median enrichment factors would range from 28.5‰ to 30.7‰ (Figure B7). Although the uncertainty in biochemical fractionation of cellulose biosynthesis has been estimated as ±1‰ (Daley et al., 2010) or ±3‰ (Zanazzi & Mora, 2005), the widely accepted value of 27‰ (Sternberg, 2009) was above the enrichment factor calculated from squeezed leaf water data, but below the enrichment factor calculated from precipitation data, suggesting that internal metabolic leaf water were indeed enriched in ^{18}O relative to precipitation, but not as much as our measured values from squeezed leaf water suggested.

2.4.4. Leaf wax hydrogen isotopes in *Sphagnum* insensitive to moisture gradient

Although *Sphagnum* cellulose $\delta^{18}O$ data showed sensitivity to record evaporative enrichment of ^{18}O in metabolic leaf water, the *n*-C_{23} $\delta^{2}H$ signals showed a muted response to moisture gradient and did not record the evaporative enrichment of ^{2}H in proportional to that was expressed in cellulose $\delta^{18}O$ dataset (Figures 2.4d and 2.5a). This requires explanation, and we propose two possible mechanisms below.

First, in general biochemical fractionations in hydrogen isotopes are much more complex than in oxygen isotopes (Yakir, 1992; Sachse et al., 2012). The pathway of biochemical fractionation in cellulose $\delta^{18}O$ lies in the post-photosynthetic (heterotrophic) exchange reactions during carbonyl hydration, with a well-conservative enrichment factor centered at ~27‰ for cellulose relative to source water (Sternberg et al., 1986; Sternberg, 2009). However, biochemical fractionations of hydrogen isotopes in either cellulose or *n*-alkanes represent a balance between autotrophic and heterotrophic metabolisms that resulted in ^{2}H depletions and enrichments in carbohydrate intermediates, respectively (Yakir, 1992; Sessions et al., 1999). A series of hydrogen addition, removal, and isotopic exchange reactions are involved in heterotrophic processing of carbohydrates (Sachse et al., 2012; Mora & Zanazzi, 2017). As a result, the hydrogen atoms on the final *n*-alkane

products could originate from metabolic leaf water, biosynthetic precursors, and NADPH (Sessions et al., 1999; Sachse et al., 2012). *Sphagnum* metabolic leaf water δ^2H variations, if any, might be smoothed in *n*-alkane δ^2H due to complex hydrogen isotope fractionation pathway.

Second, kinetic fractionation of hydrogen isotopes is smaller than oxygen isotopes. Evaporation of leaf water involves both equilibrium and kinetic isotope effects. The equilibrium fractionation factor for hydrogen isotopes differs from oxygen isotopes by a well-known factor of ~8, which accounts for the slope of GMWL in δ^2H–$\delta^{18}O$ space. A lower kinetic fractionation factor for hydrogen isotopes than oxygen isotopes accounts for the lower slope of local evaporation line (LEL) than GMWL, the former of which typically is in the range from 5 to 7. That said, theoretical prediction of the LEL (Mayr et al., 2007a) is based on the Craig–Gordon model (Craig & Gordon, 1965). Again, *Sphagnum* mosses lack stomata and evaporate leaf water through tiny pores on hyaline cells, preventing liquid-vapor interaction. Therefore, the Rayleigh model better characterizes the evaporation process in *Sphagnum* hyaline cells (Nichols et al., 2010):

$$\ln f = -\frac{\delta_s - \delta_p}{\varepsilon_e + \varepsilon_k} \tag{3}$$

where δ_s and δ_p are the isotopic composition of *Sphagnum* leaf water and precipitation, respectively; ε_e and ε_k are the equilibrium and kinetic enrichment factors, respectively; and f is the fraction of water remaining after evaporation. Then the slope (S) of LSEL under gradual *Sphagnum* leaf water loss is:

$$S = \frac{\varepsilon_e^H + \varepsilon_k^H}{\varepsilon_e^O + \varepsilon_k^O} \tag{4}$$

where ε_e^H and ε_k^H are the equilibrium and kinetic enrichment factors for hydrogen isotopes, respectively, and ε_e^O and ε_k^O are the equilibrium and kinetic enrichment factors for oxygen isotopes, respectively. As an exercise, we used an average summer mid-day time temperature (17.4 °C or 290.55 K) and relative humidity (70.0%; Loader et al.,

2016) representative for southern Patagonian peat bog conditions to derive these enrichment factors based on previously established models (Gonfiantini, 1986; Horita & Wesolowski, 1994): the ε_e^H, ε_k^H, ε_e^O, and ε_k^O are 83.83‰, 3.75‰, 9.96‰ and 4.26‰, respectively. Then Eq. (4) predicted a model-based slope of LSEL at 6.15 under an ideal Rayleigh process. If the model accurately described the moss leaf water evaporation, it implied that δ^2H increased by only 6‰ (compared to 8‰) when $\delta^{18}O$ increased by 1‰ in evaporated *Sphagnum* leaf water. This increase in leaf water δ^2H was only 1.9 times as large as the analytical uncertainty (1σ) in *n*-alkane δ^2H, but for cellulose $\delta^{18}O$ it was 4.5 times as large.

However, the model-based slope of LSEL was lower than the slopes regressed empirically from squeezed leaf water isotope data, the latter of which from our dataset were as low as 3.87, 4.83, and 5.60 (Figure 2.6a), and from Loader et al. (2016) were 3.01 and 6.03. Again, these squeezed leaf water samples might not represent internal metabolic leaf water, but they had been mixed with external water between leaves. The lower slopes observed than modelled might indicate the importance of atmospheric water vapor exchange with external leaf water, which could affect the slopes of evaporation lines (Mayr et al., 2007a). Therefore, reliable approaches to collect plant tissue water in waterlogged peatlands must be further explored to test the hypothesis on the separation of internal and external leaf water and to study peatland isotope hydrology and plant physiology (Amesbury et al., 2015).

2.4.5. Relationships between cellulose carbon and oxygen isotopes

As both *Sphagnum* cellulose $\delta^{13}C$ and $\delta^{18}O$ exhibited sensitivity to moisture gradient, scatter plots of cellulose $\delta^{18}O$ vs. $\delta^{13}C$ showed negative correlations (Figure 2.8), which were significant at sites VC ($r = -0.80$, $p < 0.001$) and MT ($r = -0.81$, $p < 0.05$), as well as among Karukinka Park region ($r = -0.67$, $p < 0.001$), but not at the other

sites (Table B3). The reason for insignificant relationships at other sites might be due to insufficient data points or narrow WC gradients. Our analysis of cellulose isotope data reported at another study site Laguna Parrillar (LP; Loader et al., 2016) with samples collected across a transect with multiple hummocks and hollows also showed a significantly negative correlation ($r = -0.51$, $p < 0.05$; Figure 2.8).

Therefore, we report, for the first time to our knowledge, the intrinsic relationship between two isotope ratios in *Sphagnum*. We show that, in *S. magellanicum*, moisture availability influences cellulose $\delta^{13}C$ via water film effect on discrimination against $^{13}CO_2$ and similarly can imprint on cellulose $\delta^{18}O$ via evaporative enrichment of ^{18}O in metabolic leaf water. Our additional observation on wet-adapted species *S. cuspidatum* showed that their isotope data were in the same trajectory as *S. magellanicum* data at the VC transect (Figures 2.5a and 2.5b). This finding is in line with increasing evidence that *Sphagnum* species-specific effects on biochemical fractionations are minimal, and that the observed inter-species differences in isotopic composition can largely be explained by their favored ecological ranges rather than by any divergences in isotopic fractionation metabolism (Rice & Giles, 1996; Loisel et al., 2009; Daley et al., 2010; El Bilali & Patterson, 2012).

More empirical data are needed to investigate if the observed relationships are robust among different species and are consistent in different regions. A caveat given by Royles and Griffiths (2015) is that bryophyte cellulose carbon isotope signal reflects the condition of maximum CO_2 assimilation, while oxygen isotope signal mainly reflects the condition of maximum cellulose biosynthesis. This temporal separation in photosynthesis and cellulose biosynthesis has been demonstrated in a controlled laboratory experiment on a desiccation-tolerant moss species *Syntrichia ruralis* (Royles et al., 2013b). This moss species experiences substantial daily fluctuations in WC, attaining moisture rapidly following a rainfall event or early morning dew and then drying out completely in hours.

The maximum cellulose biosynthesis occurs at saturation (with a WC of 400%), while the maximum CO_2 assimilation occurs at substantial desiccation (with a WC of 110%) but before complete desiccation (Royles et al., 2013b). It likely also explained a lack of correlation between cellulose $\delta^{13}C$ and $\delta^{18}O$ in Antarctic peatbank mosses *Chorisodontium aciphyllum* and *Polytrichum strictum* from non-waterlogged habitats that do not have a persistent external water film (Royles et al., 2012; Royles & Griffiths, 2015). In contrast, *Sphagnum* mosses inhabit waterlogged peatlands, retain water in their hyaline cells, have a well-developed capillary network, and maintain a persistent external water film. As a result, the short-term variation of WC is relatively much less variable (Silvola & Aaltonen, 1984; Titus & Wagner, 1984) and its influence on physiological function is minimal for this genus. The correlation between *Sphagnum* cellulose $\delta^{13}C$ and $\delta^{18}O$ suggests a possible convergence in the timing of CO_2 assimilation and cellulose biosynthesis. Undertaking experimental studies on *Sphagnum* under controlled laboratory condition is also useful to understand the coupled processes between carbon and water (H and O) isotope fractionations (Brader et al., 2010). More importantly, ecophysiological modeling on the *Sphagnum* water film effect on $\delta^{13}C$ will be useful as it can tie carbon isotope fractionation caused by water resistance of CO_2 diffusion to oxygen isotope fractionation explained by the evaporation model. The coupled water film and evaporation model could predict the theoretical value of slope in cellulose $\delta^{13}C$–$\delta^{18}O$ relationship to be compared with empirical regression values, which from our data ranged from −0.91 to −0.38 (Table B3). However, our two-tailed *t*-test with pooled variance (Armitage et al., 2001) suggested that these empirical slope values were not significantly different from each other (Table B4), thus modeling efforts may offer new insights.

2.4.6. Isotopic signals in *Sphagnum* strand increments document recent growing season conditions

We acknowledge that the phase matching between strand cellulose $\delta^{18}O$ and GNIP precipitation $\delta^{18}O$ data was arbitrary, and that moss growth was still likely during months with snow ground (May−September). However, the robust correspondence between our cellulose $\delta^{18}O$ "time-series" from long strands at site CC and the GNIP precipitation $\delta^{18}O$ record at Punta Arenas, including the relatively low $\delta^{18}O$ values in 2015 and relatively high $\delta^{18}O$ values in 2014, suggested that stem increments of *Sphagnum* could record monthly and seasonal changes in precipitation $\delta^{18}O$ signal over their growing seasons (Figures 2.7a and 2.7b). The amplitude of observed GNIP precipitation $\delta^{18}O$ variability (6.3‰ and 4.5‰ for monthly data and three-month averaged data, respectively) was more than twice as large as the variability in cellulose $\delta^{18}O$ data (2.2‰ and 1.7‰ for individual and three-point average data, respectively; Figures 2.7a and 2.7b). This discrepancy could partly be explained by newly proposed temperature-dependence of biochemical fractionation factor during cellulose biosynthesis that might play a larger role on seasonal scale (Sternberg & Ellsworth, 2011). In Punta Arenas, mean air temperature during the warmest month is ~5°C higher than that of shoulder seasons (spring and autumn). Based on Sternberg and Ellsworth (2011) model, temperature seasonality could account for ~1.6‰ difference in ε_b, which would dampen seasonal variability in cellulose $\delta^{18}O$, although temperature-dependence hypothesis was recently challenged by Zech et al. (2014). Another possibility is about *Sphagnum* metabolic leaf water turnover time, which, if lasting for months, could partly explain the dampened variability in cellulose. The *n*-C_{23} $\delta^{2}H$ signals along *Sphagnum* strands showed similar seasonal shifts, but the amplitude of variability is only 4.4‰ (10.3‰ if 1σ error was considered; Figure 2.7b). This might be explained by the same reason for the lack of variability in surface *Sphagnum n*-C_{23} $\delta^{2}H$ data or that combining ten individual strand

sections for lipid extraction would smooth out much the actual isotopic signals on each individual strand.

The apparent seasonal cycle that was recorded in the *Sphagnum* strands implied rapid strand increment at an average rate as high as 1.13±0.05 cm/month (error was standard deviation, 1σ) estimated by matching the tie points (Figures 2.7a and 2.7b), although we do not have direct dating evidence on the exact "age" of *Sphagnum* strands. This value is much higher than the average *Sphagnum* growth rates reported from boreal peatlands (Loisel et al., 2012), but consistent with the notion that Patagonian peatlands could have several times higher peat accumulation rates than boreal counterparts due to weak temperature seasonality and an even distribution of precipitation throughout the year (Loisel & Yu, 2013a). In addition, the measured WC at site CC (869% in average) is right within the optimal range of WC (700−1000%), by which *Sphagnum* gain maximum rate of photosynthesis (Schipperges & Rydin, 1998). Notably, *Sphagnum* growth rate in the literature was usually measured by the cranked wire method (Clymo, 1970; Loisel et al., 2012), which may underestimate the strand incremental rate due to disturbance and compaction (Figures 2.2a and 2.2b). Laboratory controlled experiments by Brader et al. (2010) showed that strand increment rates for *S. magellanicum* were 0.92±0.10 and 0.75±0.12 cm/month (error was standard deviation, 1σ, in their original study) in their specified dry and wet conditions, respectively, which were actually slower than other *Sphagnum* species. A field study in New Zealand showed that the dominant *S. cristatum* could have strand increment rates between 0.75 and 3 cm/month during growing seasons (Stokes et al., 1999). Our rapid *Sphagnum* growth rate inferred from the incremental $\delta^{18}O$ data is also supported by other relevant observations: (1) stem bifurcations that occur frequently in summer and autumn, but not in spring (Sobotka, 1976), have a rhythm at every ~7 cm (Figure 2.7d); (2) high concentrations of *n*-alkanes match the summer season during which water deficits occurred (Charman, 2007) and more leaf waxes were

produced to prevent water loss (Figure 2.7d); and (3) the decline in cellulose and leaf wax $\delta^{13}C$ towards recent growth increments (Figure 2.7c), likely responding to drier conditions, is consistent with a large negative precipitation anomaly (60% less precipitation than normal), and the highest cellulose $\delta^{13}C$ values at 18−20 cm section (Figure 2.7c) match the only month of positive precipitation anomaly (Figure 2.7d).

2.4.7. Implications for peat-based paleoclimate reconstructions

Our modern process study on *Sphagnum* strands showed that the temporal changes in *Sphagnum* strand cellulose $\delta^{18}O$ track monthly and seasonal changes in precipitation $\delta^{18}O$, but cellulose $\delta^{18}O$ values in surface *Sphagnum* samples along a moisture gradient are primarily influenced by moisture availability and evaporative enrichment. This begs the question about which environmental signal is primarily preserved in peat records over longer timescales. We here propose that paired carbon and water (H or O) isotope measurements in *Sphagnum* cellulose or leaf wax biomarker can be used as a new approach to constrain the effect of moisture availability and associated evaporative enrichment effect, in order to extract precipitation $\delta^{18}O$ signal in peat-based climate reconstructions.

Interpreting peat-based proxy-climate data is often complicated by mixture of autogenic (ecological) and allogenic (climatic) processes that would complicate proxy-climate relationships (Swindles et al., 2012). For example, cyclic alternations between wet- and dry-adapted plant macrofossils in peat records from the same region could have a site-specific frequency, which could be caused by ecohydrological feedback and autogenic processes in vegetation patterning (Loisel & Yu, 2013b). Therefore, multiple peat records from the same region are often needed to identify any regionally consistent signals that could have been caused by climate shifts (Barber et al., 2000; Barber et al., 2003; Booth et al., 2006).

We found that in southern Patagonian peat bogs surface *Sphagnum* cellulose $\delta^{13}C$ and $\delta^{18}O$ are negatively correlated in modern settings as a response to a common moisture gradient. Were *Sphagnum* cellulose $\delta^{13}C$ and $\delta^{18}O$ also negatively correlated in peat-core profiles, this would suggest that moisture availability and evaporative enrichment were the dominant factors controlling cellulose $\delta^{13}C$ and $\delta^{18}O$ variations that were not necessarily driven by climate shifts. For example, in peat records, a concurrent shift to higher $\delta^{13}C$ and lower $\delta^{18}O$ values could be explained by a climate-driven increase in bog surface wetness along with a decrease in precipitation $\delta^{18}O$ as in Roland et al. (2015), but it could alternatively be explained by a non-climate-driven ecohydrological feedback, such as a shift from a dry to wet microform (Loisel & Yu, 2013b) that would decrease evaporative enrichment in ^{18}O. However, if there were a lack of negative correlations, it would indicate that the down-core variations in cellulose $\delta^{18}O$ reflected climate-driven shift in precipitation $\delta^{18}O$. For example, our *Sphagnum* cellulose isotope records from a peat bog in Patagonia showed sustained positive correlations between $\delta^{13}C$ and $\delta^{18}O$ time series: higher cellulose $\delta^{13}C$ intervals implying wetter conditions were associated with higher cellulose $\delta^{18}O$ intervals that could not be explained by enhanced evaporative enrichment in ^{18}O, but rather indicated an increase in precipitation $\delta^{18}O$ (Xia et al., 2018). Therefore, in this case, although variations in cellulose $\delta^{13}C$ could still be non-climate-driven, coupling cellulose $\delta^{13}C$ and $\delta^{18}O$ as a pair has the potential to deconvolve the precipitation $\delta^{18}O$ signal from local ecohydrological noises due to evaporative enrichment. This “dual isotopes” approach is also suitable for *Sphagnum* leaf wax biomarker analysis in peat, given that many postglacial and Holocene peat deposits tend to contain poorly preserved *Sphagnum* macrofossils. *Sphagnum* *n*-C_{23} $\delta^{2}H$ data that showed insensitivity to modern moisture gradient could be used to infer large-scale shift in precipitation $\delta^{2}H$ after the fractionation factor between *n*-C_{23} and source water $\delta^{2}H$ is further constrained (Figure B7).

The coupling of isotopic fractionations associated with carbon and water cycling should be further explored empirically in *Sphagnum*-dominated peatlands as well as in other peat-forming ecosystems such as peatbanks in the Antarctic Peninsula (Royles & Griffiths, 2015). The correlations between moss carbon and water (H or O) isotope ratios could be further constrained by undertaking experimental studies under controlled laboratory conditions or by quantifying the coupling between water film and evaporation effects using ecophysiological models. Such studies would expand the toolbox in the study of peat-climate dynamics.

2.5. Conclusions

Cellulose and *n*-alkane $\delta^{13}C$ of dominant species *Sphagnum magellanicum* in southern Patagonian peat bogs were sensitive to local moisture gradients measured by water content and were strongly controlled by the water film effect. Cellulose $\delta^{18}O$ also showed a moderate response to local moisture gradient brought by differential evaporative enrichment in ^{18}O in metabolic leaf water, but *n*-alkane $\delta^{2}H$ showed a muted response, likely because hydrogen isotopes have a more complex biochemical fractionation pathway and a smaller kinetic fractionation during leaf water evaporation. Because both *Sphagnum* cellulose $\delta^{13}C$ and $\delta^{18}O$ showed response to local moisture gradient, they were negatively correlated in modern setting. The coupled *Sphagnum* carbon and water isotope fractionations observed in our study provided a conceptual model to interpret peat-core isotope data for paleoclimate reconstruction and should be further understood by more observational data, laboratory experiments, and ecophysiological modeling. Rapidly growing *Sphagnum* strands in southern Patagonia could document monthly-to-seasonal changes in precipitation $\delta^{18}O$, confirming the sensitivity of *Sphagnum* cellulose to record long-term changes in precipitation $\delta^{18}O$ in peat cores. Even if such signals were complicated by evaporative enrichment or

autogenic peatland process, paired cellulose ($\delta^{13}C$ and $\delta^{18}O$) measurements will constrain peatland paleohydrology and aid in interpreting cellulose $\delta^{18}O$ time series by examining the down-core correlation between cellulose $\delta^{13}C$ and $\delta^{18}O$ data.

2.6. Acknowledgments

We thank Rodrigo Munzenmayer, Alejandro Kusch and Daniel Terán from Karukinka Park, Chile (Wildlife Conservation Society) for permission and logistical support; Jan Lenaerts from University of Colorado Boulder for sharing high-resolution regional climate model output data; four anonymous reviewers for their constructive comments that substantially improved the manuscript; and Associate Editor Tom Wagner for editorial assistance. The work was supported by the U.S. National Science Foundation grants EAR-1502891 to Z. Yu and EAR-1502455 to Y. Huang.

References

Amesbury, M. J., Charman, D. J., Newnham, R. M., Loader, N. J., Goodrich, J., Royles, J., et al. (2015). Can oxygen stable isotopes be used to track precipitation moisture source in vascular plant-dominated peatlands? *Earth and Planetary Science Letters*, *430*, 149–159.

Anderson, W. T., Bernasconi, S. M., McKenzie, J. A., Saurer, M., & Schweingruber, F. (2002). Model evaluation for reconstructing the oxygen isotopic composition in precipitation from tree ring cellulose over the last century. *Chemical Geology*, *182*(2), 121–137.

Aravena, R., & Warner, B. G. (1992). Oxygen-18 composition of *Sphagnum*, and microenvironmental water relations. *The Bryologist*, *95*(4), 445–448.

Armitage, P., Berry, G., & Matthews, J. N. S. (2001). *Statistical Methods in Medical Research.* (4th ed.). Malden, MA, USA: Wiley-Blackwell.

Barber, K. E., Maddy, D., Rose, N., Stevenson, A. C., Stoneman, R., & Thompson, R. (2000). Replicated proxy-climate signals over the last 2000 yr from two distant UK peat bogs: new evidence for regional palaeoclimate teleconnections. *Quaternary Science Reviews*, *19*(6), 481–487.

Barber, K. E., Chambers, F. M., & Maddy, D. (2003). Holocene palaeoclimates from peat stratigraphy: macrofossil proxy climate records from three oceanic raised bogs in England and Ireland. *Quaternary Science Reviews*, *22*(5), 521–539.

Bilali, H. E., Patterson, R. T., & Prokoph, A. (2013). A Holocene paleoclimate reconstruction for eastern Canada based on $\delta^{18}O$ cellulose of *Sphagnum* mosses from Mer Bleue Bog. *The Holocene*, *23*(9), 1260–1271.

Booth, R. K., Notaro, M., Jackson, S. T., & Kutzbach, J. E. (2006). Widespread drought episodes in the western Great Lakes region during the past 2000 years: Geographic extent and potential mechanisms. *Earth and Planetary Science Letters*, *242*(3), 415–427.

Brader, A. V., van Winden, J. F., Bohncke, S. J. P., Beets, C. J., Reichart, G.-J., & de Leeuw, J. W. (2010). Fractionation of hydrogen, oxygen and carbon isotopes in *n*-alkanes and cellulose of three *Sphagnum* species. *Organic Geochemistry*, *41*(12), 1277–1284.

Bramley-Alves, J., Wanek, W., French, K., & Robinson, S. A. (2015). Moss $\delta^{13}C$: an accurate proxy for past water environments in polar regions. *Global Change Biology*, *21*(6), 2454–2464.

Brenninkmeijer, C. A. M., van Geel, B., & Mook, W. G. (1982). Variations in the D/H and $^{18}O/^{16}O$ ratios in cellulose extracted from a peat bog core. *Earth and Planetary Science Letters*, *61*(2), 283–290.

Chambers, F. M., Booth, R. K., De Vleeschouwer, F., Lamentowicz, M., Le Roux, G., Mauquoy, D., et al. (2012). Development and refinement of proxy-climate indicators from peats. *Quaternary International*, *268*, 21–33.

Charman, D. J. (2007). Summer water deficit variability controls on peatland water-table changes: implications for Holocene palaeoclimate reconstructions. *The Holocene*, *17*(2), 217–227.

Clymo, R. S. (1970). The growth of *Sphagnum*: methods of measurement. *Journal of Ecology*, *58*(1), 13–49.

Craig, H., & Gordon, L. I. (1965). Deuterium and oxygen 18 variations in the ocean and the marine atmosphere. In E. Tongiorgi (Ed.), *Stable isotopes in oceanographic studies and paleotemperatures* (pp. 9–130). Spoleto: Consiglio nazionale delle Ricerche Laboratorio di Geologia Nucleare.

Daley, T. J., Street-Perrott, F. A., Loader, N. J., Barber, K. E., Hughes, P. D. M., Fisher, E. H., & Marshall, J. D. (2009). Terrestrial climate signal of the "8200 yr B.P. cold event" in the Labrador Sea region. *Geology*, *37*(9), 831–834.

Daley, T. J., Barber, K. E., Street-Perrott, F. A., Loader, N. J., Marshall, J. D., Crowley, S. F., & Fisher, E. H. (2010). Holocene climate variability revealed by oxygen isotope analysis of *Sphagnum* cellulose from Walton Moss, northern England. *Quaternary Science Reviews*, *29*(13), 1590–1601.

Daley, T. J., Mauquoy, D., Chambers, F. M., Street-Perrott, F. A., Hughes, P. D. M., Loader, N. J., et al. (2012). Investigating late Holocene variations in hydroclimate and the stable isotope composition of precipitation using southern South American peatlands: an hypothesis. *Climate of the Past*, *8*(5), 1457–1471.

Daniels, W. C., Russell, J. M., Giblin, A. E., Welker, J. M., Klein, E. S., & Huang, Y. (2017). Hydrogen isotope fractionation in leaf waxes in the Alaskan Arctic tundra. *Geochimica et Cosmochimica Acta*, *213*, 216–236.

Dilks, T. J. K., & Proctor, M. C. F. (1979). Photosynthesis, respiration and water content in bryophytes. *New Phytologist*, *82*(1), 97–114.

El Bilali, H., & Patterson, R. T. (2012). Influence of cellulose oxygen isotope variability in sub-fossil *Sphagnum* and plant macrofossil components on the reliability of paleoclimate records at the Mer Bleue Bog, Ottawa, Ontario, Canada. *Organic Geochemistry*, *43*, 39–49.

Farquhar, G. D., Ehleringer, J. R., & Hubick, K. T. (1989). Carbon isotope discrimination and photosynthesis. *Annual Review of Plant Physiology and Plant Molecular Biology*, *40*(1), 503–537.

Finkenbinder, M. S., Abbott, M. B., & Steinman, B. A. (2016). Holocene climate change in Newfoundland reconstructed using oxygen isotope analysis of lake sediment cores. *Global and Planetary Change*, *143*, 251–261.

Gonfiantini, R. (1986). Environmental isotopes in lake studies. In P. Fritz & J.-C. Fontes (Eds.), *Handbook of environmental isotope geochemistry, The terrestrial environment, vol. 2* (Vol. 2, pp. 113–168). Amsterdam: Elsevier.

Granath, G., Rydin, H., Baltzer, J. L., Bengtsson, F., Boncek, N., Bragazza, L., et al. (2018). Environmental and taxonomic controls of carbon and oxygen stable isotope composition in *Sphagnum* across broad climatic and geographic ranges. *Biogeosciences*, *15*(16), 5189–5202.

Horita, J., & Wesolowski, D. J. (1994). Liquid-vapor fractionation of oxygen and hydrogen isotopes of water from the freezing to the critical temperature. *Geochimica et Cosmochimica Acta*, *58*(16), 3425–3437.

Kaislahti Tillman, P., Holzkämper, S., Kuhry, P., Sannel, A. B. K., Loader, N. J., & Robertson, I. (2010). Stable carbon and oxygen isotopes in *Sphagnum fuscum* peat from subarctic Canada: Implications for palaeoclimate studies. *Chemical Geology*, *270*(1), 216–226.

Kaislahti Tillman, P., Holzkämper, S., Andersen, T. J., Hugelius, G., Kuhry, P., & Oksanen, P. (2013). Stable isotopes in *Sphagnum fuscum* peat as late-Holocene climate proxies in northeastern European Russia. *The Holocene*, *23*(10), 1381–1390.

Lenaerts, J. T. M., van den Broeke, M. R., van Wessem, J. M., van de Berg, W. J., van Meijgaard, E., van Ulft, L. H., & Schaefer, M. (2014). Extreme precipitation and climate gradients in Patagonia revealed by high-resolution regional atmospheric climate modeling. *Journal of Climate*, *27*(12), 4607–4621.

Li, G., Li, L., Tarozo, R., Longo, W. M., Wang, K. J., Dong, H., & Huang, Y. (2018). Microbial production of long-chain *n*-alkanes: Implication for interpreting sedimentary leaf wax signals. *Organic Geochemistry*, *115*, 24–31.

Loader, N. J., McCarroll, D., van der Knaap, W. O., Robertson, I., & Gagen, M. (2007). Characterizing carbon isotopic variability in *Sphagnum*. *The Holocene*, *17*(3), 403–410.

Loader, N. J., Street-Perrott, F. A., Mauquoy, D., Roland, T. P., van Bellen, S., Daley, T. J., et al. (2016). Measurements of hydrogen, oxygen and carbon isotope variability in *Sphagnum* moss along a micro-topographical gradient in a southern Patagonian peatland. *Journal of Quaternary Science*, *31*(4), 426–435.

Loisel, J., Garneau, M., & Hélie, J. F. (2009). Modern *Sphagnum* $\delta^{13}C$ signatures follow a surface moisture gradient in two boreal peat bogs, James Bay lowlands, Québec. *Journal of Quaternary Science*, *24*(3), 209–214.

Loisel, J., Garneau, M., & Hélie, J.-F. (2010). *Sphagnum* $\delta^{13}C$ values as indicators of palaeohydrological changes in a peat bog. *The Holocene*, *20*(2), 285–291.

Loisel, J., Gallego-Sala, A. V., & Yu, Z. (2012). Global-scale pattern of peatland *Sphagnum* growth driven by photosynthetically active radiation and growing season length. *Biogeosciences*, *9*(7), 2737–2746.

Loisel, J., & Yu, Z. (2013a). Holocene peatland carbon dynamics in Patagonia. *Quaternary Science Reviews*, *69*, 125–141.

Loisel, J., & Yu, Z. (2013b). Surface vegetation patterning controls carbon accumulation in peatlands. *Geophysical Research Letters*, *40*(20), 5508–5513.

Markel, E. R., Booth, R. K., & Qin, Y. (2010). Testate amoebae and $\delta^{13}C$ of *Sphagnum* as surface-moisture proxies in Alaskan peatlands. *The Holocene*, *20*(3), 463–475.

Mayr, C., Lücke, A., Stichler, W., Trimborn, P., Ercolano, B., Oliva, G., et al. (2007). Precipitation origin and evaporation of lakes in semi-arid Patagonia (Argentina) inferred from stable isotopes ($\delta^{18}O$, $\delta^{2}H$). *Journal of Hydrology*, *334*(1), 53–63.

Ménot-Combes, G., Burns, S. J., & Leuenberger, M. (2002). Variations of $^{18}O/^{16}O$ in plants from temperate peat bogs (Switzerland): implications for paleoclimatic studies. *Earth and Planetary Science Letters*, *202*(2), 419–434.

Ménot, G., & Burns, S. J. (2001). Carbon isotopes in ombrogenic peat bog plants as climatic indicators: calibration from an altitudinal transect in Switzerland. *Organic Geochemistry*, *32*(2), 233–245.

Meyer, M., Seibt, U., & Griffiths, H. (2008). To concentrate or ventilate? Carbon acquisition, isotope discrimination and physiological ecology of early land plant life forms. *Philosophical Transactions of the Royal Society B: Biological Sciences*, *363*(1504), 2767–2778.

Mora, G., & Zanazzi, A. (2017). Hydrogen isotope ratios of moss cellulose and source water in wetlands of Lake Superior, United States reveal their potential for quantitative paleoclimatic reconstructions. *Chemical Geology*, *468*, 75–83.

Moschen, R., Kühl, N., Rehberger, I., & Lücke, A. (2009). Stable carbon and oxygen isotopes in sub-fossil *Sphagnum*: Assessment of their applicability for palaeoclimatology. *Chemical Geology*, *259*(3), 262–272.

Moschen, R., Kühl, N., Peters, S., Vos, H., & Lücke, A. (2011). Temperature variability at Dürres Maar, Germany during the Migration Period and at High Medieval Times, inferred from stable carbon isotopes of *Sphagnum* cellulose. *Climate of the Past*, *7*(3), 1011–1026.

Murray, K. J., Harley, P. C., Beyers, J., Walz, H., & Tenhunen, J. D. (1989). Water content effects on photosynthetic response of *Sphagnum* mosses from the foothills of the Philip Smith Mountains, Alaska. *Oecologia*, *79*(2), 244–250.

Nichols, J., Booth, R. K., Jackson, S. T., Pendall, E. G., & Huang, Y. (2010). Differential hydrogen isotopic ratios of *Sphagnum* and vascular plant biomarkers in ombrotrophic peatlands as a quantitative proxy for precipitation—evaporation balance. *Geochimica et Cosmochimica Acta*, *74*(4), 1407–1416.

Nichols, J. E., Booth, R. K., Jackson, S. T., Pendall, E. G., & Huang, Y. (2006). Paleohydrologic reconstruction based on *n*-alkane distributions in ombrotrophic peat. *Organic Geochemistry*, *37*(11), 1505–1513.

Nichols, J. E., Walcott, M., Bradley, R., Pilcher, J., & Huang, Y. (2009). Quantitative assessment of precipitation seasonality and summer surface wetness using ombrotrophic sediments from an Arctic Norwegian peatland. *Quaternary Research*, *72*(3), 443–451.

Nichols, J. E., Isles, P. D. F., & Peteet, D. M. (2014). A novel framework for quantifying past methane recycling by *Sphagnum*-methanotroph symbiosis using carbon and hydrogen isotope ratios of leaf wax biomarkers. *Geochemistry, Geophysics, Geosystems*, *15*(5), 1827–1836.

Pendall, E., Markgraf, V., White, J. W. C., Dreier, M., & Kenny, R. (2001). Multiproxy record of late Pleistocene–Holocene climate and vegetation changes from a peat bog in Patagonia. *Quaternary Research*, *55*(2), 168–178.

Price, G. D., McKenzie, J. E., Pilcher, J. R., & Hoper, S. T. (1997). Carbon-isotope variation in *Sphagnum* from hummock-hollow complexes: implications for Holocene climate reconstruction. *The Holocene*, *7*(2), 229–233.

Price, J. S., Edwards, T. W. D., Yi, Y., & Whittington, P. N. (2009). Physical and isotopic characterization of evaporation from *Sphagnum* moss. *Journal of Hydrology*, *369*(1), 175–182.

Proctor, M. C. F., Raven, J. A., & Rice, S. K. (1992). Stable carbon isotope discrimination measurements in *Sphagnum* and other bryophytes: physiological and ecological implications. *Journal of Bryology*, *17*(2), 193–202.

Proctor, M. C. F., Nagy, Z., Csintalan, Z., & Takács, Z. (1998). Water-content components in bryophytes: analysis of pressure-volume relationships. *Journal of Experimental Botany*, *49*(328), 1845–1854.

Raghoebarsing, A. A., Smolders, A. J. P., Schmid, M. C., Rijpstra, W. I. C., Wolters-Arts, M., Derksen, J., et al. (2005). Methanotrophic symbionts provide carbon for photosynthesis in peat bogs. *Nature*, *436*(7054), 1153–1156.

Rice, S. K., & Giles, L. (1996). The influence of water content and leaf anatomy on carbon isotope discrimination and photosynthesis in *Sphagnum*. *Plant, Cell & Environment*, *19*(1), 118–124.

Rice, S. K. (2000). Variation in carbon isotope discrimination within and among *Sphagnum* species in a temperate wetland. *Oecologia*, *123*(1), 1–8.

Roland, T. P., Daley, T. J., Caseldine, C. J., Charman, D. J., Turney, C. S. M., Amesbury, M. J., et al. (2015). The 5.2 ka climate event: Evidence from stable isotope and multi-proxy palaeoecological peatland records in Ireland. *Quaternary Science Reviews*, *124*, 209–223.

Royles, J., Ogée, J., Wingate, L., Hodgson, D. A., Convey, P., & Griffiths, H. (2012). Carbon isotope evidence for recent climate-related enhancement of CO_2 assimilation and peat accumulation rates in Antarctica. *Global Change Biology*, *18*(10), 3112–3124.

Royles, J., Sime, L. C., Hodgson, D. A., Convey, P., & Griffiths, H. (2013a). Differing source water inputs, moderated by evaporative enrichment, determine the contrasting $\delta^{18}O_{CELLULOSE}$ signals in maritime Antarctic moss peat banks. *Journal of Geophysical Research: Biogeosciences*, *118*(1), 184–194.

Royles, J., Ogée, J., Wingate, L., Hodgson, D. A., Convey, P., & Griffiths, H. (2013b). Temporal separation between CO_2 assimilation and growth? Experimental and theoretical evidence from the desiccation-tolerant moss *Syntrichia ruralis*. *New Phytologist*, *197*(4), 1152–1160.

Royles, J., & Griffiths, H. (2015). Invited review: climate change impacts in polar regions: lessons from Antarctic moss bank archives. *Global Change Biology*, *21*(3), 1041–1057.

Royles, J., Amesbury, M. J., Roland, T. P., Jones, G. D., Convey, P., Griffiths, H., et al. (2016). Moss stable isotopes (carbon-13, oxygen-18) and testate amoebae reflect

environmental inputs and microclimate along a latitudinal gradient on the Antarctic Peninsula. *Oecologia*, *181*(3), 931–945.
Rydin, H., & McDonald, A. J. S. (1985). Photosynthesis in *Sphagnum* at different water contents. *Journal of Bryology*, *13*(4), 579–584.
Rydin, H., & Jeglum, J. K. (2013). *The Biology of Peatlands.* (2nd ed.). Oxford, UK: Oxford University Press.
Sachse, D., Billault, I., Bowen, G. J., Chikaraishi, Y., Dawson, T. E., Feakins, S. J., et al. (2012). Molecular paleohydrology: interpreting the hydrogen-isotopic composition of lipid biomarkers from photosynthesizing organisms. *Annual Review of Earth and Planetary Sciences*, *40*(1), 221–249.
Schipperges, B., & Rydin, H. (1998). Response of photosynthesis of *Sphagnum* species from contrasting microhabitats to tissue water content and repeated desiccation. *New Phytologist*, *140*(4), 677–684.
Sessions, A. L., Burgoyne, T. W., Schimmelmann, A., & Hayes, J. M. (1999). Fractionation of hydrogen isotopes in lipid biosynthesis. *Organic Geochemistry*, *30*(9), 1193–1200.
Silvola, J., & Aaltonen, H. (1984). Water content and photosynthesis in the peat mosses *Sphagnum fuscum* and *S. angustifolium*. *Annales Botanici Fennici*, *21*(1), 1–6.
Skrzypek, G., Kałużny, A., Wojtuń, B., & Jędrysek, M.-O. (2007). The carbon stable isotopic composition of mosses: A record of temperature variation. *Organic Geochemistry*, *38*(10), 1770–1781.
Smart, R. E., & Bingham, G. E. (1974). Rapid estimates of relative water content. *Plant Physiology*, *53*(2), 258–260.
Sobotka, D. (1976). Regeneration and vegetative propagation of *Sphagnum palustre* as factor of population stability. *Acta Societatis Botanicorum Poloniae*, *45*(4), 357–368.
Sternberg, L., & Ellsworth, P. F. V. (2011). Divergent biochemical fractionation, not convergent temperature, explains cellulose oxygen isotope enrichment across latitudes. *PLOS ONE*, *6*(11), e28040.
Sternberg, L. D. S. L., Deniro, M. J., & Savidge, R. A. (1986). Oxygen isotope exchange between metabolites and water during biochemical reactions leading to cellulose synthesis. *Plant Physiology*, *82*(2), 423–427.
Sternberg, L. S. L. (2009). Oxygen stable isotope ratios of tree-ring cellulose: the next phase of understanding. *New Phytologist*, *181*(3), 553–562.
Stokes, J. R., Alspach, P. A., & Stanley, C. J. (1999). Effect of water table on growth of three New Zealand *Sphagnum* species: implications for *S. cristatum* management. *Journal of Bryology*, *21*(1), 25–29.
Swindles, G. T., Morris, P. J., Baird, A. J., Blaauw, M., & Plunkett, G. (2012). Ecohydrological feedbacks confound peat-based climate reconstructions. *Geophysical Research Letters*, *39*, L11401.
Titus, J. E., Wagner, D. J., & Stephens, M. D. (1983). Contrasting water relations of photosynthesis for two *Sphagnum* mosses. *Ecology*, *64*(5), 1109–1115.

Titus, J. E., & Wagner, D. J. (1984). Carbon balance for two *Sphagnum* mosses: water balance resolves a physiological paradox. *Ecology*, *65*(6), 1765–1774.

Turetsky, M. R., Crow, S. E., Evans, R. J., Vitt, D. H., & Wieder, R. K. (2008). Trade-offs in resource allocation among moss species control decomposition in boreal peatlands. *Journal of Ecology*, *96*(6), 1297–1305.

Turney, C. S. M., Kershaw, A. P., Clemens, S. C., Branch, N., Moss, P. T., & Keith Fifield, L. (2004). Millennial and orbital variations of El Niño/Southern Oscillation and high-latitude climate in the last glacial period. *Nature*, *428*(6980), 306–310.

Van Bellen, S., Mauquoy, D., Payne, R. J., Roland, T. P., Daley, T. J., Hughes, P. D. M., et al. (2014). Testate amoebae as a proxy for reconstructing Holocene water table dynamics in southern Patagonian peat bogs. *Journal of Quaternary Science*, *29*(5), 463–474.

Williams, T. G., & Flanagan, L. B. (1996). Effect of changes in water content on photosynthesis, transpiration and discrimination against $^{13}CO_2$ and $C^{18}O^{16}O$ in *Pleurozium* and *Sphagnum*. *Oecologia*, *108*(1), 38–46.

Woodland, W. A., Charman, D. J., & Sims, P. C. (1998). Quantitative estimates of water tables and soil moisture in Holocene peatlands from testate amoebae. *The Holocene*, *8*(3), 261–273.

Xia, Z., Yu, Z., & Loisel, J. (2018). Centennial-scale dynamics of the Southern Hemisphere Westerly Winds across the Drake Passage over the past two millennia. *Geology*, *46*(10), 855–858.

Xie, S., Nott, C. J., Avsejs, L. A., Volders, F., Maddy, D., Chambers, F. M., et al. (2000). Palaeoclimate records in compound-specific δD values of a lipid biomarker in ombrotrophic peat. *Organic Geochemistry*, *31*(10), 1053–1057.

Xie, S., Nott, C. J., Avsejs, L. A., Maddy, D., Chambers, F. M., & Evershed, R. P. (2004). Molecular and isotopic stratigraphy in an ombrotrophic mire for paleoclimate reconstruction. *Geochimica et Cosmochimica Acta*, *68*(13), 2849–2862.

Yakir, D. (1992). Variations in the natural abundance of oxygen-18 and deuterium in plant carbohydrates. *Plant, Cell & Environment*, *15*(9), 1005–1020.

Yu, Z., Loisel, J., Brosseau, D. P., Beilman, D. W., & Hunt, S. J. (2010). Global peatland dynamics since the Last Glacial Maximum. *Geophysical Research Letters*, *37*, L13402.

Zanazzi, A., & Mora, G. (2005). Paleoclimatic implications of the relationship between oxygen isotope ratios of moss cellulose and source water in wetlands of Lake Superior. *Chemical Geology*, *222*(3), 281–291.

Zech, M., Mayr, C., Tuthorn, M., Leiber-Sauheitl, K., & Glaser, B. (2014). Oxygen isotope ratios ($^{18}O/^{16}O$) of hemicellulose-derived sugar biomarkers in plants, soils and sediments as paleoclimate proxy I: Insight from a climate chamber experiment. *Geochimica et Cosmochimica Acta*, *126*, 614–623.

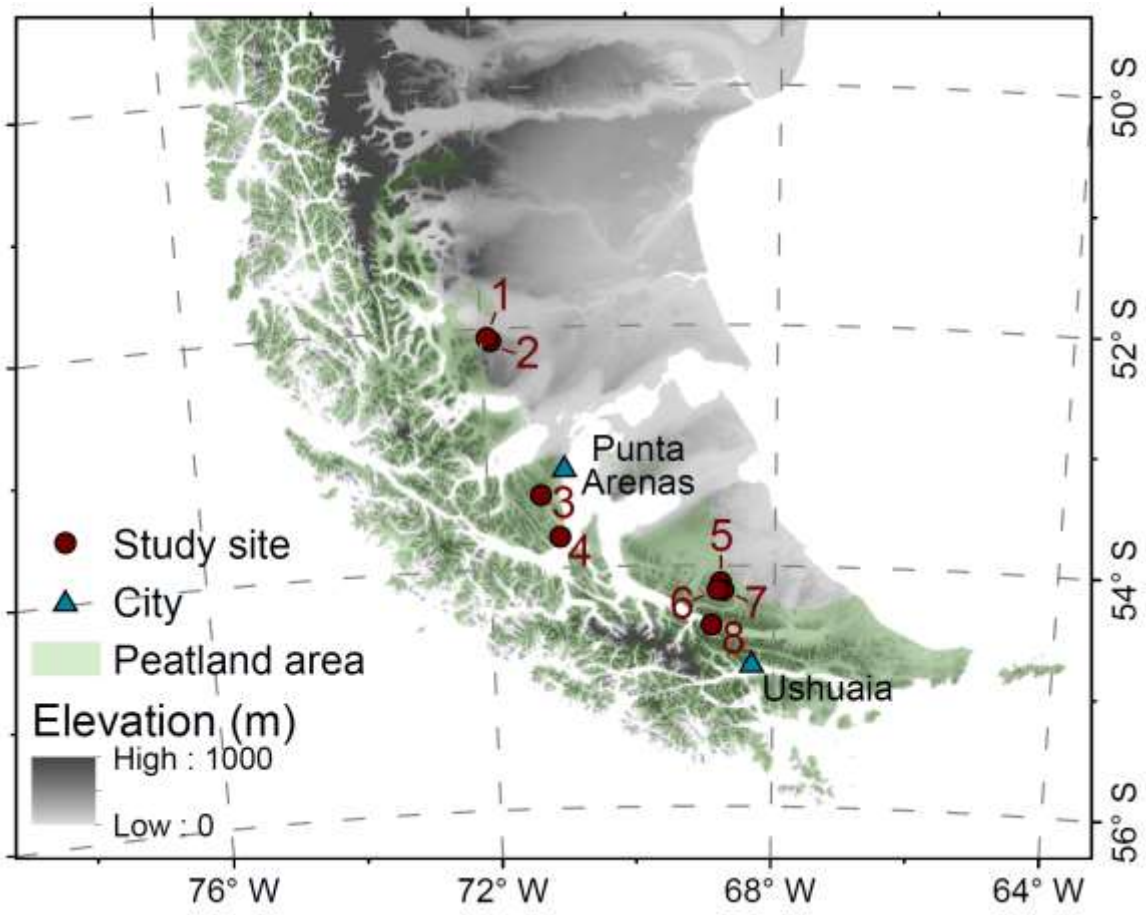

Figure 2.1. Map of southern Patagonia shown with digital elevation model and study site locations. The extent of peatland-dominated area (peatland covering at least 5% of landmass) is based on Yu et al. (2010). Dark red circles show peatland sites discussed in this study: 1–Villa Runeval (VR), 2–Cordillera Chilena (CC), 3–Laguna Parrillar (LP; Loader et al., 2016), 4–Monte Tarn (MT), 5–Mirador Laguna Cura (MLC), 6–Valle de Consejo (VC), 7–Ariel Peatland (AP), 8–Azopardo (AZ). The sites VR and CC are in the Laguna Blanca region, and the sites MLC, VC, and AP are in the Karukinka Park region. Blue triangles also show major cities in this region where the Global Network of Isotopes in Precipitation (GNIP) data are available.

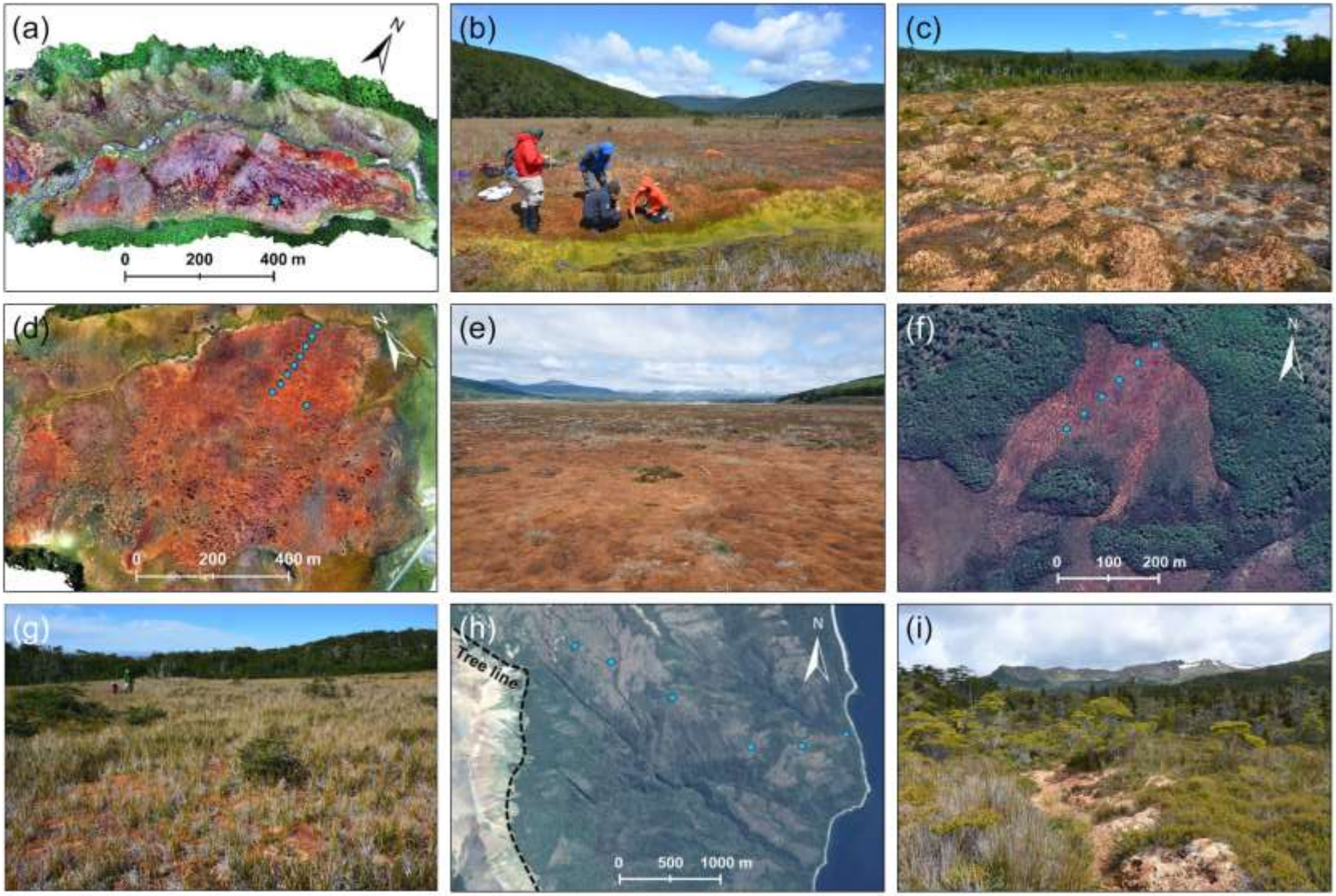
(a)
N
0 200 400 m
(b)
(c)
(d)
N
0 200 400 m
(e)
(f)
N
0 100 200 m
(g)
(h)
Tree line
N
0 500 1000 m
(i)

Figure 2.2 (previous page). Aerial and ground photos showing diverse peatland hydromorphology. (a, b) Site VC, a raised and patterned bog where a large hummock-to-pool transect was sampled with its location shown as blue star in aerial view. (c) Ground photo of site VR, a very dry bog with hummock-hollow patterning. (d, e) Site AP, an open bog with relatively flat bog surface with its center dominated by pure *Sphagnum* carpets. (f, g) Site CC, a high-elevation bog on a gentle slope. (h, i) Site MT, a wooded bog with *Sphagnum* covering vast blanket on a mountain slope, with treeline outlined on aerial view (dashed line). Filled blue symbols in some aerial photos indicate the locations of surface *Sphagnum* samples collected with a goal to capture intra-site moisture gradient. All ground photos were taken by Z. Yu. Aerial photos were taken on an unoccupied aerial vehicle (drone) by J. M. Stelling (a, d) or derived from Google Earth imagery (f, h).

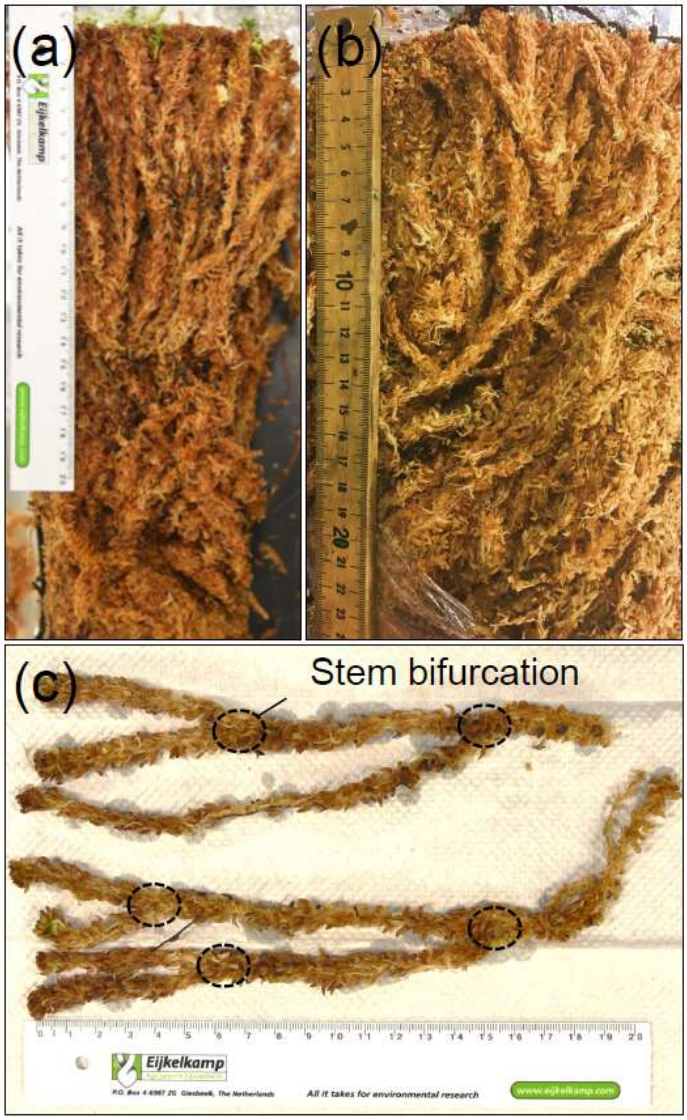

Figure 2.3. Photos of (a) monolith from site CC and (b) monolith from site VC. (c) Photo shows that long *Sphagnum* strands extracted from monolith CC were lined up for subsampling on stem increments for isotope analysis. Position of stem bifurcation are marked.

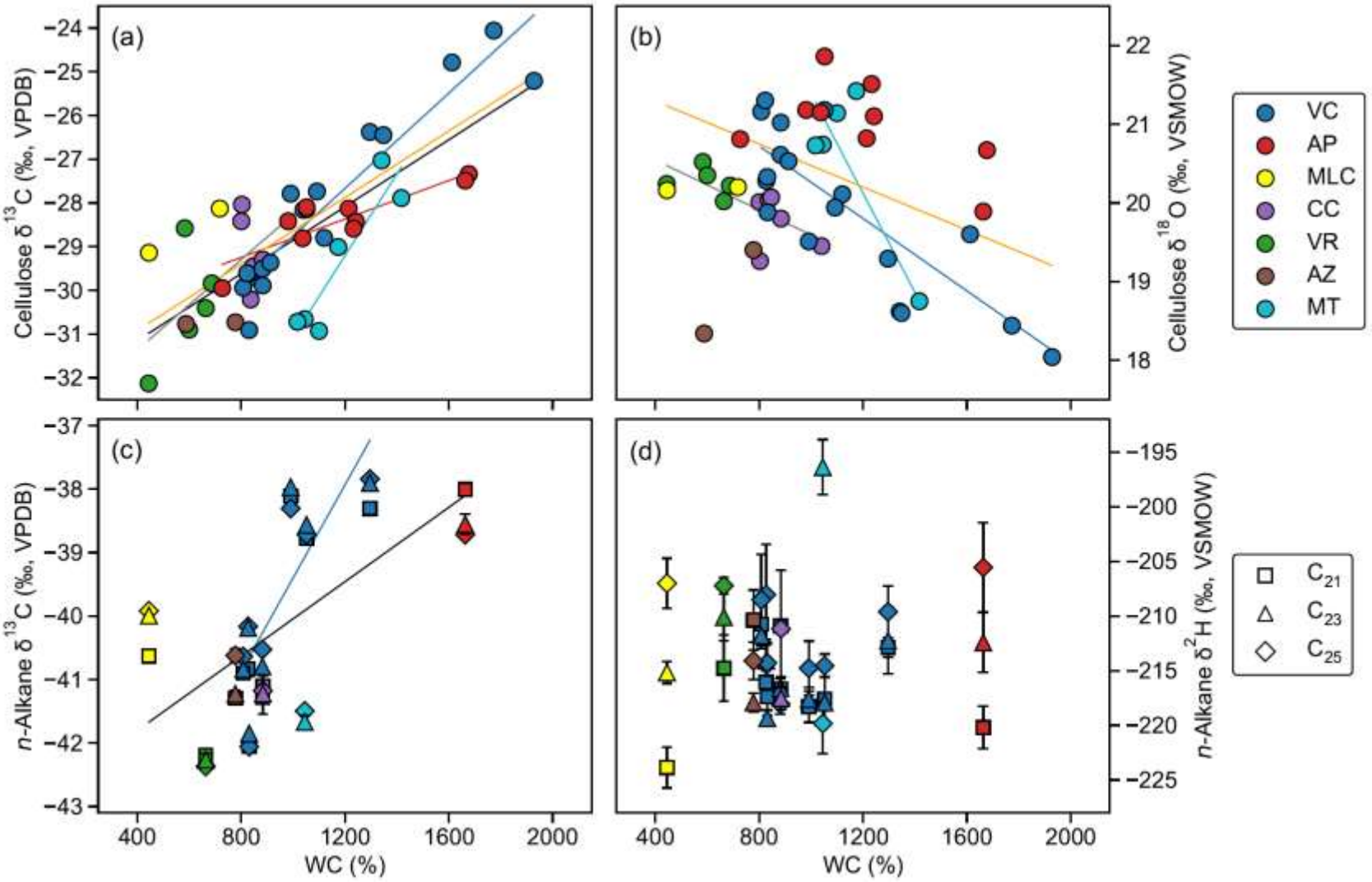
(a)
(b)
(c)
(d)
Cellulose δ13C (‰, VPDB)
Cellulose δ18O (‰, VSMOW)
n-Alkane δ13C (‰, VPDB)
n-Alkane δ2H (‰, VSMOW)
WC (%)
WC (%)
VC
AP
MLC
CC
VR
AZ
MT
C21
C23
C25

Figure 2.4 (previous page). Scatter plots showing the relationships between (a) *Sphagnum* cellulose $\delta^{13}C$ and water content (WC); (b) cellulose $\delta^{18}O$ and WC; (c) S*phagnum n*-alkane $\delta^{13}C$ and WC; and (d) *n*-alkane $\delta^{2}H$ and WC. Scatter colors represent different sites. Error bars in (c) and (d) are standard deviation (1σ) of replicate measurements in compound-specific isotope analysis. Black regression lines indicate significant correlations from all data points. Gray and orange regression lines indicate significant correlations from data points of Laguna Blanca region and Karukinka Park region, respectively. Other colored regression lines indicate site-specific significant correlations.

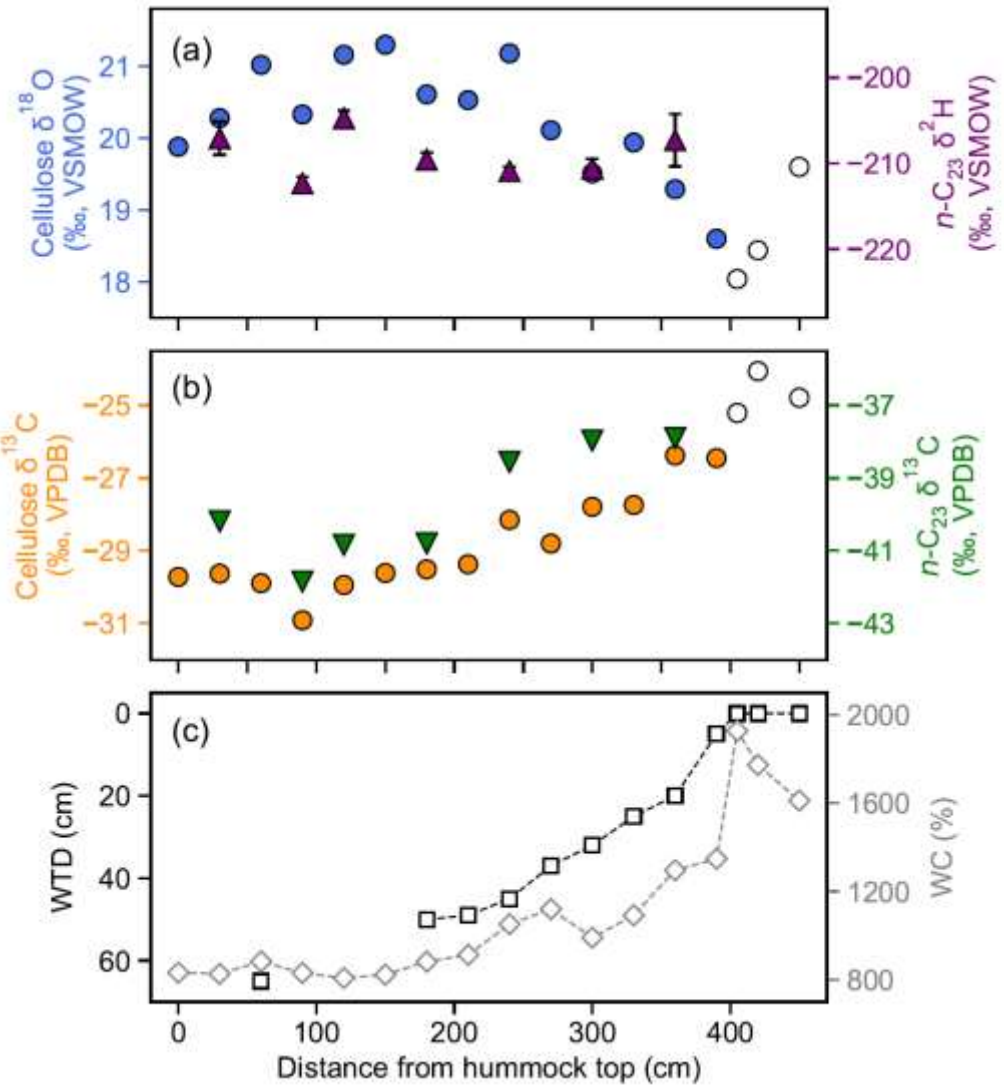

Figure 2.5. Variations in *Sphagnum* cellulose and *n*-alkane isotopic compositions along moisture gradient in hummock-to-pool transect at site VC. (a) Cellulose $\delta^{18}O$ (blue circles) and *n*-C_{23} $\delta^{2}H$ (purple triangles). (b) Cellulose $\delta^{13}C$ (orange circles) and *n*-C_{23} $\delta^{13}C$ (green inverted triangles). (c) Measured water table depth (WTD; black squares) at sampling points and measured *Sphagnum* water content (WC; gray diamonds). Open circle symbols in (a) and (b) are data points corresponding to special species *S. cuspidatum.* Error bars in (a) are standard deviation (1σ) of replicate measurements in compound-specific isotope analysis.

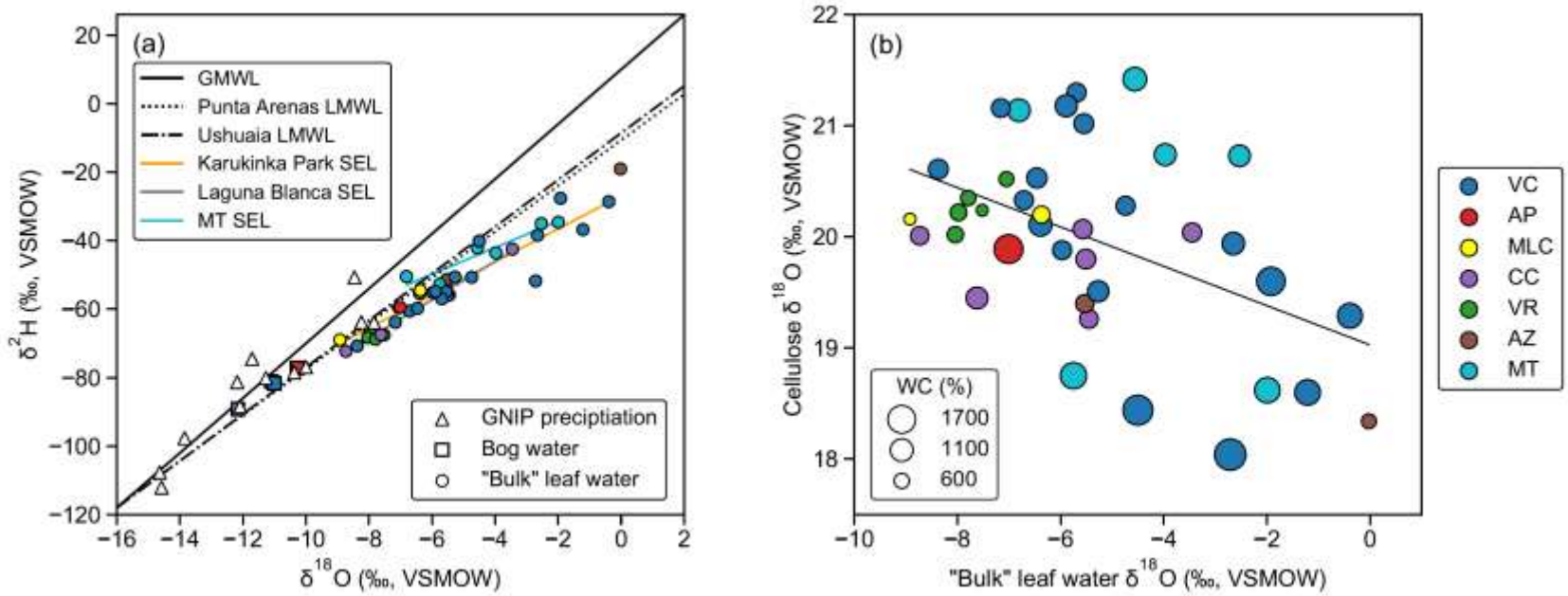
(a)
GMWL
Punta Arenas LMWL
Ushuaia LMWL
Karukinka Park SEL
Laguna Blanca SEL
MT SEL
GNIP preciptiation
Bog water
"Bulk" leaf water
δ2H (‰, VSMOW)
δ18O (‰, VSMOW)
(b)
WC (%)
1700
1100
600
VC
AP
MLC
CC
VR
AZ
MT
Cellulose δ18O (‰, VSMOW)
"Bulk" leaf water δ18O (‰, VSMOW)

Figure 2.6 (previous page). (a) Scatter plot showing the relationship between δ^2H and $\delta^{18}O$ for monthly precipitation (during year 2015, the year right prior to our sampling excursion in January 2016) based on GNIP data from Punta Arenas (white triangles), bog water (colored squares), and leaf water (colored circles). Global meteoric water line (GMWL; solid black line) and local meteoric water lines (LMWL) derived from Punta Arenas ($\delta^2H = 6.69\ \delta^{18}O - 10.65$; during 1990–2015; solid dotted line) and Ushuaia ($\delta^2H = 6.84\ \delta^{18}O - 8.57$; during 1981–2002; solid dash-dotted line) GNIP data are also shown. A few GNIP isotope data that were erroneously positive or were suspected being affected by evaporation were not included to derive LMWLs. Local *Sphagnum* evaporation lines (LSEL) are regressed from leaf water data points of Karukinka Park region ($\delta^2H = 4.83\ \delta^{18}O - 26.90$; orange line), Laguna Blanca region ($\delta^2H = 5.60\ \delta^{18}O - 23.68$; gray line), and site MT ($\delta^2H = 3.87\ \delta^{18}O - 26.60$; cyan line). (b) Scatter plot showing the relationship between cellulose $\delta^{18}O$ and leaf water $\delta^{18}O$. Larger symbols indicate wetter conditions measured by WC. The black regression line indicates significant correlation from all data points. In both (a) and (b), scatter colors represent different sites.

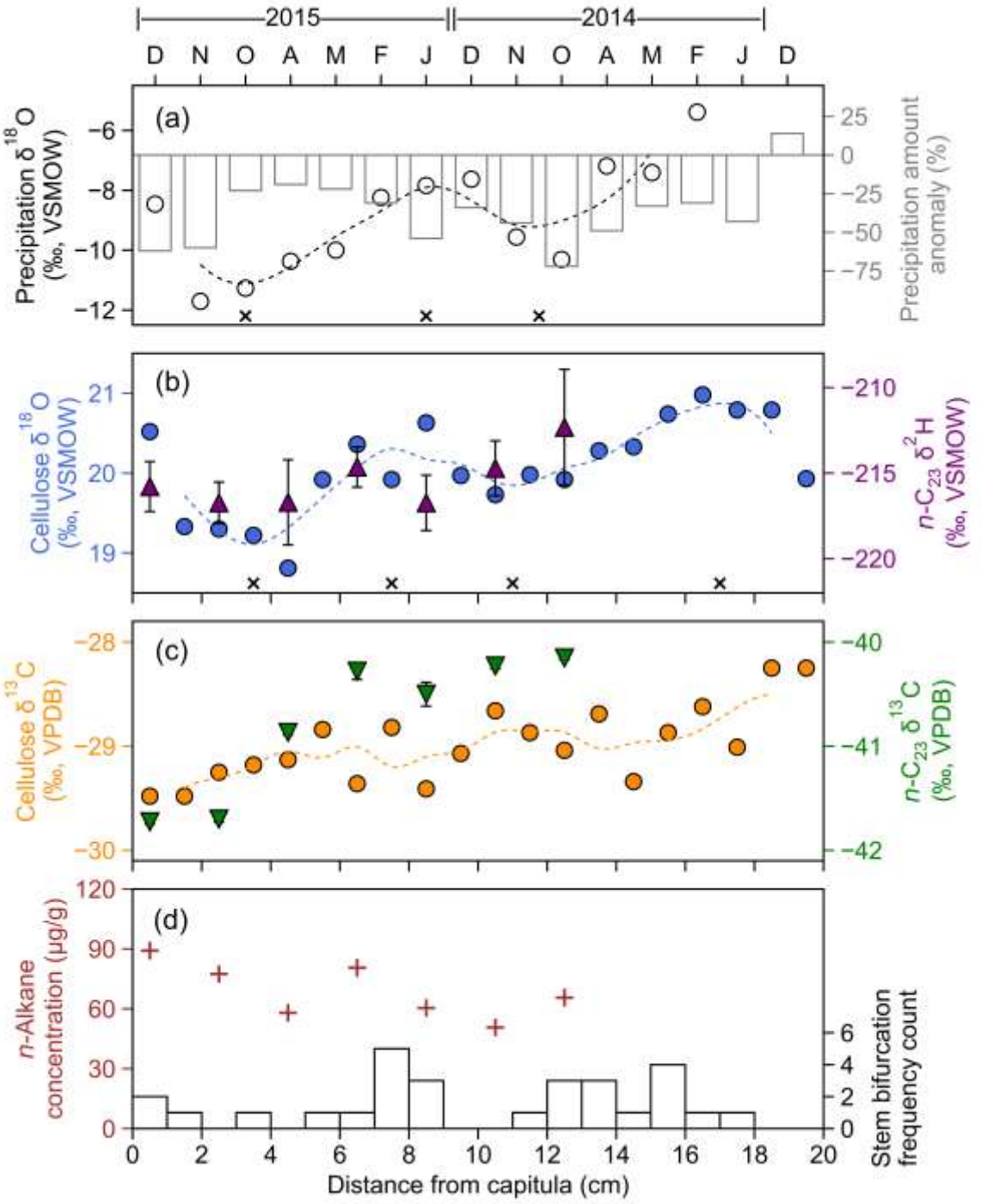

Figure 2.7. Changes in *Sphagnum* cellulose and *n*-alkane isotopic compositions along *Sphagnum* strands at site CC. (a) Growing season monthly precipitation $\delta^{18}O$ values (open circles with three-point average dashed spline line) based on GNIP data from Punta Arenas. The top *x*-axis is time (month), with tick labels D, N, O, A, M, F, and J, refer to

December, November, October, April, March, February, and January, respectively. Other months are not considered within the growing seasons. The $\delta^{18}O$ values for January 2014 and December 2013 were erroneously positive and were not shown. The bar chart plotted on the right *y*-axis is Punta Arenas monthly percentage of precipitation anomaly relative to its long-term monthly mean, based on data from the Global Historical Climatology Network (GHCN). (b) *Sphagnum* strand cellulose $\delta^{18}O$ (blue circles with three-point average spline line) and *n*-C_{23} $\delta^{2}H$ (purple triangles) versus distance from *Sphagnum* capitula. The cross symbols at bottom of (a) and (b) marked the local minimum and maximum $\delta^{18}O$ in three-point average spline lines, which were used as tie points to determine stem incremental rate. (c) *Sphagnum* strand cellulose $\delta^{13}C$ (orange circles with three-point average spline line) and *n*-C_{23} $\delta^{13}C$ (green inverted triangles) from the same sample with (b). (d) *n*-Alkane concentrations in analyzed leaf wax samples. Histogram at bottom is the frequency count of stem bifurcation positions on *Sphagnum* strands.

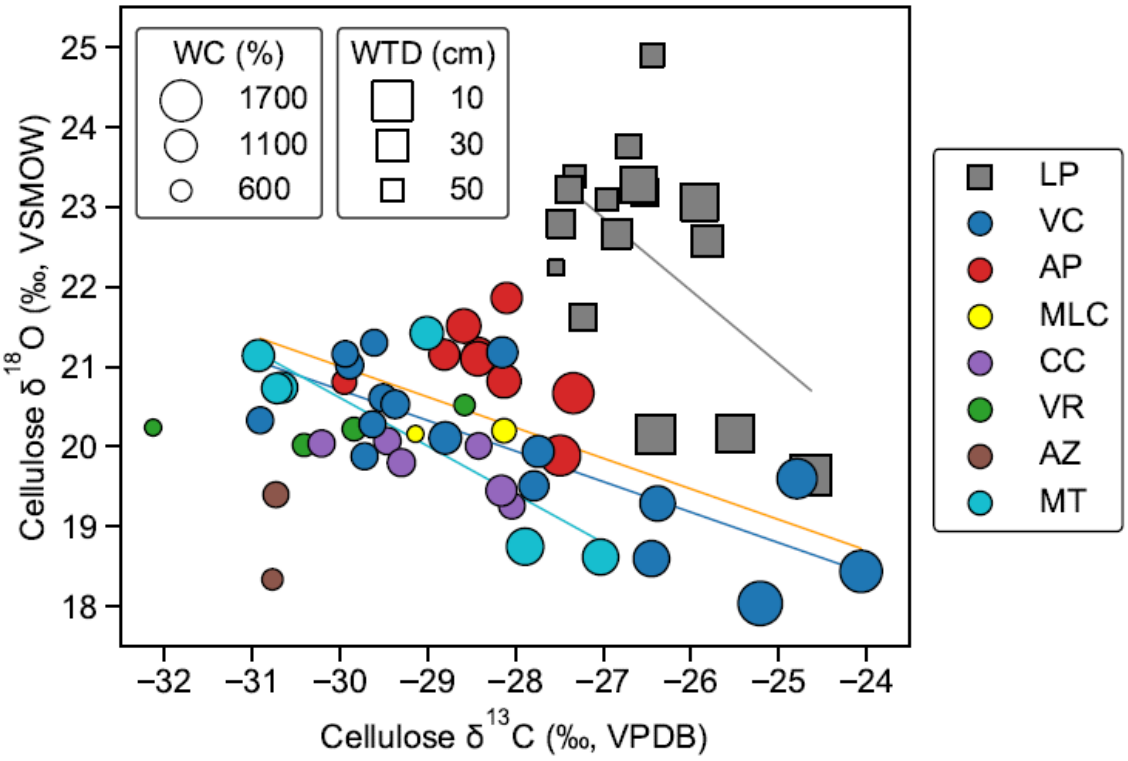

Figure 2.8. Scatter plot showing the relationship between *Sphagnum* cellulose $\delta^{13}C$ and $\delta^{18}O$ data from every site in this study, plus data from site LP (Loader et al., 2016). Larger symbols indicate wetter conditions measured by WC (sites from this study) or WTD (site LP where WC was not measured). Scatter colors represent different sites. Site-specific significant correlations are indicated by colored regression lines. Note that cellulose was extracted from *Sphagnum* capitula in Loader et al. (2016), while cellulose was extracted from *Sphagnum* stems in this study.

Table 2.1. Summary information for study sites and their peatland hydromorphology descriptions.

Site number[a]	Site name	Latitude (°S)	Longitude (°W)	Elevation (m)	MAT[b] (°C)	MAP[b] (mm)	MRH[b] (%)	Peatland area (km^2)	Hydromorphological features
1	Villa Runeval (VR)	52.08	71.92	262	3.8	1735	81	0.2	Very dry bog with hummock-hollow patterning
2	Cordillera Chilena (CC)	52.10	71.87	514–533	3.9	1475	80	0.3	High-elevation bog on hillslope
3	Laguna Parrillar (LP)[c]	53.40	71.25	309	3.7	742	80	2.9	Large open bog with dense vascular plant cover
4	Monte Tarn (MT)	53.75	71.00	24–503	3.4	2004	81	>3	Wooded bog with *Sphagnum* covering vast blanket on mountain slope
5	Mirador Laguna Cura (MLC)	54.14	68.75	391	8.0	762	76	0.06	Small bog localized on foothill surrounded by forested area
6	Valle de Consejo (VC)	54.21	68.79	229	7.9	850	78	0.2	Raised bog with significant hummock-hollow-pool patterning
7	Ariel Peatland (AP)	54.21	68.72	165	7.9	686	75	0.7	Open bog with flat surface and concentric vegetation zonation, with bog center occupied by solely *Sphagnum*
8	Azopardo (AZ)	54.50	68.88	55–110	2.6	1132	81	>2	Blanket bog on hillslope on both sides of paved road

[a] These are site numbers shown in Figure 2.1.

[b] Gridded mean annual temperature (MAT), mean annual precipitation (MAP) and mean annual relative humidity (MRH) data are from output of high-resolution (5.5 km) regional climate model applied to Patagonia and driven by the European Centre for Medium-Range Weather Forecasts (ECMWF) ERA-Interim reanalysis during AD 1979–2012 (Lenaerts et al., 2014).

[c] Site reported by Loader et al. (2016)

Appendix B: Supporting information for Chapter 2

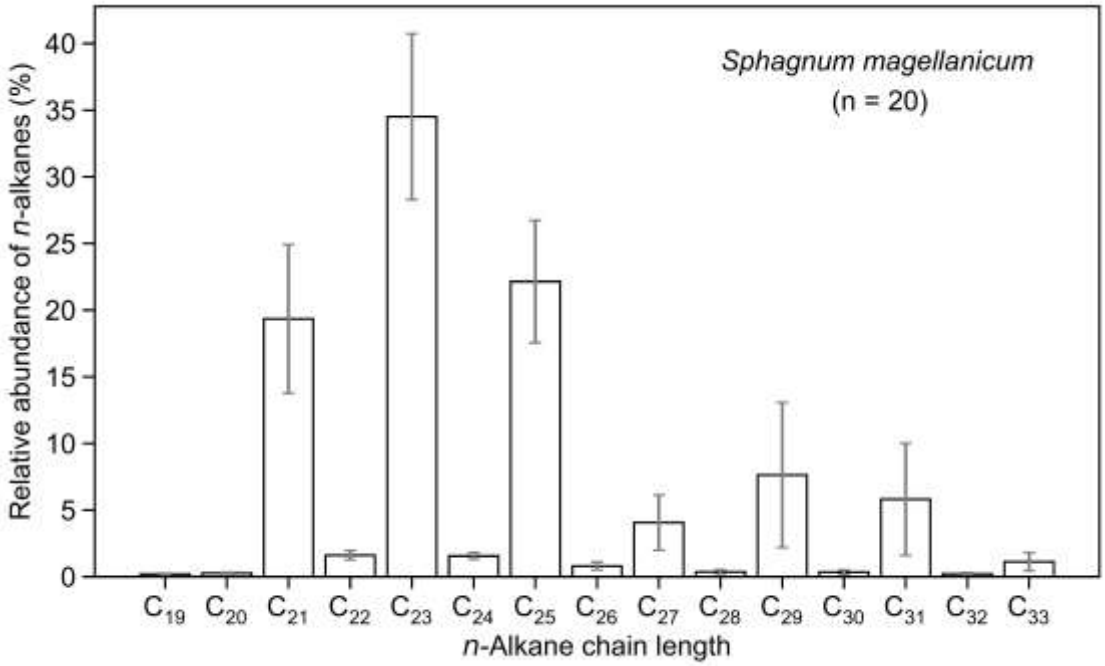

Figure B1. Average *n*-alkane distribution for analyzed *Sphagnum magellanicum* samples (including 13 surface samples and 7 strand samples). Gray error bars denote the standard deviation (1σ) of data.

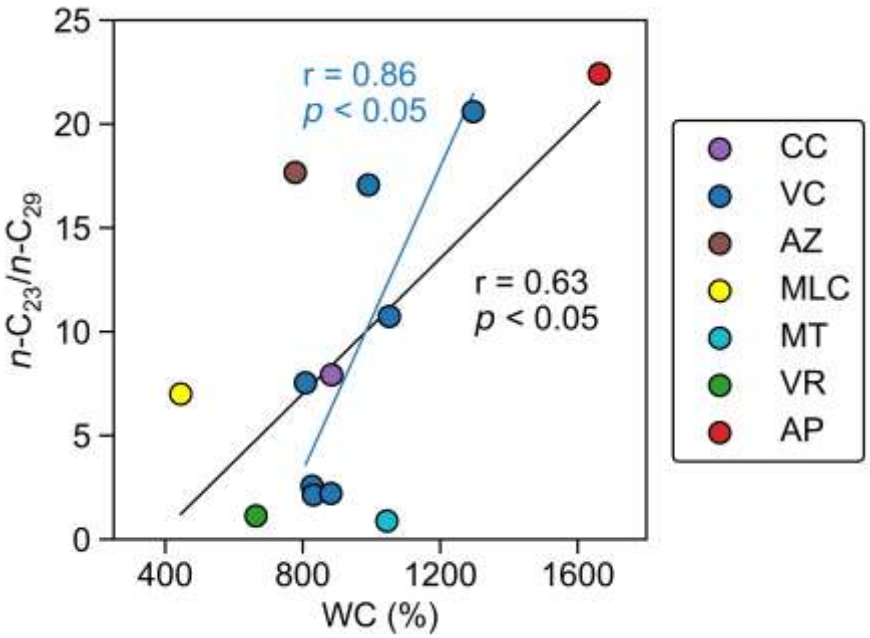

Figure B2. Correlation between n-C_{23}/n-C_{29} and water content (WC) among surface *Sphagnum* samples. Scatter colors represent different sites. Regression lines are shown with r and p values of correlation (black line for all samples and blue line for samples from site VC).

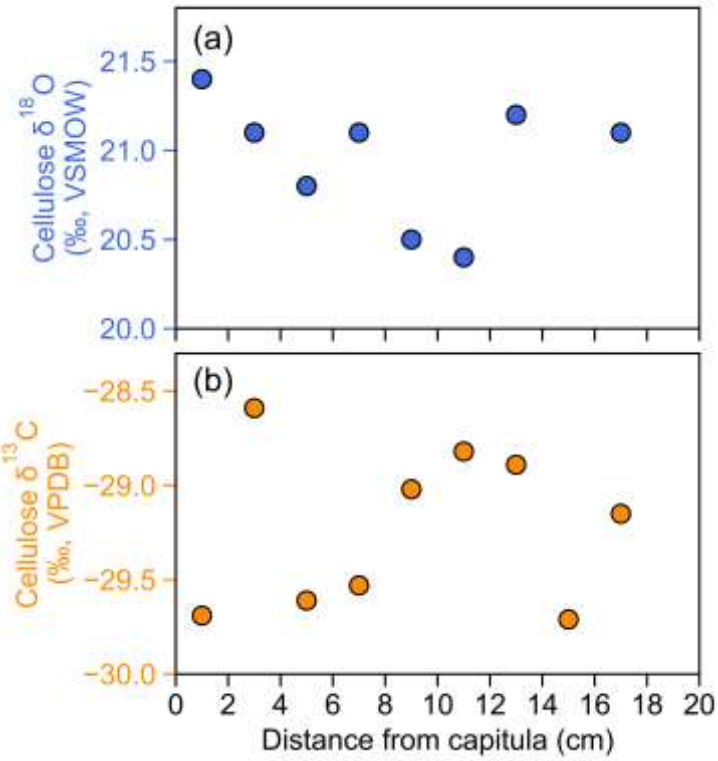

Figure B3. Cellulose (a) oxygen isotope and (b) carbon isotope compositions along *Sphagnum* strands at site VC. Isotopic variability along strands is present but less clear and less dramatic than densely analyzed strands from site CC.

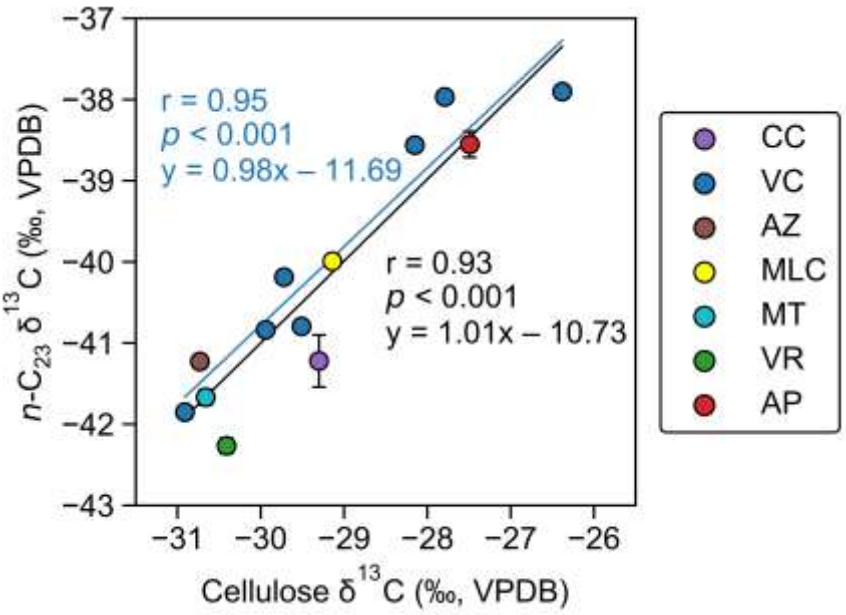

Figure B4. Correlation between *n*-C_{23} and cellulose carbon isotope compositions among surface *Sphagnum* samples. Error bar is standard deviation (1σ) of replicate measurements in compound-specific isotopic analysis. Scatter colors represent different sites. Regression lines are shown with r and *p* values of correlation as well as regression equations (black line for all samples and blue line for samples from site VC).

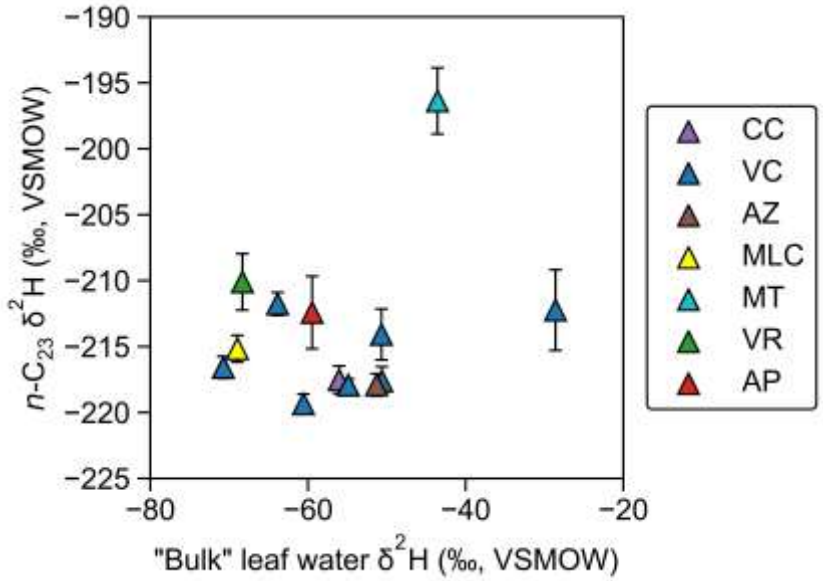

Figure B5. Correlation between *n*-C_{23} and leaf water hydrogen isotope compositions among surface *Sphagnum* samples. Error bar is standard deviation (1σ) of replicate measurements in compound-specific isotopic analysis. Scatter colors represent different sites.

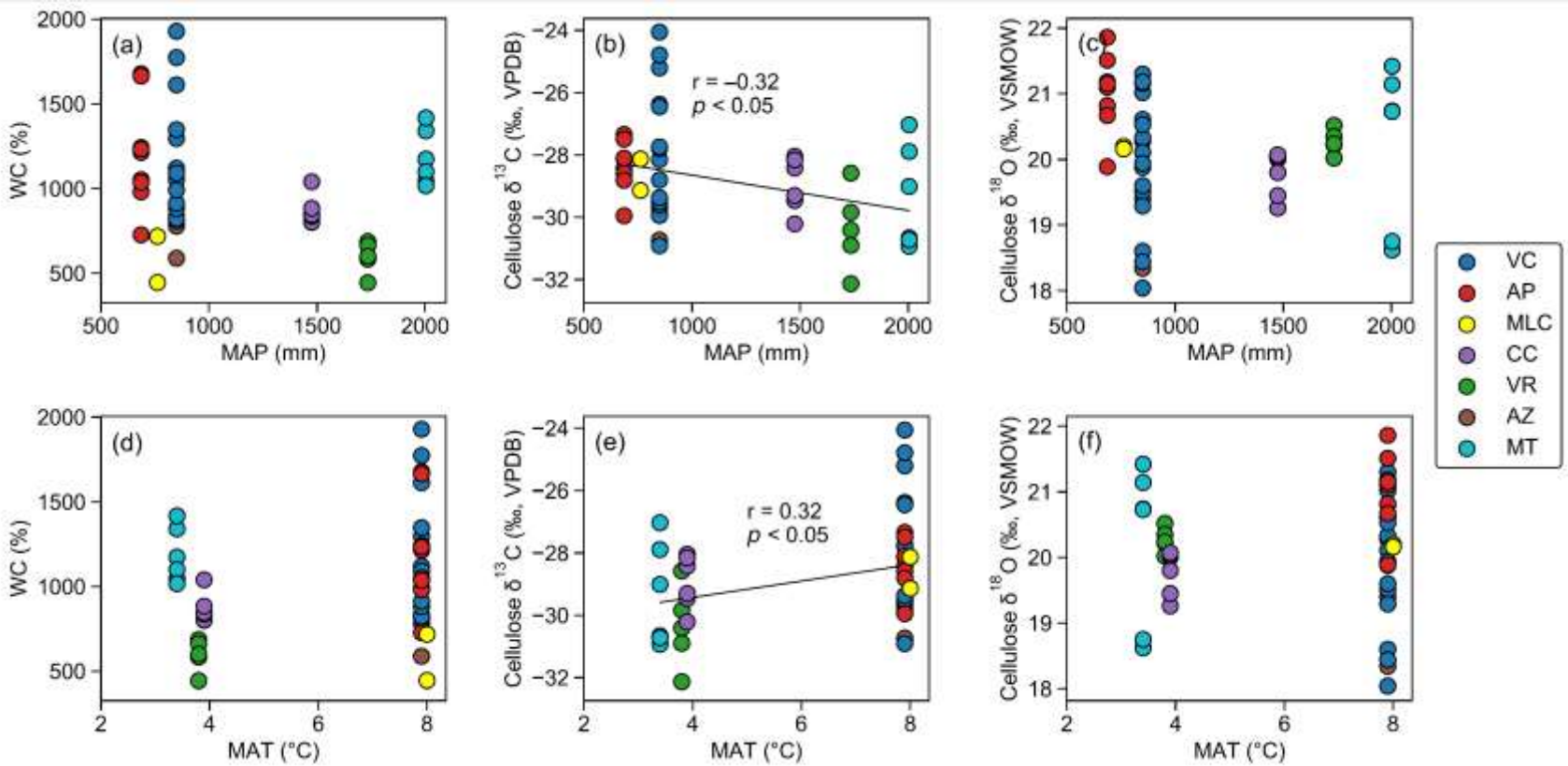
(a)
WC (%)
MAP (mm)
(b)
r = –0.32
p < 0.05
Cellulose δ13C (‰, VPDB)
MAP (mm)
(c)
Cellulose δ18O (‰, VSMOW)
MAP (mm)
(d)
WC (%)
MAT (°C)
(e)
r = 0.32
p < 0.05
Cellulose δ13C (‰, VPDB)
MAT (°C)
(f)
Cellulose δ18O (‰, VSMOW)
MAT (°C)
VC
AP
MLC
CC
VR
AZ
MT

Figure B6 (previous page). Correlations between (a) WC and MAP; (b) cellulose $\delta^{13}C$ and MAP; (c) cellulose $\delta^{18}O$ and MAP; (d) WC and MAT; (e) cellulose $\delta^{13}C$ and MAT; (f) cellulose $\delta^{18}O$ and MAT. In (b) and (e), significant correlations were found as shown in regression lines, but the correlation shown in (e) disappeared if three *S. cuspidatum* data were removed. Scatter colors represent different sites. MAT and MAP data are from Lenaerts et al. (2014).

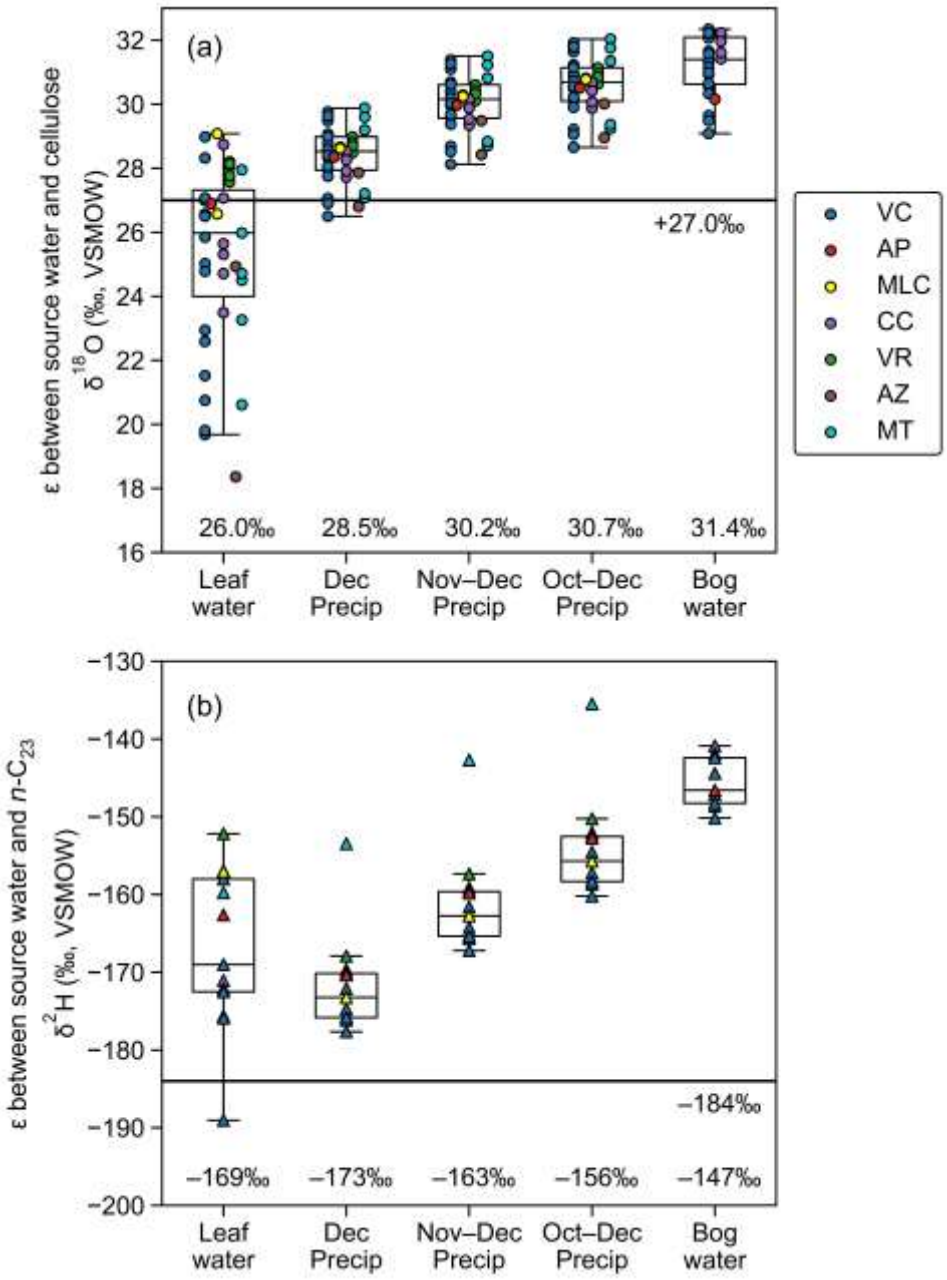

Figure B7. (a) Apparent enrichment factors shown in box and whiskers plots between cellulose $\delta^{18}O$ and different potential source water $\delta^{18}O$. (b) Apparent fractionation factors shown in box and whiskers plots between *n*-C_{23} $\delta^{2}H$ and different potential source water $\delta^{2}H$. Scatter colors represent different sites. The "*Dec Precip*" means using isotope data of Punta Arenas GNIP monthly precipitation recorded in December 2015, right before our sample collection in January 2016. Similarly, "*Nov–Dec Precip*" and "*Oct–*

Dec Precip" mean the isotopic composition of amount-weighted precipitation for two and three months prior to our sample collection. The median enrichment/fractionation factors for each source water are given at the bottom. The reference line of +27‰ in (a) is the widely tested and accepted value of biochemical enrichment factor for cellulose $\delta^{18}O$ (Sternberg, 2009). The reference line of −184‰ in (b) is the *Sphagnum n*-C_{23} $\delta^{2}H$ apparent fractionation factor given by Nichols et al. (2014a). The way to derive the "ε" is different for cellulose $\delta^{18}O$ and for *n*-C_{23} $\delta^{2}H$: the ε for $\delta^{18}O$ equal to $\delta^{18}O_{cellulose} - \delta^{18}O_{source\ water}$; the ε for $\delta^{2}H$ equal to $1000 \times [(\delta^{2}H_{lipids} + 1000)/(\delta^{2}H_{source\ water} + 1000) - 1]$, consistent with the tradition in these two fields.

Table B1. Overview of surface *Sphagnum* samples with their field data and isotope data.

Site Name	Latitude (°)	Longitude (°)	Elevation (m)	Water Content (%)	Water Table Depth (cm)	Distance from hummock top (cm)	Cellulose $\delta^{13}C$ (‰, VPDB)	Cellulose $\delta^{18}O$ (‰, VSMOW)	*n*-alkane conc. (µg/g dry wt.)	*n*-C_{23} $\delta^{13}C$ (‰, VPDB)	1σ	*n*-C_{23} $\delta^{2}H$ (‰, VSMOW)	1σ	Leaf water $\delta^{18}O$ (‰, VSMOW)	Leaf water $\delta^{2}H$ (‰, VSMOW)	Bog water $\delta^{18}O$ (‰, VSMOW)	Bog water $\delta^{2}H$ (‰, VSMOW)
VC	-54.2069	-68.7895	229	832		0	-29.7	19.9						-6.0	-55.1		
VC	-54.2069	-68.7895	229	827		30	-29.6	20.3	138.3	-40.2	n.a.	-214.1	1.9	-4.7	-50.7		
VC	-54.2069	-68.7895	229	883	65	60	-29.9	21.0						-5.6	-55.0		
VC	-54.2069	-68.7895	229	831		90	-30.9	20.3	126.3	-41.9	n.a.	-219.4	0.7	-6.7	-60.6		
VC	-54.2069	-68.7895	229	808		120	-29.9	21.2	106.6	-40.8	n.a.	-211.8	0.9	-7.2	-63.9		
VC	-54.2069	-68.7895	229	823		150	-29.6	21.3						-5.7	-57.0		
VC	-54.2069	-68.7895	229	882	50	180	-29.5	20.6	107.5	-40.8	n.a.	-216.6	0.8	-8.4	-70.7		
VC	-54.2069	-68.7895	229	913	49	210	-29.4	20.5						-6.5	-59.8		
VC	-54.2069	-68.7895	229	1052	45	240	-28.2	21.2	116.7	-38.6	n.a.	-217.9	0.5	-5.9	-54.9		
VC	-54.2069	-68.7895	229	1120	37	270	-28.8	20.1						-6.4	-55.4	-11.1	-81.1
VC	-54.2069	-68.7895	229	991	32	300	-27.8	19.5	133.0	-38.0	n.a.	-217.6	1.1	-5.3	-50.6	-11.0	-81.7
VC	-54.2069	-68.7895	229	1092	25	330	-27.7	19.9						-2.7	-38.4		
VC	-54.2069	-68.7895	229	1296	20	360	-26.4	19.3	125.9	-37.9	n.a.	-212.2	3.1	-0.4	-28.6		
VC	-54.2069	-68.7895	229	1348	5	390	-26.5	18.6						-1.2	-36.8		
VC	-54.2069	-68.7895	229	1928	0	405	-25.2	18.0						-2.7	-51.8		
VC	-54.2069	-68.7895	229	1773	0	420	-24.1	18.4						-4.5	-40.1		
VC	-54.2069	-68.7895	229	1612	0	450	-24.8	19.6						-1.9	-27.6		
AZ	-54.4963	-68.8836	110	588			-30.8	18.3						0.0	-19.1		
AZ	-54.4963	-68.8710	55	778			-30.7	19.4	61.2	-41.2	0.1	-217.9	0.9	-5.5	-51.3		
MLC	-54.1443	-68.7517	391	718			-28.1	20.2						-6.4	-54.5		
MLC	-54.1443	-68.7517	391	444		0	-29.1	20.2	151.9	-40.0	n.a.	-215.2	1.0	-8.9	-69.0		
VR	-52.0771	-71.9178	262	583		0	-28.6	20.5						-7.1	-59.6		
VR	-52.0771	-71.9178	262	687		50	-29.8	20.2						-8.0	-67.1		
VR	-52.0771	-71.9178	262	664		100	-30.4	20.0	83.3	-42.3	0.1	-210.1	2.1	-8.0	-68.3		
VR	-52.0771	-71.9178	262	600		150	-30.9	20.4						-7.8	-68.8		
VR	-52.0771	-71.9178	262	444		200	-32.1	20.2						-7.5	-67.5		
MT	-53.7418	-71.0114	503	1341			-27.0	18.6						-2.0	-34.6		
MT	-53.7431	-71.0062	446	1417			-27.9	18.8						-5.8	-52.7		
MT	-53.7461	-70.9971	637	1045			-30.7	20.7	75.5	-41.7	0.1	-196.4	2.5	-4.0	-43.6		
MT	-53.7501	-70.9856	171	1174			-29.0	21.4						-4.6	-42.1		
MT	-53.7498	-70.9776	82	1100			-30.9	21.1						-6.8	-50.5		
MT	-53.7487	-70.9706	24	1017			-30.7	20.7						-2.5	-35.0		
CC	-52.1032	-71.8739	533	801			-28.4	20.0						-8.7	-72.3		
CC	-52.1030	-71.8734	527	803			-28.0	19.3						-5.5	-55.9		
CC	-52.1027	-71.8729	525	837			-30.2	20.0						-3.5	-42.5		
CC	-52.1024	-71.8723	523	846	70		-29.5	20.1						-5.6	-53.2	-12.2	-89.2
CC	-52.1020	-71.8718	518	884			-29.3	19.8	96.3	-41.2	0.3	-217.4	1.1	-5.5	-56.0		
CC	-52.1017	-71.8313	514	1040			-28.2	19.5						-7.6	-67.5		
AP	-54.2058	-68.7155	165	727			-30.0	20.8									
AP	-54.2060	-68.7159	165	981			-28.4	21.2									
AP	-54.2061	-68.7163	165	1214			-28.1	20.8									
AP	-54.2062	-68.7167	165	1242			-28.4	21.1									
AP	-54.2064	-68.7171	165	1233			-28.6	21.5									
AP	-54.2065	-68.7175	165	1052			-28.1	21.9									
AP	-54.2066	-68.718	165	1037			-28.8	21.2									
AP	-54.2066	-68.7184	165	1677			-27.3	20.7									
AP	-54.2073	-68.7175	165	1663	42		-27.5	19.9	105.4	-38.6	0.2	-212.4	2.8	-7.0	-59.5	-10.3	-77.1

Table B2. Overview of *Sphagnum* strand isotope data

Site Name	Strand section distance to capitula (cm)	Cellulose $\delta^{13}C$ (‰, VPDB)	Cellulose $\delta^{18}O$ (‰, VSMOW)	*n*-alkane conc. (µg/g dry wt.)	*n*-C_{23} $\delta^{13}C$ (‰, VPDB)	1σ	*n*-C_{23} $\delta^{2}H$ (‰, VSMOW)	1σ
CC	0−1	-29.5	20.5	89.1	-41.7	0.0	-215.8	1.5
	1−2	-29.5	19.3					
	2−3	-29.3	19.3	77.5	-41.7	0.0	-216.7	1.2
	3−4	-29.2	19.2					
	4−5	-29.1	18.8	58.0	-40.9	0.0	-216.7	2.5
	5−6	-28.8	19.9					
	6−7	-29.4	20.4	80.5	-40.3	0.1	-214.6	1.2
	7−8	-28.8	19.9					
	8−9	-29.4	20.6	60.4	-40.5	0.1	-216.7	1.6
	9−10	-29.1	20.0					
	10−11	-28.7	19.7	50.7	-40.2	0.0	-214.7	1.6
	14−12	-28.9	20.0					
	12−13	-29.0	19.9	65.6	-40.2	0.0	-212.3	3.4
	13−14	-28.7	20.3					
	14−15	-29.3	20.3					
	15−16	-28.9	20.7					
	16−17	-28.6	21.0					
	17−18	-29.0	20.8					
	18−19	-28.3	20.8					
	19−20	-28.3	19.9					
VC	0−2	-29.7	21.4					
	2−4	-28.6	21.1					
	4−6	-29.6	20.8					
	6−8	-29.5	21.1					
	8−10	-29.0	20.5					
	10−12	-28.8	20.4					
	12−14	-28.9	21.2					
	14−16	-29.7	n.a.					
	16−18	-29.2	21.1					

Table B3. Summary of correlation coefficients between cellulose $\delta^{13}C/\delta^{18}O$ and hydrological variables (WC/WTD).

Region	Site name	No. of samples	Cellulose $\delta^{13}C$ vs. WC	Cellulose $\delta^{18}O$ vs. WC	Cellulose $\delta^{13}C$ vs. $\delta^{18}O$	
			Correlation coefficient[a]	Correlation coefficient	Correlation coefficient	Slope of regression line
Karukinka Park	VC	17 (14)[b]	**0.94***** (**0.92*****)	**−0.83***** (**−0.72****)	**−0.80***** (**−0.70****)	−0.38 (−0.4)
	AP	9	**0.89****	−0.55	−0.30	
	MLC	2	n. a.	n. a.	n. a.	
	Karukinka Park sites	28 (25)	**0.83***** (**0.69*****)	**−0.52**** (−0.16)	**−0.67***** (**−0.42***)	−0.38 (−0.29)
Laguna Blanca	CC	6	0.22	−0.34	−0.74	
	VR	5	0.58	−0.29	0.46	
	Laguna Blanca sites	11	**0.68***	**−0.71***	−0.55	
Other	AZ	2	n. a.	n. a.	n. a.	
	MT	6	**0.92****	**−0.84***	**−0.81***	−0.60
All sites		47 (44)	**0.78***** (**0.66*****)	−0.29 (−0.02)	**−0.43**** (−0.23)	−0.23

Region	Site Name	No. of samples	Cellulose $\delta^{13}C$ vs. WTD	Cellulose $\delta^{18}O$ vs. WTD	Cellulose $\delta^{13}C$ vs. $\delta^{18}O$	
			Correlation coefficient	Correlation coefficient	Correlation coefficient	Slope of regression line
Other	LP[c]	16	**−0.77*****	**0.68****	**−0.51***	−0.91

[a] The correlation coefficients in bold indicate the correlations are significant and their p values are denoted as the following: * $p < 0.05$, ** $p < 0.01$, *** $p < 0.001$.

[b] The values in parenthesis are based on data in which species *S. cuspidatum* were excluded.

[c] Data from Loader et al. (2016).

Table B4. Statistical test on the difference between cellulose $\delta^{13}C/\delta^{18}O$ regression coefficient (slope).

	VC	Karukinka Park	MT	LP
VC				
Karukinka Park	*0.0089* (41) **0.99**			
MT	*1.1405* (19) **0.27**	*1.0339* (30) **0.31**		
LP	*1.5678* (29) **0.13**	*1.6384* (40) **0.11**	*0.6238* (18) **0.54**	

The italic number is the *t* value. The number in parenthesis is the pooled degree of freedom. The bold number is the *p* value. None of the *p* values is less than 0.05, and thus every two-group comparison indicates insignificant difference in regression coefficient (slope).

References for Appendix B

Lenaerts, J. T. M., van den Broeke, M. R., van Wessem, J. M., van de Berg, W. J., van Meijgaard, E., van Ulft, L. H., & Schaefer, M. (2014). Extreme precipitation and climate gradients in Patagonia revealed by high-resolution regional atmospheric climate modeling. *Journal of Climate*, *27*(12), 4607–4621.

Loader, N. J., Street-Perrott, F. A., Mauquoy, D., Roland, T. P., van Bellen, S., Daley, T. J., et al. (2016). Measurements of hydrogen, oxygen and carbon isotope variability in *Sphagnum* moss along a micro-topographical gradient in a southern Patagonian peatland. *Journal of Quaternary Science*, *31*(4), 426–435.

Nichols, J. E., Peteet, D. M., Moy, C. M., Castañeda, I. S., McGeachy, A., & Perez, M. (2014). Impacts of climate and vegetation change on carbon accumulation in a south-central Alaskan peatland assessed with novel organic geochemical techniques. *The Holocene*, *24*(9), 1146–1155.

Sternberg, L. S. L. (2009). Oxygen stable isotope ratios of tree-ring cellulose: the next phase of understanding. *New Phytologist*, *181*(3), 553–562.

CHAPTER 3

Temperature-dependent oxygen isotope fractionation in plant cellulose biosynthesis revealed by global peat mosses

Zhengyu Xia[1] and Zicheng Yu[1,2]

[1]Department of Earth and Environmental Sciences, Lehigh University, Bethlehem, PA, USA

[2]Institute for Peat and Mire Research, School of Geographical Sciences, Northeast Normal University, Changchun, China

Abstract

The oxygen isotope ratio ($\delta^{18}O$) of plant cellulose has been widely used to study ecohydrological processes of ecosystems as well as to reconstruct past climate conditions in terrestrial climate archives. These applications are grounded on a key assumption that the biochemical fractionation during cellulose synthesis is a constant around +27‰ and is not affected by other factors. Here we revisit the influence of temperature on biochemical fractionation factor during cellulose synthesis using a global compilation of *Sphagnum* cellulose $\delta^{18}O$ data. *Sphagnum* mosses (peat mosses) often inhabit waterlogged peatlands and possess unique physiological strategy in that their cellulose $\delta^{18}O$ of newly synthesized tissues closely reflect precipitation $\delta^{18}O$ throughout their growing season. Within-site cellulose $\delta^{18}O$ variability has a median standard deviation of 0.7–0.8‰, resulting from different degree of evaporative enrichment of ^{18}O in metabolic leaf water. Whereas this evaporative enrichment is a small quantity due to the external capillary "water buffer" for *Sphagnum* mosses and could be mitigated using site-specific minimum cellulose $\delta^{18}O$ data that most likely reflect the signal of unevaporated source water. Our analysis reveals that the apparent enrichment factor between cellulose and precipitation $\delta^{18}O$ increases with decreasing air temperature. In particular, the apparent enrichment factor could be as high as +32‰ if growing temperature is below 5°C. This observational dataset extends the support for the temperature-dependent oxygen isotope fractionation in plant cellulose synthesis previously demonstrated in laboratory experiments, with important implications for paleoclimate and plant physiology studies that employ cellulose $\delta^{18}O$ measurements.

3.1. Introduction

The oxygen isotope ratio ($\delta^{18}O$) of plant cellulose (hereafter $\delta^{18}O_c$) possess a variety of climate information during tissue growth (Sternberg, 2009). It has been used as a proxy to reconstruct past climate conditions not only in tree rings (Libby et al., 1976), but also in lake sediments (Edwards & McAndrews, 1989) and peat deposits (Hong et al., 2000). Earlier studies established empirical relationships between $\delta^{18}O_c$ and climatic parameters, such as temperature, relative humidity, and precipitation amount for a specific region (Libby et al., 1976; Treydte et al., 2006; Managave et al., 2010). An improved understanding of physiological and biochemical processes enabled developing mechanistic models to quantitatively decipher the $\delta^{18}O_c$ signal for paleoclimate reconstruction (Roden et al., 2000; Kahmen et al., 2011). It has been well recognized that the source water for vascular plants, in most cases precipitation, is taken up by roots for photosynthesis in leaves, while the leaf water is enriched in ^{18}O relative to precipitation due to plant transpiration. The carbohydrate product (e.g., sucrose) that has been further enriched in ^{18}O by biochemical fractionation is then translocated to the site of cellulose synthesis, such as stem, where additional biochemical exchange reaction occurs with stem water. As such, plant $\delta^{18}O_c$ signal essentially reflects precipitation $\delta^{18}O$ (hereafter $\delta^{18}O_p$) with an offset governed by both physiological and biochemical processes (Richter et al., 2008; Sternberg, 2009).

The current mechanistic models have made progress in depicting the physiological effects including how different climatic parameters affect the degree of ^{18}O enrichment in leaf water and imprint the $\delta^{18}O_c$ signal (Kahmen et al., 2011). However, less is known about the biochemical effects that are equally important in shaping the final $\delta^{18}O_c$ signal. The combined physiological and biochemical effects could be described by the following equation (Barbour & Farquhar, 2000):

$$\delta^{18}O_c = \delta^{18}O_p + \Delta_{leaf}\,(1 - p_x p_{ex}) + \varepsilon_{bio} \quad (1)$$

where $\delta^{18}O_c$ and $\delta^{18}O_p$ are the oxygen isotope composition of cellulose and precipitation, respectively; Δ_{leaf} is the degree of ^{18}O enrichment in leaf water known as the physiological effect; p_x is the proportion of unenriched water at the site of cellulose synthesis; p_{ex} is the percentage of exchangeable oxygen in carbohydrate substrates destined for cellulose synthesis; and ε_{bio} is the biochemical enrichment (or fractionation) factor associated with the post-photosynthetic exchange of oxygen atoms between carbonyl group and medium water. The p_x is expected to be unity for stem cellulose (Cernusak et al., 2005; Kahmen et al., 2011; Sternberg & Ellsworth, 2011), but for leaf cellulose it is expected to be less than unity (Helliker & Ehleringer, 2002; Barbour, 2007; Kahmen et al., 2011; Song et al., 2014b) or even has been assumed as zero (Tuthorn et al., 2014). The p_{ex} and ε_{bio} have been successfully constrained using different approaches to be invariables at 0.42 and 27‰, but with a range of ±0.3 and ±3‰, respectively (DeNiro & Epstein, 1981; Sternberg & DeNiro, 1983; Sternberg et al., 1986; Yakir & DeNiro, 1990; Roden et al., 2000).

These biochemical factors are a net result of complex biochemical processes in cellulose biosynthesis (Waterhouse et al., 2013) and seem to contain less climatic information, thus these are almost always treated as invariants in mechanistic models. For instance, Helliker and Richter (2008) incorporated mechanistic modeling into their global tree-ring $\delta^{18}O_c$ data and inversely inferred that boreal tree-canopy temperature must be tremendously higher than ambient temperature to obtain large Δ_{leaf} and to match with observed $\delta^{18}O_c$ data. They found that tree-canopy temperature converges to ~21°C throughout a large range of latitudes. This conclusion was reached based on a constant ε_{bio} in inverse modeling. Later, Sternberg and Ellsworth (2011) challenged this conclusion by showing that the ε_{bio} is also temperature-dependent that increases with decreasing temperature. They heterotrophically generated cellulose from starch substrate at different temperatures and found that ε_{bio} could be as large as 31‰ when temperature is

5°C. However, Zech et al. (2014) indicated that the temperature-dependence of ε_{bio} shown in their laboratory experiments is an artifact from the p_{ex} that seems also temperature-dependent.

Here we use a global compilation of *Sphagnum* (peat mosses) $\delta^{18}O_c$ data to test the hypothesis that the ε_{bio} is temperature-dependent. *Sphagnum* mosses are the keystone bryophyte species in peat-forming ecosystems and are adapted to cool, waterlogged, and nutrient-poor conditions. Almost half of the boreal peatland areas are covered and built by *Sphagnum* mosses (Rydin & Jeglum, 2013). There have been a number of studies exploring the potential of stable isotopes in *Sphagnum* as proxies for peat-based paleoclimate reconstruction (e.g., Ménot-Combes et al., 2002; Daley et al., 2010; Loader et al., 2016; Granath et al., 2018). In general, *Sphagnum* mosses have many unique physiological characteristics with which their tissue $\delta^{18}O_c$ could closely track $\delta^{18}O_p$ with the only major offset from ε_{bio}. First, *Sphagnum* mosses are important peat-forming plants in rain-fed (ombrotrophic), nutrient-poor bogs where moisture is predominantly derived from precipitation. Second, *Sphagnum* mosses have no stomata and no root systems. They maintain a simple water use strategy without the ability to control evapotranspiration. The natural water loss on *Sphagnum* surface is balanced either by new precipitation input or by capillary movement of water from below (Rydin & Jeglum, 2013; McCarter & Price, 2014). Therefore, *Sphagnum* mosses passively utilize water stored in surface unsaturated and oxic peat known as the acrotelm without ability to access water at depth as vascular plants do. Third, *Sphagnum* mosses have the extraordinary capacity to store water and, more importantly, protect the metabolic water from evaporation loss. They have specialized hyaline (water-filling) cells on their leaves and outer cortex of the stems, and in some species these hyaline cells completely enclose photosynthetic cells (Loisel et al., 2009). Most of the water is, however, external capillary water held in pore spaces between leaves (Murray et al., 1989; Rydin & Jeglum, 2013).

As a result of these multiple layers of water storage in *Sphagnum* mosses, the metabolic water in photosynthetic cells could be isolated and weakly impacted by evaporative enrichment of ^{18}O. Fourth, *Sphagnum* mosses are opportunist photosynthesizers, growing and synthesizing new cellulose as long as conditions allow even in near-freezing temperature. This physiological trait allows us to explore the sensitivity of ε_{bio} to temperature in a temperature window that is too low to allow the growth of vascular plants (Clymo & Hayward, 1982). In summary, the newly compiled dataset and analysis presented in this study offer a simple but effective test of the relationship between ε_{bio} and temperature that circumvents the complex physiology of vascular plants.

3.2. Data and methods

3.2.1. *Sphagnum* oxygen isotope data

We compiled all available *Sphagnum* tissue $\delta^{18}O$ measurements reported in literature, supplemented with some new data to fill regional gaps. The final dataset includes 786 individual $\delta^{18}O$ measurements from 173 sites (Figure 3.1 and Data Set C1). Key site information and references are summarized in Table 3.1, while additional metadata are in Data Set C1. Most of these sites are bogs from boreal and sub-arctic regions, but a few bog sites are located in the tropical and subtropical regions and the Southern Hemisphere. A few fen sites were also included. The main *Sphagnum* species are the common bog species, *S. magellanicum*, *S. fuscum*, *S. cuspidatum*, and *S. capillifolium*. A few studies did not report the species (*Sphagnum* spp.). In some studies, the local microtopography information (such as hummock and hollow) or water table depth (WTD) where *Sphagnum* samples were collected are available. The *Sphagnum* tissue $\delta^{18}O$ data range from 11.5‰ to 26.6‰ (scaled to VSMOW). The uncertainty of $\delta^{18}O$ data is represented by either the long-term precision of measurements (1σ) in different laboratories or the standard deviation (1σ) of replicate measurements of the

same sample, which is less than 0.6‰ and 2.0‰, respectively. The exact materials of *Sphagnum* used for isotope analysis differ among studies and include "capitula" (the cluster of new branch leaves at the tip of moss), "capitula cellulose", "newest 1-cm stem cellulose", "leaf", "leaf cellulose", "stem cellulose", "whole plant cellulose", and "5-cm whole plant cellulose".

We applied an offset correction on raw $\delta^{18}O$ data that were measured from non-cellulose ("capitula" and "leaf") or stems ("newest 1-cm stem cellulose" and "stem cellulose"). The $\delta^{18}O$ offset between extracted cellulose and untreated bulk tissues of the same *Sphagnum* material is small, and we have determined it by a pilot experiment to be 0.69±0.83‰ (error is the standard deviation, 1σ) (Figure 3.2a). Kaislahti Tillman et al. (2010) reported that this offset is a negative value (Figure 3.2a), likely due to the fact that they measured *Sphagnum* materials from peat rather than from growing plants while untreated bulk tissues in peat probably had been contaminated by other botanical components. The $\delta^{18}O$ offset between leaf cellulose (or capitula, which is formed by branch leaves) and stem cellulose of the same *Sphagnum* material is also small and well constrained in multiple studies as 0.62±0.51‰ (Figure 3.2b). This tissue-specific offset might be due to different water pools at the site of leaf and stem cellulose biosynthesis (Moschen et al., 2009). The capitula medium water might be more enriched in ^{18}O than the matrix water below capitula where stem cellulose is synthesized. The above offset correction re-scaled these raw $\delta^{18}O$ data to their equivalent capitula or leaf $\delta^{18}O_c$ values with the involved uncertainty being propagated in the following analysis. Correction is not required for $\delta^{18}O$ data that were measured from "whole plant cellulose" or "5-cm whole plant cellulose" because our pilot experiment found that branch and leaf tissues represents 90.3±5.0% of dry mass of *Sphagnum* whole-plant and has a similar cellulose yield (45.6±4.7%) as stem tissue (48.8±8.0%). The details about our cellulose extraction methods can be found in Text C1.

3.2.2. Precipitation oxygen isotope data and climate data

We used the Online Isotopes in Precipitation Calculator (OIPC) (Bowen, 2020) to obtain monthly $\delta^{18}O_p$ for every *Sphagnum* sampling location in the dataset. In the OPIC, $\delta^{18}O_p$ at a given location is modeled based on latitude and altitude plus a residual term that is interpolated using existing $\delta^{18}O_p$ observations (Bowen et al., 2005). This model provides the best estimate for the site-specific $\delta^{18}O_p$ for our synthesis as there is no on-site precipitation $\delta^{18}O$ measurements prior to sample collection for almost all sites. The uncertainty of OIPC is depicted as the confidence interval for mean annual $\delta^{18}O_p$ prediction, which increases in regions where $\delta^{18}O_p$ observations are scarce (Bowen & Revenaugh, 2003), whereas the confidence interval for monthly $\delta^{18}O_p$ prediction is not available in the OPIC. In addition, the OIPC is for predicting long-term mean value for monthly and annual $\delta^{18}O_p$ at a given location but does not account for their inter-annual variability. This inter-annual variability is an important uncertainty source in determining ε_{bio} for *Sphagnum* as these samples were collected in different years and in some studies only their recent growth was harvested. To estimate this uncertainty, we used the archived outputs from three nudged isotope-enabled global circulation models (IsoGSM, LMDZ4, and GISS ModelE; accessible from https://data.giss.nasa.gov/swing2/swing2_mirror/) (Risi et al., 2012) to calculate the multi-model mean standard deviation of monthly $\delta^{18}O_p$ for each sample location. Therefore, we used the OIPC model that has been validated against observational $\delta^{18}O_p$ data to derive the site-specific $\delta^{18}O_p$ but used the isotope-enabled global circulation models nudged on reanalysis wind data to estimate the uncertainty associated with its inter-annual variability (at least 31 years). We acknowledge that the accuracy of monthly $\delta^{18}O_p$ generated on OIPC is unknown, but we used the prediction error for mean annual $\delta^{18}O_p$ as a reference for following discussion.

We used the NASA MERRA-2 monthly 2-m air temperature (T2M in M2IMNXASM) (GMAO, 2015c) data to infer the relevant growing temperature for each *Sphagnum* sample that was collected in different years and months. The MERRA-2 is an atmospheric reanalysis product for satellite era (beginning in 1980) and has a resolution of 0.5° for latitude and 0.625° for longitude. The raw temperature data were corrected for altitude difference between each sampling site and the corresponding MERRA-2 grid assuming a lapse rate of 0.0065 °C/m. The MERRA-2 grid altitude is inferred from the constant model parameter surface geopotential height (PHIS in M2C0NXASM) (GMAO, 2015b) as PHIS/g where g is the standard gravity at 9.8 m/s^2. Similarly, we also used the MERRA-2 monthly precipitation amount (PRECTOTCORR in M2TMNXFLX) (GMAO, 2015a) data that were combined with OPIC $\delta^{18}O_p$ data to calculate the metrics of amount-weighted $\delta^{18}O_p$ that represent the isotopic composition of the source water for *Sphagnum*. However, the MERRA-2 products do not provide the uncertainty of reanalysis data other than the temporal variance of monthly means.

3.2.3. Data analysis

We first calculated the range and standard deviation of site-specific $\delta^{18}O_c$ data that were collected from different *Sphagnum* samples during one-time sampling campaign in order to evaluate if measured WTD or microtopographical locations would explain the within-site $\delta^{18}O_c$ variability. Then we calculated the apparent enrichment factor (ε_{app}) for each $\delta^{18}O_c$ datum as $\delta^{18}O_c$ minus its corresponding $\delta^{18}O_p$, with the latter value depending on the type of materials and the sampling month. For $\delta^{18}O_c$ data derived from the recent growth parts of *Sphagnum* (capitula or the newest 1-cm stem), we used the $\delta^{18}O_p$ value of the sampling month ($\delta^{18}O_{p1}$), or the amount-weighted $\delta^{18}O_p$ of the sampling month and the previous month ($\delta^{18}O_{p2}$), or the amount-weighted $\delta^{18}O_p$ of the sampling month and previous two months ($\delta^{18}O_{p3}$). For $\delta^{18}O_c$ data derived from the

whole plant parts of *Sphagnum*, we used the amount-weighted $\delta^{18}O_p$ of the most recent growing season defined as the months with MERRA-2 temperature higher than 0°C during the most recent 12-month period ($\delta^{18}O_{pgs}$), or of the entire recent 12 months ($\delta^{18}O_{p12}$). For all these $\delta^{18}O_p$ values, we also determined the arithmetic average temperature from the MERRA-2 dataset for their corresponding periods (T_1, T_2, T_3, T_{gs}, and T_{12}). Pairing the calculated ε_{app} and temperature data, we explored their relationship between them using a null hypothesis that ε_{app} is independent from temperature. To mitigate the influence from evaporative enrichment that has caused within-site variability in $\delta^{18}O_c$ and ε_{app}, we used the site-specific minimum $\delta^{18}O_c$ ($\delta^{18}O_{cmin}$) to calculate the site-specific minimum ε_{app} (ε_{appmin}) for each site as an approximation for ε_{bio}. The precision of ε_{appmin} was assessed using the Gaussian error propagation combining the analytical uncertainty in $\delta^{18}O_c$, the uncertainty related to offset correction from raw $\delta^{18}O$ data, and the climatological uncertainty in amount-weighted $\delta^{18}O_p$ values. The accuracy of ε_{appmin} was assessed using the OPIC prediction error for mean annual $\delta^{18}O_p$.

3.3. Results and discussion

3.3.1 Within-site variability in *Sphagnum* cellulose $\delta^{18}O$

The median within-site range of $\delta^{18}O_c$ data is 1.0‰, 1.5‰,1.8‰, 2.3‰ for sites with two, three, four, and at least five measurements, respectively (Figure 3.3a). Whereas the within-site standard deviation (1σ) of $\delta^{18}O_c$ data is not influenced by the number of measurements per site and is consistently between 0.7‰ and 0.8‰ (Figure 3.3b).

This within-site $\delta^{18}O_c$ variability is the result of differential evaporative enrichment of ^{18}O in metabolic leaf water for *Sphagnum* inhabiting different microtopographical locations in peatlands, as all these samples at the same site should receive the same precipitation input. This evaporation component—which could theoretically be expressed as $\Delta_{leaf}(1 - p_x p_{ex})$ as in Eq. (1)—has modified $\delta^{18}O_p$ before the

precipitation source water is incorporated into cellulose biosynthesis. For most of sites, the $\delta^{18}O_c$ data were not derived from the same *Sphagnum* species, but recent studies suggested the species effect of leaf anatomy or physiology (biotic factor) does not directly cause the within-site $\delta^{18}O_c$ variability (El Bilali & Patterson, 2012). Instead, different *Sphagnum* species favor different microhabitats (abiotic factor) such as drier hummocks or wetter hollows that indirectly control the degree of evaporative enrichment of ^{18}O in metabolic leaf water and thus the $\delta^{18}O_c$ signal.

Our data analysis shows that most sites display positive correlations between $\delta^{18}O_c$ and WTD, meaning that *Sphagnum* associated with a deeper water table and a drier habitat would register a higher degree of evaporative enrichment (Figure 3.3c). Samples collected at hummock and hollow locations within a site also show that hummock-inhabiting *Sphagnum* have higher $\delta^{18}O_c$ in most cases (Figure 3.3d), although the WTD and the size of these microtopographical features are unknown. The mechanism behind the connection between evaporative enrichment of ^{18}O in leaf water and WTD is more complex than a simple corollary that dried habitats have caused a higher evaporation rate. In fact, the metabolic leaf water is technically difficult to collect as *Sphagnum* and other bryophytes store a large proportion of water in external capillary spaces (Dilks & Proctor, 1979). Through measuring *Sphagnum* water content (WC) and "bulk" leaf water $\delta^{18}O$, our previous study proposed that wetter *Sphagnum* evaporate water stored in external capillary spaces that indirectly protect metabolic leaf water from evaporative water loss. In contrast, drier *Sphagnum* have a smaller proportion of external capillary water and as a consequence the metabolic leaf water is also subject to some degrees of evaporation.

However, the negative correlations between $\delta^{18}O_c$ and WTD also exist (Figure 3.3c), although in at least a few cases these negative correlations are probably an artifact from a narrow range of WTD that does not represent a well-defined moisture gradient (Figure 3.3c). In addition, at a few sites hollow-inhabiting *Sphagnum* could have higher

$\delta^{18}O_c$ (Figure 3.3d). The cause for these opposite observations might be the decoupling between *Sphagnum* WC and WTD. Hollow-inhabiting *Sphagnum* have a lower proportion of structural carbohydrates and a higher collective surface area (Turetsky et al., 2008). As a result, they are more often limited by desiccation and tend to have a lower WC despite a shallower WTD than hummock-inhabiting *Sphagnum*, in particular after a sustained period of no precipitation. Studies that reported these data did not measure the *Sphagnum* WC nor had any description of their microhabitats, thus it is impossible to test this specific hypothesis.

In fact, unlike for vascular plants there is no appropriate physiological model to mechanistically derive Δ_{leaf} as in Eq. (1) for *Sphagnum* mosses that do not have stomata. Whereas the partitioning between internal and external leaf water in *Sphagnum* could explain why *Sphagnum* $\delta^{18}O_c$ exhibit relatively limited variance compared to their measured "bulk" leaf water $\delta^{18}O$ that is often highly enriched in ^{18}O (Ménot-Combes et al., 2002; Price et al., 2009; Loader et al., 2016). This "water buffer" mechanism might be unique for *Sphagnum* mosses adapted to waterlogged peatlands, but not for other bryophytes. For example, the moss species (*Polytrichum strictum* and *Chorisodontium aciphyllum*) from aerobic moss peatbanks in the Antarctic Peninsula show very high and highly variable $\delta^{18}O_c$ values (Royles et al., 2013a; Royles et al., 2016), which are only possible with an unbuffered metabolic leaf water with a significant enrichment in ^{18}O.

Due to the presence of external water buffer for *Sphagnum* mosses, we infer that the evaporative enrichment of ^{18}O in metabolic leaf water, despite being difficult to be directly measured or modeled, is a fairly small quantity compared to ε_{bio}. It should approximate to zero for *Sphagnum* inhabiting very wet habitats, in which case the metabolic leaf water is close to being completely protected by external capillary water from evaporation. For individual sites at which *Sphagnum* $\delta^{18}O_c$ data display a considerable variability, the site-specific $\delta^{18}O_{cmin}$ value represents the case that the

metabolic leaf water is least modified by evaporative enrichment. Therefore, the corresponding ε_{app} serves as an alternative measure of ε_{bio} for each of those sites.

3.3.2. Effect of temperature on biochemical enrichment factor

Defining the time span of growth and precipitation input that are most relevant for collected *Sphagnum* samples presents a main challenge in refining the relationship between ε_{app} and temperature. Both capitula and the newest 1-cm stem represent the most recent growth of *Sphagnum* right before sample collection and these tissues could register the recent input of $\delta^{18}O_p$ in cellulose. For example, Daley et al. (2010) collected *Sphagnum* capitula every two to three months and found that the $\delta^{18}O_c$ signals showed variations of more than 4‰ that were in general tracking the variations of $\delta^{18}O_p$ over seasonal scale at two of three sites in northwestern European, but at another site the variations were less than 2.5‰, despite similar $\delta^{18}O_p$ seasonality at these locations according to the OPIC model. These observations imply that *Sphagnum* capitula regenerate and refresh their $\delta^{18}O_c$ signal at bimonthly and quarterly timescales, but the rates of $\delta^{18}O_c$ "turnover" for capitula appear to be variable.

This isotopic turnover rate may depend on biotic factors such as *Sphagnum* productivity, which has been routinely determined by measuring *Sphagnum* stem height growth (Clymo, 1970). Field measurements indicate that stem height growth is enhanced with higher photosynthetic active radiation and longer growing season length (Loisel et al., 2012) but is also influenced by local ecohydrological factors (Gunnarsson, 2005; Loisel & Yu, 2013b). Whereas capitula turnover rate might be proportional to the stem increment rate as the capitula density is lower when stem growth is faster (Breeuwer et al., 2008; Loisel et al., 2012). Aldous (2002) used the ratio of number of branches per capitulum to number of branches per 1-cm of stem to normalize the turnover of capitula to stem increment. This method showed that capitula could replace themselves

completely with every 1.65-cm stem increment for a case study of *S. capillifolium* from peat bogs in the northeastern US (Aldous, 2002). Nevertheless, the exact time spans of capitula replacement and the newest 1-cm stem in the dataset are unknown.

Other than the physical replacement, capitula $\delta^{18}O_c$ turnover rate may also depend on abiotic factors such as the residence time of metabolic leaf water $\delta^{18}O$, which in principle should be governed by both the size of acrotelm water reservoir and the rate of precipitation and evaporation. The role of residence time has been proposed to explain the smaller range of along-stem $\delta^{18}O_c$ variation compared to $\delta^{18}O_p$ variation in a case study of *S. magellanicum* collected from a southern Patagonian peat bog. The turnover of $\delta^{18}O_c$ does not only influence how many months of precipitation input are relevant for *Sphagnum* cellulose biosynthesis but also the growing temperature, which are two important but potentially site-specific metrics for the following analysis on the temperature-dependence of ε_{app}.

Hereafter, for $\delta^{18}O_c$ data measured from the recent growth parts of *Sphagnum*, we used the $\delta^{18}O_{p2}$ as the most relevant precipitation input to derive ε_{app} that were paired with the T_1 as the most relevant growing temperature. This choice assumed that the sampling month temperature was the most relevant for capitula growth and the newest increment of stem, but metabolic leaf water did not only derive from the precipitation of sampling month, but also partly inherited the precipitation input in the previous month. We found that the ε_{app} increases with decreasing temperature in particular when T_1 is below 10°C (Figure 3.4b). Additional analysis indicates that the general trend towards higher ε_{app} with decreasing temperature is not affected by pairing different time spans of precipitation input (e.g., $\delta^{18}O_{p1}$, $\delta^{18}O_{p2}$, and $\delta^{18}O_{p3}$) and relevant growing temperature (e.g., T_1 and T_2) (Figures 3.4a, 3.4c, and 3.4d).

Unlike the recent growth parts of *Sphagnum*, the whole plant parts of *Sphagnum* likely integrate the growth for the time span of the entire growing season, which is best

defined as those months above 0°C. This threshold value has been used to define bioclimatic variables such as the photosynthetically active radiation during the growing season, assuming that periods with freezing temperature is unrelated to biomass production (Loisel et al., 2012; Charman et al., 2013). *Sphagnum* growth during the months of freezing temperature does occur as if snow cover is thick and persistent enough to insulate *Sphagnum* from long duration of winter frost (Dorrepaal et al., 2004; Genet et al., 2013), while shading from snow cover seems not a major limiting factor for *Sphagnum* growth (Clymo & Hayward, 1982; Küttim et al., 2020). Even so, *Sphagnum* growth during freezing months is unrelated to how low the temperature is, as unfrosted moss surface temperature maintains around 0°C under snow cover.

A reasonable measure of relevant growing temperature for the whole plant parts of *Sphagnum* is T_{gs}, the arithmetic average temperature of the months above 0°C. The accumulative temperature—such that is defined as growing degree days above zero in bioclimatic studies (Charman et al., 2013)—might be a more accurate measure of the total warmth *Sphagnum* has received. Many studies have found that *Sphagnum* productivity is enhanced during the warmest season (Krebs et al., 2016; Küttim et al., 2020), meaning that majority of biomass is produced in summer, although a few studies suggest that *Sphagnum* growth could be limited by summer desiccation stress and photoinhibition (Lindholm, 1990; Dorrepaal et al., 2004; Genet et al., 2013). Considering this, there is a possibility that T_{gs} would underestimate the mass-weighted growing temperature for the whole plant parts of *Sphagnum*. Although the freezing winter temperature is unrelated to *Sphagnum* growth, the accumulation of winter precipitation as snowpack could be an important component of source water for *Sphagnum* during the snow melt season. Indeed, direct sampling of peatland deep water reservoir show $\delta^{18}O$ values close to amount-weighted mean annual $\delta^{18}O_p$ (Ménot-Combes et al., 2002). Therefore, for $\delta^{18}O_c$ data measured from the whole plant parts of *Sphagnum*, we used the

$\delta^{18}Op_{12}$ as the most relevant precipitation input to derive ε_{app} that were paired with the T_{gs} as the most relevant growing temperature. The whole-plant data complement the recent-growth data in the temperature range from 9°C to 14°C (Figure 3.4e), but the ε_{app} does not show a clear trend with temperature.

In both recent-growth and whole-plant data synthesis, data collected from fens seem to be outliers compared to bogs and their ε_{app} could be either higher or lower than the rest of dataset. The fen outliers in recent-growth synthesis (Figure 3.4b) are samples collected from swales in the Lake Superior region where local swale water has lower $\delta^{18}O$ values than the recent precipitation (Zanazzi & Mora, 2005), leading to lower ε_{app} if scaled to $\delta^{18}O_{p2}$. The fen outliers in whole-plant synthesis (Figure 3.4e) are samples from southern Alaska (Jones et al., 2019). We speculate that *Sphagnum* inhabiting these groundwater-fed fens is not under desiccation stress, has a poorly developed capillary network, and is subjective to strong evaporative enrichment of ^{18}O in metabolic leaf water.

Merging both recent-growth and whole-plant data from bogs and plotting site-specific ε_{appmin} (for sites with at least three data points) versus relevant growing temperature, we found that the results corroborate the temperature-dependence of ε_{bio} as found in wheat seedling experiments in which cellulose was heterotrophically generated under controlled conditions from 5°C to 30°C (Sternberg & Ellsworth, 2011) (Figure 3.5). The relationship between ε_{bio} and growing temperature in wheat seedling experiments was established by assuming a known value of substrate $\delta^{18}O$ and a constant of p_{ex}, while the second order polynomial regression based on their experimental data is almost identical to that based on a compilation of aquatic plant $\delta^{18}O_c$ data (Sternberg & Ellsworth, 2011). Our compilation of *Sphagnum* $\delta^{18}O_c$ data has extended the lowest end of temperature in their results from 5°C to 0°C. The extrapolated second order polynomial regressions from Sternberg and Ellsworth (2011) fit with the ε_{appmin} derived

from the *Sphagnum* dataset and support that the ε_{bio} increases steeply with decreasing temperature when temperature is below 10°C and could be as high as +32‰ if temperature is below 5°C. Nevertheless, the sensitivity of ε_{bio} to decreasing temperature from the compilation seems weak when temperature is between 10°C and 15°C.

Although the ε_{appmin} data points are considerably scattering around the overall trend line, quantification of their involved uncertainties suggests that the deviations are overall within an acceptable range. The main uncertainty for ε_{appmin} is the limited precision of OPIC-modeled $\delta^{18}O_p$, which is related to the strength of inter-annual variability in precipitation dynamics and unfortunately could be only estimated from nudged isotope-enabled global circulation models. Notably, the accuracy of ε_{appmin} except few cases is robust compared to their precision as shown by comparing the two types of error bars (Figure 3.5).

3.4. Conclusions and implications for paleoclimate and plant physiology studies

Despite the recent progress in quantifying the physiological effects on $\delta^{18}O_c$ in plants, we known much less about the biochemical effects, which are almost always treated as invariants in mechanistic modeling. Recent experimental studies claimed that the ε_{bio} is temperature-dependent (Sternberg & Ellsworth, 2011), whereas contrasting interpretations indicate that the p_{ex}, rather than ε_{bio}, is temperature-dependent (Zech et al., 2014). To overcome the limitation of experimental approach, in this study we focused on *Sphagnum* mosses as a model plant and used an observational *Sphagnum* oxygen isotope dataset as a "natural experiment" to provide insights into the relationship between ε_{bio} and growing temperature. We summarize the following conclusion and implications of our study.

(1) Our data synthesis shows that evaporative enrichment of ^{18}O in metabolic leaf water has resulted in a within-site variability in *Sphagnum* $\delta^{18}O_c$ with a median

standard deviation of 0.7–0.8‰. *Sphagnum* mosses have no stomata and are unable to control water loss, thus the degree of evaporative enrichment depends on the size of external capillary "water buffer" determined partly by WTD or microtopographical feature. A consequence of this "water buffer" is that the degree of evaporative enrichment for *Sphagnum* metabolic leaf water is a very small quantity compared to vascular plants and other bryophytes. Therefore, the site-specific ε_{appmin} derived from $\delta^{18}O_{cmin}$ could be used as an approximation for ε_{bio}.

(2) We show that the ε_{appmin} increases with a decreasing temperature, with a steeper rate of increase when temperature is below 10°C, and reaches +32‰ if temperature is below 5°C. The general trend is remarkably similar to the relationship derived from wheat seedling experiments and aquatic plant $\delta^{18}O_c$ data (Sternberg & Ellsworth, 2011). A previous study concluding that the ε_{bio} is insensitive to temperature (Roden & Ehleringer, 2000) could be due to that the growing temperature for their plants is higher than 20°C, at which the sensitivity of ε_{bio} to temperature is weak. Our results imply that the temperature-dependence of ε_{bio} shown in heterotrophic generation of cellulose is not an artefact from variable p_{ex} (Zech et al., 2014), as we use $\delta^{18}O_{cmin}$ data by which the term Δ_{leaf} is minimized and any temperature-dependent variation in p_{ex} is too small to introduce $\delta^{18}O_c$ variation. The Δ_{leaf} is usually a large quantity for vascular plants with stomata and increases substantially with decreasing relative humidity (Tuthorn et al., 2014). Due to the large contrast between evaporated leaf water $\delta^{18}O$ and unevaporated stem water $\delta^{18}O$ in vascular plants, the p_{ex} that could vary with plant types and in response to different growing conditions could play an important role in shaping the tree-ring $\delta^{18}O_c$ (Barbour & Farquhar, 2000; Ellsworth & Sternberg, 2014; Song et al., 2014a), but this is not the case for

Sphagnum mosses. In addition, any variation in p_{ex} could be further dampened by the factor of p_x, which is less than unity for leaf tissue.

(3) Plant $\delta^{18}O_c$ is a valuable paleoclimate proxy in a range of terrestrial climate archives, but studies employing plant $\delta^{18}O_c$ data should incorporate the influence of temperature on ε_{bio} into the process-based proxy system model framework for interpreting proxy data (Dee et al., 2015; Keel et al., 2016; Okazaki & Yoshimura, 2019). The temperature effect might be small for Holocene-scale paleoclimate reconstruction as data and model showed that temperature variability is in general less than 1°C (Liu et al., 2014). However, this effect would be important for high-latitude and alpine regions as the ε_{bio} exhibits the strongest sensitivity at low temperature and long-term temperature changes at these locations could be amplified due to various feedback mechanisms (Ballantyne et al., 2010; Feng et al., 2019). Furthermore, this temperature effect could be important in cold season, potentially resulting in different biochemical enrichments in intra-annual tree-ring $\delta^{18}O_c$ that is relevant for deciphering climate seasonality from tree-ring data (Schubert & Jahren, 2015; Zeng et al., 2016).

(4) Plant $\delta^{18}O_c$ data have also been used to understand the ecohydrological processes of plants such as tracing the water source for plants (Sargeant & Singer, 2016) or inversely modeling their growing temperature (Helliker & Richter, 2008; Song et al., 2011). Assuming a constant value of ε_{bio}, Helliker and Richter (2008) showed that boreal tree-canopy temperature must be substantially higher than ambient temperature. Additional analysis by Helliker et al. (2018) found that their previously inferred high tree-canopy temperature for boreal biome is essentially the result of a similarly warm day-time air temperature during growing season but tree-canopy itself could not tremendously rise temperature. In fact, the temperature-dependence of ε_{bio} is more important for subalpine and alpine regions

where plants have a cool growing-season temperature (below 10°C) and thus a considerably elevated ε_{bio}. Indeed, existing tree-ring data from the European Alps in Switzerland (Keel et al., 2016) and the Rocky Mountains in the western US (Helliker et al., 2018) have shown that incorporating a temperature-dependent ε_{bio} into mechanistic modeling would produce a better fit for observed $\delta^{18}O_c$. In addition, a tree-ring $\delta^{18}O_c$ record from the trans-Himalayan region (Chhumuja; 4400 meter above sea level) where growing season temperature is lower than 10°C was found to be best fitted with a relative humidity of 64%, which is however lower than nearby station observations (between 70–100% during monsoon season) (Brunello et al., 2019) but could be alternatively explained by a higher ε_{bio} at low temperature.

3.5. Acknowledgements

This study was supported by US. National Science Foundation grants (ERA-1502891 and DEB-1802810) to Z. Yu. The compiled data used in this study are available from in Data Set C1.

References

Aldous, A. R. (2002). Nitrogen translocation in *Sphagnum* mosses: effects of atmospheric nitrogen deposition. *New Phytologist*, *156*(2), 241–253.

Amesbury, M. J., Charman, D. J., Newnham, R. M., Loader, N. J., Goodrich, J., Royles, J., et al. (2015). Can oxygen stable isotopes be used to track precipitation moisture source in vascular plant-dominated peatlands? *Earth and Planetary Science Letters*, *430*, 149–159.

Aravena, R., & Warner, B. G. (1992). Oxygen-18 composition of *Sphagnum*, and microenvironmental water relations. *The Bryologist*, *95*(4), 445–448.

Aucour, A. M., Hillaire-Marcel, C., & Bonnefille, R. (1996). Oxygen isotopes in cellulose from modern and quaternary intertropical peatbogs: implications for palaeohydrology. *Chemical Geology*, *129*(3), 341–359.

Ballantyne, A. P., Greenwood, D. R., Sinninghe Damsté, J. S., Csank, A. Z., Eberle, J. J., & Rybczynski, N. (2010). Significantly warmer Arctic surface temperatures during the Pliocene indicated by multiple independent proxies. *Geology*, *38*(7), 603–606.

Barbour, M. M., & Farquhar, G. D. (2000). Relative humidity- and ABA-induced variation in carbon and oxygen isotope ratios of cotton leaves. *Plant, Cell & Environment*, *23*(5), 473–485.

Barbour, M. M. (2007). Stable oxygen isotope composition of plant tissue: a review. *Functional Plant Biology*, *34*(2), 83–94.

Bowen, G. J., & Revenaugh, J. (2003). Interpolating the isotopic composition of modern meteoric precipitation. *Water Resources Research*, *39*(10), 1299.

Bowen, G. J., Wassenaar, L. I., & Hobson, K. A. (2005). Global application of stable hydrogen and oxygen isotopes to wildlife forensics. *Oecologia*, *143*(3), 337–348.

Bowen, G. J. (2020). *The Online Isotopes in Precipitation Calculator, version 3.1*. Retrieved from http://wateriso.utah.edu/waterisotopes/pages/data_access/oipc.html

Brader, A. V. (2013). Precipitation in peatlands: The stable isotope record of *Sphagnum* mosses as a proxy for environmental change (Doctoral dissertation). Amsterdam, Netherlands: Vrije Universiteit.

Breeuwer, A., Heijmans, M. M. P. D., Robroek, B. J. M., & Berendse, F. (2008). The effect of temperature on growth and competition between *Sphagnum* species. *Oecologia*, *156*(1), 155–167.

Brenninkmeijer, C. A. M., van Geel, B., & Mook, W. G. (1982). Variations in the D/H and $^{18}O/^{16}O$ ratios in cellulose extracted from a peat bog core. *Earth and Planetary Science Letters*, *61*(2), 283–290.

Brunello, C. F., Andermann, C., Helle, G., Comiti, F., Tonon, G., Tiwari, A., & Hovius, N. (2019). Hydroclimatic seasonality recorded by tree ring $\delta^{18}O$ signature across a Himalayan altitudinal transect. *Earth and Planetary Science Letters*, *518*, 148–159.

Cernusak, L. A., Farquhar, G. D., & Pate, J. S. (2005). Environmental and physiological controls over oxygen and carbon isotope composition of Tasmanian blue gum, *Eucalyptus globulus*. *Tree Physiology*, *25*(2), 129–146.

Charman, D. J., Beilman, D. W., Blaauw, M., Booth, R. K., Brewer, S., Chambers, F. M., et al. (2013). Climate-related changes in peatland carbon accumulation during the last millennium. *Biogeosciences*, *10*(2), 929–944.

Clymo, R. S. (1970). The growth of *Sphagnum*: methods of measurement. *Journal of Ecology*, *58*(1), 13–49.

Clymo, R. S., & Hayward, P. M. (1982). The Ecology of *Sphagnum*. In A. J. E. Smith (Ed.), *Bryophyte Ecology* (pp. 229–289). Dordrecht: Springer Netherlands.

Daley, T. J. (2007). Tracking Holocene climate change using peat bog stable isotopes (Doctoral dissertation). Southampton, UK: University of Southampton.

Daley, T. J., Barber, K. E., Street-Perrott, F. A., Loader, N. J., Marshall, J. D., Crowley, S. F., & Fisher, E. H. (2010). Holocene climate variability revealed by oxygen isotope analysis of *Sphagnum* cellulose from Walton Moss, northern England. *Quaternary Science Reviews*, *29*(13), 1590–1601.

Dee, S., Emile-Geay, J., Evans, M. N., Allam, A., Steig, E. J., & Thompson, D. M. (2015). PRYSM: An open-source framework for PRoxY System Modeling, with applications to oxygen-isotope systems. *Journal of Advances in Modeling Earth Systems*, *7*(3), 1220–1247.

DeNiro, M. J., & Epstein, S. (1981). Isotopic composition of cellulose from aquatic organisms. *Geochimica et Cosmochimica Acta*, *45*(10), 1885–1894.

Dilks, T. J. K., & Proctor, M. C. F. (1979). Photosynthesis, respiration and water content in bryophytes. *New Phytologist*, *82*(1), 97–114.

Dorrepaal, E., Aerts, R., Cornelissen, J. H. C., Callaghan, T. V., & Van Logtestijn, R. S. P. (2004). Summer warming and increased winter snow cover affect *Sphagnum* fuscum growth, structure and production in a sub-arctic bog. *Global Change Biology*, *10*(1), 93–104.

Edwards, T. W. D., & McAndrews, J. H. (1989). Paleohydrology of a Canadian Shield lake inferred from ^{18}O in sediment cellulose. *Canadian Journal of Earth Sciences*, *26*(9), 1850–1859.

El Bilali, H., & Patterson, R. T. (2012). Influence of cellulose oxygen isotope variability in sub-fossil *Sphagnum* and plant macrofossil components on the reliability of paleoclimate records at the Mer Bleue Bog, Ottawa, Ontario, Canada. *Organic Geochemistry*, *43*, 39–49.

Ellsworth, P. V., & Sternberg, L. S. L. (2014). Biochemical effects of salinity on oxygen isotope fractionation during cellulose synthesis. *New Phytologist*, *202*(3), 784–789.

Feng, X., Zhao, C., D'Andrea, W. J., Liang, J., Zhou, A., & Shen, J. (2019). Temperature fluctuations during the Common Era in subtropical southwestern China inferred from brGDGTs in a remote alpine lake. *Earth and Planetary Science Letters*, *510*, 26–36.

Finsinger, W., Schoning, K., Hicks, S., Lücke, A., Goslar, T., Wagner-cremer, F., & Hyyppä, H. (2013). Climate change during the past 1000 years: a high-temporal-

resolution multiproxy record from a mire in northern Finland. *Journal of Quaternary Science*, *28*(2), 152–164.

Genet, H., Oberbauer, S. F., Colby, S. J., Staudhammer, C. L., & Starr, G. (2013). Growth responses of *Sphagnum* hollows to a growing season lengthening manipulation in Alaskan Arctic tundra. *Polar Biology*, *36*(1), 41–50.

GMAO. (2015a). *MERRA-2 instM_2d_asm_Nx: 2d,Monthly mean,Single-Level,Assimilation,Single-Level Diagnostics V5.12.4, Greenbelt, MD, USA, Goddard Earth Sciences Data and Information Services Center (GES DISC)*.

GMAO. (2015b). *MERRA-2 const_2d_asm_Nx: 2d, constants V5.12.4, Greenbelt, MD, USA, Goddard Earth Sciences Data and Information Services Center (GES DISC)*.

GMAO. (2015c). *MERRA-2 tavgM_2d_flx_Nx: 2d,Monthly mean,Time-Averaged,Single-Level,Assimilation,Surface Flux Diagnostics V5.12.4, Greenbelt, MD, USA, Goddard Earth Sciences Data and Information Services Center (GES DISC)*.

Granath, G., Rydin, H., Baltzer, J. L., Bengtsson, F., Boncek, N., Bragazza, L., et al. (2018). Environmental and taxonomic controls of carbon and oxygen stable isotope composition in *Sphagnum* across broad climatic and geographic ranges. *Biogeosciences*, *15*(16), 5189–5202.

Gunnarsson, U. (2005). Global patterns of *Sphagnum* productivity. *Journal of Bryology*, *27*(3), 269–279.

Helliker, B. R., & Ehleringer, J. R. (2002). Differential ^{18}O enrichment of leaf cellulose in C_3 versus C_4 grasses. *Functional Plant Biology*, *29*(4), 435–442.

Helliker, B. R., & Richter, S. L. (2008). Subtropical to boreal convergence of tree-leaf temperatures. *Nature*, *454*(7203), 511–514.

Helliker, B. R., Song, X., Goulden, M. L., Clark, K., Bolstad, P., Munger, J. W., et al. (2018). Assessing the interplay between canopy energy balance and photosynthesis with cellulose $\delta^{18}O$: large-scale patterns and independent ground-truthing. *Oecologia*, *187*(4), 995–1007.

Hong, B., Liu, C., Lin, Q., Yasuyuki, S., Leng, X., Wang, Y., et al. (2009). Temperature evolution from the $\delta^{18}O$ record of Hani peat, Northeast China, in the last 14000 years. *Science in China Series D: Earth Sciences*, *52*(7), 952–964.

Hong, Y. T., Jiang, H. B., Liu, T. S., Zhou, L. P., Beer, J., Li, H. D., et al. (2000). Response of climate to solar forcing recorded in a 6000-year $\delta^{18}O$ time-series of Chinese peat cellulose. *The Holocene*, *10*(1), 1–7.

Jones, M. C., Anderson, L., Keller, K., Nash, B., Littell, V., Wooller, M., & Jolley, C. A. (2019). An assessment of plant species differences on cellulose oxygen isotopes from two Kenai Peninsula, Alaska peatlands: implications for hydroclimatic reconstructions. *Frontiers in Earth Science*, *7*(25).

Kahmen, A., Sachse, D., Arndt, S. K., Tu, K. P., Farrington, H., Vitousek, P. M., & Dawson, T. E. (2011). Cellulose $\delta^{18}O$ is an index of leaf-to-air vapor pressure difference (VPD) in tropical plants. *Proceedings of the National Academy of Sciences*, *108*(5), 1981–1986.

Kaislahti Tillman, P., Holzkämper, S., Kuhry, P., Sannel, A. B. K., Loader, N. J., & Robertson, I. (2010). Stable carbon and oxygen isotopes in *Sphagnum fuscum* peat from subarctic Canada: Implications for palaeoclimate studies. *Chemical Geology*, *270*(1), 216–226.

Keel, S. G., Joos, F., Spahni, R., Saurer, M., Weigt, R. B., & Klesse, S. (2016). Simulating oxygen isotope ratios in tree ring cellulose using a dynamic global vegetation model. *Biogeosciences*, *13*(13), 3869–3886.

Krebs, M., Gaudig, G., & Joosten, H. (2016). Record growth of *Sphagnum papillosum* in Georgia (Transcaucasus): rain frequency, temperature and microhabitat as key drivers in natural bogs. *Mires & Peat*, *18*(4), 1–16.

Küttim, M., Küttim, L., Ilomets, M., & Laine, A. M. (2020). Controls of *Sphagnum* growth and the role of winter. *Ecological Research*, *35*(1), 219-234.

Libby, L. M., Pandolfi, L. J., Payton, P. H., Marshall, J., Becker, B., & Giertz-Sienbenlist, V. (1976). Isotopic tree thermometers. *Nature*, *261*(5558), 284–288.

Lin, Q., Hong, Y., Zhu, Y., Dong, L., Wang, Y., Leng, X., & Li, H. (2001). The carbon and oxygen isotope composition of modern plants from typical peat bogs in China and its significance on the palaeoclimatic study. *Bulletin of Mineralogy, Petrology and Geochemistry*, *20*(2), 93–97. In Chinese with English abstract.

Lindholm, T. (1990). Growth dynamics of the peat moss *Sphagnum fuscum* on hummocks on a raised bog in southern Finland. *Annales Botanici Fennici*, *27*(1), 67–78.

Liu, J. (2017). The oxygen isotope composition of modern plants in Dajiuhu peat bog and its climate significance (Master's thesis). Nanjing, China: Nanjing Normal University.

Liu, Z., Zhu, J., Rosenthal, Y., Zhang, X., Otto-Bliesner, B. L., Timmermann, A., et al. (2014). The Holocene temperature conundrum. *Proceedings of the National Academy of Sciences*, *111*(34), E3501–E3505.

Loader, N. J., Street-Perrott, F. A., Mauquoy, D., Roland, T. P., van Bellen, S., Daley, T. J., et al. (2016). Measurements of hydrogen, oxygen and carbon isotope variability in *Sphagnum* moss along a micro-topographical gradient in a southern Patagonian peatland. *Journal of Quaternary Science*, *31*(4), 426–435.

Loisel, J., Garneau, M., & Hélie, J. F. (2009). Modern *Sphagnum* $\delta^{13}C$ signatures follow a surface moisture gradient in two boreal peat bogs, James Bay lowlands, Québec. *Journal of Quaternary Science*, *24*(3), 209–214.

Loisel, J., Gallego-Sala, A. V., & Yu, Z. (2012). Global-scale pattern of peatland *Sphagnum* growth driven by photosynthetically active radiation and growing season length. *Biogeosciences*, *9*(7), 2737–2746.

Loisel, J., & Yu, Z. (2013). Surface vegetation patterning controls carbon accumulation in peatlands. *Geophysical Research Letters*, *40*(20), 5508–5513.

Managave, S. R., Sheshshayee, M. S., Borgaonkar, H. P., & Ramesh, R. (2010). Past break-monsoon conditions detectable by high resolution intra-annual $\delta^{18}O$ analysis of teak rings. *Geophysical Research Letters*, *37*, L05702.

McCarter, C. P. R., & Price, J. S. (2014). Ecohydrology of *Sphagnum* moss hummocks: mechanisms of capitula water supply and simulated effects of evaporation. *Ecohydrology*, *7*(1), 33–44.

Ménot-Combes, G., Burns, S. J., & Leuenberger, M. (2002). Variations of $^{18}O/^{16}O$ in plants from temperate peat bogs (Switzerland): implications for paleoclimatic studies. *Earth and Planetary Science Letters*, *202*(2), 419–434.

Mora, G., & Zanazzi, A. (2017). Hydrogen isotope ratios of moss cellulose and source water in wetlands of Lake Superior, United States reveal their potential for quantitative paleoclimatic reconstructions. *Chemical Geology*, *468*, 75–83.

Moschen, R., Kühl, N., Rehberger, I., & Lücke, A. (2009). Stable carbon and oxygen isotopes in sub-fossil *Sphagnum*: Assessment of their applicability for palaeoclimatology. *Chemical Geology*, *259*(3), 262–272.

Murray, K. J., Harley, P. C., Beyers, J., Walz, H., & Tenhunen, J. D. (1989). Water content effects on photosynthetic response of *Sphagnum* mosses from the foothills of the Philip Smith Mountains, Alaska. *Oecologia*, *79*(2), 244–250.

Okazaki, A., & Yoshimura, K. (2019). Global evaluation of proxy system models for stable water isotopes with realistic atmospheric forcing. *Journal of Geophysical Research: Atmospheres*, *124*(16), 8972–8993.

Price, J. S., Edwards, T. W. D., Yi, Y., & Whittington, P. N. (2009). Physical and isotopic characterization of evaporation from *Sphagnum* moss. *Journal of Hydrology*, *369*(1), 175–182.

Richter, S. L., Johnson, A. H., Dranoff, M. M., & Taylor, K. D. (2008). Continental-scale patterns in modern wood cellulose $\delta^{18}O$: Implications for interpreting paleo-wood cellulose $\delta^{18}O$. *Geochimica et Cosmochimica Acta*, *72*(12), 2735–2743.

Risi, C., Noone, D., Worden, J., Frankenberg, C., Stiller, G., Kiefer, M., et al. (2012). Process-evaluation of tropospheric humidity simulated by general circulation models using water vapor isotopologues: 1. Comparison between models and observations. *Journal of Geophysical Research: Atmospheres*, *117*, D05303.

Roden, J. S., Lin, G., & Ehleringer, J. R. (2000). A mechanistic model for interpretation of hydrogen and oxygen isotope ratios in tree-ring cellulose. *Geochimica et Cosmochimica Acta*, *64*(1), 21–35.

Roden, J. S., & Ehleringer, J. R. (2000). There is no temperature dependence of net biochemical fractionation of hydrogen and oxygen isotopes in tree-ring cellulose. *Isotopes in Environmental and Health Studies*, *36*(3), 303–317.

Royles, J., Sime, L. C., Hodgson, D. A., Convey, P., & Griffiths, H. (2013). Differing source water inputs, moderated by evaporative enrichment, determine the contrasting $\delta^{18}O_{CELLULOSE}$ signals in maritime Antarctic moss peat banks. *Journal of Geophysical Research: Biogeosciences*, *118*(1), 184–194.

Royles, J., Amesbury, M. J., Roland, T. P., Jones, G. D., Convey, P., Griffiths, H., et al. (2016). Moss stable isotopes (carbon-13, oxygen-18) and testate amoebae reflect environmental inputs and microclimate along a latitudinal gradient on the Antarctic Peninsula. *Oecologia*, *181*(3), 931–945.

Rydin, H., & Jeglum, J. K. (2013). *The Biology of Peatlands.* (2nd ed.). Oxford, UK: Oxford University Press.

Sargeant, C. I., & Singer, M. B. (2016). Sub-annual variability in historical water source use by Mediterranean riparian trees. *Ecohydrology*, *9*(7), 1328–1345.

Schubert, B. A., & Jahren, A. H. (2015). Seasonal temperature and precipitation recorded in the intra-annual oxygen isotope pattern of meteoric water and tree-ring cellulose. *Quaternary Science Reviews*, *125*, 1–14.

Song, X., Barbour, M. M., Saurer, M., & Helliker, B. R. (2011). Examining the large-scale convergence of photosynthesis-weighted tree leaf temperatures through stable oxygen isotope analysis of multiple data sets. *New Phytologist*, *192*(4), 912–924.

Song, X., Clark, K. S., & Helliker, B. R. (2014a). Interpreting species-specific variation in tree-ring oxygen isotope ratios among three temperate forest trees. *Plant, Cell & Environment*, *37*(9), 2169–2182.

Song, X., Farquhar, G. D., Gessler, A., & Barbour, M. M. (2014b). Turnover time of the non-structural carbohydrate pool influences $\delta^{18}O$ of leaf cellulose. *Plant, Cell & Environment*, *37*(11), 2500–2507.

Sternberg, L., & Ellsworth, P. F. V. (2011). Divergent biochemical fractionation, not convergent temperature, explains cellulose oxygen isotope enrichment across latitudes. *PLOS ONE*, *6*(11), e28040.

Sternberg, L. D. S. L., Deniro, M. J., & Savidge, R. A. (1986). Oxygen isotope exchange between metabolites and water during biochemical reactions leading to cellulose synthesis. *Plant Physiology*, *82*(2), 423–427.

Sternberg, L. d. S. L. O. R., & DeNiro, M. J. D. (1983). Biogeochemical implications of the isotopic equilibrium fractionation factor between the oxygen atoms of acetone and water. *Geochimica et Cosmochimica Acta*, *47*(12), 2271–2274.

Sternberg, L. S. L. (2009). Oxygen stable isotope ratios of tree-ring cellulose: the next phase of understanding. *New Phytologist*, *181*(3), 553–562.

Taylor, M. (2008). Continental-scale validation of the temperature signal in oxygen isotopes of *Sphagnum* cellulose and its application as a paleoclimate proxy (Master's thesis). Retrieved from ProQuest. (https://search.proquest.com/docview/304464820). Laramie, WY: University of Wyoming.

Treydte, K. S., Schleser, G. H., Helle, G., Frank, D. C., Winiger, M., Haug, G. H., & Esper, J. (2006). The twentieth century was the wettest period in northern Pakistan over the past millennium. *Nature*, *440*(7088), 1179–1182.

Turetsky, M. R., Crow, S. E., Evans, R. J., Vitt, D. H., & Wieder, R. K. (2008). Trade-offs in resource allocation among moss species control decomposition in boreal peatlands. *Journal of Ecology*, *96*(6), 1297–1305.

Tuthorn, M., Zech, M., Ruppenthal, M., Oelmann, Y., Kahmen, A., Valle, H. F. d., et al. (2014). Oxygen isotope ratios ($^{18}O/^{16}O$) of hemicellulose-derived sugar biomarkers in plants, soils and sediments as paleoclimate proxy II: Insight from a climate transect study. *Geochimica et Cosmochimica Acta*, *126*, 624–634.

Waterhouse, J. S., Cheng, S., Juchelka, D., Loader, N. J., McCarroll, D., Switsur, V. R., & Gautam, L. (2013). Position-specific measurement of oxygen isotope ratios in cellulose: Isotopic exchange during heterotrophic cellulose synthesis. *Geochimica et Cosmochimica Acta*, *112*, 178–191.

Yakir, D., & DeNiro, M. J. (1990). Oxygen and hydrogen isotope fractionation during cellulose metabolism in *Lemna gibba* L. *Plant Physiology*, *93*(1), 325–332.

Yu, Z., Loisel, J., Brosseau, D. P., Beilman, D. W., & Hunt, S. J. (2010). Global peatland dynamics since the Last Glacial Maximum. *Geophysical Research Letters, 37*, L13402.

Zanazzi, A., & Mora, G. (2005). Paleoclimatic implications of the relationship between oxygen isotope ratios of moss cellulose and source water in wetlands of Lake Superior. *Chemical Geology*, *222*(3), 281–291.

Zech, M., Mayr, C., Tuthorn, M., Leiber-Sauheitl, K., & Glaser, B. (2014). Oxygen isotope ratios ($^{18}O/^{16}O$) of hemicellulose-derived sugar biomarkers in plants, soils and sediments as paleoclimate proxy I: Insight from a climate chamber experiment. *Geochimica et Cosmochimica Acta*, *126*, 614–623.

Zeng, X., Liu, X., Evans, M. N., Wang, W., An, W., Xu, G., & Wu, G. (2016). Seasonal incursion of Indian Monsoon humidity and precipitation into the southeastern Qinghai–Tibetan Plateau inferred from tree ring $\delta^{18}O$ values with intra-seasonal resolution. *Earth and Planetary Science Letters*, *443*, 9–19.

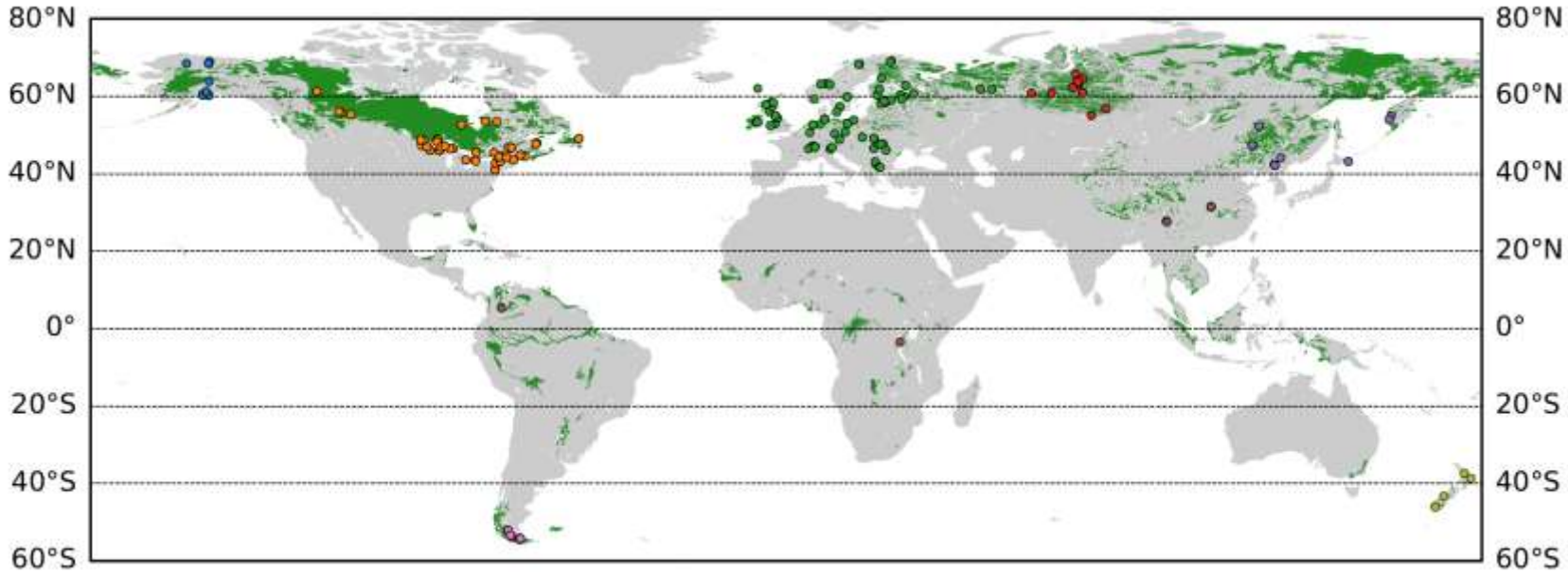
80°N
60°N
40°N
20°N
0°
20°S
40°S
60°S
80°N
60°N
40°N
20°N
0°
20°S
40°S
60°S

Figure 3.1 (previous page). Global map of peatland regions (green areas; Yu et al., 2010) and sites with *Sphagnum* $\delta^{18}O_c$ data presented in this study. Sites are color-coded to represent different regions: Alaska (blue), Canada and Contiguous US (orange), Europe (green), New Zealand (yellow), Patagonia (pink), Temperate East Asia (purple), Tropics and Subtropics (brown), and West Siberia (red).

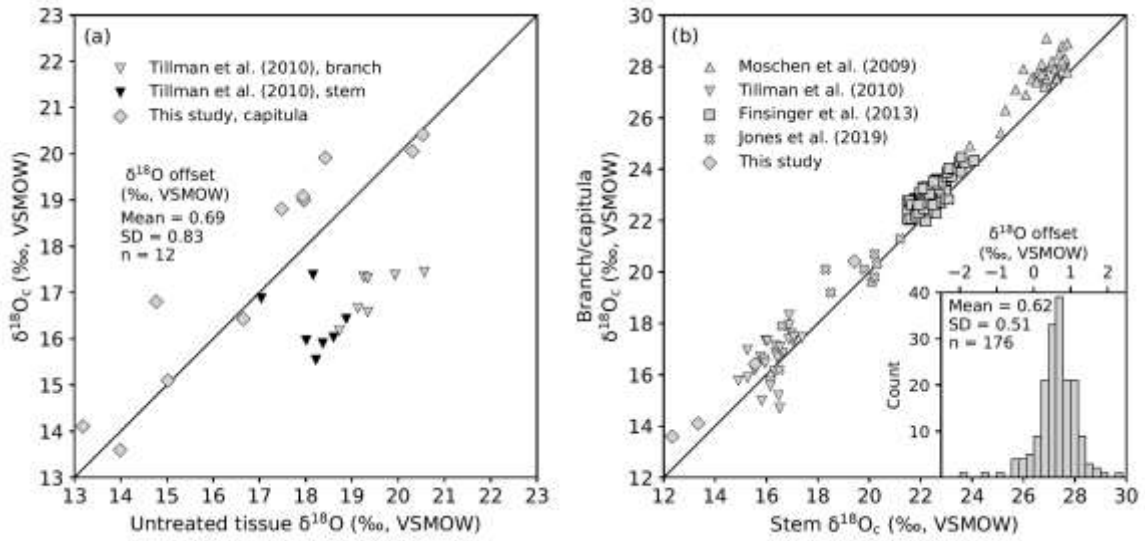

Figure 3.2. Oxygen isotope offset between different *Sphagnum* materials. (a) Biplot showing the relationship between $\delta^{18}O_c$ and untreated bulk tissue $\delta^{18}O$. Data reported from Kaislahti Tillman et al. (2010) were derived from subfossil *Sphagnum* branches or stems in peat and are plotted below the 1:1 line, indicating that $\delta^{18}Oc$ are lower than untreated bulk tissue $\delta^{18}O$ in peat. Data from this study were derived from fresh capitula material and are plotted above the 1:1 line, indicating that $\delta^{18}Oc$ are higher than untreated fresh capitula $\delta^{18}O$. (b) Biplot showing the relationship between branch/capitula $\delta^{18}O_c$ and corresponding stem $\delta^{18}O_c$. Data reported from Moschen et al. (2009), Kaislahti Tillman et al. (2010), and Finsinger et al. (2013), were derived from subfossil *Sphagnum* branches or stems in peat, while data from Jones et al. (2019) and this study were derived from fresh plants. The results tend to show that branch or capitula $\delta^{18}O_c$ are higher than stem $\delta^{18}O_c$ and the offset (branch/capitula $\delta^{18}O_c$ minus stem $\delta^{18}O_c$) resembles a Gaussian distribution as shown in the inset histogram.

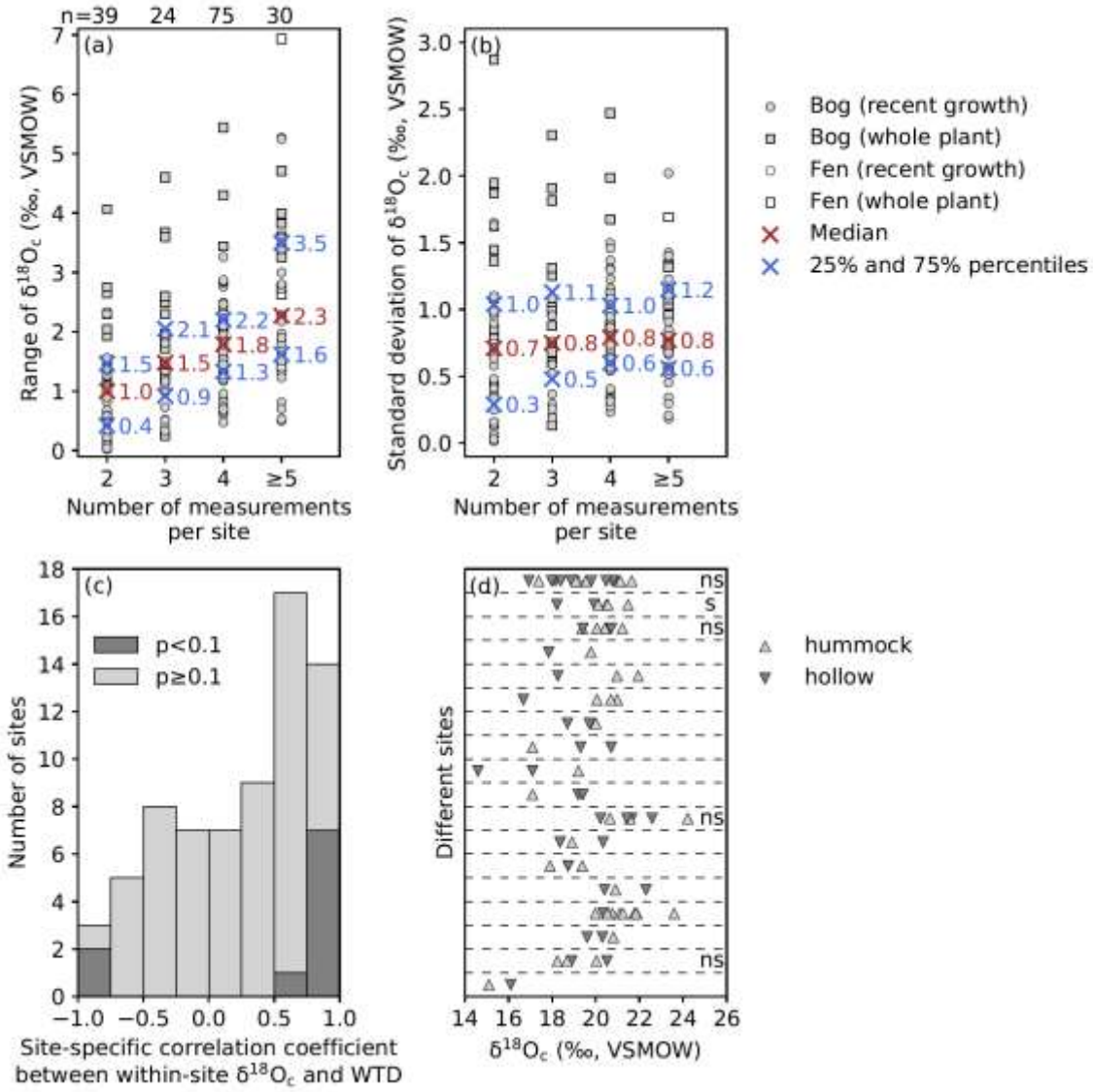

Figure 3.3. Within-site variability of *Sphagnum* $\delta^{18}O_c$ data. (a) Range of within-site $\delta^{18}O_c$ data. (b) Standard deviation of within-site $\delta^{18}O_c$ data for each site. In both (a) and (b), results are separated for the number of measurements per site. Individual site data are separated for bogs and fens and for recent growth and whole plant parts. Also shown are median and lower/upper quartile values of the range and the standard deviation as cross symbols. The numbers of sites are indicated on top of plot in (a). (c) Histogram of site-specific correlation coefficient between within-site $\delta^{18}O_c$ and WTD data from studies by Loader et al. (2016), Granath et al. (2018), and Jones et al. (2019) in which WTD

measurements are available. The significant correlations with *p*-value lower than 0.1 are shown as dark gray color. Positive correlation indicates that high $\delta^{18}O_c$ correspond with deep WTD. (d) Within-site $\delta^{18}O_c$ data from studies by Taylor (2008) and Brader (2013), plus a site from this study, in which samples were collected at microtopographical locations of hummock and hollow. Data from different sites are separated by horizontal lines. The "ns" and "s" denote "not significant" and "significant (if *p*-value is lower than 0.1)" difference between hummock and hollow $\delta^{18}O_c$ data determined by Student's t-test if there are at least two data points for either hummock or hollow.

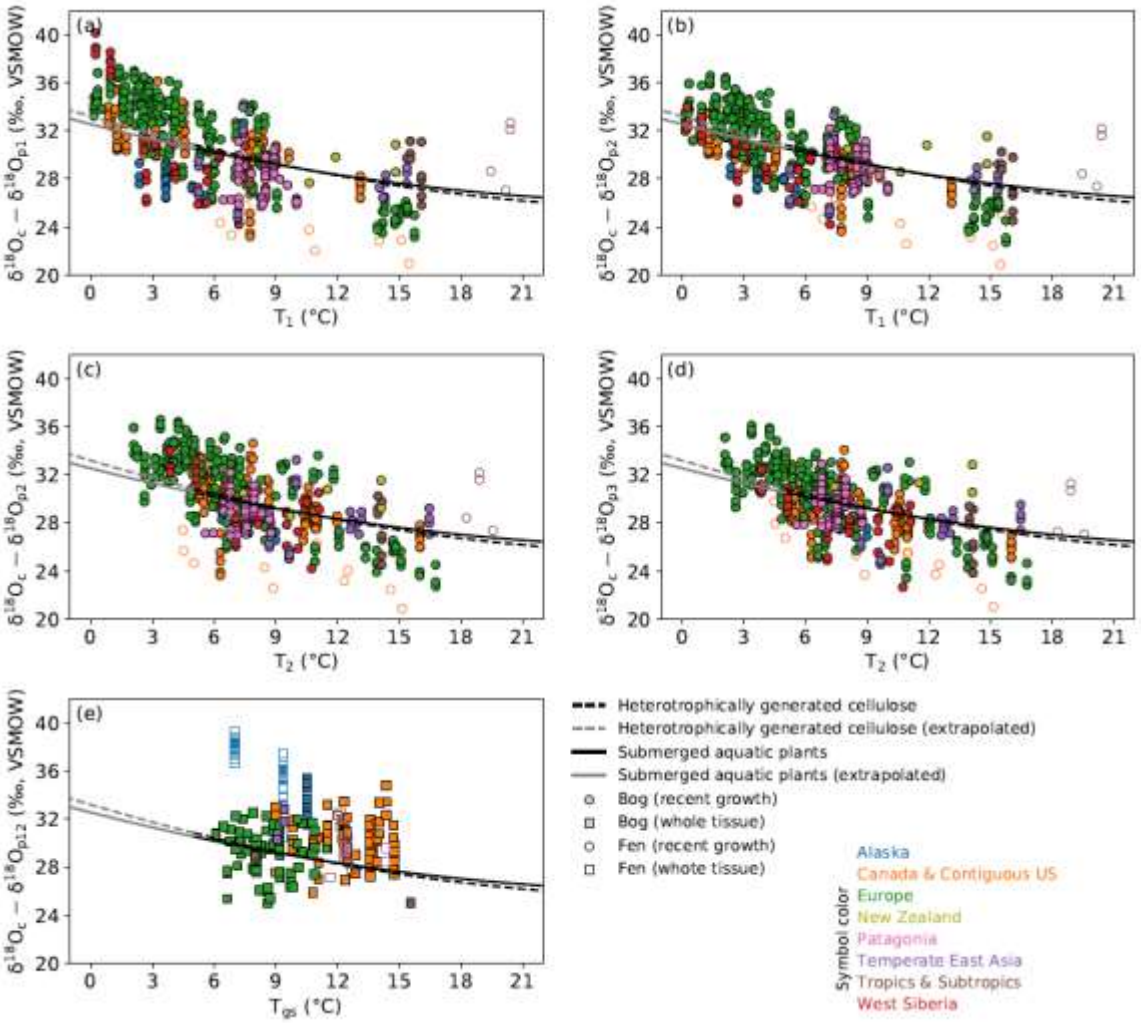

Figure 3.4. The biplots between ε_{app} and temperature for all *Sphagnum* $\delta^{18}O_c$ data. For the recent-growth parts of *Sphagnum*, data are plotted using the pair of (a) $\delta^{18}O_{p1}$ and T_1, (b) $\delta^{18}O_{p2}$ and T_1, (c) $\delta^{18}O_{p2}$ and T_2, and (d) $\delta^{18}O_{p3}$ and T_2. For the whole plant parts of *Sphagnum*, data are plotted using the pair of $\delta^{18}O_{12}$ and T_{gs}. Data are color-coded to represent different regions as shown in Figure 3.1 and are separated for bogs and fens. Also shown are the second order polynomial regressions fitted by data from heterotrophic generation of cellulose and data from submerged aquatic plants by Sternberg and Ellsworth (2011) and their extrapolations.

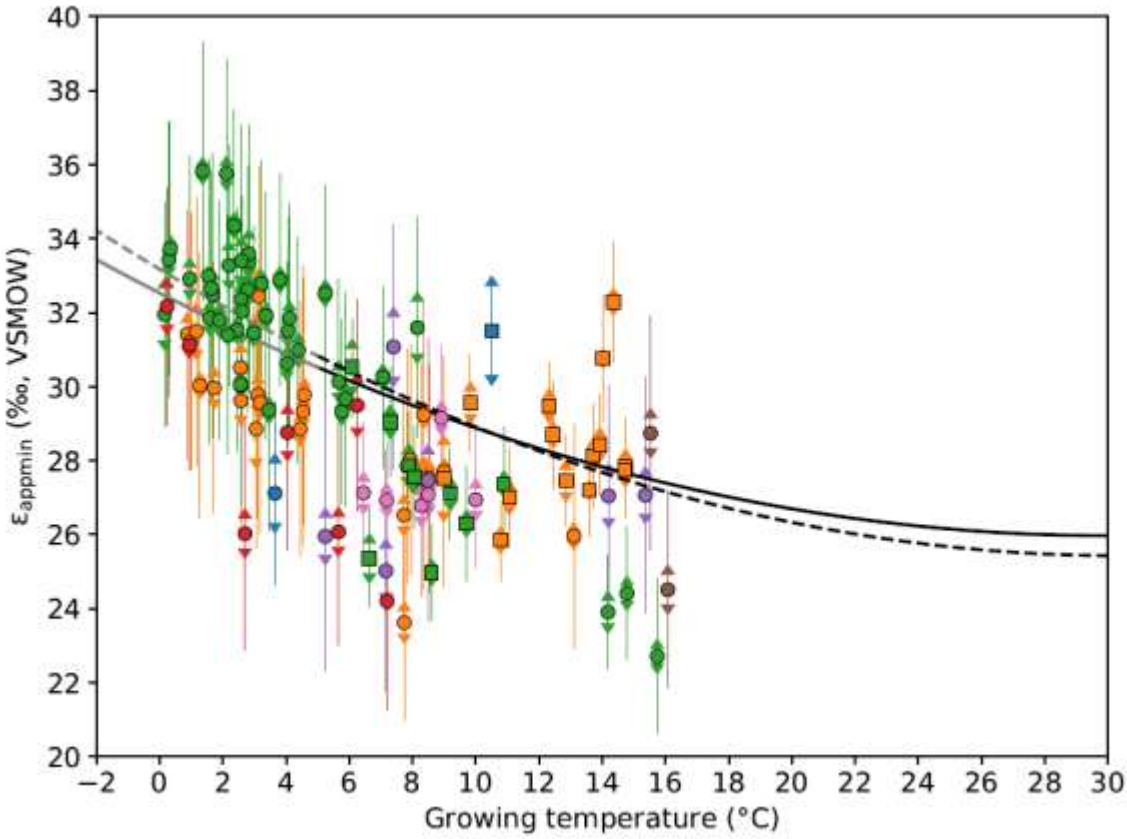

Figure 3.5. The biplot between ε_{appmin} and the most relevant growing temperature for sites with at least three collected samples and measurements. Data are color-coded to represent different regions as shown in Figure 3.1. The 95% prediction interval of OPIC-based mean annual $\delta^{18}O_p$ at each sampling location is shown as error bar with arrow caps. The precision (2σ) of ε_{appmin} is denoted as error bar without caps. Also shown are the second order polynomial regressions given by Sternberg and Ellsworth (2011) and their extrapolations. Note that the full range of temperature in laboratory experiments by Sternberg and Ellsworth (2011) is shown to illustrate that the sensitivity of ε_{app} to temperature is very weak if the temperature is high.

Table 3.1. Summary information about the compiled *Sphagnum* $\delta^{18}O$ data.

References	Region[a]	Habitat[b]	Analyzed material[c]	Number of sites	Number of data	Sampling year and month[d]
This study	AK, CCUS, TST, TEA, and PAT	B and F	RG and WP	15	72	A
Aravena and Warner (1992)	CCUS	B	WP	3	13	A
Aucour et al. (1996)	TST	B	WP	1	1	A
Amesbury et al. (2015)	NZ	B	RG	4	5	A
Brader (2013)	EU	B	WP	16	31	NA
Brenninkmeijer et al. (1982)	EU	B	WP	1	4	NA
Daley (2007) and Daley et al. (2010)	CCUS and EU	B	RG	4	78	A
Granath et al. (2018)	AK, CCUS, EU, TEA, and WS	B	RG	92	335	A
Hong et al. (2009)	TEA	F	WP	1	3	NA
Jones et al. (2019)	AK	F	WP	2	31	A
Lin et al. (2001)	TEA	F	WP	2	5	NA
Loader et al. (2016)	PAT	B	RG	1	16	A
Liu (2017)	TST	F	WP	1	11	A
Ménot-Combes et al. (2002)	WEU	B	WP	13	38	A
Taylor (2008)	AK and CCUS	B	WP	17	83	A
Chapter 2	PAT	B	RG	7	47	A
Zanazzi and Mora (2005) and Mora and Zanazzi (2017)	CCUS	F	RG	3	12	A

[a]Region includes Alaska (AK), Patagonia (PAT), Europe (EU), New Zealand (NZ), Temperate East Asia (TEA), Tropics and Subtropics (TST), Canada and Contiguous US (CCUS), and West Siberia (WS).
[b]Habitat includes bogs (B) and fens (F).
[c]Analyzed material includes recent growth (RG) and whole plant (WP) parts of *Sphagnum*.
[d]Sampling time is available (A) or not available (NA).

Appendix C: Supporting information for Chapter 3

Data Set C1

The compiled dataset and metadata are archived on:
https://github.com/zhx215/global-peat-moss-d18O

Text C1

1. Cellulose extraction method

The method of cellulose extraction followed the alkaline bleaching method (Kaislahti Tillman et al., 2010). In our previous study, we extracted cellulose from *Sphagnum* stems. In this study, we mainly extracted cellulose from *Sphagnum* capitula. For each individual sample, capitula from at least five *Sphagnum* shoots were harvested and homogenized using an ultrasonic probe. The homogenized capitula materials were then transferred to disposable polypropylene columns (Poly-Prep). Samples were subjected to 5 rounds of 1.4% (w/v) sodium chlorite bleaching acidified with glacial acetic acid in a hot water bath at 80°C, each round for 50 min. Then, they were reacted with 10% (w/v) sodium hydroxide at 75°C for 45 min and another 2 rounds of acidified sodium chlorite bleaching. The yielded α-cellulose was rinsed with distilled deionized water and transferred to small vials. Afterwards, samples were homogenized using an ultrasonic probe and freeze-dried.

2. Isotope analysis

For oxygen isotope analysis, ~0.4 mg cellulose materials were enclosed in silver capsules. Oxygen isotope compositions were determined on an Elementar PyroCube interfaced to an Isoprime VisION isotope-ratio mass spectrometer (IRMS), at the Stable Isotope Facility (SIF) of University of California, Davis. By convention, results of

isotope ratio measurements were reported as δ notation (in per mille) referenced to VSMOW (Vienna Standard Mean Ocean Water). During analysis, samples were interspersed with replicates of established calibration standards and several check standards with known isotopic compositions. The check standards were used to monitor the analytical drift and size effect and corrections were applied when necessary to ensure analytical accuracy for sample measurements. The precision (1σ) of measurements was about 0.3‰ for $\delta^{18}O$.

References for Appendix C:

Kaislahti Tillman, P., Holzkämper, S., Kuhry, P., Sannel, A. B. K., Loader, N. J., & Robertson, I. (2010). Stable carbon and oxygen isotopes in *Sphagnum fuscum* peat from subarctic Canada: Implications for palaeoclimate studies. *Chemical Geology*, *270*(1), 216–226.

CHAPTER 4

Centennial-scale dynamics of the Southern Hemisphere westerly winds across the Drake Passage over the past two millennia

Zhengyu Xia[1], Zicheng Yu[1,2], and Julie Loisel[3]

[1]Department of Earth and Environmental Sciences, Lehigh University, Bethlehem, Pennsylvania 18015, USA

[2]School of Geographical Sciences, Northeast Normal University, Changchun 130024, China

[3]Department of Geography, Texas A&M University, College Station, Texas 77843, USA

Abstract

The Southern Hemisphere Westerly Winds (SHWW) exert important controls on regional and global climates. Instrumental and reanalysis records indicated strengthening and poleward contraction of the SHWW belt since the late twentieth century. Such changes also have implications for Southern Ocean upwelling and CO_2 degassing. Therefore, a better understanding of the long-term SHWW behaviors and dynamics beyond recent decades is critical for projecting future changes. Here we apply isotope analysis of *Sphagnum* moss cellulose from a peat bog in southernmost Patagonia (~54° S) to reconstruct changes in oxygen isotope composition of precipitation ($\delta^{18}O_p$) that could elucidate past shifts in moisture sources and trajectories. We interpret that positive shifts in $\delta^{18}O_p$ indicate weaker SHWW and importantly more frequent easterly flows that enhance moisture supply sourced from the Atlantic Ocean. In contrast, negative shifts in $\delta^{18}O_p$ indicate stronger SHWW and intensification of the Andean rain shadow. Our data, along with other evidence from southernmost Patagonia and the Antarctic Peninsula, suggest a coherent pattern of centennial-scale variability in SHWW strength on either side of the Drake Passage over the past two millennia, probably as a teleconnection response to El Niño–Southern Oscillation-like variability. Our study implies that investigating past changes in the SHWW and their teleconnection mechanisms should consider synoptic-scale atmospheric circulation patterns, rather than seeing SHWW as a simplistic west-to-east (zonal) wind flow pattern, particularly on the timescales when the SHWW express zonal asymmetry among different sectors of the Southern Ocean.

4.1. Introduction

The lack of extensive landmass in Southern Hemisphere (SH) mid-latitudes allows for development of the strong Southern Hemisphere Westerly Winds (SHWW) that are important components of the global ocean-atmosphere coupled system. Their strength and latitudinal position are largely controlled by the Southern Annular Mode (SAM)—a dominant pattern of SH extratropical climate variability—defined as the gradient of zonal mean sea level pressure (SLP) between 40° S and 65° S (Marshall, 2003). The observed late-twentieth-century positive shift in the SAM as well as the strengthening and poleward contraction of the SHWW have influenced temperature and precipitation distribution in the SH extratropics (Gillett et al., 2006; Villalba et al., 2014). This recent shift has been attributed to ozone depletion and rising greenhouse gas concentrations, both of which are anthropogenic in origin (Abram et al., 2014). However, long-term natural variability and dynamics of the SHWW are still poorly understood.

Several studies have suggested that pronounced and zonally symmetric changes in SHWW strength and/or position over millennial timescales regulated atmospheric CO_2 concentration, including its rise during the last deglaciation (Fletcher & Moreno, 2012; Mayr et al., 2013). However, there is a lack of agreement as to variability and dynamics of the SHWW during the Holocene (Lamy et al., 2010; Moreno et al., 2010), particularly since the mid-Holocene when modern ENSO regime was established (Fletcher & Moreno, 2012; Mariani et al., 2017). This uncertainty impedes our understanding of the drivers of SHWW variability and their teleconnection mechanisms. Hence, it is essential to develop continuous paleoclimate records in SHWW-influenced region with robust chronology and reliable proxy interpretations. This study focuses on centennial-scale SHWW variability in southernmost Patagonia over the past two millennia by developing a new high-resolution, radiocarbon-dated peat record.

4.2. Westerly vs. easterly winds in Patagonia

Southern Patagonia is the only continental landmass within the SHWW core belt (~50°–55° S). The Patagonian Andes lies perpendicular to the prevailing westerly winds and constitutes an orographic divide with a dramatic decrease in precipitation from the Pacific to the Atlantic coast (Figure 4.1B). This mountain chain creates tight coupling between wind speed and hydrology, with stronger westerly wind inducing more precipitation on the windward side, but less precipitation (rain shadow) and more evaporative condition on the leeward side (Garreaud et al., 2013). Recent studies have suggested that the easterly wind flows, despite being less frequent in this region, tend to cause intense rainfall events fed by moisture from the Atlantic Ocean, which is an additional source of precipitation for eastern side of Patagonia (Schneider et al., 2003; Mayr et al., 2007a; Agosta et al., 2015; Quade & Kaplan, 2017). Backward trajectory analysis of present-day air parcels indeed shows two dominant air parcel transport pathways: one from the westerly winds, and the other with a (north)easterly origin (Figure 4.1A). If the easterly wind frequency and the proportion of Atlantic-sourced moisture were greater when the SHWW were blocked/weaker, the westerly-caused rain shadow effect operating today would be reduced, thus it would be wetter on the eastern side of Andean climate divide (Mayr et al., 2007a).

The contribution of easterly wind moisture in the past can be traced using water isotopes. The easterly wind flows experience less upstream orographic and rainout effects than the westerly wind flows (Stern & Blisniuk, 2002; Daley et al., 2012). This results in their much higher values of oxygen isotope ratio in precipitation ($\delta^{18}O_p$) as indicated by an event-based rainfall isotope study at ~52° S of Argentinian Patagonia (RG and study site “d” in Figure 4.1B) that showed a ~7‰ difference between westerly and easterly signatures (Mayr et al., 2007b).

Here we used paired measurements of oxygen and carbon isotopes from *Sphagnum* (peat moss) cellulose along a peat core in southernmost Patagonia as proxies to trace the atmospheric circulation and hydroclimate changes, respectively. This peatland site is closer to the Atlantic coast, thus more sensitive to easterly flows that bring in Atlantic moisture, than other sites near the Andes (Figure 4.1B). The physiological simplicity of *Sphagnum* mosses, which exclusively use meteoric water for photosynthesis, makes the oxygen isotope composition of their cellulose ($\delta^{18}O_{cell}$) document growing-season (mainly during summer) $\delta^{18}O_p$ by a biochemical enrichment factor of ca. +27‰ (Daley et al., 2010).

4.3. Material and methods

Sphagnum-dominated peat bogs in southernmost Patagonia are mostly found on the leeward side of the Andes within the cool-temperate deciduous and evergreen forest ecoregion. These ecosystems are characterized by simple plant communities, with *Sphagnum magellanicum* covering the entire ground layers (Loisel & Yu, 2013a). Our study site, Ariel Peatland (AP, ~54.2° S; Figure 4.1B), is located in the Isla Grande of Tierra del Fuego. The region has a mean annual precipitation of ~480 mm that is uniformly distributed through all seasons. The bog surface today is flat without apparent hummock-hollow patterning, and the center is dominated by pure carpets of *S. magellanicum*, with *S. cuspidatum* and *Drepanocladus* spp. (brown moss) occasionally occupying small inundated hollows (Figure D1). Other bog plants are mainly herbaceous (sedges, rushes, and grasses) or ligneous shrubs, and are mostly found along the edge of the bog. A 205-cm peat core (PAT16-AP1) was retrieved at the center of the bog in January 2016.

Sphagnum macrofossil remains were used for AMS ^{14}C dating, and age-depth modeling was performed using Bacon program (Figure D2 and Table D1). Plant

macrofossils were analyzed at every centimeter to characterize changes in peat botanical composition over time (Loisel & Yu, 2013b). For the top 109-cm section (representing past two millennia), we picked well-preserved *Sphagnum* macrofossil stem fragments (at least 30 pieces from each sample), removed branches and leaves, and extracted cellulose following the alkaline bleaching method (Daley et al., 2010). The purified cellulose samples were measured for oxygen isotope composition on an Elementar PyroCube interfaced to an Isoprime VisION isotope-ratio mass spectrometer (IRMS), and for carbon isotope composition using a PDZ Europa ANCA-GSL elemental analyzer interfaced to a PDZ Europa 20–20 IRMS, both at the Stable Isotope Facility of University of California, Davis. The laboratory analytical precision is 0.3‰ for $\delta^{18}O$ and 0.2‰ for $\delta^{13}C$.

4.4. Isotope evidence for atmospheric circulation and hydroclimate changes

Our $\delta^{18}O_{cell}$ record shows several centennial-scale shifts with an average amplitude of ~2.5‰ over the past two millennia (Figure 4.2A). Evaporative enrichment of moss leaf water prior to cellulose biosynthesis is an additional factor influencing $\delta^{18}O_{cell}$. Although previous studies showed that evaporation effect is minimal in some peat bogs (Daley et al., 2010), our modern process study suggests that this effect is considerable, which contributes an offset of 1–4‰ between $\delta^{18}O_{cell}$ and $\delta^{18}O_p$ (Figure D4; also see Loader et al., 2016), probably due to windy conditions. However, changes in the extent of evaporative enrichment in moss leaf water are unlikely to explain the observed variations of $\delta^{18}O_{cell}$ over time. We use cellulose carbon isotope composition ($\delta^{13}C_{cell}$) that have been corrected for the Suess effect (Leuenberger, 2007) to constrain the growth conditions of *Sphagnum*, with lower $\delta^{13}C_{cell}$ values indicating more discrimination against atmospheric $^{13}CO_2$ due to a thinner water film, and thus drier and/or more evaporative environment, and vice versa (Rice & Giles, 1996). The results show that

down-core $\delta^{18}O_{cell}$ and $\delta^{13}C_{cell}$ data have a positive correlation ($r = 0.43$, $p < 0.001$ for 20-year resampled time series; Figure 4.2A), inconsistent with the effect of evaporation that should have resulted in negative correlation as found in our modern process study (Figures D4 and D5). This observation, however, does not exclude the influence of evaporative enrichment on $\delta^{18}O_{cell}$ values, but suggests that it is not the primary cause for the observed $\delta^{18}O_{cell}$ shifts over time. Instead, we propose that $\delta^{18}O_{cell}$ preserve the signal of $\delta^{18}O_p$ in this region.

Daley et al. (2012) showed that monthly $\delta^{18}O_p$ values in southernmost Patagonia are neither correlated with temperature nor precipitation amount. Again, it implies that moisture sources and trajectories are important in influencing $\delta^{18}O_p$ in this region with unique development of isotopic rain shadow (Stern & Blisniuk, 2002). This interpretation is supported by the observation that $\delta^{18}O_{cell}$ record shows negative correlation with SAM index reconstruction over the last millennium ($r = -0.36$, $p < 0.01$ for 20-year resampled time series; Figures 4.3B and 4.3C; Abram et al., 2014). In summary, the $\delta^{18}O_{cell}$ record documents changes in growing-season $\delta^{18}O_p$, reflecting centennial-scale shifts in the relative strength between westerly and easterly winds as well as the relative contribution between Pacific- and Atlantic-sourced moisture. Without a conspicuous long-term trend, our record shows shifts to weaker SHWW with more frequent easterly flows during A.D 180–420, 660–810, 900–1020, 1390–1670, and 1840–1970, and shifts to stronger SHWW with less frequent easterly flows during A.D. 100–180, 420–660, 810–900, 1020–1390, and 1670–1840. The negative shift in $\delta^{18}O_{cell}$ at A.D. 1970 further demonstrates the sensitivity of our proxy to the observed recent atmospheric circulation change (Figure D7).

The positive correlation between peat-core $\delta^{18}O_{cell}$ and $\delta^{13}C_{cell}$ data indicates a connection between atmospheric circulation and hydroclimate on the eastern side of the Andes in southernmost Patagonia. The $\delta^{13}C_{cell}$ record supports that wetter habitats

occurred during the periods of weaker SHWW, and vice versa due to the rain shadow effect (Figure 4.2A). Macrofossil data similarly show that *Sphagnum* were largely replaced by dry-adapted vascular plants when the SHWW were stronger and became dominant when the easterly flows were more frequent (Figures 4.2B and D3). While we acknowledge that the interpretations can be confounded by localized ecohydrological feedbacks through internal regulations of hydrological condition and vegetation communities (Loisel & Yu, 2013b), the bog surface moisture signals recorded at our site seem to be primarily controlled by regional atmospheric circulation patterns.

4.5. SHWW variability across the Drake Passage

Paleoclimate studies from the rain shadow area of southernmost Patagonia are in general agreement with our interpretation of centennial-scale SHWW variability in strength. For example, the carbonate $\delta^{18}O$ record of closed-basin Lago Guanaco, which reflects the extent of wind-driven evaporative enrichment, shows periods of stronger SHWW centered at A.D. 1250 and 1700 and weaker SHWW centered at A.D. 950, 1450 and 1850 (Figure 4.3F; Moy et al., 2008). Likewise, a paleoecological record of forest cover fragmentations from Lago Cipreses shows recurrent centennial-scale positive SAM-like dry/warm intervals; the recorded shifts at LC have similar timing as the ones in our record, with the exception of the A.D. 1670–1840 interval, which is absent from the Lago Cipreses record (Figure 4.3G; Moreno et al., 2014). Desiccated wetland-remains at the Catalon Marsh dated back to A.D. 1050–1300 were interpreted to reflect a period of enhanced rain shadow effect caused by strengthening of the SHWW during the "medieval time" (Figure 4.3E; Stine, 1994). Furthermore, our $\delta^{18}O_{cell}$ record of SHWW variability shows an in-phase relationship with James Ross Island ice-core δD record from the Antarctic Peninsula on centennial scale (Figure 4.3A; Mulvaney et al., 2012)—a record also used in SAM index reconstruction over the last millennium (Abram et al., 2014)—

but importantly the relationship is persistent even before the last millennium. Together these records demonstrate a coherent pattern of centennial-scale variability in SHWW strength on either side of the Drake Passage during the late-Holocene with large magnitudes comparable with the recent anthropogenic shift.

Our analysis reveals a vigorous and pronounced variability in SHWW strength on centennial-scale, while last millennium climate simulations driven by radiative forcing showed muted SAM variability before anthropogenic period (Abram et al., 2014). This contrast implies the importance of a teleconnection response to El Niño–Southern Oscillation (ENSO)-like variability as a dynamical driver of SAM or SHWW changes throughout the past two millennia (Moreno et al., 2018). Through Rossby wave chain, ENSO could influence the strength of Amundsen–Bellingshausen Seas Low, which in turn influences the phase of SAM on interannual scale, with an association between El Niño (La Niña) condition and negative (positive) phase of SAM (Fogt et al., 2011). Based on backward trajectory analysis, we find that the monthly frequency of easterly flows arriving to our study site is related to a dipole pattern of SLP anomaly between northern Patagonia and the Antarctic Peninsula–Bellingshausen Sea area, the latter of which is located within the ENSO-teleconnection domain (Figure 4.1C). Hence, the SHWW dynamics might reflect certain aspects in the strength of ENSO teleconnection. Indeed, the stronger SHWW during A.D. 1670–1840 is in phase with the Niño3.4 sea surface temperature (SST) minimum, while weaker SHWW during A.D. 1390–1670 and 1840–1970 are in phase with SST maximum (Figure 4.3D; Emile-Geay et al., 2013), indicating strong signature of ENSO-like states modulating SHWW strength on centennial-scale before the recent anthropogenic shift. Although the limited length of Niño3.4 SST reconstruction prevents further comparison prior to A.D. 1150, La Niña-like condition during the "Medieval Climate Anomaly" proposed by other studies (e.g., Cobb et al., 2003) might explain intensification of the SHWW started from A.D. 1020. Reliable

ENSO reconstruction is needed to further verify if the teleconnection persisted before the last millennium.

4.6. Conclusions and implication

Our peat moss $\delta^{18}O_{cell}$ record from southernmost Patagonia, along with other records, reveals the primacy of centennial-scale variability in SHWW strength across the Drake Passage throughout past two millennia that is comparable in magnitude with the recent anthropogenic shift. The record based on the use of water isotope tracer strongly supports that other moisture sources and trajectories other than westerly could be more important in the past in this region. Attributing regional hydroclimate changes to solely westerly flow controls is an oversimplification of climate dynamics in southernmost Patagonia. Moreover, the same is likely true in other mid- and high-latitude regions of the SH. In particular, establishment of modern ENSO regime since the mid-Holocene has been shown to break the SHWW zonal symmetry (Fletcher & Moreno, 2012; but see Fletcher et al., 2018). Our study provides evidence that synoptic-scale atmospheric circulations in different sectors (Atlantic, Pacific, and Indian Ocean) of the Southern Ocean and their teleconnections/relationships with dominant climate modes need to be considered to better understand regional climate dynamics and CO_2 degassing process in the past and future (Landschützer et al., 2015).

4.7. Acknowledgments

We thank Jonathan Stelling and Yinsui Zheng for field assistance; Rodrigo Munzenmayer, Alejandro Kusch and Daniel Terán from the Karukinka Park (Wildlife Conservation Society) for permission and logistical support; Yongsong Huang for discussion; and three anonymous reviewers for their constructive comments. This project was supported by U.S. NSF P2C2 Program (EAR 1502891).

References

Abram, N. J., Mulvaney, R., Vimeux, F., Phipps, S. J., Turner, J., & England, M. H. (2014). Evolution of the Southern Annular Mode during the past millennium. *Nature Climate Change*, *4*(7), 564–569.

Agosta, E., Compagnucci, R., & Ariztegui, D. (2015). Precipitation linked to Atlantic moisture transport: clues to interpret Patagonian palaeoclimate. *Climate Research*, *62*(3), 219–240.

Cobb, K. M., Charles, C. D., Cheng, H., & Edwards, R. L. (2003). El Niño/Southern Oscillation and tropical Pacific climate during the last millennium. *Nature*, *424*(6946), 271–276.

Daley, T. J., Barber, K. E., Street-Perrott, F. A., Loader, N. J., Marshall, J. D., Crowley, S. F., & Fisher, E. H. (2010). Holocene climate variability revealed by oxygen isotope analysis of *Sphagnum* cellulose from Walton Moss, northern England. *Quaternary Science Reviews*, *29*(13), 1590–1601.

Daley, T. J., Mauquoy, D., Chambers, F. M., Street-Perrott, F. A., Hughes, P. D. M., Loader, N. J., et al. (2012). Investigating late Holocene variations in hydroclimate and the stable isotope composition of precipitation using southern South American peatlands: an hypothesis. *Climate of the Past*, *8*(5), 1457–1471.

Emile-Geay, J., Cobb, K. M., Mann, M. E., & Wittenberg, A. T. (2013). Estimating central equatorial Pacific SST variability over the past millennium. Part II: Reconstructions and implications. *Journal of Climate*, *26*(7), 2329–2352.

Fletcher, M.-S., & Moreno, P. I. (2012). Have the Southern Westerlies changed in a zonally symmetric manner over the last 14,000 years? A hemisphere-wide take on a controversial problem. *Quaternary International*, *253*, 32–46.

Fletcher, M.-S., Benson, A., Bowman, D. M. J. S., Gadd, P. S., Heijnis, H., Mariani, M., et al. (2018). Centennial-scale trends in the Southern Annular Mode revealed by hemisphere-wide fire and hydroclimatic trends over the past 2400 years. *Geology*, *46*(4), 363–366.

Fogt, R. L., Bromwich, D. H., & Hines, K. M. (2011). Understanding the SAM influence on the South Pacific ENSO teleconnection. *Climate Dynamics*, *36*(7), 1555–1576.

Garreaud, R., Lopez, P., Minvielle, M., & Rojas, M. (2013). Large-scale Control on the Patagonian Climate. *Journal of Climate*, *26*(1), 215–230.

Gillett, N. P., Kell, T. D., & Jones, P. D. (2006). Regional climate impacts of the Southern Annular Mode. *Geophysical Research Letters*, *33*, L23704.

Lamy, F., Kilian, R., Arz, H. W., Francois, J.-P., Kaiser, J., Prange, M., & Steinke, T. (2010). Holocene changes in the position and intensity of the southern westerly wind belt. *Nature Geoscience*, *3*(10), 695–699.

Landschützer, P., Gruber, N., Haumann, F. A., Rödenbeck, C., Bakker, D. C. E., van Heuven, S., et al. (2015). The reinvigoration of the Southern Ocean carbon sink. *Science*, *349*(6253), 1221–1224.

Leuenberger, M. (2007). To what extent can ice core data contribute to the understanding of plant ecological developments of the past? In T. Dawson & R. Siegwolf (Eds.), *Stable Isotopes as Indicators of Ecological Change* (Vol. 1, pp. 211–233). London: Elsevier Academic Press.

Loader, N. J., Street-Perrott, F. A., Mauquoy, D., Roland, T. P., van Bellen, S., Daley, T. J., et al. (2016). Measurements of hydrogen, oxygen and carbon isotope variability in *Sphagnum* moss along a micro-topographical gradient in a southern Patagonian peatland. *Journal of Quaternary Science*, *31*(4), 426–435.

Loisel, J., & Yu, Z. (2013a). Surface vegetation patterning controls carbon accumulation in peatlands. *Geophysical Research Letters*, *40*(20), 5508–5513.

Loisel, J., & Yu, Z. (2013b). Holocene peatland carbon dynamics in Patagonia. *Quaternary Science Reviews*, *69*, 125–141.

Mariani, M., Fletcher, M.-S., Drysdale, R. N., Saunders, K. M., Heijnis, H., Jacobsen, G., & Zawadzki, A. (2017). Coupling of the Intertropical Convergence Zone and Southern Hemisphere mid-latitude climate during the early to mid-Holocene. *Geology*, *45*(12), 1083–1086.

Marshall, G. J. (2003). Trends in the Southern Annular Mode from Observations and Reanalyses. *Journal of Climate*, *16*(24), 4134–4143.

Mayr, C., Lücke, A., Stichler, W., Trimborn, P., Ercolano, B., Oliva, G., et al. (2007a). Precipitation origin and evaporation of lakes in semi-arid Patagonia (Argentina) inferred from stable isotopes ($\delta^{18}O$, $\delta^{2}H$). *Journal of Hydrology*, *334*(1), 53–63.

Mayr, C., Wille, M., Haberzettl, T., Fey, M., Janssen, S., Lücke, A., et al. (2007b). Holocene variability of the Southern Hemisphere westerlies in Argentinean Patagonia (52°S). *Quaternary Science Reviews*, *26*(5), 579–584.

Mayr, C., Lücke, A., Wagner, S., Wissel, H., Ohlendorf, C., Haberzettl, T., et al. (2013). Intensified Southern Hemisphere Westerlies regulated atmospheric CO_2 during the last deglaciation. *Geology*, *41*(8), 831–834.

Moreno, P. I., Francois, J. P., Moy, C. M., & Villa-Martínez, R. (2010). Covariability of the Southern Westerlies and atmospheric CO_2 during the Holocene. *Geology*, *38*(8), 727–730.

Moreno, P. I., Vilanova, I., Villa-Martínez, R., Garreaud, R. D., Rojas, M., & De Pol-Holz, R. (2014). Southern Annular Mode-like changes in southwestern Patagonia at centennial timescales over the last three millennia. *Nature Communications*, *5*, 4375.

Moreno, P. I., Vilanova, I., Villa-Martínez, R., Dunbar, R. B., Mucciarone, D. A., Kaplan, M. R., et al. (2018). Onset and evolution of Southern Annular Mode-like changes at centennial timescale. *Scientific Reports*, *8*, 3458.

Moy, C. M., Dunbar, R. B., Moreno, P. I., Francois, J.-P., Villa-Martínez, R., Mucciarone, D. M., et al. (2008). Isotopic evidence for hydrologic change related to the westerlies in SW Patagonia, Chile, during the last millennium. *Quaternary Science Reviews*, *27*(13), 1335–1349.

Mulvaney, R., Abram, N. J., Hindmarsh, R. C. A., Arrowsmith, C., Fleet, L., Triest, J., et al. (2012). Recent Antarctic Peninsula warming relative to Holocene climate and ice-shelf history. *Nature*, *489*(7414), 141–144.

New, M., Lister, D., Hulme, M. and Makin, I. (2002). A high-resolution data set of surface climate over global land areas. *Climate Research*, *21*(1), 1–25.

Quade, J., & Kaplan, M. R. (2017). Lake-level stratigraphy and geochronology revisited at Lago (Lake) Cardiel, Argentina, and changes in the Southern Hemispheric Westerlies over the last 25 ka. *Quaternary Science Reviews*, *177*, 173–188.

Rice, S. K., & Giles, L. (1996). The influence of water content and leaf anatomy on carbon isotope discrimination and photosynthesis in *Sphagnum*. *Plant, Cell & Environment*, *19*(1), 118–124.

Schneider, C., Glaser, M., Kilian, R., Santana, A., Butorovic, N., & Casassa, G. (2003). Weather observations across the southern Andes at 53°S. *Physical Geography*, *24*(2), 97–119.

Stern, L. A., & Blisniuk, P. M. (2002). Stable isotope composition of precipitation across the southern Patagonian Andes. *Journal of Geophysical Research: Atmospheres*, *107*(D23), 4667.

Stine, S. (1994). Extreme and persistent drought in California and Patagonia during mediaeval time. *Nature*, *369*(6481), 546–549.

Villalba, R., Lara, A., Masiokas, M. H., Urrutia, R., Luckman, B. H., Marshall, G. J., et al. (2012). Unusual Southern Hemisphere tree growth patterns induced by changes in the Southern Annular Mode. *Nature Geoscience*, *5*(11), 793–798.

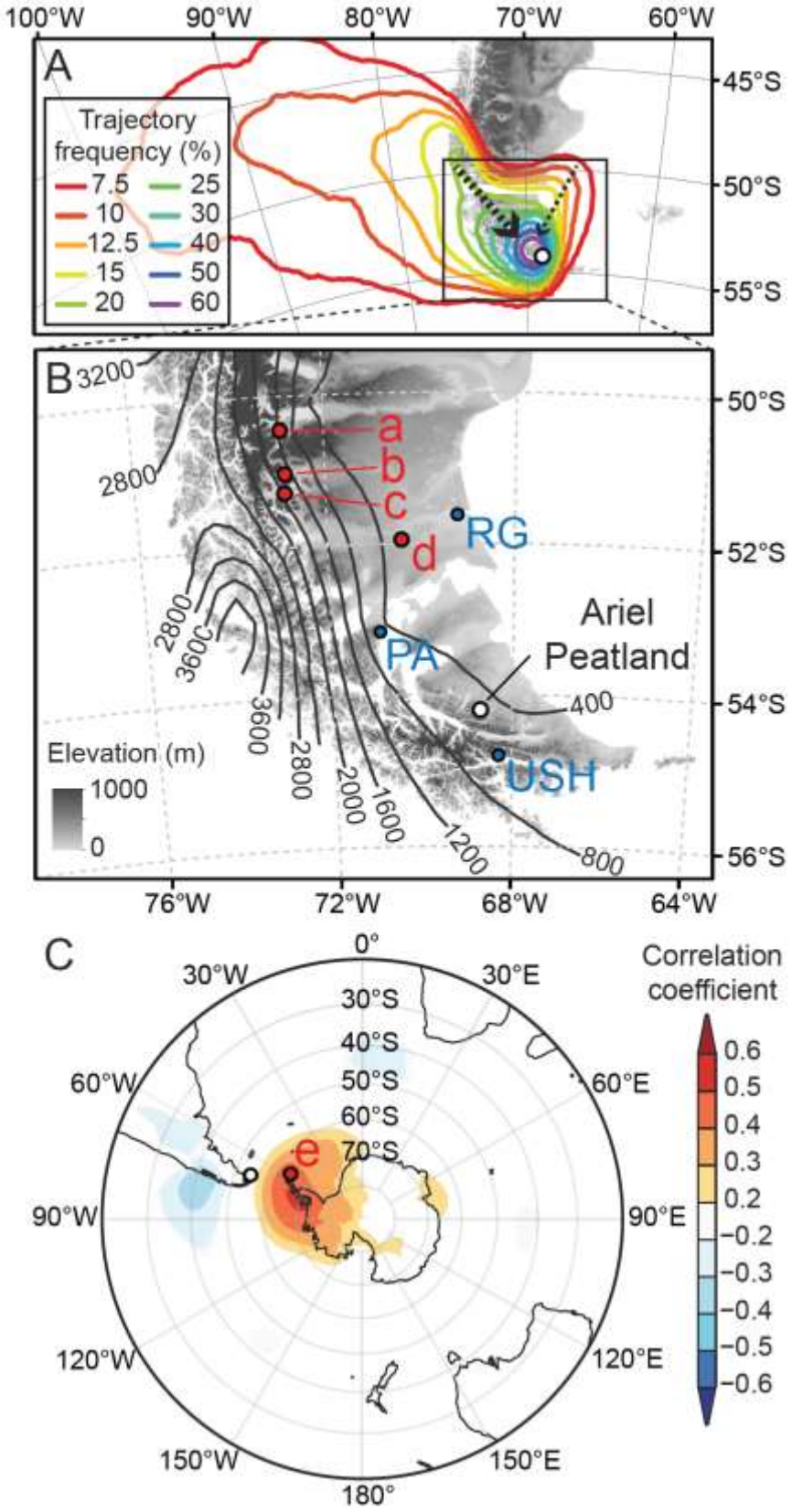
A
Trajectory frequency (%)
7.5
10
12.5
15
20
25
30
40
50
60
100°W
90°W
80°W
70°W
60°W
45°S
50°S
55°S
B
3200
2800
a
b
c
d
RG
PA
Ariel Peatland
400
USH
2800
3600
3600
2800
2000
1600
1200
800
Elevation (m)
1000
0
50°S
52°S
54°S
56°S
76°W
72°W
68°W
64°W
C
0°
30°W
30°E
30°S
40°S
50°S
60°S
70°S
60°W
60°E
e
90°W
90°E
120°W
120°E
150°W
150°E
180°
Correlation coefficient
0.6
0.5
0.4
0.3
0.2
−0.2
−0.3
−0.4
−0.5
−0.6

Figure 4.1 (previous page). Location of paleoclimate sites and atmospheric trajectories. (A) Trajectory frequency contour showing two dominant moisture sources and transport pathways (indicated by arrows). All rainfall-producing backward trajectories during September–May, 2005–2017, were modeled using HYSPLIT starting from the Ariel Peatland (AP; marked by white circle) at a height of 500 m for 120 h duration, and trajectory path data were binned by 1° × 1° to produce the contour. (B) Digital elevation map of southernmost Patagonia overlaid by isohyet (black lines; New et al., 2002). (C) Spatial correlation between the percentage of monthly easterly-related trajectories (extracted from trajectory data in (A); Figure D6) and ERA-Interim reanalysis sea level pressure. Red symbols in (B) and (C) show sites discussed in this study: a–Catalon Marsh, b–Lago Guanaco, c–Lago Cipreses, d–Laguna Potrok Aike, e–James Ross Island. Blue symbols in B also show major cities in this region: RG–Río Gallegos, PA–Punta Arenas, and USH–Ushuaia.

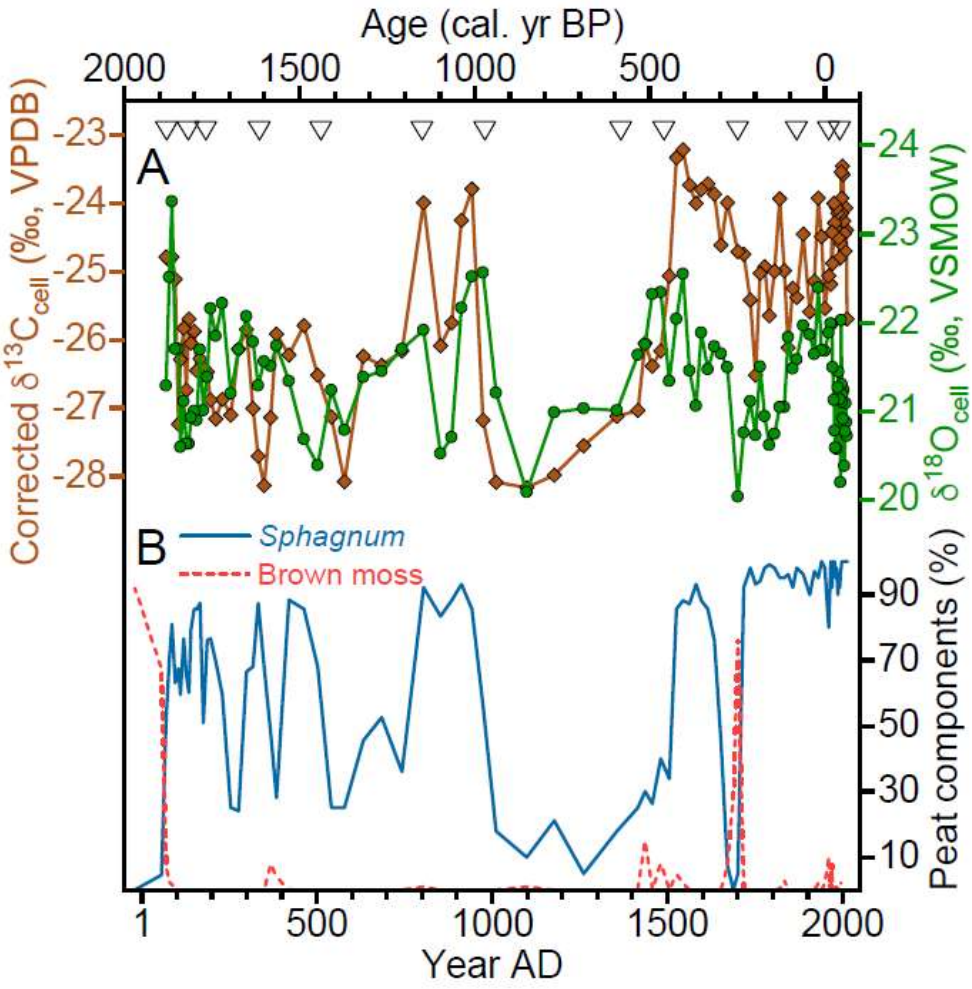

Figure 4.2. Summary results of AP peat-core analysis. (A) *Sphagnum*-specific cellulose $\delta^{18}O$ (green circles) and Suess-effect corrected cellulose $\delta^{13}C$ (brown diamonds) records. (B) *Sphagnum* (blue) and brown moss (dashed red) macrofossil percentages. Other peat components are mostly highly decomposed vascular plant remains. Triangles on top represent Bacon-modeled median calendar ages at the depth where ^{14}C dates were measured.

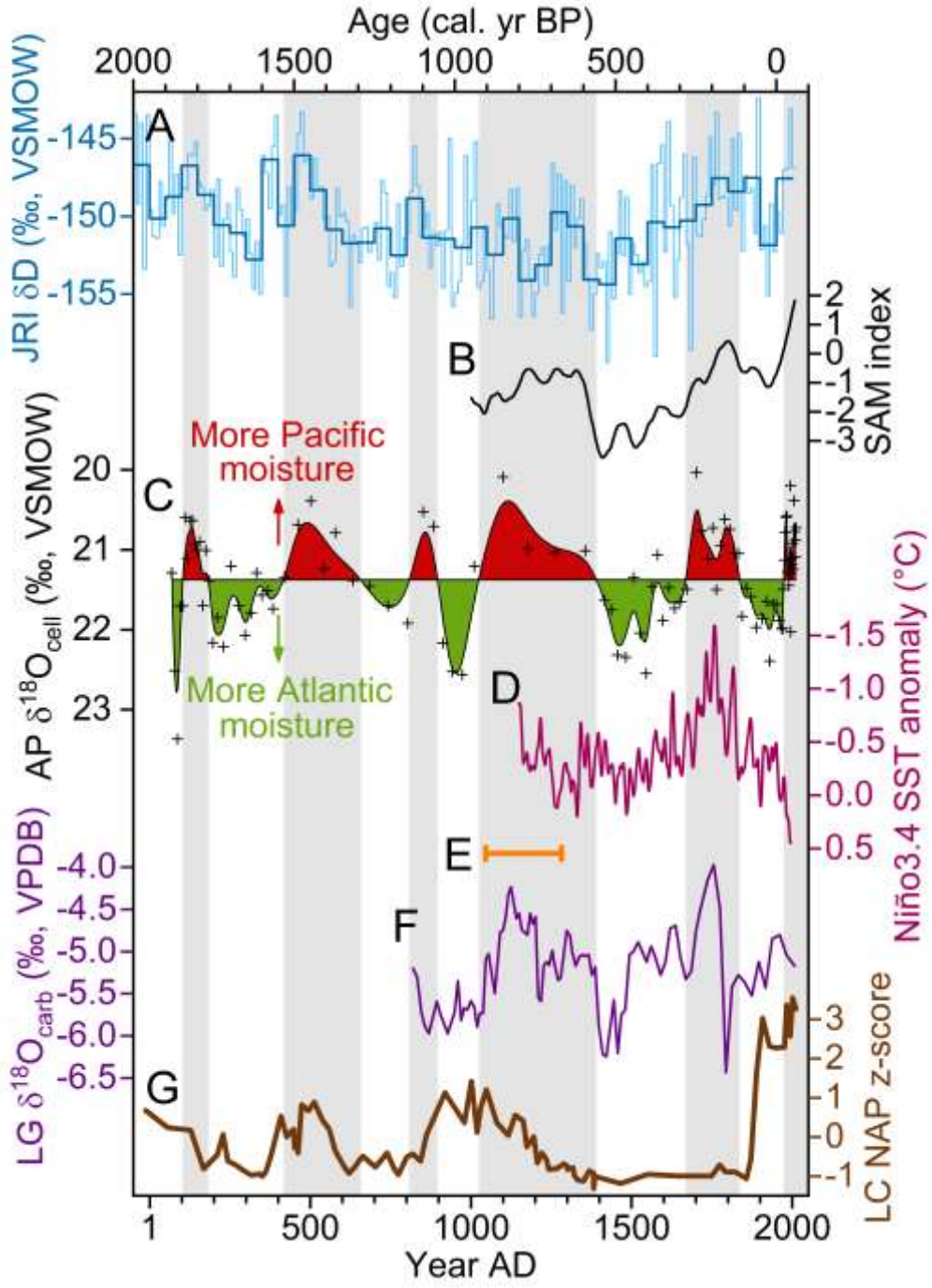

Figure 4.3. Coherent centennial-scale SHWW variability. (A) James Ross Island ice core δD record from the Antarctic Peninsula shown as 10-year (thin light blue) and 50-year bin values (thick dark blue) (Mulvaney et al., 2012). (B) SAM index reconstruction (70-year filtered; Abram et al., 2014). (C) Ariel Peatland cellulose $\delta^{18}O$ record shown as

cross symbols (raw data) and a LOESS ($\alpha = 0.05$) spline trend line, with periods of below and above the 2000-year cellulose $\delta^{18}O$ mean value filled by red and green color, respectively (this study; reverse scale on *y*-axis). (D) Niño3.4 sea surface temperature (SST) reconstruction (Emile-Geay et al., 2013; reverse scale on *y*-axis). (E) ^{14}C-dated interval of desiccated wetland-remains from Catalon Marsh (Stine, 1994). (F) Lago Guanaco (LG) carbonate $\delta^{18}O$ record (Moy et al., 2008). (G) Lago Cipreses (LC) non-arboreal pollen percentage (NAP) z-score record (Moreno et al., 2014). Grey shaded vertical bars indicate the periods of stronger SHWW.

Appendix D: Supporting Information for Chapter 4

1. Site information

Ariel Peatland (AP; unofficial name) is an ombrotrophic bog situated in the Karukinka Park, Isla Grande of Tierra del Fuego, Chile (54.20732° S, 68.71739° W; elevation 169 m above sea level). The peatland has a surface area of ~0.5 km^2 and a bog water pH of 4.3 (measured in January 2016). The site is surrounded by forested upland area on the north, south and west, while on the east it opens to a large floodplain, where a meandering river ~250 m away is flowing northward (Figure D1). At present the bog surface is relatively dry, in agreement with the fact that it is located at the driest end of the climate space of peat bog ecosystems in southernmost Patagonia (Loisel & Yu, 2013). It is also flat with limited developments of hummock-hollow and pool patterns (Figure D1). Single-species *Sphagnum magellanicum* dominates the center of bog, while vascular plants (mixture of herbaceous and ligneous plants) are more abundant near the edge of bog. The vegetation of peat bogs in Patagonia has been described and summarized by Loisel & Yu (2013).

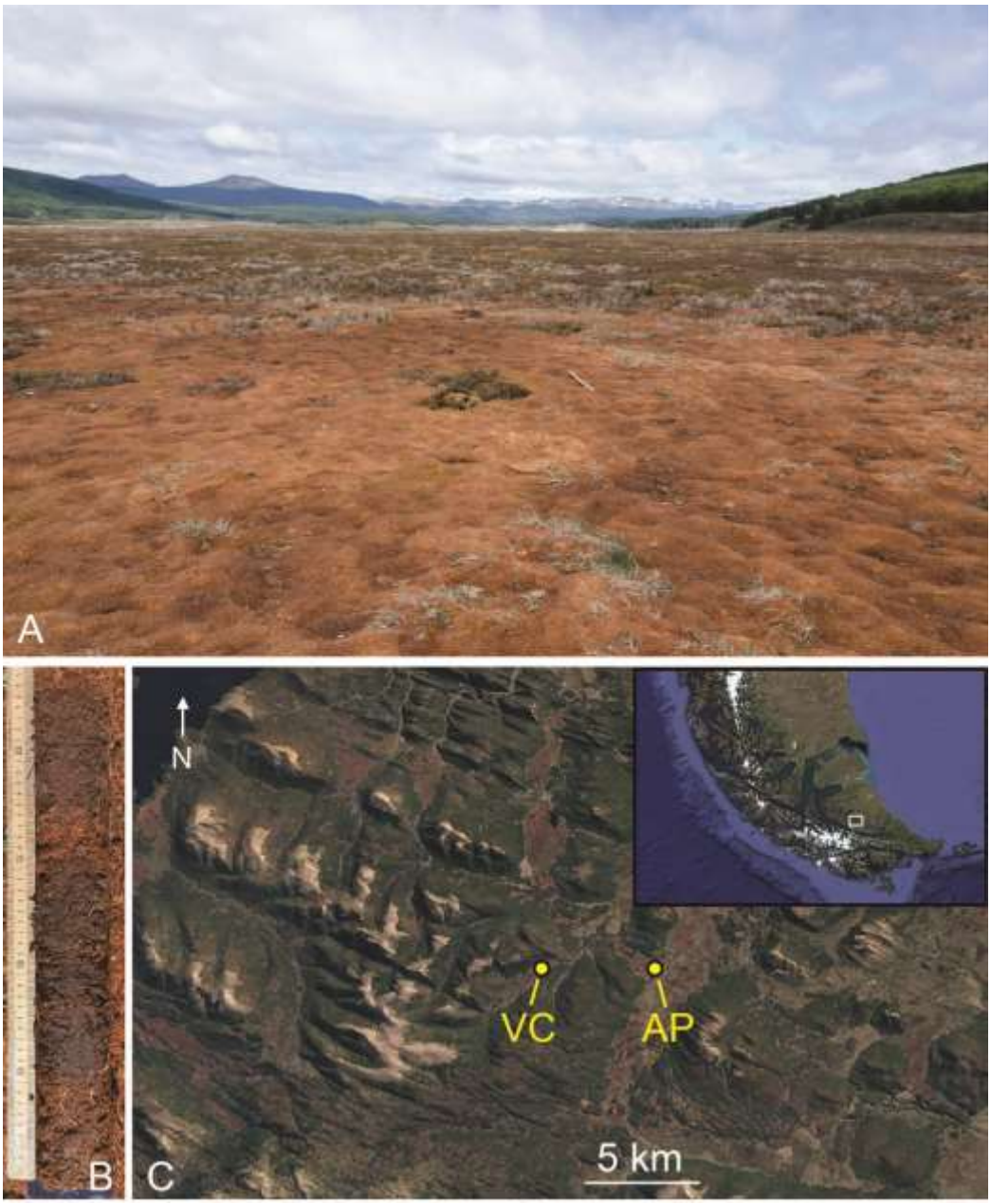

Figure D1. (A) Field photo of Ariel Peatland (AP) taken from the bog center towards its edge, looking toward east. (B) Core photo of 50–100 cm section from core PAT16-AP1 collected using a Russian peat sampler. (C) Google Earth images showing the geographical context and location of Ariel Peatland and Valle de Consejo (VC), another peatland site discussed below in Section 4 below in this appendix. The main image is the "zoom-in" of white square area in inset image on top right.

2. Age-depth model and loss-on-ignition results from core PAT16-AP1

Table D1. Radiocarbon dates of core PAT16-AP1 from Ariel Peatland.

Lab ID (UCIAMS)	Depth (cm)	Corrected depth (cm)*	Dated material	Radiocarbon age (^{14}C yr BP) or fraction modern (%FM)	δ^{13}C (‰, VPDB)	Median age (cal. yr BP)#	2σ range (cal. yr BP)#
185565	15–16	15.5	*Sphagnum* stems/leaves	113.11 ± 0.17 %FM†	-25.1	-	-
185566	25–26	25.5	*Sphagnum* stems/leaves	131.8 ± 0.2 %FM†	-24.6	-	-
193654	32–33	32.5	*Sphagnum* stems/leaves	200 ± 15	-26.1	202	0–284
179329	44–45	44.4	*Sphagnum* stems/leaves	185 ± 20	-23.9	186	0–281
185567	56–57	56.4	125–250 µm bulk peat & *Sphagnum* stems/leaves	395 ± 15	-26.0	399	327–491
193655	60–61	60.6	*Sphagnum* stems/leaves	690 ± 15	-26.6	598	561–657
193656	65–66	66	*Sphagnum* stems/leaves	1130 ± 20	-26.4	981	934–1056
185568	70–71	71.2	*Sphagnum* stems/leaves	1270 ± 15	-24.7	1131	1069–1184
193657	76–77	77.3	*Sphagnum* stems/leaves	1610 ± 15	-26.9	1462	1411–1523
185569	82–83	83.6	*Sphagnum* stems/leaves	1740 ± 15	-26.7	1600	1543–1698
179331	90–91	91.7	*Sphagnum* stems/leaves	1905 ± 20§	-25.1	1793	1734–1870
193658	96–97	98.3	*Sphagnum* stems/leaves	1910 ± 15§	-26.5	1798	1742–1868
185570	108–109	109	*Sphagnum* stems/leaves	1915 ± 15§	-25.1	1810	1744–1872
179333	131–132	131.6	*Sphagnum* stems/leaves	3275 ± 20	-25.3	3450	3382–3557
179330	159–160	160	*Sphagnum* stems/leaves	3865 ± 20	-26.3	4212	4094–4400
179332	203–204	203.6	>63 µm bulk peat	4660 ± 20	-27.8	5410	5295–5462

(previous table) *Some drives of peat core were slightly compressed during transport from field to lab, and for each subsample we used their corrected depths, assuming uniform compression of an individual core drive.

#Radiocarbon ages were calibrated to calendar ages using SHCal 13 dataset (Hogg et al., 2013) with Calib v7.10 (http://calib.org/calib/calib.html).

†These are post-bomb ^{14}C dates, which were originally reported as the fraction relative to modern ^{14}C (FM). Using calibration curve of Bomb 13 SH 1–2 dataset (Hua et al., 2013) on OxCal v4.3 (https://c14.arch.ox.ac.uk/oxcal/OxCal.html), sample 185565 was calibrated to A.D. 1959 (7.8% probability) and A.D. 1993 (87.6%). Sample 185566 was calibrated to A.D. 1963 (1.8%) and A.D. 1978 (93.6%). For the first sample, considering the stratigraphic position, we rejected the possibility of A.D. 1959 and assigned it an age of A.D. 1993. For the second sample, considering accumulation rates, we assigned its age at A.D. 1963 as that better fitted the expected peat accumulation pattern. In Bacon program, we input these two dates manually to their calibrated calendar years to avoid modeling age-depth relationships based simply on probability of post-bomb dates.

§Three identical ^{14}C dates within the uncertainty range suggested rapid accumulation of *Sphagnum* peat in this interval.

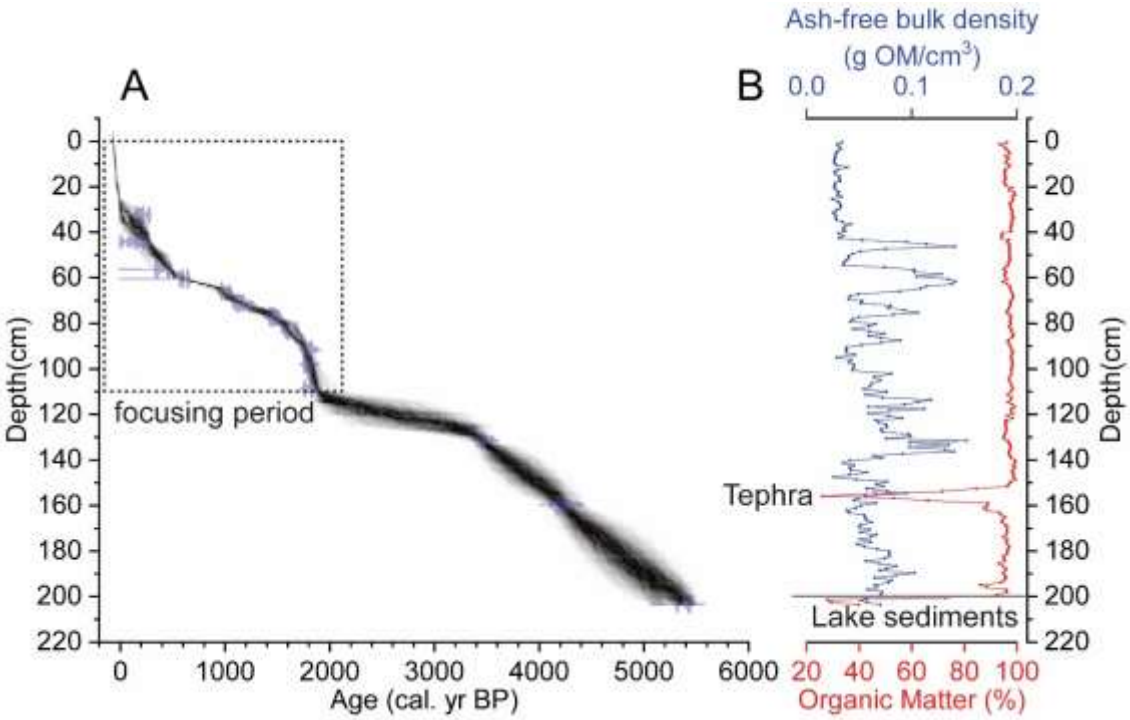

Figure D2. (A) Bacon age-depth model of core PAT16-AP1. (B) Organic matter percentage and ash-free bulk density of peat core from loss-on-ignition (LOI) analysis. The down-core variation of ash-free bulk density mainly reflected changes in botanical composition and the degree of decomposition of peat (Loisel et al., 2014). Organic matter percentage was higher than 95% throughout the core with very low mineral materials, except a tephra layer at 154–157 cm, suggesting the absence of fluvial influence on the peat bog.

3. Macrofossil analysis from Ariel Peatland

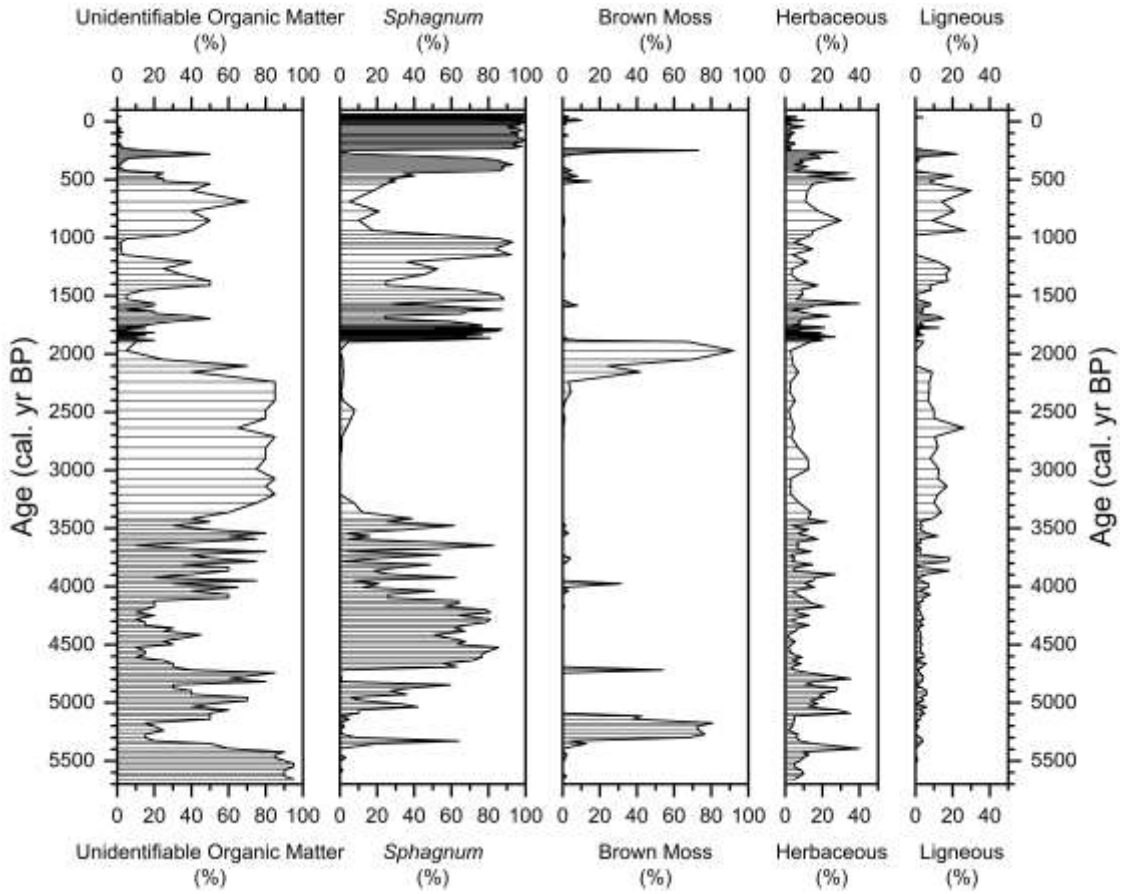

Figure D3. Peat component and macrofossil diagram of peat core PAT16-AP1. The lowest section (older than 5400 cal. yr BP based on interpolated ages) was likely lake sediments with low organic matter (<30%; Figure D2). The apparent gap of *Sphagnum* from 3200 cal. yr BP to 1900 cal. yr BP led us to develop a *Sphagnum*-specific cellulose isotope record only for the past two millennia. *Sphagnum* macrofossils shown here are all from *S. magellanicum* as we did not find macrofossils of any other species (such as *S. cuspidatum*) in the core that could be present at wet locations near hollows and pools.

4. Evaluation of evaporative effect on oxygen isotopes of moss cellulose

We conducted a modern process study using surface *Sphagnum* samples across a hummock-hollow microtopographic gradient to further understand the influence of moisture condition on stable isotope compositions in *Sphagnum* cellulose. Site Valle de Consejo (VC; Figure D1C), located at about 4.5 km west to our peat-core study site AP, has considerable developments of surface hummock-hollow patterning, creating an ideal setting to carry out modern process study. In addition to field measurements of *in situ* hydrological variables, we collected *Sphagnum* samples at every 30-cm along a north-facing hummock-hollow transect of >400 cm in length and extracted cellulose from *Sphagnum* capitula (the very top of actively growing portion of mosses that represents the recent growth, i.e., during the summer) and then carried out isotope analysis following the same lab procedure as for down-core samples. Our results showed a strong negative correlation between $\delta^{18}O_{cell}$ and $\delta^{13}C_{cell}$ values ($r = -0.8$; $p < 0.001$), implying a common environmental factor governing the intra-site variation of both isotope ratios (Figure D5). Likewise, this negative correlation was also found from another similar study at a *Sphagnum*-dominated peatland site in southernmost Patagonia (Figure D5; Loader et al., 2016). Many studies on carbon isotope composition of mosses concluded that moisture availability exerts a critical influence (Rice & Giles, 1996; Price et al., 1997; Ménot & Burns, 2001; Loisel et al., 2009), although other studies indicated potential influence of temperature, probably due to intrinsic relation between temperature and moisture-related environmental factors (e.g., Ménot & Burns, 2001; Moschen et al., 2011). Other influencing factors include CO_2 concentration (White et al., 1994) and recycled CH_4-derived CO_2 (Price et al., 1997). On the other hand, oxygen isotope composition of mosses is mainly controlled by the oxygen isotope composition of meteoric water and its subsequent evaporative enrichment in ^{18}O of leaf water. For moss samples along our local hydrological transect, they should receive the same source of moisture, i.e., from

precipitation. Therefore, evaporative enrichment played a key role modifying/elevating the source water $\delta^{18}O$ values (Ménot-Combes et al., 2002; Zanazzi & Mora, 2005). Our calibration data from site VC showed that $\delta^{18}O_{cell}$ values had a range of ~18–21‰ (Figure D4). We made the following two assumptions to quantify the evaporative enrichment on $\delta^{18}O_{cell:}$

(1) Summer precipitation input has an average $\delta^{18}O$ value of about −10‰ based on the Global Network of Isotopes in Precipitation (GNIP) data in Ushuaia, the nearest GNIP station to our study site, also located on the east side of the Andes divide.

(2) Biochemical enrichment factor (ε_b) during cellulose biosynthesis has a constant value of ca. +27‰ that has been widely accepted in the literature (e.g., Zanazzi & Mora, 2005; Sternberg, 2009; Daley et al., 2010; Sternberg & Ellsworth, 2011). This fractionation factor seems to be conservative and independent of species (Daley et al., 2010). Recently, this biochemical enrichment factor has been considered to be temperature-dependent (Sternberg & Ellsworth, 2011):

$$\varepsilon_b = 0.0073T^2 - 0.4375T + 35.528$$

where T denotes temperature. If using average summer day-time temperature (~15 °C) in our study region (Loader et al., 2016), the temperature-calibrated ε_b would be slightly higher, at around +27.5 ‰. However, it should be noted that the ε_b-temperature relationship reported by Sternberg & Ellsworth (2011) was based on limited number of data and did not provide the uncertainty range. Thereafter, we still used +27‰ as the value of ε_b to estimate the extent of evaporative enrichment shown below.

We then calculated the hypothetical values of $\delta^{18}O_{cell}$ without considering any evaporative enrichment in leaf water using the equation (Daley et al., 2010):

$$\delta^{18}O_{cell} = \delta^{18}O_p + \varepsilon_b$$

The derived hypothetical $\delta^{18}O_{cell}$ value is ~17‰, which is at least about 1‰ lower than the $\delta^{18}O_{cell}$ values (~18–21‰) observed from the surface *Sphagnum* samples. We

thus concluded that the extent of evaporative enrichment contributed an offset of ca. 1–4‰ between $\delta^{18}O_{cell}$ and $\delta^{18}O_p$. The uncertainties in $\delta^{18}O_p$ and ε_b values would only influence the magnitude of evaporative enrichment, but they would not hamper our inference that evaporation isotopically enriched the leaf water, and played a key role modifying/elevating $\delta^{18}O_{cell}$ values.

We suggest that moisture condition or evaporative enrichment are the only possible mechanism to explain the negative correlation between $\delta^{18}O_{cell}$ and $\delta^{13}C_{cell}$ in our dataset. Hummock-growing *Sphagnum* mosses are away from the water table and thus drier with a thinner water film, which results in stronger discrimination against atmospheric $^{13}CO_2$ and lower $\delta^{13}C_{cell}$ values. Because hummock-growing *Sphagnum* are in deficiency of water, moss leaf water is subject to enhanced evaporative enrichment in ^{18}O, resulting in higher $\delta^{18}O_{cell}$ values. By contrast, hollow-growing *Sphagnum* mosses are near the water table and thus wetter with a thicker water film, which results in less discrimination against atmospheric $^{13}CO_2$ and higher $\delta^{13}C_{cell}$ values. Also, leaf water in hollow-growing *Sphagnum* mosses are near saturated, and leaf water is more protected from evaporative enrichment, which results in lower $\delta^{18}O_{cell}$ values. Therefore, we propose that paired measurements of moss $\delta^{18}O_{cell}$ and $\delta^{13}C_{cell}$ in the same cellulose samples allow us to elucidate the effect of moisture condition or evaporation in peat-core analysis. If negative correlations between those isotopes were also found in peat cores, the relationships likely indicated changes in bog surface moisture conditions. However, in our peat-core analysis of core PAT16-AP1, we did not observe such negative correlation. Therefore, we conclude that moisture condition or evaporation are unlikely to be the dominant factors that explain the changes in $\delta^{18}O_{cell}$. Instead $\delta^{18}O_{cell}$ primarily document changes in $\delta^{18}O_p$.

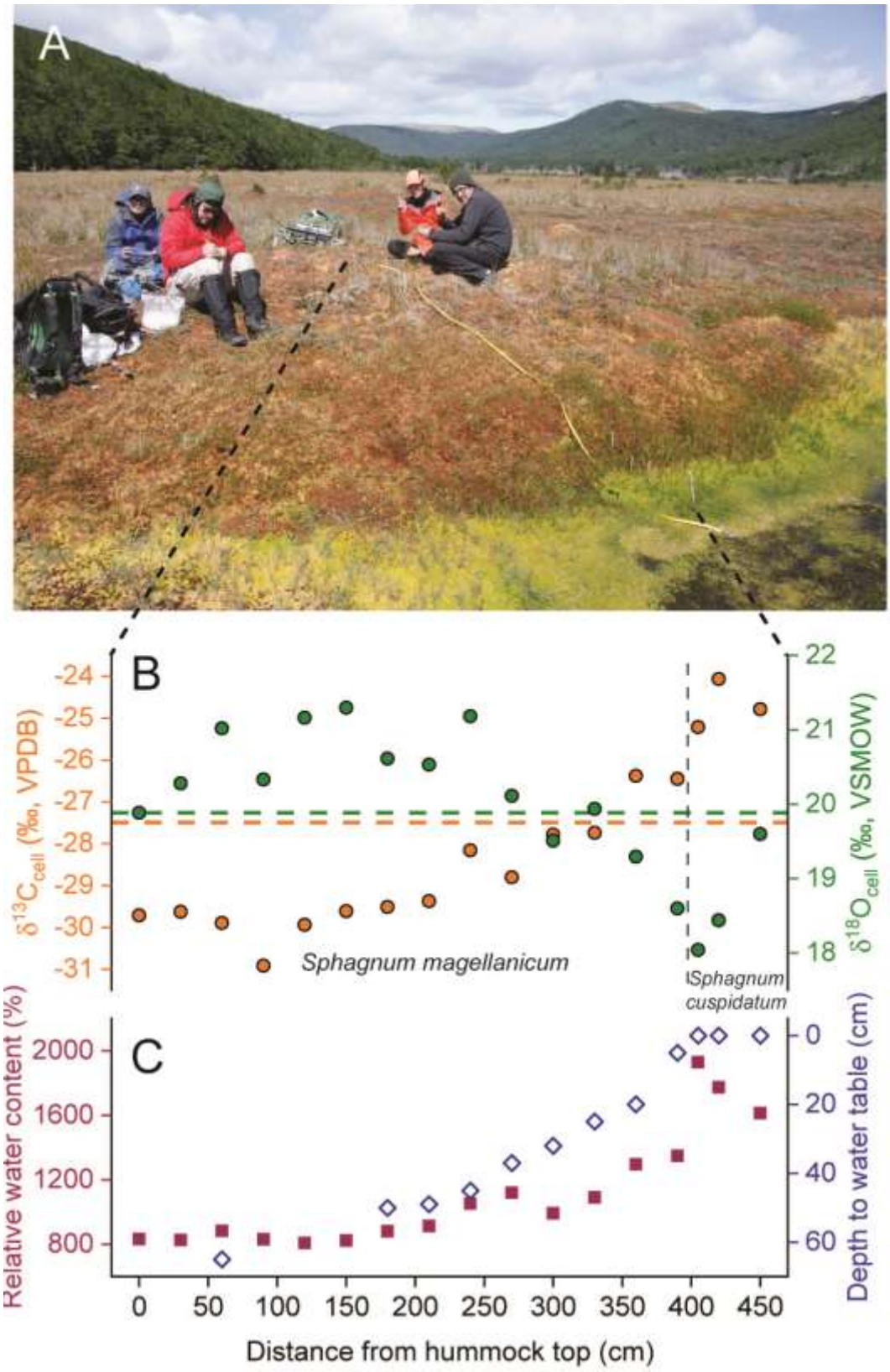
A
B
C
-24
-25
-26
-27
-28
-29
-30
-31
δ13Ccell (‰, VPDB)
22
21
20
19
18
δ18Ocell (‰, VSMOW)
Sphagnum magellanicum
Sphagnum cuspidatum
2000
1600
1200
800
Relative water content (%)
0
20
40
60
Depth to water table (cm)
0
50
100
150
200
250
300
350
400
450
Distance from hummock top (cm)

Figure D4 (previous page). (A) Field photo of the hummock-hollow transect at site Valle de Consejo (VC) for our modern process study. (B) *Sphagnum* $\delta^{18}O_{cell}$ (green circles) and $\delta^{13}C_{cell}$ (orange circles) variations across hummock-hollow hydrological gradient. Data points on the right side of black vertical dashed line are from different species: green-color *S. cuspidatum*. Green and orange horizontal dashed lines are the $\delta^{18}O_{cell}$ and $\delta^{13}C_{cell}$ values of surface *Sphagnum* moss capitula from the coring location of site Ariel Peatland. (C) Field measurements of relative water content (water mass/dry moss mass; pink filled squares) and water table depth (blue open diamonds) on the hummock-hollow transect.

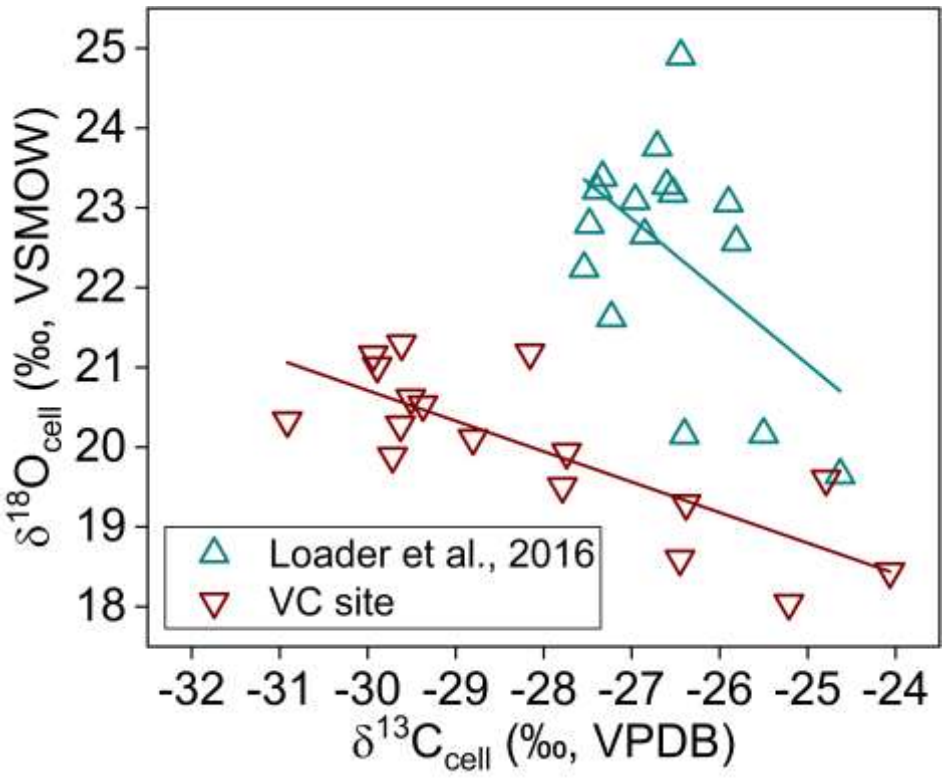

Figure D5. Negative correlation between *Sphagnum* $\delta^{18}O_{cell}$ and $\delta^{13}C_{cell}$ from surface samples along hydrological gradient within a single site. Data from site VC (Figure D4) show negative correlation ($r = -0.8$, $p < 0.001$) with a slope of −0.38 in regression line. Data from the site in Laguna Parrillar National Reserve about 35 km southwest to Punta Arenas were collected across multiple hummock-hollow transects (Loader et al., 2016) but a weaker negative correlation ($r = -0.51$, $p < 0.05$) with a slope of −0.91 in regression line could still be found.

5. Air-parcel backward trajectory analysis using HYSPLIT model

We used a Python package (PySPLIT; Cross, 2015) interfaced with NOAA's HYbrid Single-Particle Lagrangian Integrated Trajectory (HYSPLIT) (Stein et al., 2015) to analyze the backward trajectories of rainfall-producing air masses from our study site Ariel Peatland. We used the Global Data Assimilation System (GDAS) at 1° × 1° resolution as the gridded meteorological data. By running the "mass-production" trajectory generation code in PySPLIT, we calculated 120-hour back-trajectories at every 6-hour interval for September–May (austral spring, summer and autumn, i.e., most likely growing seasons) during the period 2005–2017. Air parcels were initialized at 500 m, 1000 m, 1500 m, and 2000 m above ground level (AGL), but we restricted following analysis to only trajectories with initialization altitude at 500-m AGL (~900 mb) as air parcel movements at this level are more sensitive to synoptic conditions, particularly to the days with easterly winds (Agosta et al., 2015). We further filtered trajectories based on two criteria: (1) trajectory is rainfall-producing at starting point (time = 0); and (2) integration error calculated from "reverse trajectory" is lower than two units of standard deviation of the mean (Cross, 2015; Scroxton et al., 2017). This resulted in total of 2506 trajectories, which were then binned by 1° × 1° to count the trajectory frequency and produce frequency contour (Caves et al., 2015). We then used Python to further extract the back-trajectories that passed over the Atlantic Ocean within 20 hours before arriving the location (Figure D6). Monthly percentage of easterly-related trajectories during the months from September to May in the period 2005–2017, were then used to investigate the correlation with ERA-Interim sea level pressure on Climate Explorer (http://climexp.knmi.nl) (Krklec & Domínguez-Villar, 2014).

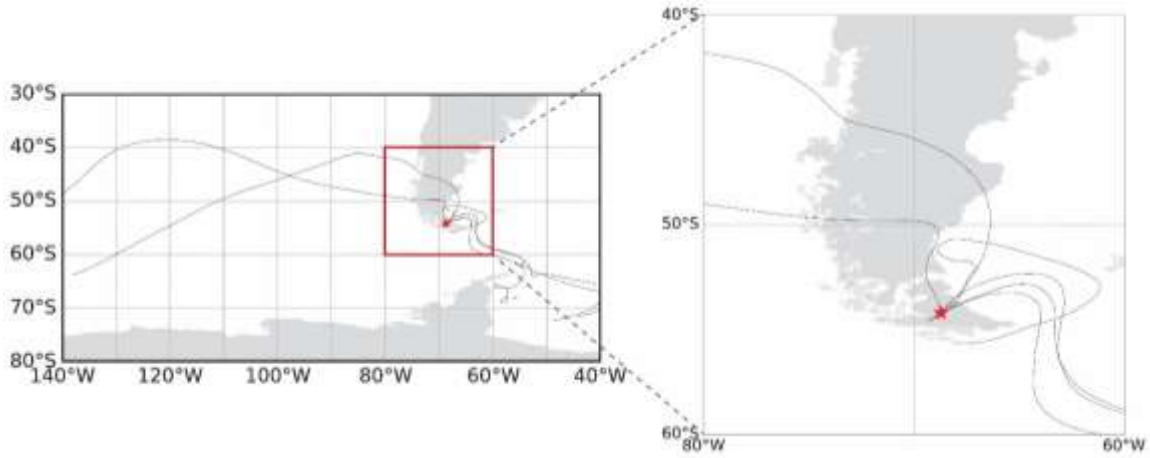

Figure D6. Easterly-related trajectories extracted from rainfall-producing trajectories in April 2017 as an example. Red star is our study site Ariel Peatland.

6. A close-up look of PAT16-AP1 proxy record for the last 150 years

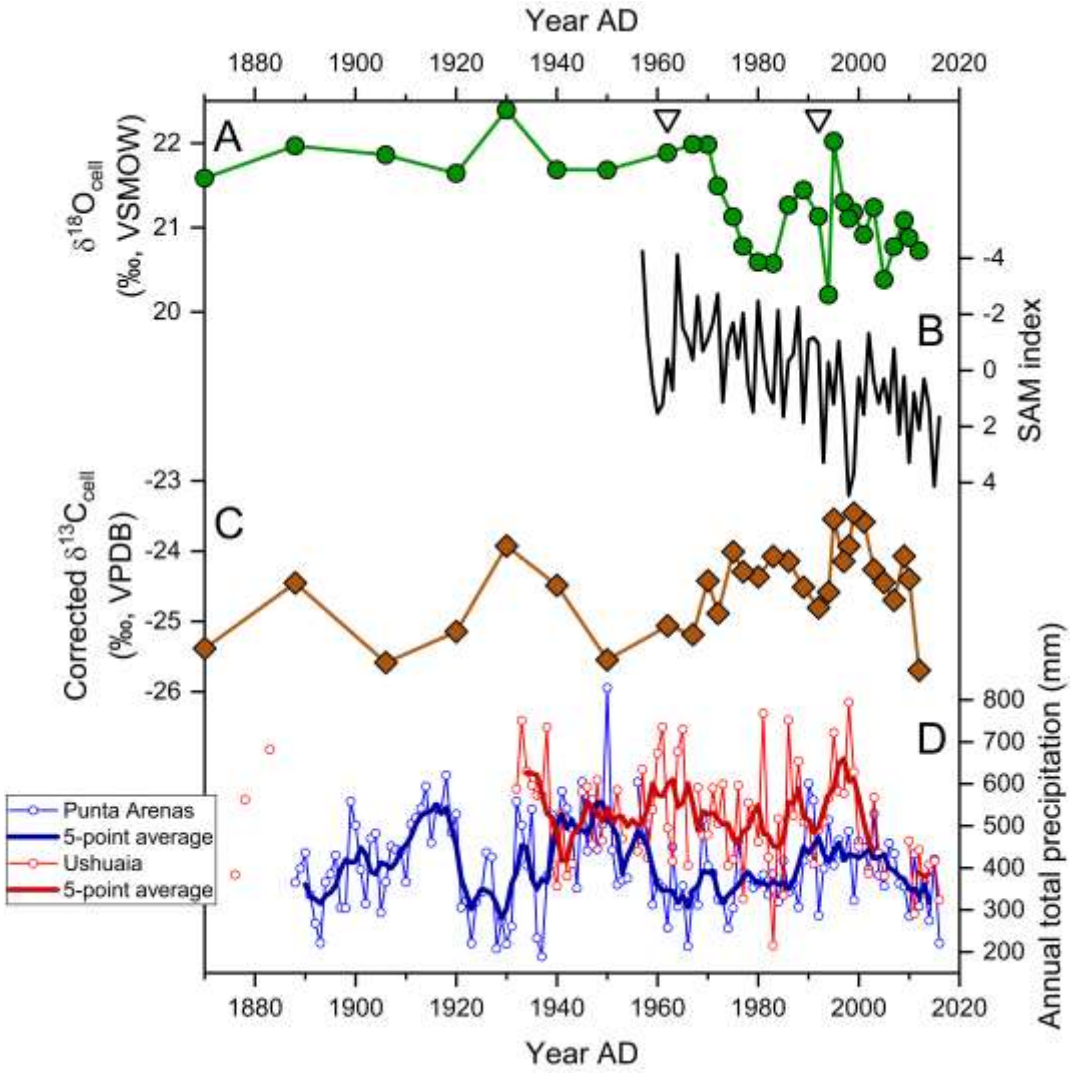

Figure D7. A close-up look at proxy records of peat core PAT16-AP1 during the recent 150 years in comparison with instrumental records. (A) *Sphagnum* $\delta^{18}O_{cell}$ record. (B) Marshall annual SAM index (reverse scale on *y*-axis). (C) *Sphagnum* corrected $\delta^{13}C_{cell}$ record. (D) Punta Arenas and Ushuaia station-based annual total precipitation records; data source is the Global Historical Climatology Network (GHCN) dataset. Triangles on top are the level dated by post-bomb radiocarbon (Table D1).

References for Appendix D:

Agosta, E., Compagnucci, R., & Ariztegui, D. (2015). Precipitation linked to Atlantic moisture transport: clues to interpret Patagonian palaeoclimate. *Climate Research*, *62*(3), 219–240.

Caves, J. K., Winnick, M. J., Graham, S. A., Sjostrom, D. J., Mulch, A., & Chamberlain, C. P. (2015). Role of the westerlies in Central Asia climate over the Cenozoic. *Earth and Planetary Science Letters*, *428*, 33–43,

Cross, M. (2015). *PySPLIT: a Package for the Generation, Analysis, and Visualization of HYSPLIT Air Parcel Trajectories.* Paper presented at Proceedings of the 14th Python in Science Conference (SciPy 2015), Austin, TX.

Daley, T. J., Barber, K. E., Street-Perrott, F. A., Loader, N. J., Marshall, J. D., Crowley, S. F., & Fisher, E. H. (2010). Holocene climate variability revealed by oxygen isotope analysis of *Sphagnum* cellulose from Walton Moss, northern England. *Quaternary Science Reviews*, *29*(13), 1590–1601.

Hogg, A. G., Hua, Q., Blackwell, P. G., Niu, M., Buck, C. E., Guilderson, T. P., et al. (2013). SHCal13 Southern Hemisphere calibration, 0–50,000 years cal BP. *Radiocarbon*, *55*(04), 1889–1903.

Hua, Q., Barbetti, M., & Rakowski, A. Z. (2013). Atmospheric radiocarbon for the period 1950–2010: *Radiocarbon*, *55*(4), 2059–2072.

Krklec, K., & Domínguez-Villar, D. (2014). Quantification of the impact of moisture source regions on the oxygen isotope composition of precipitation over Eagle Cave, central Spain. *Geochimica et Cosmochimica Acta*, *134*, 39–54.

Loader, N. J., Street-Perrott, F. A., Mauquoy, D., Roland, T. P., van Bellen, S., Daley, T. J., et al. (2016). Measurements of hydrogen, oxygen and carbon isotope variability in *Sphagnum* moss along a micro-topographical gradient in a southern Patagonian peatland. *Journal of Quaternary Science*, *31*(4), 426–435.

Loisel, J., Garneau, M., & Hélie, J. F. (2009). Modern *Sphagnum* $\delta^{13}C$ signatures follow a surface moisture gradient in two boreal peat bogs, James Bay lowlands, Québec. *Journal of Quaternary Science*, *24*(3), 209–214.

Loisel, J., & Yu, Z. (2013). Holocene peatland carbon dynamics in Patagonia. *Quaternary Science Reviews*, *69*, 125–141.

Loisel, J., Yu, Z., Beilman, D. W., Camill, P., Alm, J., Amesbury, M. J., et al. (2014). A database and synthesis of northern peatland soil properties and Holocene carbon and nitrogen accumulation. *The Holocene*, *24*(9), 1028–1042.

Ménot-Combes, G., Burns, S. J., & Leuenberger, M. (2002). Variations of $^{18}O/^{16}O$ in plants from temperate peat bogs (Switzerland): implications for paleoclimatic studies. *Earth and Planetary Science Letters*, *202*(2), 419–434.

Ménot, G., & Burns, S. J. (2001). Carbon isotopes in ombrogenic peat bog plants as climatic indicators: calibration from an altitudinal transect in Switzerland. *Organic Geochemistry*, *32*(2), 233–245.

Moschen, R., Kühl, N., Peters, S., Vos, H., & Lücke, A. (2011). Temperature variability at Dürres Maar, Germany during the Migration Period and at High Medieval Times, inferred from stable carbon isotopes of *Sphagnum* cellulose. *Climate of the Past*, *7*(3), 1011–1026.

Price, G. D., McKenzie, J. E., Pilcher, J. R., & Hoper, S. T. (1997). Carbon-isotope variation in *Sphagnum* from hummock-hollow complexes: implications for Holocene climate reconstruction. *The Holocene*, *7*(2), 229–233.

Rice, S. K., & Giles, L. (1996). The influence of water content and leaf anatomy on carbon isotope discrimination and photosynthesis in *Sphagnum*. *Plant, Cell & Environment*, *19*(1), 118–124.

Scroxton, N., Burns, S. J., McGee, D., Hardt, B., Godfrey, L. R., Ranivoharimanana, L., & Faina, P. (2017). Hemispherically in-phase precipitation variability over the last 1700 years in a Madagascar speleothem record. *Quaternary Science Reviews*, *164*, 25–36.

Stein, A. F., Draxler, R. R., Rolph, G. D., Stunder, B. J. B., Cohen, M. D., & Ngan, F. (2015). NOAA's HYSPLIT atmospheric transport and dispersion modeling system. *Bulletin of the American Meteorological Society*, *96*(12), 2059–2077.

Sternberg, L., & Ellsworth, P. F. V. (2011). Divergent biochemical fractionation, not convergent temperature, explains cellulose oxygen isotope enrichment across latitudes. *PLOS ONE*, *6*(11), e28040.

Sternberg, L. S. L. (2009). Oxygen stable isotope ratios of tree-ring cellulose: the next phase of understanding. *New Phytologist*, *181*(3), 553–562.

White, J. W. C., Ciais, P., Figge, R. A., Kenny, R., & Markgraf, V. (1994). A high-resolution record of atmospheric CO_2 content from carbon isotopes in peat. *Nature*, *367*(6459), 153–156.

Zanazzi, A., & Mora, G. (2005). Paleoclimatic implications of the relationship between oxygen isotope ratios of moss cellulose and source water in wetlands of Lake Superior. *Chemical Geology*, *222*(3), 281–291.

CONCLUDING REMARKS

This dissertation represents an interdisciplinary case study combining modern and paleo perspectives to provide a process-driven and cross-scale understanding of climate change in the remote Southern Hemisphere. The approaches and results presented in this dissertation provide new thinking and critical insights to several disciplines, including stable isotope geochemistry, atmospheric sciences, plant physiology, and paleoclimatology.

As one of the main contributions of this dissertation, the approach presented in Chapter 1 offers new opportunities for studying hydrological processes using precipitation isotope data from large-scale monitoring network such as the GNIP program. These isotope data are often measured from monthly-composited precipitation as mixing signals, and many studies usually regard each monthly precipitation isotope datum as just a single and simple value. Whereas my approach can resolve and quantify the composition of these collected precipitation samples that likely explain the consequence of the mixing signals, and, as such, will provide a window to investigate the processes responsible for each datum. In a broader perspective, this approach could be further explored and incorporated into the current studies of isotope-based ecohydrology.

Isotope proxies are widely used in paleoclimate reconstruction for decades, while the climate interpretations on the isotope data differ in different regions or timescales and are often vague or contentious. These interpretations are often based on the classic temperature or precipitation-amount effects that have emerged from the empirical correlations on spatial or seasonal datasets. However, these empirical correlations do not explain the processes-based mechanisms and likely are not the appropriate analogue to explain the long-term variations in precipitation isotopes at a location. As such, many studies found that neither temperature nor amount effects could satisfyingly explain

isotope data for paleoclimate reconstruction. Whereas it has been well recognized that on paleoclimate timescales, changes in precipitation isotopes reflect the integration of changes in large-scale atmospheric circulation. With the observational evidence from Chapter 1, Chapter 4 further extends the idea that changes in precipitation isotopes at a location reflect the shifting synoptic-scale patterns rather than local climatic parameters. This idea should be paid more attention for all other isotope-based paleoclimate reconstruction.

In recent decades, there is an increasing interest in characterizing the stable isotopes of plants and plant-derived compounds, such as cellulose and leaf wax, in the studies of paleoclimate and biogeochemical cycle. Compared to mineral-based approach, such as measuring carbon and oxygen isotopes in carbonates, stable isotopes in plants provide various information about biotic or plant-mediated processes, including water and nutrient cycling, ecosystem dynamics, and bioclimatic conditions. While tremendous progress has been made, the attendant challenges also emerge. Isotopic fractionations occurred in plants are almost all complex kinetic processes that are difficult to characterize by first principles, and, from another point of view, are black box processes. An example for this is the "apparent" fractionation factor for plants, which essentially reflect the fact that there are very limited knowledges about how stable isotope compositions of plants are controlled by both biotic and abiotic factors. Chapter 2 and Chapter 3 demonstrate that understanding the plant physiology is the key step in deciphering the mystery mechanisms that govern isotopic variations in plants. For example, we measure the water content of *Sphagnum* mosses to characterize their moisture availability at different microtopographical locations in peat bogs. The water content measurements were widely used in physiology studies of bryophytes several decades ago but have rarely, if ever, been used to calibrate any bryophyte-related proxies, and it is the same case for vascular plant leaves. With new knowledge in isotopic

physiology of plants, I refine the isotope-based approach in paleoenvironmental analysis of peat cores, and thanks to this, I am able to reconstruct past SHWW variability with confidence in proxy signal interpretation.

Lastly, the prominent contribution of this dissertation is to reveal the diverse synoptic-scale behaviors within the realm of SHWW. For a very long time, the SHWW have been regarded as a hemisphere-wide, unidirectional, zonal wind-flow pattern. From paleo perspectives, researchers usually focus on the strength and position of the SHWW and how such changes affect the Southern Ocean system and the Antarctic cryosphere. This dissertation shows that synoptic weather types associated with non-westerlies could be very important in the SHWW realm, not only in Patagonia, but also in other sectors of the Southern Ocean. Such diverse synoptic-scale patterns could play a dominant role in regulating regional climate and Southern Ocean CO_2 degassing. Indeed, the asymmetric behavior of the SHWW has been invoked to explain the highly variable CO_2 exchange pattern over different sectors of the Southern Ocean during the instrumental period (Landschützer et al., 2015).

As such, I propose that climate shifts occurred in the SHWW realm reflect more shifts in synoptic-scale patterns than the large-scale condition of the SHWW. For example, isotope data from Ariel Peatland suggest that non-westerlies contribute 30% more precipitation during the early twentieth century in southern Patagonia. It could occur under an anomalous synoptic-scale pattern over the Drake Passage as strong high-latitude blocking conditions under a negative phase of the SAM. Coincidently, the Antarctic Peninsula was 3°C colder than today during that period (Stenni et al., 2017), which could be attributed to the same synoptic-scale pattern. There is increasing evidence that the Antarctic Peninsula is one of fastest warming spot on the Earth in the global warming era. From the point of view of synoptic-scale pattern, I propose that such fast warming in the Antarctic Peninsula could simply emerge from a shifting atmospheric

circulation pattern over the last century that might be driven by the tropical ocean-atmosphere system. If so, the temperature sensitivity to CO_2 forcing in the global warming trend might be overestimated in the Antarctic Peninsula, because of the strong natural climate variability in this region (Turner et al., 2016)

References:

Landschützer, P., Gruber, N., Haumann, F. A., Rödenbeck, C., Bakker, D. C. E., van Heuven, S., et al. (2015). The reinvigoration of the Southern Ocean carbon sink. *Science*, *349*(6253), 1221–1224.

Stenni, B., Curran, M. A., Abram, N., Orsi, A., Goursaud, S., Masson-Delmotte, V., et al. (2017). Antarctic climate variability on regional and continental scales over the last 2000 years. *Climate of the Past*, *13*, 1609–1634.

Turner, J., Lu, H., White, I., King, J. C., Phillips, T., Hosking, J. S., et al. (2016). Absence of 21st century warming on Antarctic Peninsula consistent with natural variability. *Nature*, *535*(7612), 411–415.

Appendix E

The expression of "4.2 ka event" in southern Patagonia under a quiet ENSO regime

1. Introduction

Widespread evidence have documented the global expression of a climate anomaly that occurred 4200 cal. yr BP, known as the 4.2 ka event (Booth et al., 2005). This "4.2 ka event" initially was identified as a megadrought in the tropical and subtropical regions of the Northern Hemisphere and has been recoganized as the possible climatic driver of the collapse of major ancient civilizations (Cullen et al., 2000; Staubwasser et al., 2003). Recently, the "4.2 ka even"t has been approved as the chronostratigraphic boundary to divide the Middle and Late Holocene Sub-series/Sub-epoch by the Global boundary Stratotype Section and Point (GSSP), based on a speleothem $\delta^{18}O$ record in India that indicates an abrupt monsoon weakening (Walker et al., 2019). Controversies also arise about the nature of "4.2 ka event", such as the strength and direction of the event (wet or dry) and the duration of the event. Other controversies include whether it was driven by internal or external forcing, whether it was a climate "regime transition" or "transient anomaly", and whether it was really global or only regional.

A recent synthesis by Railsback et al. (2018) has provided a comprehensive overview on the global expression of this event and suggested that wetter conditions could occur in southern Africa that contrast with the widespread droughts in the Northern Hemisphere. This synthesis also points to the possibility of a southward movement of global atmospheric circulation cells including the Intertropical Convergence Zone (ITCZ) as the driver of the event, that potentially also affect the Southern Hemisphere mid-

latitude regions. I extend the cellulose isotope analysis of the peat core from Ariel Peatland (AP) in Chapter 4 to the rest of the entire core to investigate the expression of "4.2 ka event" in southern Patagonia, taking advantage that *Sphagnum* mosses dominate the peat macrofossils throughout this interval. However, I find that the record provides better evidence for the weaker teleconnection of the El Niño-Southern Oscillation (ENSO) during that time.

2. Methods

A major volcanic eruption of the Mount Burney also occurred 4200 cal. yr BP at coincidence (Stern, 2008). The peat core has a 1-cm visible tephra layer, but loss-on-ignition data suggest that the ashes spread across 5-cm peat section due to the reworking process. Based on the interpolation from multiple tephra layer records, it has been estimated that the original tephra layer should be between 0.1 and 1 cm in thickness at the site AP (Kilian et al., 2006). Considering that tephra deposition could cause long-lasting ecosystem damage and perturbations of paleoclimate proxy records (Kilian et al., 2006), caution should be taken for data interpretation. In addition, the current age-depth model is poorly constrained for the lower half of this peat core, with only three age determinations from ^{14}C dating analysis during the period 5400–3300 cal. yr BP (Figure D2).

3. Results and Discussion

The results are presented in Figure E1. Cellulose $\delta^{13}C$ data show a short shift towards lower values around 4200 cal. yr BP, suggesting that peat mosses became drier. This isotope shift occurred below the tephra layer, so this signal is not affected by tephra deposition. This dry interval is also supported by a lower lake-level with a less surface runoff inferred from multi-proxy data at Laguna Potrok Aike (LPA) in Argentina (52°S) (Mayr et al., 2007). As a preliminary inference, these consistent signals depict the "4.2 ka

event" as a drier interval on the leeward side of southern Patagonia. However, I acknowledge that this change did not stand out as a major event but actually there are several larger-magnitude shifts over the last 5400 years at the site.

Cellulose $\delta^{18}O$ data show a short shift slightly towards higher values during the interval when cellulose $\delta^{13}C$ values were the lowest. The apparent negative correlation between *Sphagnum* cellulose $\delta^{13}C$ and $\delta^{18}O$ data indicates that the increase in cellulose $\delta^{18}O$ could be explained by a greater evaporative enrichment as discussed in Chapter 2. This explanation is different from Chapter 4, in which cellulose $\delta^{18}O$ data were argued to reflect the changes in precipitation $\delta^{18}O$ as a result of changes in atmospheric circulation pattern.

Furthermore, the cellulose $\delta^{18}O$ data show much smaller centennial-scale fluctuations from 5400 to 3300 cal. yr BP than during the last 2000 years. I propose that a lack of centennial-scale variability in precipitation $\delta^{18}O$ prevailed during 5400–3300 cal. yr BP, which is remarkably different from the recent 2000 years. Recent studies from tropical corals suggest that the ENSO variance was significantly weaker during 5000–3000 cal. yr BP than pre-industrial period (Grothe et al., 2019). If ENSO regime was quiet, its Rossby wave teleconnection to southern Patagonia would be much reduced. As such, the synoptic weather types with blocking conditions that favor easterly winds would not occur frequently. I hypothesize that synoptic-scale patterns in southern Patagonia were persistently dominated by disturbance-embedded westerlies during 5000–3000 cal. yr BP, despite that the overall strength of westerlies could vary on centennial timescale. Notably, airborne pollen data from LPA suggest that the westerlies became stronger around the "4.2 ka event" that might enhance the rain shadow condition in southern Patagonia (Mayr et al., 2007) but increase precipitation delivery to the Andean *Nothofagus* forest (Moreno et al., 2018). However, the stronger westerlies did not decrease the precipitation $\delta^{18}O$ relative to the periods when the westerlies were weaker. If

the westerlies were indeed weaker prior to the "4.2 ka event", during that time easterly winds bringing in precipitation with higher $\delta^{18}O$ that occur as an important synoptic weather type in recent century was not yet established. This could explain the lack of variability in precipitation $\delta^{18}O$ in southern Patagonia when ENSO was quiet.

Overall, the stronger westerlies and the enhanced rain shadow around the "4.2 ka event" in southern Patagonia could be driven by a "southward push" mechanism of ITCZ that has occurred during the last deglaciation (Montade et al., 2015). Therefore, it supports the notion that the "4.2 ka event" is also a result of global ocean-atmosphere reorganization.

4. Acknowledgements

This study benefited from discussion with Julie Loisel. Christoph Mayr provided raw data from Laguna Potrok Aike with an updated age-depth model.

5. References

Booth, R. K., Jackson, S. T., Forman, S. L., Kutzbach, J. E., Bettis, E. A., Kreigs, J., & Wright, D. K. (2005). A severe centennial-scale drought in midcontinental North America 4200 years ago and apparent global linkages. *The Holocene*, *15*(3), 321–328.

Cullen, H. M., deMenocal, P. B., Hemming, S., Hemming, G., Brown, F. H., Guilderson, T., & Sirocko, F. (2000). Climate change and the collapse of the Akkadian empire: Evidence from the deep sea. *Geology*, *28*(4), 379–382.

Grothe, P. R., Cobb, K. M., Liguori, G., Di Lorenzo, E., Capotondi, A., Lu, Y., et al. (2019). Enhanced El Niño-Southern Oscillation variability in recent decades. *Geophysical Research Letters*, *46*.

Kilian, R., Biester, H., Behrmann, J., Baeza, O., Fesq-Martin, M., Hohner, M., et al. (2006). Millennium-scale volcanic impact on a superhumid and pristine ecosystem. *Geology*, *34*(8), 609–612.

Mayr, C., Wille, M., Haberzettl, T., Fey, M., Janssen, S., Lücke, A., et al. (2007). Holocene variability of the Southern Hemisphere westerlies in Argentinean Patagonia (52°S). *Quaternary Science Reviews*, *26*(5), 579–584.

Montade, V., Kageyama, M., Combourieu-Nebout, N., Ledru, M. P., Michel, E., Siani, G. and Kissel, C. (2015). Teleconnection between the Intertropical Convergence Zone and southern westerly winds throughout the last deglaciation. *Geology*, *43*(8), 735–738.

Moreno, P. I., Vilanova, I., Villa-Martínez, R., Dunbar, R. B., Mucciarone, D. A., Kaplan, M. R., et al. (2018). Onset and evolution of Southern Annular Mode-like changes at centennial timescale. *Scientific Reports*, *8*, 3458.

Railsback, L. B., Liang, F., Brook, G. A., Voarintsoa, N. R. G., Sletten, H. R., Marais, E., et al. (2018). The timing, two-pulsed nature, and variable climatic expression of the 4.2 ka event: A review and new high-resolution stalagmite data from Namibia. *Quaternary Science Reviews*, *186*, 78–90.

Staubwasser, M., Sirocko, F., Grootes, P. M., & Segl, M. (2003). Climate change at the 4.2 ka BP termination of the Indus valley civilization and Holocene south Asian monsoon variability. *Geophysical Research Letters*, *30*(8).

Stern, C. R. (2008). Holocene tephrochronology record of large explosive eruptions in the southernmost Patagonian Andes. *Bulletin of Volcanology*, *70*(4), 435–454.

Walker, M., Gibbard, P., Head, M. J., Berkelhammer, M., Björck, S., Cheng, H., et al. (2019). Formal subdivision of the Holocene series/epoch: a summary. *Journal of the Geological Society of India*, *93*(2), 135–141.

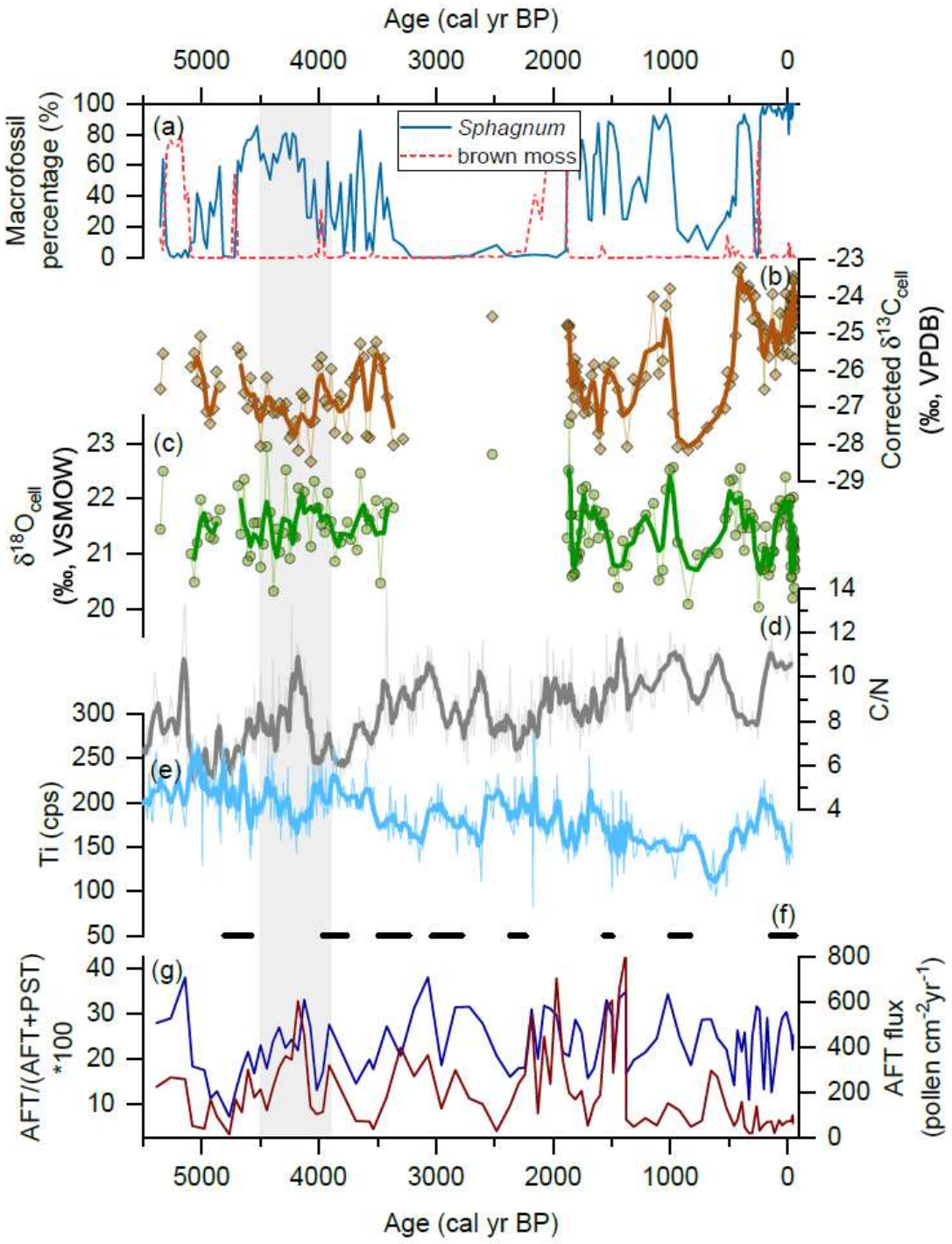

Figure E1. Summary of the whole peta-core analysis of PAT16-AP1 and comparison with other records. (a) AP macrofossil percentage; (b) AP *Sphagnum* cellulose $\delta^{13}C$ corrected for $\delta^{13}C$ of atmospheric CO_2 (see Chapter 4); (c) AP *Sphagnum* cellulose $\delta^{18}O$;

(d) LPA organic matter C:N ratios with higher values indicating lower lake levels (Mayr et al., 2007); (e) LPA sediment Ti content with lower values indicating lower surface runoff (Mayr et al., 2007); (f) The warm/dry intervals documented by paleoecological records from Lago Cipreses close to Andean *Nothofagus* forests (Moreno et al., 2018); (g) LPA airborne pollen index including the ratio of Andean forest taxa (AFT) to AFT plus Patagonian steppe taxa (PST) (blue) and AFT pollen flux (red) (Mayr et al., 2007). The light gray vertical bar indicates the period between 4500–3900 cal. yr BP bracketing the "4.2 ka event" considering the large uncertainty of current age-depth model.

Appendix F

Late Holocene hydroclimate of South Georgia inferred from carbon and oxygen isotope analysis of *Sphagnum* and brown mosses in peat

1. Introduction

As discussed in Chapter 4 and the general conclusion of this dissertation, diverse synoptic-scale patterns play a more important role in regulating regional climate in the mid-latitude regions of the Southern Hemisphere. Therefore, developing new paleoclimate records from different sectors of the Southern Ocean will provide a more complete view on the past climate variability in this region that potentially provide new insights into the evolution of the SHWW. This study focuses on the island of South Georgia located in the South Atlantic Ocean. There have been a number of studies that have investigated glacier and ecosystem changes in South Georgia during the late glacial and Holocene (e.g., Birnie, 1990; Van der Putten et al., 2004; Van der Putten et al., 2009; Clapperton et al., 1989; Oppedal et al., 2018). Notably, South Georgia is in the locus of complex ocean water mass circulation in the Southern Ocean. As a result, regional climate is sensitive to latitudinal variations in the position of the Antarctic Polar Front that is itself modulated by the SHWW. The regional topography of South Georgia is comparable to southern Patagonia. It has glaciated mountains on the west and partly vegetated coastal areas on the east, but South Georgia is located south of the Antarctic Polar Front so its climate is much colder than Patagonia.

Extensive and diverse types of peat-forming ecosystems are found on the deglaciated part of eastern South Georgia, including some bogs with *Sphagnum* mosses (Van der Putten et al., 2012). Prince Olav Bog (POB) is such a *Sphagnum*-dominated

peat bog, located in the Prince Olav Harbour by the Possession Bay. At this site, *Sphagnum fimbriatum* form dry hummock-like patches, surrounded by wet hollows that are dominated by monocots and brown mosses. A peat core was collected at one of the *Sphagnum* patches in 2008 and is under a multi-proxy investigation to reconstruct climatic and environmental history in South Georgia. The entire core is 380-long with visible peat layers of different botanical compositions. The complete chronology is still pending but has been constrained by several ^{14}C dates, and peat was initiated around 9500 cal. yr BP at this site.

2. Methods

Peat macrofossils were analyzed at every 4 cm to characterize the botanical composition of these peat samples. For samples that have abundant identifiable *Sphagnum fimbriatum* and brown moss (*Warnstorfia sp.* or cf. *Drepanocladus sp.*) macrofossils, I picked out these macrofossils for cellulose extraction. For *Sphagnum*, I used stem macrofossils for cellulose extraction following the method presented in Chapters 2 and 4. For brown mosses, I used bulk (whole plant) macrofossils for cellulose extraction. The cellulose yield is much lower for brown mosses than *Sphagnum*, thus the brown moss macrofossils were only subjected to two rounds of acidified sodium chlorite bleaching before being treated with sodium hydroxide, with another one round of acidified sodium chlorite bleaching after. Other procedures including cellulose isotope analysis follow the Chapters 2 and 4. From *Sphagnum*, *Warnstorfia*, and cf. *Drepanocladus* macrofossils, there are 42, 22, and 5 cellulose samples measured for $\delta^{13}C$, and there are 45, 36, and 5 cellulose samples measured for $\delta^{18}O$, respectively.

3. Results and Discussion

Selective moss macrofossil abundances and isotope data are presented in Figure F1 with a preliminary age-depth model (not shown). The moss-dominated vegetation was established around 7,000 cal. yr BP and probably even earlier. For intervals with low moss macrofossil abundances, these peat samples mainly compose of either unidentifiable organic matter particles (smaller than 250 μm) or monocots (grasses). The moss species had multiple turnovers over time, except between 2500 and 1000 cal. yr BP, during which the monocots became dominant plants. If samples were analyzed at every centimeter, I expect that moss species turnover might be even more frequent.

Cellulose $\delta^{13}C$ data show a long-term decreasing trend of >4‰ from 5000 cal yr BP to present, with the recent >2‰ shift that seems not entirely caused by the Suess effect (~1.5‰), although the current chronology has not been completed for the recent peat section. *Warnstorfia* cellulose $\delta^{13}C$ are around 2‰ higher than *Sphagnum* cellulose $\delta^{13}C$, suggesting that *Warnstorfia* leaves might have a thicker external water film layer. *Sphagnum* cellulose $\delta^{18}O$ data show an increasing trend from 5000 to 2500 cal. yr BP and then a plateau with some fluctuations. *Warnstorfia* cellulose $\delta^{18}O$ are around 2.5‰ higher than *Sphagnum* cellulose $\delta^{18}O$ and have a larger variability. These observations conform to the unique "water buffer" physiology in *Sphagnum* that preserve a smaller degree of evaporative enrichment signal even though brown mosses often prefer a wetter habitat (see Chapter 3).

Sphagnum cellulose $\delta^{13}C$ and $\delta^{18}O$ have a negative correlation (Figure F2), except the most recent 4 samples that likely have been contaminated by the Suess effect and could be corrected once a complete ^{210}Pb chronology is available. This down-core negative correlation implies a common main driver. From the detailed isotopic physiology study presented in Chapter 2, I infer that both variations in cellulose $\delta^{13}C$ and $\delta^{18}O$ are mainly controlled by changes in *Sphagnum* water content over time. Under this scenario, *Sphagnum* cellulose $\delta^{13}C$ data indicate that POB site likely experienced a long-

term trend of peat bog drying and became the driest during the recent period. The increase in cellulose $\delta^{18}O$ from 5000 to 2500 cal. yr BP suggests that the degree of evaporative enrichment became larger with drying, although variations in precipitation $\delta^{18}O$ are also possible to affect cellulose $\delta^{18}O$ signals throughout the record but difficult to constrain. Whereas the similar correlation is not found for *Warnstorfia* data, meaning that isotopic variations in brown mosses are more physiologically complex and subjected to other processes. Although *Sphagnum* and *Warnstorfia* cellulose $\delta^{18}O$ have an overall parallel trend, the correlation is not significant for samples where both *Sphagnum* and *Warnstorfia* cellulose $\delta^{18}O$ data are available (Figure F2).

The millennial-scale peat bog drying inferred from the dual isotope analysis might be driven by climate shift. Paleoecological analysis from another peatland core in South Georgia also showed that a shift from wet to dry condition occurred around 4000 cal. yr BP and the dry condition sustained until 2800 cal. yr BP (Van der Putten et al., 2004). Similar drying shift was also found from another peatbank core in South Georgia at 4400 cal. yr BP (Van der Putten et al., 2009). These changes are similar to what the POB record implied that likely will be further constrained by an improved chronology. The consistent observations among multiple peat records from South Georgia indicate the trend shown in POB data is less likely caused by site-specific ecohydrological self-regulating processes. The cause for the drying trend might be increasing temperature rather than decreasing precipitation. Modeling studies suggest that temperature changes cause lasting alternations to bog surface wetness, but precipitation changes only cause transient shifts that then have homeostatic recovery (Morris et al., 2015). This possibility is supported by the multi-proxy and temperature reconstruction from Fan Lake on Annenkov Island, west off the main island of South Georgia, which showed the Mid-Holocene Hypsithermal period between 4500 and 2800 cal. yr BP (Foster et al., 2016). Another warming period from Fan Lake record is the Medieval Climate Anomaly

between 1200 and 600 cal yr BP, while POB *Sphagnum* cellulose $\delta^{18}O$ data also show increasing values in response to this warming interval.

4. Acknowledgements

The POB samples were provided by Stephen Roberts and Dominic Hodgson from the British Antarctic Survey. Other personnel also contribute to chronology development and multi-proxy analysis of POB.

5. References

Birnie, J. (1990). Holocene environmental change in South Georgia: Evidence from lake sediments. *Journal of Quaternary Science*, *5*(3), 171–187.

Clapperton, C. M., Sugden, D. E., Birnie, J., & Wilson, M. J. (1989). Late-Glacial and Holocene Glacier Fluctuations and Environmental Change on South Georgia, Southern Ocean. *Quaternary Research*, *31*(2), 210–228.

Foster, L. C., Pearson, E. J., Juggins, S., Hodgson, D. A., Saunders, K. M., Verleyen, E., & Roberts, S. J. (2016). Development of a regional glycerol dialkyl glycerol tetraether (GDGT)–temperature calibration for Antarctic and sub-Antarctic lakes. *Earth and Planetary Science Letters*, *433*, 370–379.

Morris, P. J., Baird, A. J., Young, D. M., & Swindles, G. T. (2015). Untangling climate signals from autogenic changes in long-term peatland development. *Geophysical Research Letters*, *42*(24), 10788–10797.

Oppedal, L. T., Bakke, J., Paasche, Ø., Werner, J. P., & van der Bilt, W. G. M. (2018). Cirque glacier on South Georgia shows centennial bariability over the last 7000 years. *Frontiers in Earth Science*, *6*(2).

Risi, C., Noone, D., Worden, J., Frankenberg, C., Stiller, G., Kiefer, M., et al. (2012). Process-evaluation of tropospheric humidity simulated by general circulation models using water vapor isotopologues: 1. Comparison between models and observations. *Journal of Geophysical Research: Atmospheres*, *117*, D05303.

Rubino, M., Etheridge, D. M., Trudinger, C. M., Allison, C. E., Battle, M. O., Langenfelds, R. L., et al. (2013). A revised 1000 year atmospheric $\delta^{13}C$-CO_2 record from Law Dome and South Pole, Antarctica. *Journal of Geophysical Research: Atmospheres*, *118*(15), 8482–8499.

Van der Putten, N., Stieperaere, H., Verbruggen, C., & Ochyra, R. (2004). Holocene palaeoecology and climate history of South Georgia (sub-Antarctica) based on a macrofossil record of bryophytes and seeds. *The Holocene*, *14*(3), 382–392.

Van der Putten, N., Verbruggen, C., Ochyra, R., Spassov, S., de Beaulieu, J. L., De Dapper, M., et al. (2009). Peat bank growth, Holocene palaeoecology and climate history of South Georgia (sub-Antarctica), based on a botanical macrofossil record. *Quaternary Science Reviews*, *28*(1), 65–79.

Van der Putten, N., Mauquoy, D., Verbruggen, C., & Björck, S. (2012). Subantarctic peatlands and their potential as palaeoenvironmental and palaeoclimatic archives. *Quaternary International*, *268*, 65–76.

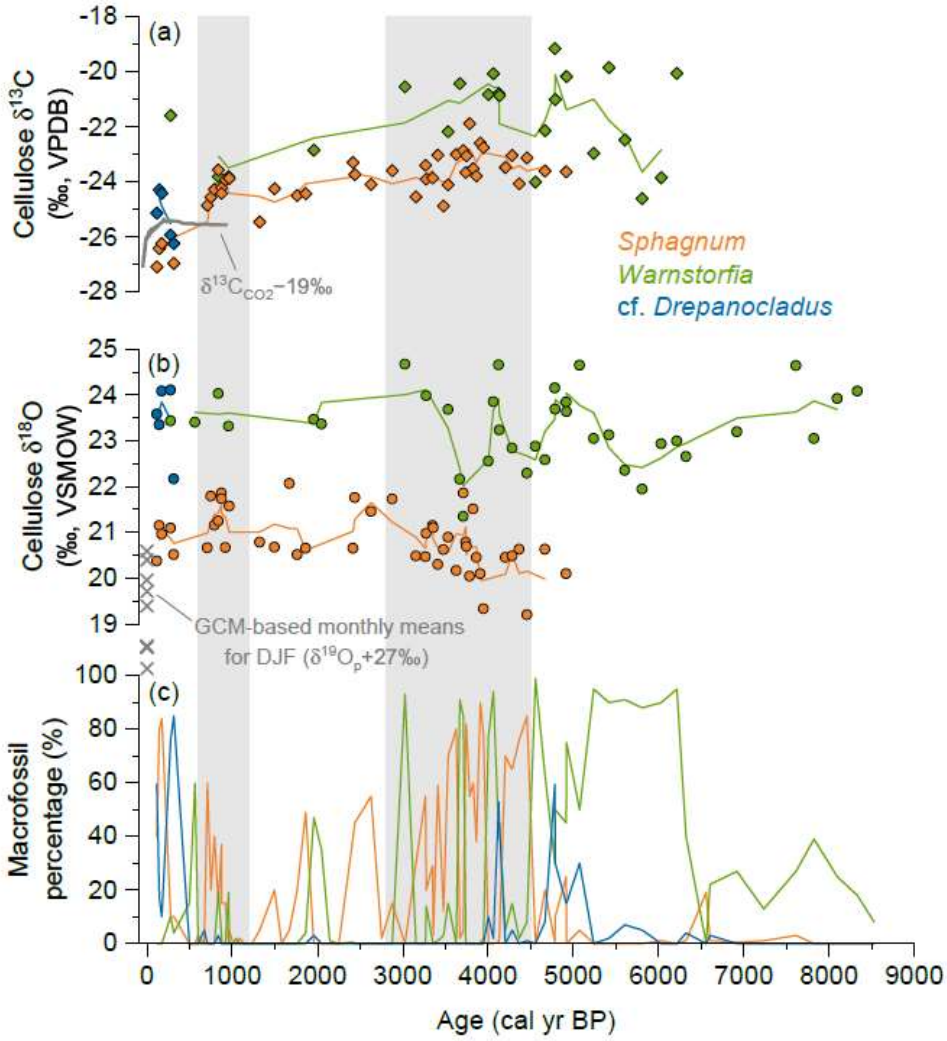

Figure F1. Summary of POB peat core analysis. Results for (a) cellulose $\delta^{13}C$, (b) cellulose $\delta^{18}O$, and (c) macrofossil analysis are plotted against preliminary chronology. Individual cellulose data points are presented as dots with three-point average as lines. Different colors refer to different mosses. The scale of Suess effect on $\delta^{13}C$ of atmospheric CO_2 is presented in (a) for reference (Rubino et al., 2013). Monthly mean precipitation $\delta^{18}O$ from nudged isotope-enabled global circulation models (see Chapter 3; Risi et al., 2012) at site POB for austral summer at POB is shown as crosses in (b). The gray vertical bars indicate warming periods from Fan Lake (Foster et al., 2016).

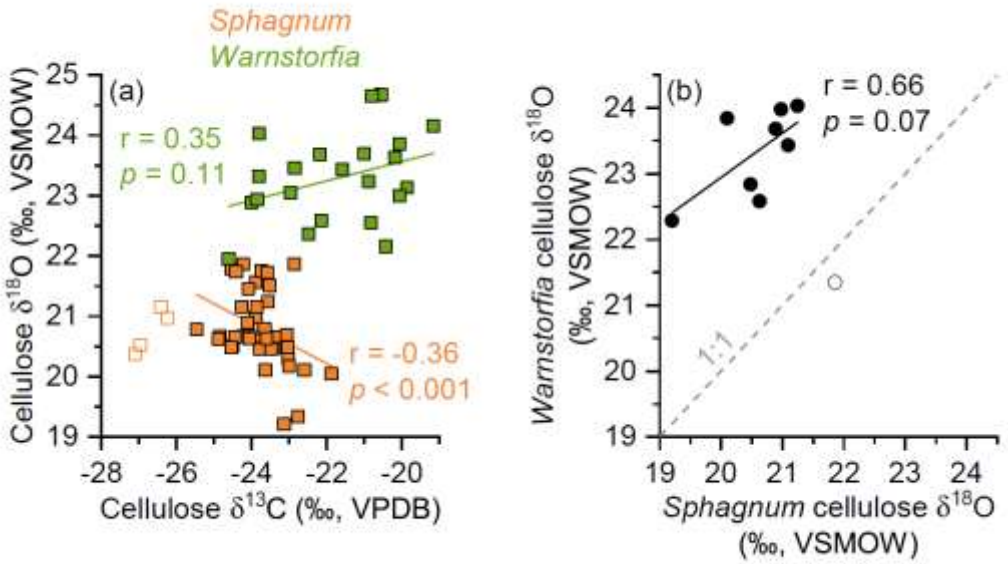

Figure F2. Correlations between moss cellulose isotope data from POB peat core. (a) Correlation between cellulose $\delta^{13}C$ and cellulose $\delta^{18}O$ for *Sphagnum* and *Warnstorfia*. Results are shown with regression line. The open orange squares are data from the the most recent 4 samples that likely have been contaminated by the Suess effect. (b) Correlation between *Warnstorfia* cellulose $\delta^{18}O$ and *Sphagnum* cellulose $\delta^{18}O$. The regression line (black line) could be established only after an outlier (open dots) was removed. Also shown were the 1:1 line that illustrates *Warnstorfia* cellulose $\delta^{18}O$ are apparently higher than *Sphagnum* cellulose $\delta^{18}O$ from the same peat sample.

Appendix G

Roles of temperature and meltwater in affecting peat accumulation of a glacier-fed peat bog on South Georgia

1. Introduction

Appendix II has briefly introduced the importance of developing new paleoclimate records from peat bogs in currently unglaciated terrains on South Georgia. Glaciers in South Georgia are sensitive to regional climate change, and there have been some studies exploring past glacier variability in this region. One of the approaches is using sedimentary records from glacier-fed lakes and peat bogs to reconstruct the past size of up-valley glaciers. One of such studies have been carried out on Diamond glacier in the Olsen Valley of Cumberland West Bay, where there is a pair of lake (Diamond Lake) and bog (Diamond bog; DB) in downstream location fed by glacier meltwater (Oppedal et al., 2018). Past variability of the Diamond glacier has been reconstructed using a multi-proxy approach that showed consistent sedimentary signals in both lake and bog records. For example, both records showed a sudden and large increase in silt and sand at about 2600 cal. yr BP. That study raised the potential of using glacier-fed bogs as the archive to reconstruct past glacier variability. Similar peat-forming ecosystems could also be found in down-stream settings in South Georgia and elsewhere.

I extended the analysis of the peat core collected from the DB to understand how past glacier activity has affected peat bog habitat and development, using plant macrofossils, cellulose carbon and oxygen isotopes of brown mosses, and peat accumulation calculation. Peat-forming ecosystems like the DB are very common on many recently deglaciated “frontier” areas. These peat bogs usually first colonize shallow

depression inundated by meltwater and their functions are not stable and strongly affected by glacier processes. Compared to mature *Sphagnum*-dominated peat bogs that dominate boreal regions, there are less studies to characterize the ecosystem processes of these "frontier" peat bogs using peat core data. However, these peat bogs including the DB could be seen as an early stage of peat bog development. Therefore, understanding the ecosystem processes of these peat bogs and their interactions with nearby glaciers could improve our understanding of the promoting and limiting factors for peat initiation, accumulation, and expansion.

2. Materials and methods

The 204-cm-long DB peat core was collected from an exposed section of a stream cut bank, by which the meltwater stream has cut deep meanders into the bog. The chronology of this peat core has been constrained by multiple ^{14}C ages (Oppedal et al., 2018). The lithology of peat core could be divided into two distinct parts: the lower section (204–95 cm) of dense black peat (Unit A), and the upper section (95–0 cm) of clayey peat interbedded with minerogenic materials (Unit B). The transition occurred around 2600 cal. yr BP.

Plant macrofossils were analyzed at every 2-cm. For brown moss-dominated samples, I analyzed cellulose $\delta^{13}C$ and $\delta^{18}O$ from the bulk tissues of hand-picked brown moss macrofossils following the same method presented in Appendix F. Most of the isotope analysis was carried out on *Warnstorfia sp.*, plus a few on *Sanionia sp.*, which could be the dominant macrofossil in a few samples. Using the updated age-depth model and loss-on-ignition data, I calculated the accumulation rate of organic matter (OM) and inorganic matter (IOM) throughout the peat core.

3. Results

The results are presented in Figure G1 with comparisons with other proxy data from the same core or from other sites in the region. The Unit A section shows fluctuations in abundance of brown mosses versus monocots. After the transition into the Unit B around 2600 cal. yr BP, the plant macrofossils were dominated by monocots. At around 500 cal. yr BP, brown mosses replaced monocots and then disappeared since 150 cal. yr BP.

The brown moss cellulose $\delta^{13}C$ and $\delta^{18}O$ data show very large ranges of variability, up to 18‰ and 8‰, respectively, and these two isotope ratios are positively correlated. Notably, there are four "spikes" in negative $\delta^{13}C$ and $\delta^{18}O$ excursions at 4200, 3800, 3100, and 100 cal. yr BP.

The OM accumulation rate shows variability spanning over an order of magnitude that could be as high as 100–500 g OM m^{-2} yr^{-1} for Unit A and as low as 30 g OM m^{-2} yr^{-1} for the period 2400–1800 cal. yr BP. The OM accumulation rate increased steadily since 1800 cal. yr BP, reaching a value of 140 gOM m^{-2} yr^{-1} at 500 cal. yr BP, followed by a recent jump that could be attributed to the lack of decomposition in recently accumulated OM. The accumulation rate of IOM seems to be parallel with OM for the Unit A, but since the transition to the Unit B the two trends seem negatively correlated on shorter timescale but positively correlated on longer timescale, until to the similar recent jump (Figure G2). This recent abrupt increase in IOM accumulation rate might be due to the impact of recent meandering stream that reached close to coring location, thereby the mineral materials were transported by glacial meltwater when the stream flooded the peatland.

4. Discussion

4.1 The direct and indirect effect of temperature on ecosystem processes and peat accumulation

The OM accumulation rate at the DB shows good correspondence with the quantitative summer temperature reconstruction from Fan Lake on a small island, just west of the main island of South Georgia (Foster et al., 2016). The Fan Lake is located in a different regional topographical configuration from the DB, but the temperature change at Fan Lake should reflect regional feature that is related to the position of the Antarctic Polar Front. The three temperature maxima at 3500, 2600 and 600 cal yr BP were associated with the three OM accumulation maxima at the DB. In particular, the OM accumulation rate could be as high as 500 g OM m^{-2} yr^{-1} during 3900–3600 cal yr BP. If this highest value was converted to carbon accumulation rate using a normal carbon content of OM at 50%, a corresponding carbon accumulation rate of 250 gC m^{-2} yr^{-1} is very high among any peat-forming ecosystems (Gallego-Sala et al., 2018).

I propose that temperature exerts both direct and indirect controls on peat accumulation rate at the DB. As for the direct effect, increasing temperature would lengthen the growing season and enhance plant productivity that could be more than accelerating peat decomposition. This mechanism has been well demonstrated from global peat accumulation data (Gallego-Sala et al., 2018).

As for the indirect effect, increasing temperature would decrease the glacier size and limit the influx of sediment-laden glacial meltwater that would have disturbed the peat-forming ecosystem at the DB. When the OM accumulation rate was higher under a warmer climate as seen in the Unit A, botanical composition of peat was dominated by brown mosses. The OM accumulation rate was extremely low after the apparent lithological change at 2600 cal. yr BP that indicates an abrupt glacier advance and the initiation of large influx of glacial sediments to both the lake and bog. This shift seems to disrupt the local peat bog habitat, when brown mosses were replaced by monocots. Similar replacements of brown mosses also occurred within the Unit A, such as at 3300 cal yr BP, when magnetic susceptibility data show relatively higher values. These

coherent shifts in depositional environments, local peat-forming plants, and peat accumulation rate, imply that brown mosses do not favor disturbance such as the increased glacial sediments, without which brown mosses could have persisted in a very productive peat-forming ecosystem. This hypothesis is further supported by the observation that the OM and IOM accumulation rates are negatively correlated on shorter timescale since the glacial meltwater started to persistently affect the DB at 2600 cal yr BP.

4.2 The role of snow meltwater pulses in maintaining peat accumulation

Before 2600 cal yr BP, the glacial meltwater has not yet affected the DB. This observation has been argued to reflect a much smaller cirque glacier (Oppedal et al., 2018). Under such a warmer climate, although the plant productivity was enhanced, the ensuing high evaporation demand would have limited the production of brown mosses and the preservation of peat due to an overall drier condition. I propose that the snow meltwater, in contrast to the glacier meltwater, has maintained such an overall rapid peat accumulation of brown mosses.

This hypothesis is based on the paired cellulose $\delta^{13}C$ and $\delta^{18}O$ data that indicate frequent inundations for the Unit A. The large ranges of cellulose $\delta^{13}C$ and $\delta^{18}O$ variability and their negative correlation throughout the peat core provide direct clues on their environmental controlling factors. The extremely low cellulose $\delta^{13}C$ value (Markel et al., 2010) is not common in bryophytes but could be only explained by the uptake of recycled and methane-derived CO_2 for photosynthesis or an extremely wet or sub-aquatic habitat (Zibulski et al., 2017). These extremely low cellulose $\delta^{13}C$ occurred with corresponding very low cellulose $\delta^{18}O$ that are only possible with a distinct water source with very low $\delta^{18}O$. I infer that this water source was snow (winter precipitation) meltwater. The coupled cellulose $\delta^{13}C$ and $\delta^{18}O$ data suggest several intervals of

snowmelt inundations that based on the current age-depth model could persist for several decades. The snow meltwater wetted peat bogs and played an important role in maintaining brown moss habitat and peat accumulation. In addition, one of such snowmelt inundations seems to initiate the peat accumulation at this site at 4200 cal. yr BP. By contrast, the relatively high cellulose $\delta^{13}C$ and $\delta^{18}O$ values at 3600–3200 cal. yr BP suggest the moisture source for brown mosses is mainly derived from summer precipitation. During this interval, without moisture input from snow meltwater, the OM accumulation rate decreased from 500 to 100 g OM m^{-2} yr^{-1}, which was followed by another inundation interval with high OM accumulation rate of 200 g OM m^{-2} yr^{-1}.

This snow meltwater could be derived from valley slope or within the local basin, but not directly from glacial meltwater that should have transported a large volume of glacial sediments and disturbed the site. This opposite consequence of snow- and glacier-derived meltwater could also explain the varying correlation between OM and IOM accumulation rates throughout the core. When the site was not affected by glacier meltwater, snowmelt water could also transport some paraglacial sediments that did not strongly disturb but could moisten the brown moss habitat. Such inundations could be formed by an increased snow accumulation in cold season and an increased warm season temperature that enhanced the melting of snow. Alternatively, such inundations also could be caused by non-climatic factors, such as change in local topography and vegetation cover that affected water flows.

4.3 Promoting and limiting factors of "frontier" peat-forming ecosystems

It has been well recognized that temperature and moisture balance exert a coordinated control on peat accumulation rate, while temperature and plant productivity might be more important in enhancing the carbon sink capacity of peatlands in cold regions. This knowledge has been gained from global peat core data that were mainly

collected from stable *Sphagnum*-dominated peat bogs in boreal regions (Gallego-Sala et al., 2018). This direct temperature effect was also demonstrated at the DB as shown by the rapid peat accumulation rate during the Mid Holocene Hypsithermal, during which summer temperature was at least 5°C higher than today (Foster et al., 2016).

On the other hand, peat accumulation in an unstable and dynamic peat-forming environment is highly sensitive to the frequent snow and glacier meltwater inputs. From the peat core analysis of the DB, I found that glacier meltwater accompanying with a large influx of glacial sediments is an important limiting factor that could disrupt or even terminate the peat-forming processes. Whereas the snow meltwater—which is also remobilizing some but less paraglacial sediments nearby—could be a promoting factor to sustain a rapid peat accumulation from the biomass of non-*Sphagnum* bryophyte species.

Taking the observations from the DB into the general process understanding of peatlands, my results suggest that peat initiation, accumulation, and expansion are best favored by stable hydrological conditions. This might further explain the 4000-yr delay between deglaciation and peatland initiation in North America (Gorham et al., 2007). Many of current frontier peat-forming ecosystems are strongly limited by the instability brought by the ice sheet- and glacier-derived meltwater. This new conceptual framework helps to understand the current and future fate of global carbon sequestration capacity for frontier peat-forming ecosystems worldwide.

5. Acknowledgements

The DB samples are provided by Jostein Bakke from University of Bergen. This work is only possible with the previous core analysis by Lea Toska Oppedal. The age-depth model was developed by Johannes Werner.

6. References

Foster, L. C., Pearson, E. J., Juggins, S., Hodgson, D. A., Saunders, K. M., Verleyen, E., & Roberts, S. J. (2016). Development of a regional glycerol dialkyl glycerol tetraether (GDGT)–temperature calibration for Antarctic and sub-Antarctic lakes. *Earth and Planetary Science Letters*, *433*, 370–379.

Gallego-Sala, A. V., Charman, D. J., Brewer, S., Page, S. E., Prentice, I. C., Friedlingstein, P., et al. (2018). Latitudinal limits to the predicted increase of the peatland carbon sink with warming. *Nature Climate Change*, *8*(10), 907–913.

Gorham, E., Lehman, C., Dyke, A., Janssens, J., & Dyke, L. (2007). Temporal and spatial aspects of peatland initiation following deglaciation in North America. *Quaternary Science Reviews*, *26*(3), 300–311.

Markel, E. R., Booth, R. K., & Qin, Y. (2010). Testate amoebae and $\delta^{13}C$ of *Sphagnum* as surface-moisture proxies in Alaskan peatlands. *The Holocene*, *20*(3), 463–475.

Oppedal, L. T., Bakke, J., Paasche, Ø., Werner, J. P., & van der Bilt, W. G. M. (2018). Cirque glacier on South Georgia shows centennial variability over the last 7000 years. *Frontiers in Earth Science*, *6*(2).

Zibulski, R., Wesener, F., Wilkes, H., Plessen, B., Pestryakova, L. A., & Herzschuh, U. (2017). C/N ratio, stable isotope ($\delta^{13}C$, $\delta^{15}N$), and *n*-alkane patterns of brown mosses along hydrological gradients of low-centred polygons of the Siberian Arctic. *Biogeosciences*, *14*(6), 1617–1630.

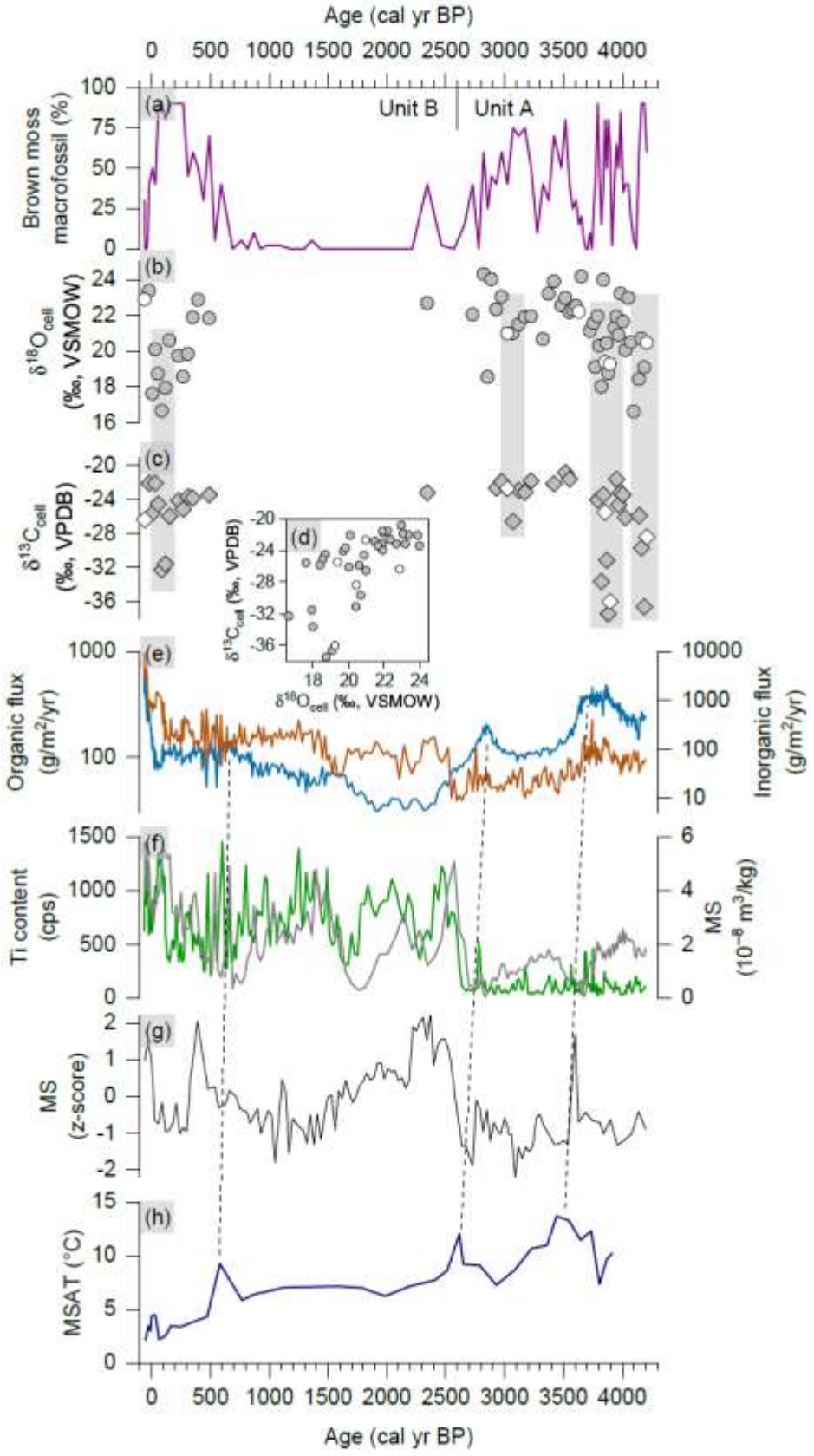
Age (cal yr BP)
0 500 1000 1500 2000 2500 3000 3500 4000
(a)
Unit B
Unit A
Brown moss macrofossil (%)
100 75 50 25 0
(b)
$\delta^{18}O_{cell}$ (‰, VSMOW)
24 22 20 18 16
(c)
$\delta^{13}C_{cell}$ (‰, VPDB)
-20 -24 -28 -32 -36
(d)
$\delta^{13}C_{cell}$ (‰, VPDB)
-20 -24 -28 -32 -36
18 20 22 24
$\delta^{18}O_{cell}$ (‰, VSMOW)
(e)
Organic flux (g/m²/yr)
1000 100
10000 1000 100 10
Inorganic flux (g/m²/yr)
(f)
Ti content (cps)
1500 1000 500 0
6 4 2 0
MS (10^{-8} m³/kg)
(g)
MS (z-score)
2 1 0 -1 -2
(h)
MSAT (°C)
15 10 5 0
0 500 1000 1500 2000 2500 3000 3500 4000
Age (cal yr BP)

Figure G1. Summary of analysis on peat core DB and comparisons with other regional records. (a) The percentage of brown moss macrofossil of peat core DB. The transition between the Unit A and Unit B is shown on top axis. (b) Brown moss cellulose $\delta^{18}O$. (c) Brown moss cellulose $\delta^{13}C$. (d) The biplot between cellulose $\delta^{18}O$ and $\delta^{13}C$. In (b) and (c), the gray vertical bars indicate the inferred inundation intervals. In (b)–(d), gray and white symbols are data points from *Warnstorfia* and *Sanionia* macrofossils, respectively. (e) Organic matter (blue) and inorganic matter (brown) accumulation rates of peat core DB on log scale. (f) Ti content (green; cps: counts per second) and magnetic susceptibility (gray) of peat core DB (Oppedal et al., 2018). (g) Magnetic susceptibility (gray) of core collected from Diamond Lake (Oppedal et al., 2018). (h) Mean summer air temperature reconstructed from Fan Lake (Foster et al., 2016). The dashed lines between (e) and (h) show the possible matches between high organic accumulation rate of peat core DB and high regional temperature.

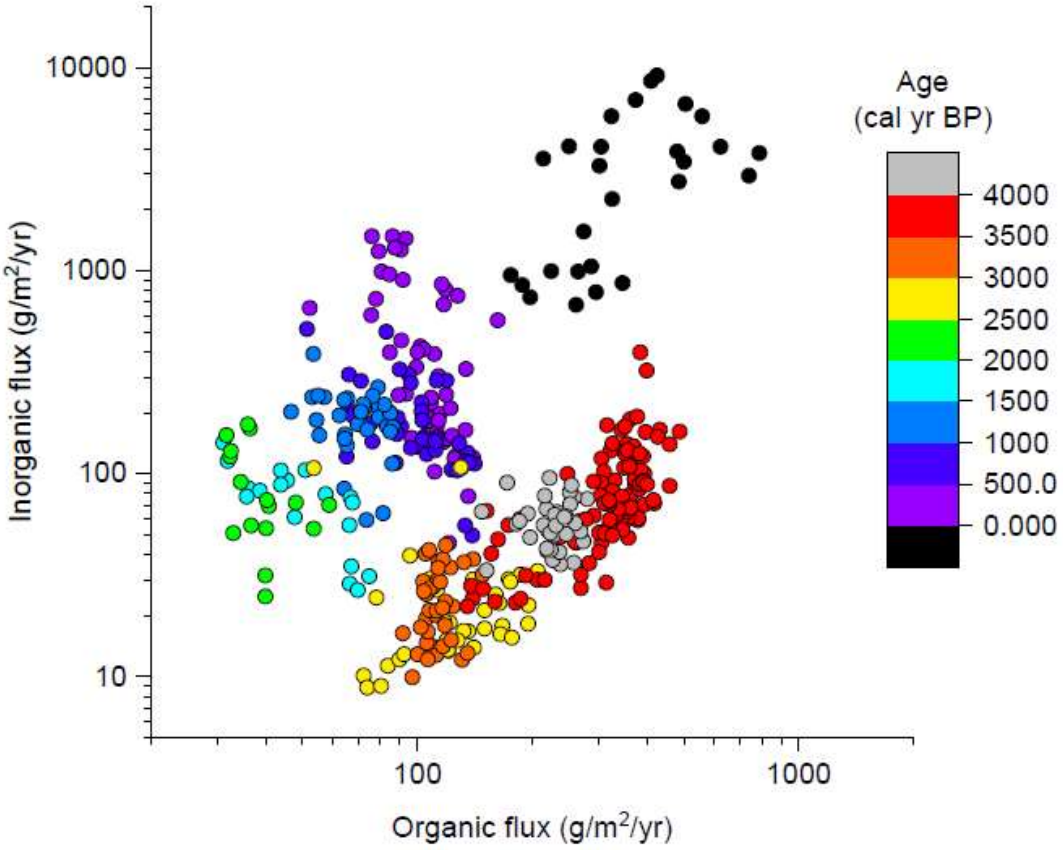

Figure G2. Biplot between inorganic matter and organic matter accumulation rates of peat core DB on log scale. The different colors of dots correspond to ages.

Appendix H

Evidence for a longer but variable growing season length over the last century for peat patch *Sphagnum* on Arctic tundra of the North Slope of Alaska

1. Introduction

The Arctic tundra landscape has been seen as a net source of CO_2 to the atmosphere due to elevated CO_2 release during the snow-covered season (Euskirchen et al., 2012). On North Slope of Alaska, *Sphagnum* peat is widespread as individual patches on tussock tundra. The recent study by Cleary (2015) indicated that these *Sphagnum* peat patches were not in this landscape until the past century, and the onset of *Sphagnum* peat patches represents an important transformation for tundra landscape. Given that *Sphagnum* mosses are the keystone species in boreal peat-forming ecosystems, *Sphagnum* expansion might turn the extant tundra into peatlands in the future as the hotspot of carbon sequestration. The onset and expansion of *Sphagnum* peat patches are likely caused by progressive soil drying as a result of regional climate warming, an active layer deepening and an earlier snowmelt, and a longer growing season.

2. Methods

Based on the previous work by Cleary (2015) who has established the carbon accumulation history and the ecological change for several short peat soil cores from the North Slope of Alaska, I additionally analyzed *Sphagnum* cellulose $\delta^{13}C$ and $\delta^{18}O$ from these short cores to provide an overall trend of growing season condition that allows persistent *Sphagnum* peat growth. The cellulose extraction and isotope analysis methods followed Chapter 4.

Chronology for these cores were established with multiple ^{14}C dates and age-depth modeling using CLAM program (Cleary, 2015). However, it is noted that the uncertainty in ^{14}C-based chronology is large for establishing proxy time series for the recent decades, so additional effort is required to fully account for the range of uncertainty of proxy data derived from these peat cores using a Monte Carlo method, but it still remains to do.

3. Results and discussion

The results are summarized in Figure H1. Due to the uncertainty in chronology, I mainly discuss the results from UIC13-3 that has the best chronology. The cellulose $\delta^{13}C$ data show negative shift that seems slightly larger than the Suess effect. The cellulose $\delta^{18}O$ data show an overall increasing trend of at least 2‰ during the twentieth century with an interval of relatively low values around 1970–1980 AD. The highest cellulose $\delta^{18}O$ values occurred around 2000–2010 AD, but since 2010 AD there is a decreasing trend. I argue that *Sphagnum* cellulose $\delta^{18}O$ reflect the growing season length, with higher values indicating more snow-free days. If the snow-free condition lasted longer, the source water for *Sphagnum* was predominantly derived from summer precipitation with high $\delta^{18}O$ values. By contrast, if the snow-free days condition was shorter, snowmelt with much lower $\delta^{18}O$ values of winter precipitation would be more important source water for *Sphagnum* in that short window of growth. It could explain the decreasing trend of cellulose $\delta^{18}O$ since 2007 AD as the Toolik Research Station also recorded almost two months' shortening of snow-free days before the sampling campaign in 2014.

The overall results seem to support that the growing season for *Sphagnum* has lengthened over the past century, but there is also a large natural variability in growing season lengths, such as during the recent years when Toolik monitoring data are available and suggest a shortening in snow-free days. The growing season length should be

determined by both the summer temperature and the thickness of winter snow. The regional warming is well documented by weather station data and proxy records that and has been invoked to explain the ecosystem state shift in permafrost peatlands in this region (Taylor et al., 2019). However, the *Sphagnum* cellulose $\delta^{18}O$ data suggest that winter precipitation and snow accumulation also matter to determine the length of following growing season, at least for *Sphagnum* patches. Additional studies are needed to determine what controls the length of snow-free days each year on tundra landscape, while *Sphagnum* cellulose $\delta^{18}O$ could serve as the potential proxy for the growing season length on multidecadal timescale.

4. Acknowledgments

I thank Kate Cleary for her previous work on these peat soil cores.

5. References

Cleary, K. (2015). Shrub Expansion, *Sphagnum* Peat Growth, and Carbon Sequestration in Arctic Tundra on the North Slope of Alaska (Master's thesis). Bethlehem, PA: Lehigh University.

Euskirchen, E. S., Bret-Harte, M. S., Scott, G. J., Edgar, C., & Shaver, G. R. (2012). Seasonal patterns of carbon dioxide and water fluxes in three representative tundra ecosystems in northern Alaska. *Ecosphere*, *3*(1), 4.

Rubino, M., Etheridge, D. M., Trudinger, C. M., Allison, C. E., Battle, M. O., Langenfelds, R. L., et al. (2013). A revised 1000 year atmospheric $\delta^{13}C$-CO_2 record from Law Dome and South Pole, Antarctica. *Journal of Geophysical Research: Atmospheres*, *118*(15), 8482–8499.

Taylor, L. S., Swindles, G. T., Morris, P. J., Gałka, M., & Green, S. M. (2019). Evidence for ecosystem state shifts in Alaskan continuous permafrost peatlands in response to recent warming. *Quaternary Science Reviews*, *207*, 134–144.

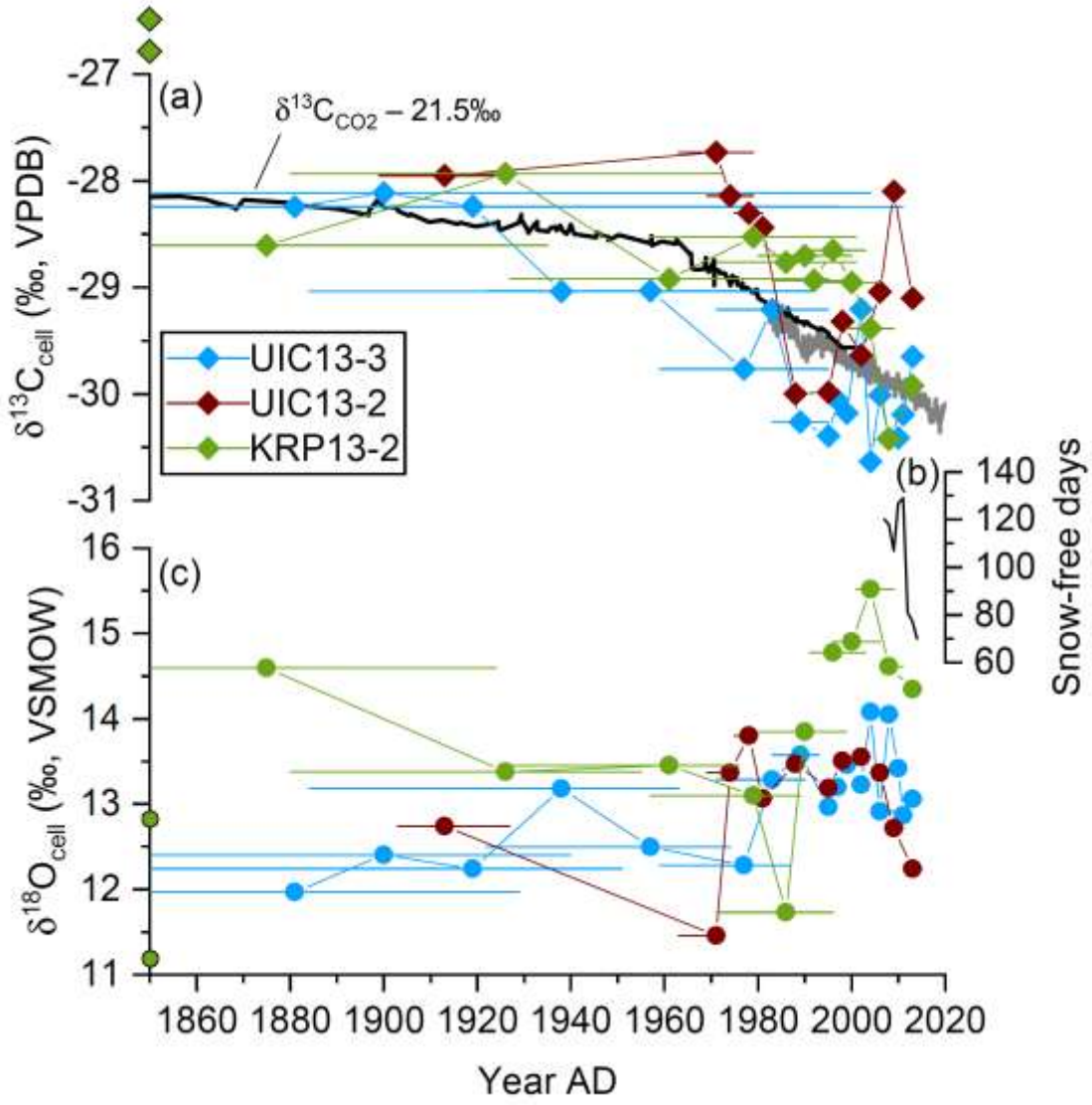

Figure H1. Summary of *Sphagnum* cellulose isotope analysis on three peat soil cores, UIC13-3 and UIC 13-2 (collected from upper Imnavait Creek), and KRP13-2 (collected from the Kuparuk River Peatland). (a) and (c) show the cellulose $\delta^{13}C$ and $\delta^{18}O$ data, respectively. The horizontal error bars are the 95% range of uncertainty of individual sample ages based on the original CLAM-based age-depth models (Cleary, 2015). The two KRP13-2 data points plotted on the vertical axis were from samples collected from the bottom half of that peat core with ages of around 3300–3500 cal yr BP. The scale of Suess effect on $\delta^{13}C$ of atmospheric CO_2 (black curve) is presented in (a) for reference,

including the data from ice cores (black line; Rubino et al., 2013) and from modern gas measurements from Barrow (now called Utqiagvik), Alaska (gray line; from https://scrippsco2.ucsd.edu/data/atmospheric_co2/ptb.html). (b) The number of snow-free days during 2007–2014 AD provided by Toolik Field Station Environmental Data Center (https://toolik.alaska.edu/edc/journal/annual_summaries.php?summary=snow).

Appendix I

Isotope data for peat core PAT16-AP1

Data Set I1: *Sphagnum* cellulose isotope data presented in Chapter 4 and Appendix E with Bacon-model age (cal yr BP).

Age	$\delta^{18}O$	$\delta^{13}C$	Age	$\delta^{18}O$	$\delta^{13}C$	Age	$\delta^{18}O$	$\delta^{13}C$	Age	$\delta^{18}O$	$\delta^{13}C$
-62	20.7	-25.7	249	20.0	-24.7	1696	21.2	-27.1	3976	21.5	-25.7
-60	20.9	-24.4	279	21.5	-24.0	1720	22.2	-26.9	4007	21.8	-25.9
-59	21.1	-24.1	298	21.6	-24.6	1739	21.8	-27.2	4037	22.3	-27.4
-57	20.8	-24.7	316	21.7	-23.9	1753	22.2	-26.9	4068	21.1	-28.5
-55	20.4	-24.4	334	21.5	-23.7	1764	21.4	-26.5	4123	22.1	-26.7
-53	21.2	-24.3	353	21.9	-23.8	1774	21.0	-26.4	4146	22.0	-26.6
-51	20.9	-23.6	369	21.1	-24.0	1784	21.7	-26.3	4173	22.2	-28.2
-49	21.2	-23.5	386	21.5	-23.7	1793	20.9	-26.5	4198	21.3	-27.4
-48	21.1	-23.9	405	22.5	-23.2	1801	21.0	-25.9	4222	21.3	-27.7
-47	21.3	-24.1	424	22.0	-23.3	1809	20.9	-26.1	4249	20.9	-27.8
-45	22.0	-23.5	444	21.3	-25.1	1816	20.6	-25.7	4280	22.5	-26.9
-44	20.2	-24.6	468	22.3	-26.2	1823	20.6	-26.7	4306	21.4	-27.1
-42	21.1	-24.8	494	22.3	-26.4	1831	21.1	-25.8	4332	21.0	-26.9
-39	21.4	-24.5	513	21.8	-26.1	1839	20.6	-26.3	4357	21.5	-27.2
-36	21.3	-24.1	534	21.6	-27.0	1846	21.7	-27.2	4385	20.3	-27.2
-33	20.6	-24.1	594	21.0	-27.1	1854	21.7	-25.1	4416	21.7	-26.9
-30	20.6	-24.4	688	21.0	-27.6	1863	23.4	-24.8	4445	22.9	-26.2
-27	20.8	-24.3	772	21.0	-28.0	1871	22.5	-24.8	4472	21.2	-27.1
-25	21.1	-24.0	851	20.1	-28.2	1881	21.3	-24.8	4497	20.8	-28.1
-22	21.5	-24.9	939	21.2	-28.1	2518	22.8	-24.5	4524	21.6	-27.0
-20	22.0	-24.4	977	22.6	-27.2	3281	n.a.	-27.9	4556	21.6	-26.8
-17	22.0	-25.2	1007	22.5	-23.8	3362	21.8	-28.0	4582	21.0	-26.2
-10	21.9	-25.1	1037	22.2	-24.3	3416	21.9	-26.7	4608	20.9	-27.0
0	21.7	-25.5	1065	20.7	-25.8	3444	21.7	-25.7	4636	22.3	-26.6
10	21.7	-24.5	1098	20.5	-26.1	3475	20.5	-25.9	4663	21.4	-25.6
20	22.4	-23.9	1146	21.9	-24.0	3511	22.0	-25.2	4691	22.2	-25.4
30	21.6	-25.1	1208	21.7	-26.2	3541	n.a.	-25.5	4846	21.8	-26.4
44	21.9	-25.6	1266	21.5	-26.4	3567	21.6	-27.8	4872	21.6	-26.1
62	22.0	-24.5	1317	21.4	-26.2	3592	21.4	-27.8	4899	21.3	-27.1
80	21.6	-25.4	1371	20.8	-28.1	3619	21.8	-25.7	4927	21.3	-27.5
93	21.5	-25.2	1408	21.2	-27.1	3646	22.5	-25.3	4954	21.7	-27.1
106	21.8	-26.1	1448	20.4	-26.5	3674	21.1	-26.1	4981	21.6	-26.4
117	21.0	-25.0	1488	20.7	-25.8	3699	n.a.	-26.2	5009	22.0	-25.1
130	21.0	-23.9	1530	21.3	-26.2	3727	21.3	-26.3	5036	21.2	-26.3
144	20.7	-25.0	1565	21.7	-25.9	3755	21.6	-27.8	5062	20.5	-25.5
160	20.6	-25.6	1582	21.5	-27.1	3812	21.2	-26.7	5090	21.0	-25.9
173	20.9	-24.9	1600	21.6	-28.1	3835	21.3	-26.8	5329	22.5	-25.5
186	21.5	-25.0	1617	21.3	-27.7	3864	20.9	-27.7	5352	21.4	-26.5
198	20.7	-26.5	1633	21.8	-27.0	3896	21.6	-26.0			
213	21.1	-25.4	1652	22.1	-25.8	3923	22.1	-27.0			
232	20.8	-24.8	1673	21.7	-26.1	3950	21.4	-26.8			

Vita

Zhengyu Xia
Department of Earth and Environmental Sciences, Lehigh University
1 West Packer Avenue, Bethlehem, PA 18015-3001, USA
Personal E-mail: zhyxia@hotmail.com
Website: https://zhx215.github.io

RESEARCH INTERESTS

- Paleoclimatology: linking modern climate, through analyses on observational data and through underpinning the atmospheric dynamics, with paleoclimate data, to provide a cross-scale understanding on the climate system
- Biogeochemistry: the fundamental mechanisms and processes in terrestrial water, carbon, and nutrient cycle through stable isotopes and other lens of geochemical measurements to understand the feedbacks and consequences of global change

EDUCATION

- 2015–2020 Ph.D. in Earth and Environmental Sciences, Lehigh University, USA
- 2011–2015 B.S. in Geology, China University of Geosciences, Wuhan, P.R. China

PROFESSIONAL EXPERIENCE

- 2017–2019, 2020 Teaching Assistant, Lehigh University
  1) Teach and lead geoscience lab class EES022 (*Exploring Earth*) for both classroom and online for three semesters
  2) Assist with lab section and grading for EES152 (*Ecology*), EES357 (*Paleoecology and Landscape History*), and EES386 (*Wetland Ecology*)
- 2016–2017, 2019 Research Assistant, Lehigh University

PUBLICATIONS

- Peer-reviewed journal articles:

Xia, Z., and Butorovic, N. The influence of moisture transport pathways on monthly oxygen isotope composition of precipitation in southern Patagonia. *Journal of Geophysical Research: Atmospheres* (revision submitted on 03/05/2020)

Xia, Z., Zheng, Y., Stelling, J. M., Loisel, J., Huang, Y., and Yu, Z. Environmental controls on the carbon and water (H and O) isotopes in peatland *Sphagnum* mosses. *Geochimica et Cosmochimica Acta* (revision submitted on 01/15/2020)

Treat, C. C., Kleinen, T., Broothaerts, N., Dalton A. S., Dommain, R., Douglas, T. A., Drexler, J., Finkelstein S. A., Grosse, G., Hope, G., Hutchings, J., Jones, M. C., Kuhry, P., Lacourse, T., Lähteenoja, O., Loisel, J., Notebaert, B., Payne, R., Peteet, D., Sannel A. B. K., Stelling, J. M., Strauss, J., Swindles, G. T., Talbot, J., Tarnocai, C., Verstraeten, G., Williams, C. J., Xia, Z., Yu, Z., Väliranta, M., Hättestrand, M., Alexanderson, H., and Brovkin, V., 2019. Widespread global peatland establishment and persistence over the last 130,000 y. *Proceedings of the National Academy of Sciences*, *116*(11), 4822–4827.

Xia, Z., Yu, Z., and Loisel, J., 2018. Centennial-scale dynamics of the Southern Hemisphere Westerly Winds across the Drake Passage over the past two millennia. *Geology*, *46*(10), 855–858.

- Peer-reviewed book chapters:

Xia, Z. and Yu, Z. Applications of stable isotopes to studies of paleohydrology and Paleoclimatology. *Encyclopedia of Water: Science, Technology and Society*, Ed. P. A. Maurice, Wiley. doi: 10.1002/9781119300762.wsts0042

CONFERENCE ABSTRACTS

Xia, Z., Zheng, Y., Stelling, J. M., Loisel, J., Huang, Y., and Yu, Z. Environmental controls on the carbon and water (H and O) isotopes in peatland *Sphagnum* mosses. AGU Fall Meeting 2019, San Francisco, USA

Xia, Z. Investigating the influence of moisture sources and trajectories on monthly isotopic composition of precipitation using daily weather station data, HYSPLIT backward trajectory modeling, and moisture uptake analysis. AGU Fall Meeting 2018, Washington D.C., USA

Xia, Z., Yu, Z., Zheng, Y., Loisel J., and Huang, Y. Late-Holocene hydroclimate and atmospheric circulation variability in southern Patagonia: insights from triple stable isotopes ($\delta^{18}O$, $\delta^{13}C$, δD) of peat bog *Sphagnum* moss. AGU Fall Meeting 2017, New Orleans, USA

Treat, C. C., Broothaerts, N., Dalton, A., Dommain, R., Finkelstein, S., Grosse, G., Jones, M. C., Kleinen, T., Kuhry, P., Lacourse, T., Lähteenoja, O., Notebaert, B., Payne, R., Peteet, D. M., Sannel, B., Stelling, J., Strauss, J., Swindles, G., Talbot, J., Tarnocai, C., Verstraeten, G., Williams, C., Xia, Z., Yu, Z., and Brovkin, V. Buried Peats: Past Peatland Distribution as an Indicator of Hydroclimate and Temperature. AGU Fall Meeting 2016, San Francisco, USA

Yu, Z., Beilman D., Loisel J., Stelling, J. M., Xia, Z., Parnikoza, I. Solar heating, microclimate, and the formation of peat-accumulating ecosystems in Antarctica. XXXIV SCAR Open Science Conference (2016), Kuala Lumpur, Malaysia

Xia, Z., Yu, Z., Loisel, J., and Stelling J. M. A 500-year record of atmospheric circulation change in southern Patagonia from dual water isotopes of subfossil *Sphagnum* moss cellulose. VIII Southern Connection Congress (2016), Punta Arenas, Chile

ORAL PRESENTATIONS

School of Geographical Sciences, Northeast Normal University, Changchun, China (2019)

PAGES CLIVASH2k Workshop, British Antarctic Survey, Cambridge, UK (2018)

Paleoclimatology and Paleoceanography section at AGU Fall Meeting, New Orleans, USA (2017)

HONORS AND AWARDS

Lehigh University EES Graduate Symposium Best Talk Winner (2018, 2020)

Lehigh University Williams-Upton Summer Fellowship (2019)

The University of Utah SPATIAL short course participant support award (2019)

Lehigh University College of Arts and Sciences Summer Research Fellowship (2018)

Lehigh University Presidential Fellowship (2015)

FIELD WORK EXPERIENCE

Toolik Field Station area, Alaska North Slope (2019)

Antarctic Peninsula Palmer Station area (2018–2019)

Patagonian peatlands in Chile (2016)

Peatlands in northeastern and central China (2014)

Geological field work training in China (2012–2014)

SERVICES

Reviewer for *The Holocene* (2), *Climate of the Past*, *Experimental Results*

PROFESSIONAL AFFILIATION

American Geophysical Union (2017–pres.)